

**THE SYNTHESIS AND REACTIVITY OF LOW-COORDINATE ENAMIDO-  
PHOSPHINIMINE IRON COMPLEXES**

by

Nicholas M. Hein

B.Sc.(H), The University of Minnesota, 2012

A THESIS SUBMITTED IN PARTIAL FULFILLMENT OF  
THE REQUIREMENTS FOR THE DEGREE OF

DOCTOR OF PHILOSOPHY

in

THE FACULTY OF GRADUATE AND POSTDOCTORAL STUDIES  
(Chemistry)

THE UNIVERSITY OF BRITISH COLUMBIA

(Vancouver)

May, 2017

© Nicholas M. Hein, 2017

## Abstract

Unsymmetrical, bidentate ancillary ligand scaffolds containing enamido-phosphinimine donors (NpN) were developed for the synthesis of low-coordinate iron complexes. A variety of ligands varying in steric hindrance were synthesized through the modularity of the Staudinger reaction. Trigonal planar and dimeric tetrahedral iron bromide complexes were fully characterized and served as precursors for further reactivity.

The reduction chemistry of NpN iron bromide complexes was investigated and a number of end-on bridging N<sub>2</sub> complexes were characterized by X-ray crystallography. Analysis of the coordinated N<sub>2</sub> bond length indicated that the NpN scaffold does not contribute to enhanced bond activation in comparison to well-established  $\beta$ -diketimate iron N<sub>2</sub> complexes. Additionally, an NpN ligand with an indene linker was synthesized with the intent of generating an anionic indenyl moiety that would contribute electron density to the Fe–N<sub>2</sub> backbonding interaction. Unfortunately, DFT results indicated that minimal enhancement to activation results from this effect. A reoccurring observation in the attempted synthesis of NpN dinitrogen complexes was that the P=N bond of the phosphinimine was susceptible to cleavage under reducing conditions.

A low-coordinate, dimeric NpN iron hydride was synthesized and its reactivity with unsaturated substrates was explored. The products from hydride insertion into azobenzene, 3-hexyne, and 1-azidoadamantane were characterized and did not vary significantly from the analogous products reported for the reactivity of  $\beta$ -diketimate iron hydrides. Surprisingly, the NpN iron hydride displays unprecedented reactivity towards hexafluorobenzene, affording an NpN iron fluoride complex and pentafluorobenzene as products. The NpN iron hydride is a

precatalyst for catalytic hydrodefluorination of perfluorinated aromatics in the presence of silane. Kinetic studies indicated that the rate-determining step during catalysis involved silane.

Enamine-phosphazide intermediates were isolated during the Staudinger reaction and were stable to deprotonation and coordination to Fe(II) and Co(II) halides. The enamido-phosphazide iron bromide complex displayed unusual reactivity upon treatment with potassium triethylborohydride, affording a dimeric phosphinimido species with an Fe–Fe bond. Isotopic labeling studies indicated that cleavage of the phosphazide N–C(aryl) bond occurred through a radical process.

## **Lay Summary**

Inorganic chemistry has many facets, one of which is the study of coordination compounds. Coordination compounds, also known as metal complexes, are species that have a metal atom with various other molecules (ligands) bonded to the metal. An important area of research in coordination chemistry is the study of how ligands can impact the structure and reactivity of the resulting metal complex. By careful design of the ligand scaffold coordinated to a metal, desirable reactivity can be obtained. This may have beneficial outcomes for society, as chemical processes that were once difficult or produced large amounts of waste can be facilitated and made more efficient through the utilization of carefully designed metal complexes as catalysts.

The work presented in this thesis outlines the study of a newly designed ligand and how it bonds to iron to form new complexes. The structure and reactivity of the resulting complexes is described herein.

## Preface

I, in consultation with my research supervisor Dr. Michael D. Fryzuk, designed and performed all experiments described in this thesis. I performed the synthesis, NMR spectroscopic characterization, and analysis for all new compounds described in Chapters 2, 3, 4, and 5. For compounds listed below that had been previously prepared or characterized by X-ray crystallography, I repeated the syntheses and NMR characterization. All NMR spectra and analyses presented in this thesis were performed by myself. Dr. Vincent T. Annibale, Fraser S. Pick, Dr. Richard Burford, and Alyssa Yeo collected the X-ray crystallographic data, which was analyzed by myself. In addition, I wrote all content presented in this thesis, with feedback and revisions from Dr. Richard Burford and Dr. Michael D. Fryzuk.

Portions of Chapter 2 have been published: [Hein, N. M.]; Suzuki, T.; Ogawa, T.; Fryzuk, M. D. *Dalton Trans.* **2016**, *45*, 14697-14708. I wrote the above manuscript, with input from Dr. Michael D. Fryzuk. Compounds **2.16a-b** and **2.17a-b** were originally synthesized by Dr. Truman Wambach. Dr. Tatsuya Suzuki originally prepared ligand **2.18c** and complexes **2.23c** and **2.25c**. He also grew X-ray quality crystals of **2.25c**. Ligand **2.18a** was originally described by Dr. Takahiko Ogawa. Dr. Brian O. Patrick aided in the analysis of the X-ray crystallographic data for **2.26**. Mössbauer spectroscopy of **2.25c** was performed by Professor Yoichi Sakai at Daido University.

Chapter 4 is largely based on the publication: Ogawa, T.; Suzuki, T.; [Hein, N. M.]; Pick, F. S.; Fryzuk, M. D. *Dalton Trans.* **2015**, *44*, 54-57. Dr. Michael D. Fryzuk wrote the above manuscript but Chapter 4 was written by myself, with contributions not featured in the aforementioned publication. Dr. Takahiko Ogawa originally prepared ligand **4.6**, potassium

complex **4.7**, and the iron complexes **4.8** and **4.9**. In addition, Dr. Ogawa also grew X-ray quality crystals of **4.6**, **4.7**, **4.8**, and **4.9**. Dr. Tatsuya Suzuki performed preliminary experiments that indicated the conversion of **4.8** to **4.9** operated through a radical process. I resynthesized all compounds for full characterization and provided additional evidence for the radical pathway. Fraser S. Pick transported samples of **4.8** and **4.9** to Simon Fraser University for Mössbauer analysis. John R. Thompson performed the Mössbauer spectroscopy for **4.8** and **4.9**.

# Table of Contents

<b>Abstract.....</b>	<b>ii</b>
<b>Lay Summary .....</b>	<b>iv</b>
<b>Preface.....</b>	<b>v</b>
<b>Table of Contents .....</b>	<b>vii</b>
<b>List of Figures.....</b>	<b>xi</b>
<b>List of Schemes .....</b>	<b>xxi</b>
<b>List of Symbols .....</b>	<b>xxvi</b>
<b>List of Abbreviations .....</b>	<b>xxviii</b>
<b>Acknowledgements .....</b>	<b>xxxii</b>
<b>Dedication .....</b>	<b>xxxiii</b>
<b>Chapter 1: Introduction .....</b>	<b>1</b>
1.1 Low-Coordinate Transition Metal Complexes .....	1
1.2 First-Row Transition Metal Complexes Featuring $\beta$ -Diketiminato Ligands .....	3
1.3 Ligand Design Used in This Thesis .....	10
1.4 Phosphinimine Synthesis and First-Row Transition Metal Complexes Containing Phosphinimine Ligands.....	11
1.5 Characterization Techniques for Paramagnetic Complexes .....	14
1.5.1 General Considerations .....	14
1.5.2 The Paramagnetic $^1\text{H}$ NMR Experiment.....	15
1.5.3 Magnetic Susceptibility .....	20
1.5.4 Mössbauer Spectroscopy .....	22

1.6	Scope of Thesis .....	23
<b>Chapter 2: Iron Dinitrogen Complexes .....</b>		<b>26</b>
2.1	Introduction.....	26
2.1.1	Dinitrogen Activation .....	26
2.1.2	$\beta$ -diketimate Iron Dinitrogen Complexes .....	28
2.2	Ligand Synthesis.....	33
2.3	Synthesis of Iron Dinitrogen Complexes.....	38
2.3.1	Synthesis of Low-Coordinate Iron Bromide Complexes.....	38
2.3.2	Reduction Chemistry .....	47
2.3.3	DFT Analysis .....	61
2.4	Dianionic Indenyl Ligand and Coordination Attempts.....	65
2.5	Conclusions.....	70
<b>Chapter 3: Iron Hydride Complexes.....</b>		<b>72</b>
3.1	Introduction.....	72
3.2	Synthesis of Low-Coordinate Iron Hydride Complexes.....	75
3.3	Hydride Insertion Reactivity.....	86
3.4	Catalytic Hydrodefluorination .....	93
3.4.1	HDF Utilizing Low-Coordinate Iron Hydride Precatalysts .....	93
3.4.2	Mechanistic Considerations .....	102
3.5	Attempts at an Alternate Synthesis for Iron(II) Fluoride Complexes.....	108
3.6	Conclusions.....	109
<b>Chapter 4: Enamido-Phosphazide Complexes of Iron and Cobalt.....</b>		<b>111</b>
4.1	Introduction.....	111

4.2	Enamido-Phosphazide Synthesis .....	112
4.3	Synthesis of an Iron(II) Phosphazide Complex and Hydride Metathesis Reactivity..	115
4.4	Cobalt Enamido-Phosphazide Complexes .....	123
4.5	Conclusions.....	129
<b>Chapter 5: Thesis Overview and Future Directions.....</b>		<b>130</b>
5.1	Overview.....	130
5.2	Future Directions .....	132
5.2.1	Alternative Synthesis of Reactive Low-Coordinate Hydrides.....	132
5.2.2	Further Investigations into Catalysis .....	135
5.2.2.1	Alkene Isomerization .....	135
5.2.2.2	C–H Bond Activation .....	138
<b>Chapter 6: Experimental Details.....</b>		<b>146</b>
6.1	General Procedures .....	146
6.2	Starting Materials and Reagents .....	148
6.3	Synthesis of Compounds.....	149
6.3.1	Compounds Pertaining to Chapter 2.....	149
6.3.2	Compounds Pertaining to Chapter 3.....	166
6.3.3	Compounds Pertaining to Chapter 4.....	174
6.3.4	Compounds Pertaining to Chapter 5.....	180
<b>Bibliography .....</b>		<b>183</b>
<b>Appendices.....</b>		<b>191</b>
Appendix A - Crystallographic Information.....		191
Appendix B - Kinetics for HDF of C <sub>5</sub> F <sub>5</sub> N – Production of Et <sub>3</sub> SiF.....		207

## List of Tables

<b>Table 2.1:</b> Comparison of Bond Distances and Angles Obtained From Various Fe-N <sub>2</sub> Complexes.....	53
<b>Table 2.2:</b> Select Calculated Bond Distances and Atomic Charges.....	63
<b>Table 3.1:</b> Hydrodefluorination Results Utilizing the Iron(II) Hydride Complex <b>3.6a</b> in Comparison to the Catalytic Activity of the $\beta$ -diketiminato Iron(II) Fluoride Catalyst <b>3.5</b> .....	99
<b>Table 3.2:</b> Parameters for Kinetic Investigation of C <sub>5</sub> F <sub>5</sub> N HDF.....	102

## List of Figures

<b>Figure 1.1:</b> Some examples of low-coordinate complexes utilizing sterically demanding ligands. <b>1.1</b> see ref 4. <b>1.2</b> see ref 7. <b>1.3</b> see ref 8. <b>1.4</b> see ref 14.....	2
<b>Figure 1.2:</b> Homoleptic $\beta$ -diketiminato complexes are isolated if substituents at R are sterically unencumbered.....	4
<b>Figure 1.3:</b> Examples of $\beta$ -diketiminato complexes used in small molecule activation, <b>1.10</b> (ref 35) and <b>1.11</b> (ref 34), catalysis, <b>1.12</b> (ref 41) and <b>1.13</b> (ref 23), and as models for active sites of metalloproteins, <b>1.14</b> (ref 43) and <b>1.15</b> (ref 44).....	5
<b>Figure 1.4:</b> A comparison of the steric coverage of Co (G parameter) to reactivity. The less sterically hindered species <b>1.12</b> can perform hydrosilylation catalysis at lower catalytic loadings and at lower temperatures compared to the more sterically encumbered species <b>1.16</b> .....	7
<b>Figure 1.5:</b> A comparison of the catalytic activity for carbodiimide formation displayed by three $\beta$ -diketiminato complexes featuring varying degrees of steric hindrance. The most sterically bulky precatalyst <b>1.17</b> gives high product yields at lower temperature and shorter reaction times compared to the less sterically encumbered precatalysts investigated.....	8
<b>Figure 1.6:</b> Catalytic oxidation of cyclohexane with hydrogen peroxide using $\beta$ -diketiminato copper acetate complexes. When electron-withdrawing groups are installed at position R, catalytic activity is observed. In contrast, when R = Me there is zero reactivity.....	9
<b>Figure 1.7:</b> Comparison of a generic $\beta$ -diketiminato coordination complex (A) to the ligand scaffold presented in this thesis (B).....	10

**Figure 1.8:** A comparison of the steric profile of a cyclopentadienyl ligand compared to a phosphinimide in a generic metallocene species. Also shown are the two major resonance forms of a phosphinimine.....12

**Figure 1.9:** Examples of first-row transition metal complexes bearing phosphinimine containing ligands. **1.20** is used in Kumada cross-coupling reactions (ref 64). **1.21** displays transfer hydrogenation (ref 65). **1.22** is utilized in lactide polymerization (ref 66). **1.23** can be reduced to give a N<sub>2</sub> complex (ref 72). A variety of derivatives of **1.24** (ref 68) and **1.26** (ref 52) are ethylene polymerization catalysts. **1.25** is reported in ref 71.....13

**Figure 1.10:** (a) The splitting of energy levels for a 1/2 spin nucleus in an external magnetic field. As the strength of the external magnetic field (B<sub>0</sub>) increases, the energy difference (ΔE) between the spin +1/2 state and the spin -1/2 state also increases. (b) The resulting population distribution of nuclei with the +1/2 spin-state is slightly greater than the number of nuclei with the -1/2 spin state, resulting in a net magnetization vector pointing in the same orientation as the external magnetic field.....16

**Figure 1.11:** A paramagnetic metal M in an external magnetic field B<sub>0</sub>. The magnetic dipole of the unpaired electron(s) orients along the external field, resulting in a dipolar magnetic field. Proton H<sub>A</sub> is situated such that the external magnetic field and the dipolar magnetic field are additive, whereas H<sub>B</sub> is located at a position where the dipolar magnetic field subtracts from the external magnetic field.....17

**Figure 1.12:** The use of different aryl azides in the Staudinger reaction allows for synthetic modularity in the generation of sterically unsymmetrical ligand scaffolds.....24

**Figure 2.1:** The Iron-Molybdenum cofactor found within the nitrogenase enzyme.....27

<b>Figure 2.2:</b> Catalytic systems capable of converting N <sub>2</sub> to NH <sub>3</sub> . <b>2.1</b> see ref 100. All three variations of <b>2.2</b> where E = B, Si, and C are reported in ref 101. <b>2.3</b> see ref 102. <b>2.4</b> see ref 103. <b>2.5</b> see ref 104. <b>2.6</b> see ref 105. The NH <sub>3</sub> equivalents shown are the highest single run values reported for each complex.....	28
<b>Figure 2.3:</b> ORTEP drawing of the solid-state molecular structure of <b>2.19</b> .....	35
<b>Figure 2.4:</b> ORTEP drawing of the solid-state molecular structure of <b>2.20</b> .....	36
<b>Figure 2.5:</b> ORTEP drawing of the solid-state molecular structure of <b>2.22</b> .....	38
<b>Figure 2.6:</b> <sup>1</sup> H NMR spectra for [C <sup>Y5</sup> NpN <sup>DIPP,DIPP</sup> ]FeBr <b>2.23a</b> in <i>d</i> <sub>6</sub> -benzene (top), <i>d</i> <sub>2</sub> -DCM (middle), and <i>d</i> <sub>8</sub> -THF (bottom).....	40
<b>Figure 2.7:</b> <sup>1</sup> H NMR spectra for [C <sup>Y5</sup> NpN <sup>DIPP,Mes</sup> ]FeBr <b>2.23c</b> in <i>d</i> <sub>6</sub> -benzene (top), <i>d</i> <sub>2</sub> -DCM, (middle) and <i>d</i> <sub>8</sub> -THF (bottom).....	41
<b>Figure 2.8:</b> <sup>1</sup> H NMR spectra for <b>2.23a</b> (top), <b>2.23b</b> (middle), and <b>2.23c</b> (bottom) (400 MHz, <i>d</i> <sub>8</sub> -THF, 298 K).....	42
<b>Figure 2.9:</b> ORTEP drawing of the solid-state molecular structure of <b>2.23a</b> .....	43
<b>Figure 2.10:</b> ORTEP drawing of the solid-state molecular structure of <b>2.24</b> .....	45
<b>Figure 2.11:</b> ORTEP drawing of the solid-state molecular structure of <b>2.23c</b> .....	46
<b>Figure 2.12:</b> ORTEP drawing of the solid-state molecular structure of <b>2.23b</b> .....	47
<b>Figure 2.13:</b> ORTEP drawing of the solid-state molecular structure of <b>2.25a</b> .....	48
<b>Figure 2.14:</b> <sup>1</sup> H NMR spectra for the mixture of products obtained from the reduction of [C <sup>YP</sup> NpN <sup>DIPP,DIPP</sup> ]FeBr <b>2.23a</b> with KC <sub>8</sub> in the presence of N <sub>2</sub> (top spectrum) and the reduction of <b>2.23a</b> under vacuum to give exclusively [C <sup>YP</sup> NpN]Fe(μ-N-DIPP)Fe[NP <sup>CYP</sup> ] <b>2.26</b> (bottom) (300 MHz, <i>d</i> <sub>6</sub> -benzene, 298 K).....	49
<b>Figure 2.15:</b> ORTEP drawing of the solid-state molecular structure of <b>2.26</b> .....	50

<b>Figure 2.16:</b> ORTEP drawing of the solid-state molecular structure of <b>2.25c</b> .....	52
<b>Figure 2.17:</b> <sup>1</sup> H NMR spectra for the reduction of <b>2.23c</b> under vacuum for 1 day, followed by exposure to N <sub>2</sub> (top spectrum), the reduction of <b>2.23c</b> under vacuum for 4 days, followed by exposure to N <sub>2</sub> (middle), and the spectrum for [( <sup>CYP</sup> NpN <sup>DIPP,Mes</sup> )Fe] <sub>2</sub> (μ-N <sub>2</sub> ) <b>2.25c</b> produced from the reduction of <b>2.23c</b> under an atmosphere of N <sub>2</sub> (bottom). Impurities denoted with (*) (300 MHz, <i>d</i> <sub>6</sub> -benzene, 298 K).....	54
<b>Figure 2.18:</b> Mössbauer spectrum for <b>2.25c</b> .....	55
<b>Figure 2.19:</b> ORTEP drawing of the solid-state molecular structure of <b>2.25b</b> .....	58
<b>Figure 2.20:</b> ORTEP drawing of the solid-state molecular structure of <b>2.27</b> .....	59
<b>Figure 2.21:</b> A comparison of the <sup>1</sup> H NMR spectra obtained for <b>2.27</b> (top spectrum) and for the product obtained from treatment of <b>2.27</b> with n-butyllithium (bottom spectrum). (300 MHz, <i>d</i> <sub>6</sub> -benzene, 298 K).....	60
<b>Figure 2.22:</b> The predicted identity for complex [ <b>2.28</b> ]. The lithium cations are omitted from the above structure, as they are from the DFT calculations to follow.....	61
<b>Figure 2.23:</b> Visualization of Natural Population Analysis results showing charge distribution within <b>2.27</b> and [ <b>2.28</b> ]. Intensity of color indicates magnitude of charge, where green indicates positive charge, red indicates negative charge, and black indicates neutral charge. The numerical values associated with the atoms in <b>Figure 2.23</b> are summarized in <b>Table 2.2</b> .....	62
<b>Figure 2.24:</b> Alpha molecular orbitals for the dπ-N <sub>2</sub> π* interaction in <b>2.27</b> (a) and [ <b>2.28</b> ] (b). The molecular orbitals associated with the overlap between the aromatic system of the ligand backbone and the π orbital of N <sub>2</sub> are shown in (c) for <b>2.27</b> and (d) for [ <b>2.28</b> ].....	64
<b>Figure 2.25:</b> ORTEP drawing of the solid-state molecular structure of <b>2.29</b> .....	66

<b>Figure 2.26:</b> $^1\text{H}$ NMR comparison between <b>2.22</b> (top spectrum) (400 MHz, $d_6$ -benzene, 298 K) and <b>2.29</b> (bottom spectrum) (400 MHz, $d_8$ -THF, 298 K).....	67
<b>Figure 2.27:</b> $^1\text{H}$ NMR comparison between <b>2.29</b> (top spectrum) (400 MHz, $d_8$ -THF, 298 K) and <b>[2.30]</b> (bottom spectrum) (400 MHz, $d_6$ -benzene, 298 K).....	68
<b>Figure 2.28:</b> ORTEP drawing of the solid-state molecular structure of <b>2.31</b> .....	69
<b>Figure 3.1:</b> Select examples of catalytic hydrodefluorination (HDF) reported for iron(II) fluoride $\beta$ -diketimate complex <b>3.5</b> . Each reaction was performed in $d_8$ -THF using 20 mol% of catalyst. Triethylsilane was used as a hydride source.....	74
<b>Figure 3.2:</b> ORTEP drawing of the solid-state molecular structure of <b>3.6a</b> .....	76
<b>Figure 3.3:</b> $^1\text{H}$ NMR spectra for <b>3.6a</b> in $d_6$ -benzene (top) and $d_8$ -THF (bottom). Both spectra were collected at 400 MHz at 25 °C.....	77
<b>Figure 3.4:</b> ORTEP drawing of the solid-state molecular structure of <b>3.7</b> .....	78
<b>Figure 3.5:</b> $^1\text{H}$ NMR spectra for <b>3.6a</b> (top), <b>3.8a</b> (middle), and the product mixture from which single crystals of <b>3.7</b> were grown (bottom). Red triangles for <b>3.6a</b> and blue circles for <b>3.8a</b> are used to mark discernable signals belonging to their respective compounds in the complicated product mixture shown in the bottom spectrum. All spectra recorded at 300 MHz in $d_6$ -benzene at 25 °C.....	80
<b>Figure 3.6:</b> ORTEP drawing of the solid-state molecular structure of <b>3.8a</b> .....	81
<b>Figure 3.7:</b> The $^1\text{H}$ NMR spectrum for the reaction of <b>3.6a</b> with $\text{BEt}_3$ at 60 °C for 2h (300 MHz, $d_8$ -toluene, 25 °C) compared to the $^1\text{H}$ NMR spectrum for <b>3.8a</b> (300 MHz, $d_6$ -benzene, 25 °C).....	81

<b>Figure 3.8:</b> $^1\text{H}$ NMR spectra for the reaction of <b>2.23c</b> with $\text{KBEt}_3\text{H}$ at $-35\text{ }^\circ\text{C}$ with a reaction time under 5 minutes (300 MHz, $d_8$ -toluene, $25\text{ }^\circ\text{C}$ ), and the reaction of <b>2.23c</b> with $\text{KBEt}_3\text{H}$ at $25\text{ }^\circ\text{C}$ with an overnight reaction time (300 MHz, $d_6$ -benzene, $25\text{ }^\circ\text{C}$ ).....	82
<b>Figure 3.9:</b> $^1\text{H}$ NMR spectra for the reaction of <b>2.23c</b> with $\text{KBEt}_3\text{H}$ at $-35\text{ }^\circ\text{C}$ with a reaction time under 5 minutes (300 MHz, $d_8$ -toluene, $25\text{ }^\circ\text{C}$ ) in comparison to the iron ethyl complex <b>3.8b</b> (300 MHz, $d_6$ -benzene, $25\text{ }^\circ\text{C}$ ). The presence of complex <b>3.8b</b> is observed in the product mixture obtained from the reaction of <b>2.23c</b> with $\text{KBEt}_3\text{H}$ .....	83
<b>Figure 3.10:</b> ORTEP drawing of the solid-state molecular structure of <b>3.8b</b> .....	84
<b>Figure 3.11:</b> ORTEP drawing of the solid-state molecular structure of <b>3.6b</b> .....	85
<b>Figure 3.12:</b> ORTEP drawing of the solid-state molecular structure of <b>3.9</b> .....	87
<b>Figure 3.13:</b> $^1\text{H}$ NMR spectra for complex <b>3.9</b> heated to $50\text{ }^\circ\text{C}$ over the course of 24 hours. Conversion is nearly complete after 7 hours of heating to $50\text{ }^\circ\text{C}$ . The new paramagnetic species formed is the anilido complex <b>3.12</b> ( $d_6$ -benzene, 300 MHz, $25\text{ }^\circ\text{C}$ ).....	88
<b>Figure 3.14:</b> ORTEP drawing of the solid-state molecular structure of <b>3.12</b> .....	89
<b>Figure 3.15:</b> ORTEP drawing of the solid-state molecular structure of <b>3.10</b> .....	90
<b>Figure 3.16:</b> ORTEP drawing of the solid-state molecular structure of <b>3.11</b> .....	91
<b>Figure 3.17:</b> $^1\text{H}$ NMR spectra for complex <b>3.11</b> in comparison to [ <b>3.13</b> ], the product formed from heating <b>3.11</b> to $80\text{ }^\circ\text{C}$ for 3 days ( $d_6$ -benzene, 300 MHz, $25\text{ }^\circ\text{C}$ ).....	92
<b>Figure 3.18:</b> $^{19}\text{F}$ NMR spectra for the stoichiometric reaction of <b>3.6a</b> with $\text{C}_6\text{F}_6$ at $70\text{ }^\circ\text{C}$ in $d_8$ -THF. $^{19}\text{F}$ NMR spectra were collected after 15 minutes, 1 hour, 2 hours, and 1 day ( $d_8$ -THF, 282 MHz, $25\text{ }^\circ\text{C}$ ).....	94
<b>Figure 3.19:</b> ORTEP drawing of the solid-state molecular structure of <b>3.14</b> .....	96

**Figure 3.20:**  $^{19}\text{F}$  NMR for the catalytic HDF of pentafluoropyridine ( $\text{C}_5\text{F}_5\text{N}$ ) using  $\text{Et}_3\text{SiH}$  as the fluoride trap and 5 mol% of **3.6a** as the precatalyst ( $d_8$ -THF,  $50\text{ }^\circ\text{C}$ ). After 18 hours, the appearance of the ortho and meta  $^{19}\text{F}$  resonances belonging to 2,3,5,6-tetrafluoropyridine (*p*- $\text{C}_5\text{HF}_4\text{N}$ ), along the  $^{19}\text{F}$  resonance for  $\text{Et}_3\text{SiF}$  are observed. After 3 days, the resonance belonging to the para-F of  $\text{C}_5\text{F}_5\text{N}$  is no longer observed, indicating complete consumption of  $\text{C}_5\text{F}_5\text{N}$ .

Fluorobenzene was used as the internal standard and is denoted with \*.....98

**Figure 3.21:** Stacked variable temperature for a  $d_8$ -THF solution of the dimeric iron hydride

**3.6a**. There is not an appreciable difference in the spectra across the various temperatures

recorded. Spectra collected at 400 MHz.....100

**Figure 3.22:** Stacked variable temperature for a  $d_8$ -THF solution of the dimeric iron hydride

**3.6a**. This zoomed-in region shows a new set of resonances that appear at  $\delta$  37.3 and 35.4 at  $60$

$^\circ\text{C}$ , designated with “\*”. These same signals disappear upon cooling the NMR sample to  $25\text{ }^\circ\text{C}$ .

Spectra collected at 400 MHz.....101

**Figure 3.23:** Progress of HDF for pentafluoropyridine showing the changes in rate due to

changes in substrate concentration relative to a reference experiment with  $[\text{silane}]=[\text{PyF}]=0.11$

$\text{M}$ ,  $[\text{Fe}]=5.5 \times 10^{-3}\text{ M}$  using  $d_8$ -THF at  $50\text{ }^\circ\text{C}$ .....102

**Figure 3.24:** A comparison of the  $^1\text{H}$  NMR spectra collected at the final time points of various

HDF catalytic runs using different substrates. With the exception of the trial utilizing *n*- $\text{BuSiH}_3$

as the fluoride acceptor, all observed resonances are consistent between trials. This indicates that

the HDF catalytic resting state is independent of the fluorinated substrate. All spectra collected in

$d_8$ -THF at 300 MHz at  $25\text{ }^\circ\text{C}$ .....104

**Figure 3.25:** A comparison of the  $^1\text{H}$  NMR spectra for **3.6a**, **3.14**, and the final time points for the HDF catalytic runs (2 days) using **3.6a** and **3.14** as precatalysts. The resting state during catalysis is not the hydride species **3.6a**, nor apparently the fluoride species **3.14**. Spectra collected in  $d_8$ -THF at 300 MHz at 25 °C.....105

**Figure 3.26:**  $^1\text{H}$  NMR spectra for **3.6a** (top spectrum), the reaction between **3.6a** and  $\text{C}_6\text{F}_6$  (middle spectrum), and following reaction with  $\text{Et}_3\text{SiH}$  (bottom spectrum). Resonances belonging to the hydride **3.6a** are observed following the reaction with  $\text{Et}_3\text{SiH}$  are denoted with red circles. All spectra collected in  $d_8$ -THF at 300 MHz at 25 °C.....106

**Figure 4.1:** The only literature reported transition metal phosphazide complexes. **4.1** and **4.2** see ref. 168. **4.3** and **4.4** see ref 167. **4.5** see ref. 173.....111

**Figure 4.2:** ORTEP drawing of the solid-state molecular structure of **4.6**.....114

**Figure 4.3:** ORTEP drawing of the solid-state molecular structure of **4.7**.....115

**Figure 4.4:** ORTEP drawing of the solid-state molecular structure of **4.8**.....116

**Figure 4.5:** ORTEP drawing of the solid-state molecular structure of **4.9**.....117

**Figure 4.6:**  $^2\text{H}$  NMR spectrum for the reaction of complex **4.8** with  $\text{KBET}_3\text{D}$  in a sealed J. Young tube with protio-THF as the solvent.  $\text{D}_2$  is observed at  $\delta$  4.52. The natural abundance of  $^2\text{H}$  in THF gave the observed THF signals (400 MHz, THF, 298 K).....118

**Figure 4.7:** Gas chromatogram (a) and corresponding mass spectrum (b) obtained from a sample of authentic *m*-xylene dissolved in  $d_8$ -THF to act as a control. Gas chromatogram (c) and corresponding mass spectra obtained from the volatiles isolated from the reaction of complex **4.8** with  $\text{KBET}_3\text{H}$  in  $d_8$ -THF. The peak at 5.40 minutes in the GC corresponds to 2- $d_1$ -xylene. Note the signal intensity of the mass peak 107.1 for *m*-xylene (e) to that found in (b). The species observed at 6.17 minutes in the GC is from triethylborane (a by-product of the reaction) having

reacted with water vapor in air. The observed mass spectrum (f) matches the predicted spectrum for 2,4,6-triethylboroxin.....119

**Figure 4.8:**  $^{13}\text{C}\{^1\text{H}\}$  NMR (aromatic region) comparison of *m*-xylene (top) to the isolated volatiles (*d*<sub>8</sub>-THF as solvent) from the radical trapping experiment (bottom) (**Scheme 4.3** in text). The  $^1\text{H}$ - $^{13}\text{C}$  HSQC of *m*-xylene was used to confirm deuterium incorporation (1:1:1 triplet) at carbon position 1 in 1-*d*<sub>1</sub>-2,6-Me<sub>2</sub>C<sub>6</sub>H<sub>3</sub> (400 MHz, *d*<sub>8</sub>-THF, 298 K).....120

**Figure 4.9:**  $^{57}\text{Fe}$  Mössbauer spectra for powdered samples obtained at 295 K.

Complex **4.8** (a); dimeric species **4.9** (b). Solid red lines correspond to simulated data. The spectrum of **4.8** was fit as a quadrupole doublet with  $\delta = 0.92 \text{ mms}^{-1}$  and  $\Delta E_{\text{q}} = 2.40 \text{ mms}^{-1}$ . The signal intensity for **4.8** is consistently weak, even after over 10 days collection due to a poor recoil-free fraction. The symmetric dimer **4.9** can be fit as a single quadrupole doublet with  $\delta = 0.34 \text{ mms}^{-1}$  and  $\Delta E_{\text{q}} = 1.26 \text{ mms}^{-1}$  for the equivalent iron centers.....123

**Figure 4.10:** ORTEP drawing of the solid-state molecular structure of **4.11**.....124

**Figure 4.11:** A comparison of the  $^1\text{H}$  NMR spectra for the iron phosphazide complex **4.8** (top spectrum), the putative cobalt phosphazide THF complex [**4.12**] (middle) and the cobalt phosphazide pyridine complex **4.11** (bottom). All spectra collected at 300 MHz in *d*<sub>6</sub>-benzene at 298 K.....125

**Figure 4.12:** ORTEP drawing of the solid-state molecular structure of **4.13**.....127

**Figure 4.13:** A comparison of the  $^1\text{H}$  NMR spectra obtained for **4.11** (top spectrum) and **4.13** (bottom spectrum). Both spectra collected at 300 MHz in *d*<sub>6</sub>-benzene at 298 K.....128

**Figure 5.1:** Steric interaction between the *para* methyl groups of the mesityl moiety likely destabilizes the dimeric form of **3.6b** in solution, resulting in a higher concentration of the monomeric species.....133

<b>Figure 5.2:</b> A depiction of the steric influence affecting the isomerization of terminal alkenes to internal alkenes. Steric interaction with the NacNac scaffold prohibits the formation of the square planar transition state for E-2-hexene and Z-3-hexene.....	136
<b>Figure 5.3:</b> A hypothetical cobalt n-hexyl complex <b>[5.2]</b> and the implications of ligand sterics on the Z-3-hexene square planar transition state <b>[5.2]‡</b> .....	137
<b>Figure 5.4:</b> ORTEP drawing of the solid-state molecular structure of <b>5.12</b> .....	142

## List of Schemes

<b>Scheme 1.1:</b> The three-coordinate Mo complex <b>1.5</b> is capable of cleaving the N <sub>2</sub> triple bond to give the Mo nitride complex <b>1.6</b> (see ref 18). The three-coordinate Ta species <b>1.7</b> is capable of cleaving the CO triple bond to give the dicarbide <b>1.8</b> and the oxo complex <b>1.9</b> (see ref 17).....	3
<b>Scheme 1.2:</b> The condensation reaction between a β-diketone and a primary amine to generate the general β-diketimininate, where R, R', and R'' are sites of potential modification.....	4
<b>Scheme 1.3:</b> The mechanism for the Staudinger reaction. A phosphine performs a nucleophilic attack on an organic azide (1) to generate a phosphazide intermediate (2). The phosphazide goes through a four-membered ring transition state (3) which undergoes loss of N <sub>2</sub> and forms the phosphinimine (4).....	11
<b>Scheme 2.1:</b> Reduction of iron chloride complexes <b>2.7</b> and <b>2.8</b> with KC <sub>8</sub> in the presence of N <sub>2</sub> yields the bridging N <sub>2</sub> complexes <b>2.9</b> and <b>2.10</b> .....	29
<b>Scheme 2.2:</b> Reduction of the N <sub>2</sub> complexes <b>2.9</b> and <b>2.10</b> with KC <sub>8</sub> yields the further reduced N <sub>2</sub> complexes <b>2.11</b> and <b>2.12</b> .....	30
<b>Scheme 2.3:</b> Reduction of the β-diketimininate FeCl complex in the absence of N <sub>2</sub> leads to the formation of Fe(I) KCl adducts. If a crown ether is used to stabilize the generated KCl adduct, complex <b>2.13</b> can be isolated. Exposure of the KCl adducts to N <sub>2</sub> leads to the formation of <b>2.10</b> .....	30
<b>Scheme 2.4:</b> Reduction of <b>2.14</b> with KC <sub>8</sub> under an atmosphere of N <sub>2</sub> leads to the formation of <b>2.15</b> in which N <sub>2</sub> has been fully reduced to two N <sup>3-</sup> .....	31
<b>Scheme 2.5:</b> General ligand synthesis for the preparation of the enamine-phosphinimine ligands <b>2.18a-c</b> .....	33

<b>Scheme 2.6:</b> Synthesis for the indene ligand scaffold to the point where the enamine-phosphazide <b>2.20</b> was isolated.....	34
<b>Scheme 2.7:</b> Deprotonation with KH yields the corresponding potassium enamido-phosphinimine salts.....	37
<b>Scheme 2.8:</b> The salt metathesis reactions between the potassium salts <b>2.21a-c</b> and <b>2.22</b> with FeBr <sub>2</sub> (THF) <sub>2</sub> .....	39
<b>Scheme 2.9:</b> Proposed mechanism for the formation of complex <b>2.26</b> .....	51
<b>Scheme 2.10:</b> Reduction of <b>2.23c</b> with KC <sub>8</sub> under an atmosphere of N <sub>2</sub> leads to formation of <b>2.25c</b> .....	52
<b>Scheme 2.11:</b> Reduction of <b>2.23b</b> leads to a mixture of products, one of which is <b>2.25b</b> , as characterized by X-ray crystallography.....	57
<b>Scheme 2.12:</b> Treatment of <b>2.24</b> with KC <sub>8</sub> under an atmosphere of N <sub>2</sub> leads to the isolation of <b>2.27</b> .....	59
<b>Scheme 2.13:</b> Deprotonation of <b>2.22</b> with n-butyllithium yields the dianionic ligand salt <b>2.29</b> .....	65
<b>Scheme 2.14:</b> Oxidation of <b>2.29</b> by FeBr <sub>2</sub> (THF) <sub>2</sub> to yield <b>2.31</b> .....	70
<b>Scheme 3.1:</b> The dimeric β-diketiminato iron hydride <b>3.1</b> inserts into unsaturated substrates. Insertion into azobenzene yields the hydrido complex <b>3.2</b> (ref 132). Reaction with 3-hexyne gives complex <b>3.3</b> (ref 132) and reaction with 1-azidoadamantane yields the triazenido species <b>3.4</b> (ref 130).....	72
<b>Scheme 3.2:</b> General HDF catalytic cycle involving a metal hydride/fluoride couple.....	73
<b>Scheme 3.3:</b> Treatment of the iron bromide complex <b>2.23a</b> with KBEt <sub>3</sub> H at -35 °C affords the dimeric iron hydride <b>3.6a</b> .....	75

<b>Scheme 3.4:</b> The dimeric iron hydride complex <b>3.6a</b> reacts with triethylborane to give the dihydridoborate species <b>3.7</b> and the three-coordinate iron ethyl complex <b>3.8a</b> . The iron ethyl complex <b>3.8a</b> can be independently synthesized through treatment of <b>2.23a</b> with a THF solution of EtMgCl.....	79
<b>Scheme 3.5:</b> The reaction of <b>2.23c</b> with KBEt <sub>3</sub> H for the attempted synthesis of the dimeric iron hydride complex <b>3.6b</b> .....	82
<b>Scheme 3.6:</b> Insertion products isolated from the reaction of the iron hydride complex <b>3.6a</b> with azobenzene ( <b>3.9</b> ), 3-hexyne ( <b>3.10</b> ), and 1-azidoadamantane ( <b>3.11</b> ).....	86
<b>Scheme 3.7:</b> Thermolysis of the N–N bond of the hydrazido ligand leads to the formation of the anilido complex <b>3.12</b> , with the putative formation of half an equivalent of azobenzene.....	89
<b>Scheme 3.8:</b> Heating <b>3.11</b> to 80 °C results in the quantitative conversion to the likely amido species [ <b>3.13</b> ].....	93
<b>Scheme 3.9:</b> The reaction of <b>3.6a</b> with excess C <sub>6</sub> F <sub>6</sub> in THF afforded the dimeric iron(II) fluoride complex <b>3.14</b> .....	95
<b>Scheme 3.10:</b> A proposed catalytic cycle for HDF of C <sub>6</sub> F <sub>6</sub> with Et <sub>3</sub> SiH as the fluoride acceptor.....	107
<b>Scheme 3.11:</b> The attempted transmetallation of <b>3.8a</b> with Me <sub>3</sub> SnF.....	108
<b>Scheme 4.1:</b> Synthetic scheme for the formation of the enamine-phosphazide <b>4.6</b> and its deprotonation with KH to form the polymeric ligand potassium salt <b>4.7</b> .....	113
<b>Scheme 4.2:</b> Iron complex <b>4.8</b> is synthesized through the salt metathesis reaction between the ligand potassium salt <b>4.7</b> with FeBr <sub>2</sub> (THF) <sub>2</sub> . The reaction of <b>4.8</b> with KBEt <sub>3</sub> H yields the dimeric phosphinimido complex <b>4.9</b> .....	117

<b>Scheme 4.3:</b> The two deuterium labeling experiments used to propose the reaction mechanism for the conversion of <b>4.8</b> to <b>4.9</b> . Analysis of the products formed from the reaction of <b>4.8</b> with $\text{KBET}_3\text{D}$ in proteo-THF by $^2\text{H}$ NMR spectroscopy and GC/MS indicated that deuterium was not incorporated into <i>m</i> -xylene, but rather was lost as $\text{D}_2$ (Reaction 1). Treatment of <b>4.8</b> with $\text{KBET}_3\text{H}$ in $d_8$ -THF yielded 1- <i>d</i> <sub>1</sub> -2,6- $\text{Me}_2\text{C}_6\text{H}_3$ , as observed by $^{13}\text{C}\{^1\text{H}\}$ NMR spectroscopy and GC/MS (Reaction 2).....	121
<b>Scheme 4.4:</b> A possible radical pathway leading to the conversion of the phosphinimido complex <b>4.9</b> from the phosphazide complex <b>4.8</b> upon reaction with the hydride reagent $\text{KBET}_3\text{H}$ .....	122
<b>Scheme 4.5:</b> Treatment of the ligand potassium salt <b>4.7</b> with $\text{CoCl}_2(\text{Py})_4$ leads to the isolation of the cobalt phosphazide complex <b>4.11</b> . The cobalt alkyl species <b>4.13</b> is synthesized from the reaction of <b>4.11</b> with $\text{LiCH}_2\text{Si}(\text{Me})_3$ .....	126
<b>Scheme 5.1:</b> (a) The proposed synthesis of <b>3.6b</b> through reduction of <b>2.23c</b> and exposure to an atmosphere of $\text{H}_2$ . (b) A possible mechanism for the process of binuclear oxidative addition of $\text{H}_2$ via an Fe(I) intermediate.....	134
<b>Scheme 5.2:</b> Complex <b>5.1</b> catalyzes the isomerization of terminal alkenes to the internal <i>Z</i> -isomer through an alkyl mechanism (shown to the left).....	135
<b>Scheme 5.3:</b> Salt metathesis reaction between <b>2.21c</b> and $\text{CoCl}_2(\text{THF})_{1.5}$ yields the low-coordinate cobalt complex [ <b>5.3</b> ].....	138
<b>Scheme 5.4:</b> Complex <b>5.4</b> catalyzes the amination of toluene.....	139
<b>Scheme 5.5:</b> Some examples of intramolecular C–H bond activation from transient iron imido species.....	140

**Scheme 5.6:** Treatment of the  $\beta$ -diketiminato iron N<sub>2</sub> complex **2.9** with 1-azidoadamantane gives the three-coordinate imido complex **5.9**. Addition of <sup>t</sup>BuPy causes intramolecular H-atom abstraction in the absence of weak C–H bonds, yielding **5.10**. In the presence of substrates containing weak C–H bonds, intermolecular H-atom abstraction is possible.....141

**Scheme 5.7:** Treatment of **2.23c** with 1-azidoadamantane affords **5.12**.....142

**Scheme 5.8:** Proposed synthesis for an alternate ligand scaffold suitable for intermolecular C–H bond activation.....144

## List of Symbols

$\alpha$	-	Spin-up
$\text{\AA}$	-	Ångström = $10^{-10}$ meters
$\beta$	-	Refers to 1,3-substitution, the 2 <sup>nd</sup> carbon atom from a metal center, or spin-down
$B_0$	-	An external magnetic field
$c$	-	Concentration (g/mL)
$C_1$	-	A point group that only features the identity symmetry operation.
$C_{2v}$	-	A point group with four symmetry operations: the identity operation, two mirror planes, and a two-fold rotation axis
$C_s$	-	A point group with the identity symmetry operation and the mirror plane operation
$\chi_m$	-	Molar magnetic susceptibility
$^{\circ}\text{C}$	-	Degrees Celsius
$\Delta$	-	Heat
$\Delta E_Q$	-	Quadrupole splitting
$\delta$	-	Chemical shift in NMR spectroscopy, measured in parts per million (ppm) or isomer shift, measured in mm/s
$\delta\nu$	-	Shift in frequency
$E_\alpha$	-	Energy state associated with $\alpha$ spin
$E_\beta$	-	Energy state associated with $\beta$ spin
$I$	-	Nuclear spin quantum number

J	-	Joule (N x m)
k	-	Boltzmann constant ( $1.3806 \times 10^{-23} \text{ m}^2\text{kgs}^{-2}\text{K}^{-1}$ )
K	-	Kelvin
<i>m</i>	-	spin angular momentum quantum number or 1,3-substitution (meta)
M	-	Molarity
$\mu_B$	-	Bohr magneton
$\mu_{\text{eff}}$	-	Effective magnetic moment
$\nu_0$	-	Operating frequency of NMR spectrometer
N	-	Avogadro's number ( $6.022 \times 10^{23}$ )
<i>p</i>	-	1,4-substitution (para)
S	-	Spin angular momentum
$\tau$	-	Structural Parameter
T	-	Tesla ( $\text{kgA}^{-1}\text{s}^{-2}$ ) or temperature

## List of Abbreviations

18-Crown-6	-	1,4,7,10,13,16-hexaoxacyclooctadecane
Ad	-	Adamantyl
Anal.	-	Analysis
Ar	-	Aryl
ATP	-	Adenosine triphosphate
BAr <sup>F</sup>	-	[[3,5-(CF <sub>3</sub> ) <sub>2</sub> C <sub>6</sub> H <sub>3</sub> ] <sub>4</sub> B] <sup>-</sup>
Bn	-	Benzyl
C <sub>6</sub> D <sub>6</sub>	-	Benzene- <i>d</i> <sub>6</sub>
Calcd.	-	Calculated
Cp*	-	Pentamethylcyclopentadienyl
CY5	-	Cyclopentylidene
DFT	-	Density Functional Theory
DIPP	-	2,6-diisopropylphenyl
DMP	-	2,6-dimethylphenyl
Et	-	Ethyl
Et <sub>2</sub> O	-	Diethyl ether
GC	-	Gas Chromatography
h	-	Hours
HDF	-	Hydrodefluorination
HOMO	-	Highest Occupied Molecular Orbital
HSQC	-	Heteronuclear Single Quantum Coherence

Hz	-	Hertz (seconds <sup>-1</sup> )
IND	-	Indene
<sup>i</sup> Pr	-	Isopropyl
KC <sub>8</sub>	-	Potassium graphite
M	-	Metal
M <sub>w</sub>	-	Molecular weight
Me	-	Methyl
Mes	-	Mesityl (2,4,6-trimethylphenyl)
MS	-	Mass Spectrometry
<i>n</i> -BuLi	-	<i>n</i> -butyllithium
NacNac	-	β-diketiminate
NBO	-	Natural Bond Order
NMR	-	Nuclear Magnetic Resonance
NPA	-	Natural Population Analysis
NpN	-	Enamido-phosphinimine
ORTEP	-	Oak Ridge Thermal-Ellipsoid Plot Program
Ph	-	Phenyl
ppm	-	Parts per million
R	-	A variable group
silox	-	Siloxane
THF	-	Tetrahydrofuran
TON	-	Turn Over Number
<sup>t</sup> Bu	-	<i>tert</i> -butyl

- TZV - The valence triple-zeta basis set
- UB3LYP - A functional. Unrestricted Becke, 3-parameter, Lee-Yang-Parr

## Acknowledgements

I would like to thank Dr. Michael D. Fryzuk for allowing me the opportunity to work in his lab, even though I initially had zero experience in air-sensitive chemistry. I would also like to thank him for allowing me creative freedom in how I approached my research projects. My gratitude is extended to all Fryzuk group members, past and present, for their contribution to research ideas and lab culture. Truman Wambach was the “soul” of the Fryzuk lab during my PhD and his desire to bring the group together through coffee breaks and beer outings was much appreciated. I owe thanks to Lee Wence for first showing me how to use a Schlenk line. I thank Alyssa Yeo for understanding my fondness for snacks and using it as a bonding opportunity. Amanda Zimmerman and I started our PhDs in the same year, and it has been fun sharing the struggles of graduate school together. Dr. Vincent Annibale and Dr. Richard Burford never failed to provide...interesting conversations at lunch. I would also like to thank Rich for all of his contributions to chemistry ideas and to the better presentation of this thesis. Fraser Pick, my iron brother, receives extra special thanks for helping me understand paramagnetic  $^1\text{H}$  NMR spectroscopy and for all of his help with DFT. I also owe Fraser and Vince thanks for their willingness to run my not-so-single crystals for X-ray diffraction. They sunk many hours into helping me acquire the structures that litter this thesis.

My gratitude is extended to the UBC chemistry staff for their maintenance of infrastructure and equipment. I especially would like to thank Dr. Brian Patrick for his help with difficult X-ray structures.

To the friends I've made during my time in Vancouver, I would like to thank you for being a part of my life. Love-Ese Chile, Maria Cleveland, and Guillaume Beaulieu-Houle stuck

with me through difficult times and I hope we stay in touch, no matter where life takes us. The time I've spent with you has been a positive component of my life. I would also like to thank my close friend from my undergraduate studies, Leandra Brickson, for always believing that I could make it through a PhD. I'm glad we've stayed in touch.

My greatest depth of gratitude is owed to Dr. Thomas Ostapowicz. Your presence in the lab was a turning point for me and you provided me with the guidance necessary for me to make it through this. You taught me to approach problems methodically and how to communicate like a scientist. Above all else, you were a fantastic friend.

## **Dedication**

This work was initially set in motion by the nurturing influence of my middle school science teacher, Kate Yockey and my high school physics teacher, Paul Lulai. For sparking my interest in science and for providing much needed encouragement during my adolescence, I dedicate this dissertation to you. The progress of science is incremental, and many discoveries go unnoticed; a parallel can be drawn to work of teachers. Here is a record of the positive impact you had on my life.

# Chapter 1: Introduction

## 1.1 Low-Coordinate Transition Metal Complexes

Low-coordinate, paramagnetic complexes violate the well-known 18-electron rule used to predict stability of transition metal complexes. Low-coordinate complexes, defined in this thesis as complexes where the metal has three or fewer donor ligands, are electronically unsaturated. To achieve such a coordination environment, sterically-crowded ligands are required to minimize access to the ligated metal center. Some of the earliest reported example of two and three-coordinate transition metal complexes utilized bulky dialkylamides and disilylamides to generate species such as  $\text{Cr}(\text{N}^i\text{Pr}_2)_3$ <sup>1</sup> and  $\text{Co}[\text{N}(\text{SiMe}_3)_2]_2$ <sup>2</sup>, respectively. Since these early examples, a wide-range of sterically demanding ligands have been developed to stabilize low-coordinate complexes.<sup>3-14</sup> A small selection of these species is shown in **Figure 1.1**. An important characteristic of low-coordinate complexes is that they often display enhanced reactivity in comparison to coordinatively saturated species.<sup>15</sup> For instance, small molecules such as carbon monoxide (CO) and dinitrogen (N<sub>2</sub>) can access the metal center and form  $\pi$  interactions with high-energy *d*-orbitals of the correct symmetry. Back-bonding from metal *d*-orbitals into the antibonding orbitals of a small molecule can lead to weakening and sometimes cleavage of the molecule's bonds.<sup>16</sup>

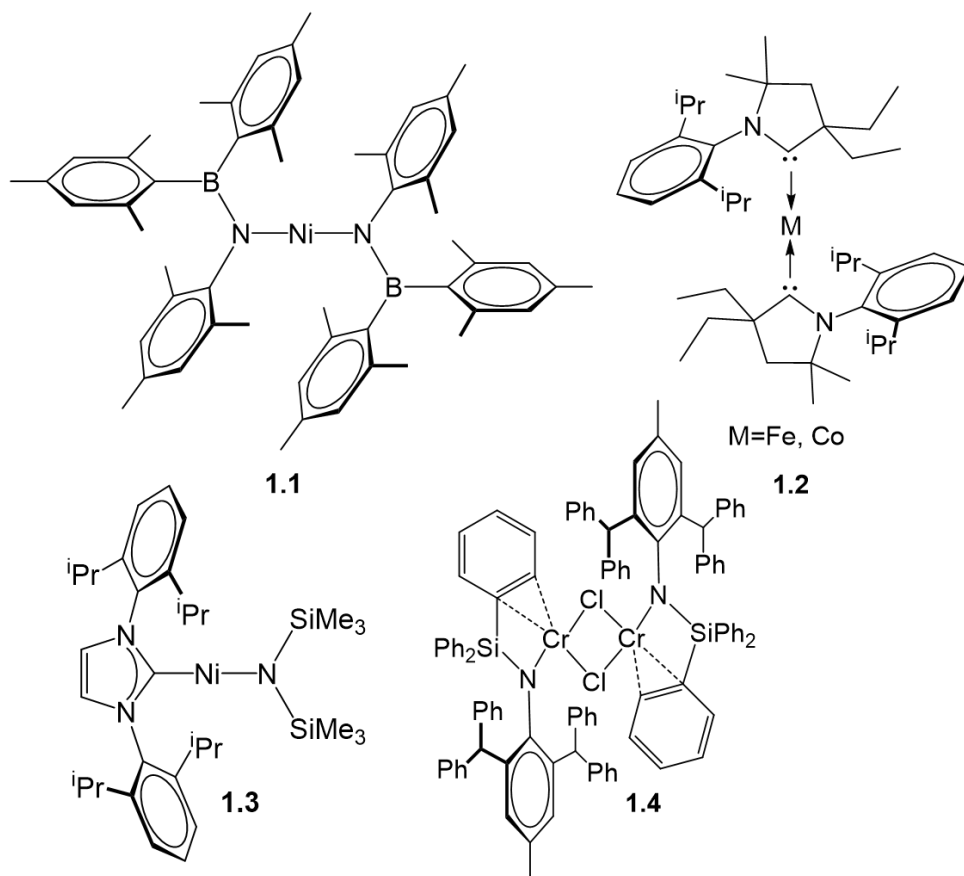
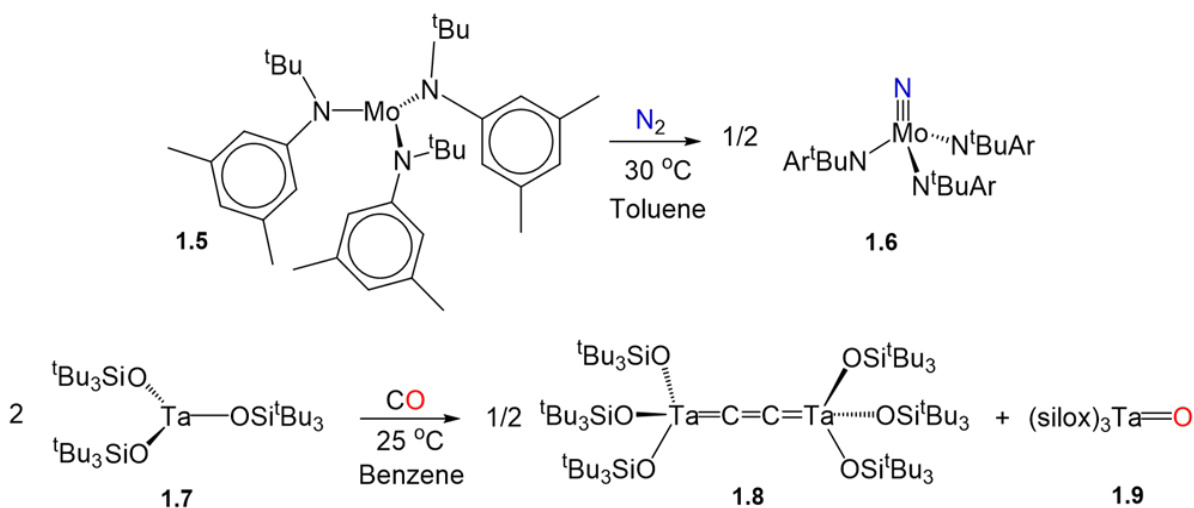


**Figure 1.1:** Some examples of low-coordinate complexes utilizing sterically demanding ligands. **1.1** see ref 4. **1.2** see ref 7. **1.3** see ref 8. **1.4** see ref 14.

Pioneering work in the utilization of low-coordinate early metal complexes for the cleavage of strong bonds in small molecules was performed by the groups of Wolczanski and Cummins.<sup>17-18</sup> For example, the three coordinate molybdenum complex **1.5** is able to fully cleave the N<sub>2</sub> triple bond at 30 °C to form the molybdenum nitride **1.6**.<sup>18</sup> The authors state that the severe steric constraints at the molybdenum center prevent dimerization and instead allow for coordination and reduction of N<sub>2</sub>.<sup>18</sup> Likewise, the sterically hindered three-coordinate tantalum siloxane complex **1.7** is able to cleave the strong carbon-oxygen triple bond of carbon monoxide to give the dicarbide species **1.8** along with formation of the tantalum oxo species **1.9**.<sup>17</sup> These two examples highlight the reactivity of low-coordinate complexes with small molecules and aid

in framing the context behind the increased interest in the synthesis of coordinatively unsaturated species.

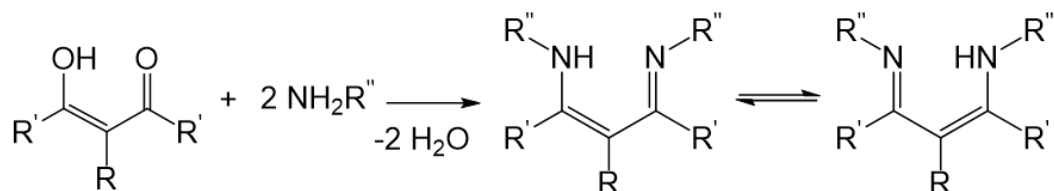


**Scheme 1.1:** The three-coordinate Mo complex **1.5** is capable of cleaving the N<sub>2</sub> triple bond to give the Mo nitride complex **1.6** (see ref 18). The three-coordinate Ta species **1.7** is capable of cleaving the CO triple bond to give the dicarbide **1.8** and the oxo complex **1.9** (see ref 17).

The following section focuses on a specific ligand scaffold capable of stabilizing low-coordinate environments at a metal. The  $\beta$ -diketiminato ligand (also referred to as NacNac) is ubiquitous throughout inorganic chemistry and is of particular relevance to this thesis. An overview into advances in the design of NacNac frameworks and emphasis on the coordination of NacNac to first-row transition metals will be highlighted below.

## 1.2 First-Row Transition Metal Complexes Featuring $\beta$ -Diketiminato Ligands

$\beta$ -diketiminates are conveniently synthesized through the condensation reaction between a  $\beta$ -diketone and a primary amine. The synthesis is modular, and allows for a wide-range of steric and electronic variability depending on the substituents at positions R, R', and R'' (**Scheme 1.2**). Simple diones and aryl amines can undergo condensation through a one-step reaction, but



**Scheme 1.2:** The condensation reaction between a  $\beta$ -diketone and a primary amine to generate the general  $\beta$ -diketiminato, where  $R$ ,  $R'$ , and  $R''$  are sites of potential modification.

more sterically challenged substituents often require harsher reaction conditions, such as the formation of oxonium salts, in order to generate the desired  $\beta$ -diketiminato.<sup>19-20</sup>  $\beta$ -diketiminatos are typically depicted as the enamine-imine tautomer, but bond metrics obtained through X-ray crystallography indicate substantial conjugation between the C–C and C–N bonds, with distances intermediate of those for single and double bonds.<sup>21</sup> Alkali metal complexes can be prepared by treatment of the desired  $\beta$ -diketiminato with an appropriate base, yielding monoanionic precursors appropriate for salt metathesis reactions.<sup>19</sup>

The first reported NacNac transition metal complexes were made in 1968 and used sterically-unhindered  $\beta$ -diketiminatos that afforded homoleptic complexes unsuitable for further reactivity (**Figure 1.2**).<sup>22-23</sup> Further innovation wasn't made until the late 1990's when incorporation of increased steric hindrance at the  $R$  groups of the N-donors allowed for isolation

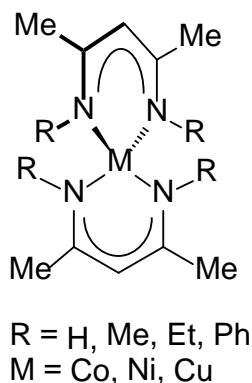


**Figure 1.2:** Homoleptic  $\beta$ -diketiminato complexes are isolated if substituents at  $R$  are sterically unencumbered (see ref 22).

of species in which a single NacNac is coordinated to the metal center, making reactivity at the metal a possibility.<sup>20, 24-27</sup> These early reports of low-coordinate  $\beta$ -diketiminato complexes spurred a renewed interest in the  $\beta$ -diketiminato scaffold and benefitted numerous research programs focused on small molecule activation,<sup>28-36</sup> catalysis,<sup>24, 37-42</sup> and the modeling of active sites found in metalloproteins,<sup>27, 43-47</sup> to name a few examples. Representative examples highlighting the aforementioned systems are shown in **Figure 1.3**. While the synthesis and characterization of iron dinitrogen complexes with the  $\beta$ -diketiminato scaffold have been the subject of intense research, an analysis of these systems is provided in Chapter 2.1.2 and not in the current section.

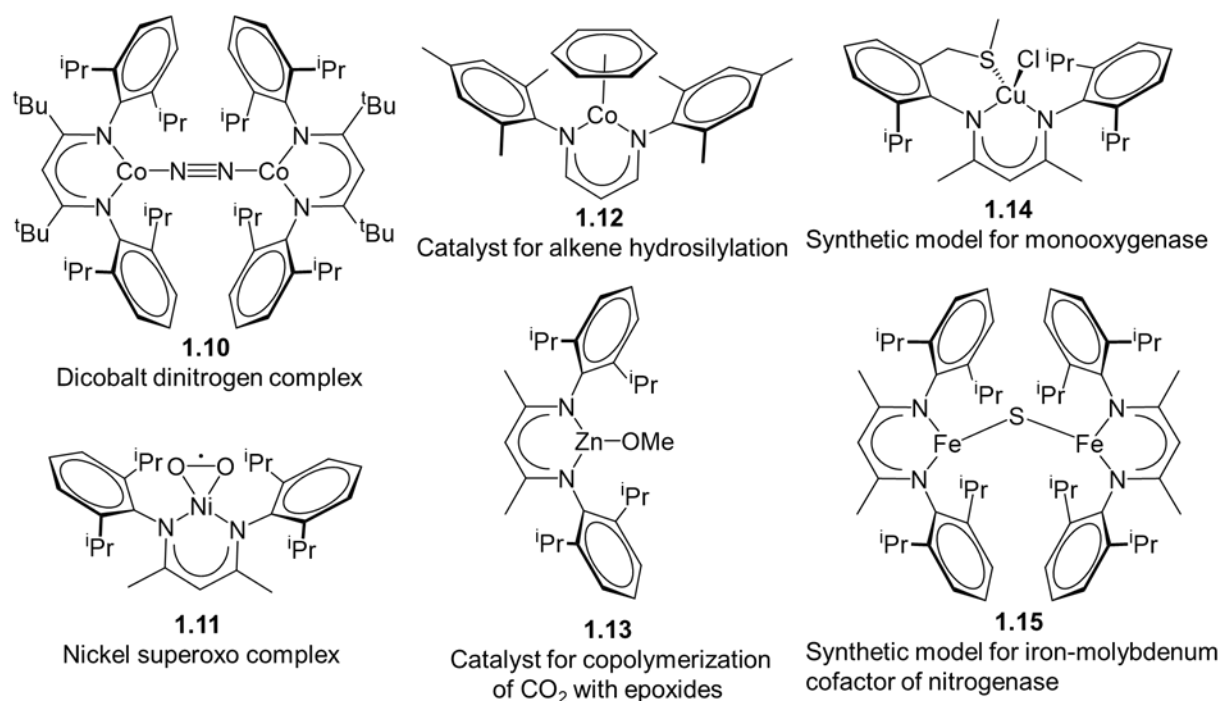
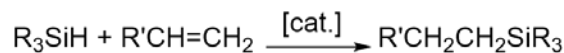
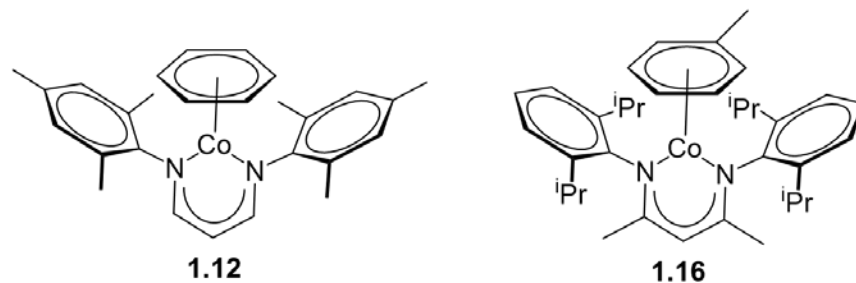


**Figure 1.3:** Examples of  $\beta$ -diketiminato complexes used in small molecule activation, **1.10** (ref 35) and **1.11** (ref 34), catalysis, **1.12** (ref 41) and **1.13** (ref 23), and as models for active sites of metalloproteins, **1.14** (ref 43) and **1.15** (ref 44).

The  $\beta$ -diketiminato ligand is typically viewed as an ancillary ligand but can also display redox non-innocent behavior. However, the redox non-innocence of  $\beta$ -diketiminato scaffolds is beyond the scope of this thesis and the reader is directed to a comprehensive review on the subject.<sup>48</sup> Instead, emphasis will be placed on the importance of tuning the steric and electronic properties of NacNac and the implications for the reactivity of the resulting complexes.

The incorporation of steric bulk into the  $\beta$ -diketiminato scaffold has a profound impact on the observed reactivity and selectivity of the corresponding complex in both stoichiometric and catalytic reactions. In general, a complex featuring a sterically hindered  $\beta$ -diketiminato often performs reactions at slower rates due to increased steric strain in transition states or intermediates, but allows for the isolation of transient species.<sup>49</sup> Positions R' and R'' seen previously in **Scheme 1.2** contribute the most to steric hindrance. At the R'' position on the N-donor, the substitution at the *ortho* positions (when R'' = Ar) contributes the largest steric effect. An example highlighting the impact of steric bulk in catalysis is found in the hydrosilylation catalysis performed by the cobalt complex **1.12**.<sup>42</sup> **Figure 1.4** compares the catalytic activity for sterically unencumbered **1.12** and the more sterically hindered complex **1.16**. The *G* parameter is a quantification of the ligand coverage over the coordinated metal and provides a means for size comparison between ligands.<sup>50</sup> The low steric encumbrance of complex **1.12** makes hydrosilylation catalysis possible in neat substrates at 25 °C with only 0.05% catalyst loading, whereas more hindered **1.16** requires higher loadings, a higher temperature, and longer reaction time and gives lower yields compared to **1.12**. In this case, lower steric bulk gives improved activity.

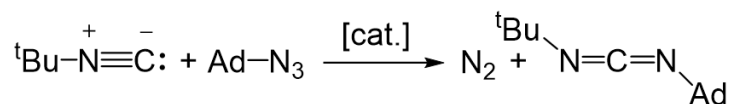
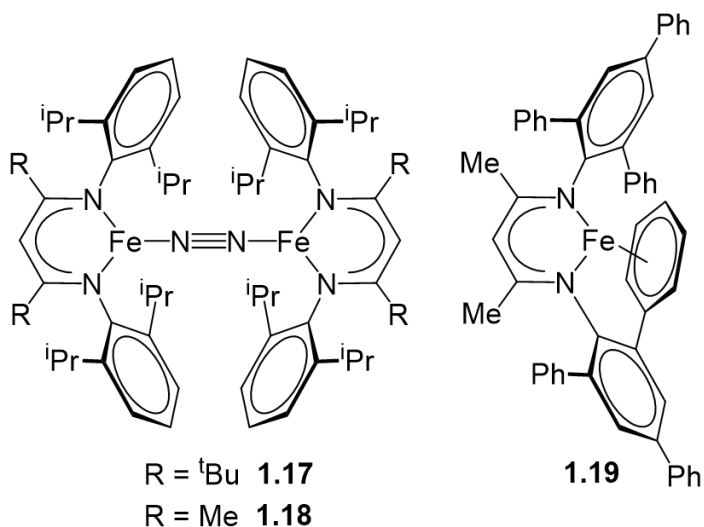
While the above example illustrated the benefits of utilizing an unencumbered  $\beta$ -diketiminato scaffold, there are instances where more sterically hindered complexes display



Complex	<b>1.12</b>	<b>1.16</b>
G Parameter	26%	54%
Catalyst loading	0.05%	1.0%
Reaction Conditions	Neat, 25 °C, 1 h	1 M, 40 °C, 2 h
Yield (Selectivity)	97% (>98%)	91% (>98%)

**Figure 1.4:** A comparison of the steric coverage of Co (G parameter) to reactivity. The less sterically hindered species **1.12** can perform hydrosilylation catalysis at lower catalytic loadings and at lower temperatures compared to the more sterically encumbered species **1.16**.

enhanced reactivity.<sup>49</sup> The catalytic formation of carbodiimides from isocyanide and organic azides using reduced iron NacNac precatalysts exemplifies this point.<sup>39</sup> During catalytic carbodiimide formation, the catalytic resting state is an Fe(I) tris(isocyanide) species that must undergo loss of isocyanide in order to coordinate the organic azide. Sterically hindered  $\beta$ -diketiminates favor a lower coordination number at the metal center, and loss of isocyanide is more facile. **Figure 1.5** illustrates the correlation between increased catalytic activity and steric bulk, with the activity of **1.17** > **1.19** > **1.18**.<sup>39</sup>



Precatalyst	Temp (°C)	Time (h)	Yield (%)
<b>1.17</b>	60	1	>95
<b>1.18</b>	80	20	74
<b>1.19</b>	80	14	>95

**Figure 1.5:** A comparison of the catalytic activity for carbodiimide formation displayed by three  $\beta$ -diketiminato complexes featuring varying degrees of steric hindrance. The most sterically bulky precatalyst **1.17** gives high product yields at lower temperature and shorter reaction times compared to the less sterically encumbered precatalysts investigated.

The electronic properties of the  $\beta$ -diketiminato scaffold also influence the reactivity of the resulting complex. Generally, the greatest electronic effects result from the R and R' substituents in the NacNac backbone. Installation of electron-withdrawing or donating groups at these positions cause changes in the electron density present on the metal center, which can impact reactivity. One example of such an effect is seen in the catalytic oxidation of alkanes to alcohols and ketones using  $\beta$ -diketiminato copper acetate complexes (**Figure 1.6**).<sup>37</sup> Catalysis is observed

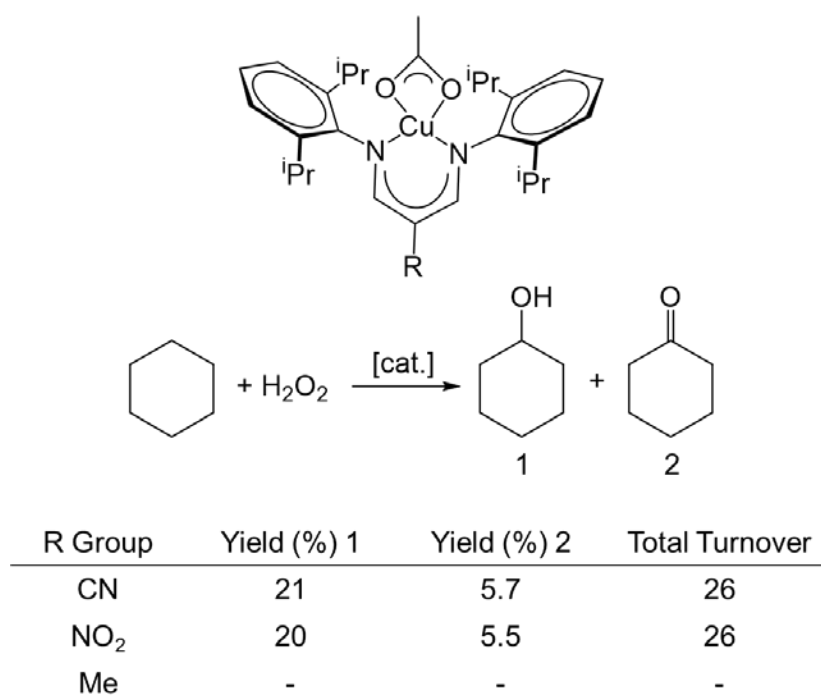


**Figure 1.6:** Catalytic oxidation of cyclohexane with hydrogen peroxide using  $\beta$ -diketiminato copper acetate complexes. When electron-withdrawing groups are installed at position R, catalytic activity is observed. In contrast, when R = Me there is zero reactivity.

when electron-withdrawing groups (CN, NO<sub>2</sub>) are installed at position R, whereas there is no catalysis when R = Me. The catalytically active intermediate is hypothesized to be a bis( $\mu$ -oxo)dicopper(III) species; thus, the presence of electron-withdrawing groups in the ligand framework leads to a more reactive high valent copper complex able to oxidize alkanes.

### 1.3 Ligand Design Used in This Thesis

The above examples illustrate the varied reactivity of first-row transition metal  $\beta$ -diketiminate complexes and the dependence of reactivity on the steric and electronic parameters of the NacNac ligand. Judicious modifications to the  $\beta$ -diketiminate scaffold can result in steric and electronic coordination environments favorable for a plethora of reactivity pathways. The work presented in this thesis was inspired by the modular reactivity possible through modification to the NacNac scaffold. A new ligand design was proposed in which the symmetrical ligand environment present in NacNac was modified to an unsymmetrical analogue by replacing one of the imine functionalities with a phosphinimine unit. This is shown in **Figure 1.7**, where the metal  $\beta$ -diketiminate (**A**) is compared with the metal enamido-phosphinimine

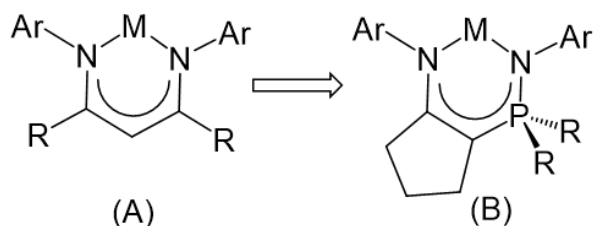


**Figure 1.7:** Comparison of a generic  $\beta$ -diketiminate coordination complex (**A**) to the ligand scaffold presented in this thesis (**B**).

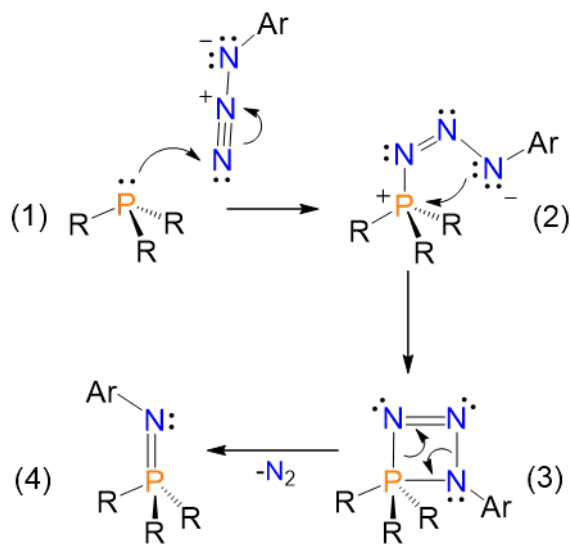
ligand scaffold (**B**). Phosphinimines, also known as iminophosphoranes, are easily synthesized using the Staudinger reaction, in which a phosphine is oxidized by an organic azide via a phosphazide intermediate.<sup>51,52</sup> While the resulting phosphinimine unit still allows for  $\pi$  delocalization,<sup>53</sup> one could imagine the resultant unsymmetrical metal complex **B** would not have the same degree of charge delocalization in the ligand backbone that is present in the  $\beta$ -diketiminate system **A**. In addition, the sterics of the phosphinimine unit are also amenable to modification through the use of different aryl azides during the Staudinger reaction, allowing for a modular ligand synthesis with similar or very different N-substituents.<sup>51</sup> The use of the

cyclopentylidene ring as a ligand backbone ensures the donor functionalities will be locked in a *syn* orientation.<sup>54</sup> What also made this an attractive foray was that previous work in the Fryzuk lab utilized the parent imine-phosphine ligand sets based on N-aryl-cyclopentylidene imine precursors, which were investigated for their ability to act in a cooperative manner when coordinated to iridium and ruthenium.<sup>55-56</sup>

The following section provides some context as to the synthesis of phosphinimines and their use as ligands in coordination compounds. Some examples highlighting the reactivity of phosphinimine complexes will be provided.

#### 1.4 Phosphinimine Synthesis and First-Row Transition Metal Complexes Containing Phosphinimine Ligands

Phosphinimines are synthesized through the Staudinger reaction, the mechanism of which is shown below in **Scheme 1.3**.<sup>52</sup> A phosphine is oxidized by an organic azide (1), which



**Scheme 1.3:** The mechanism for the Staudinger reaction. A phosphine performs a nucleophilic attack on an organic azide (1) to generate a phosphazide intermediate (2). The phosphazide goes through a four-membered ring transition state (3) which undergoes loss of  $N_2$  and forms the phosphinimine (4).

generates a phosphazide intermediate (2) (isolable if sufficient steric bulk is present at the phosphorus center or the organic azide). The stabilization of phosphazides is the subject of Chapter 4. Computational studies have determined that the phosphazide intermediate is stabilized in the *cis* conformation due to an electrostatic interaction between the phosphorus and the distal nitrogen of the azide<sup>52</sup>, though examples of phosphazides in the *trans* conformation have been isolated and characterized.<sup>57</sup> The phosphazide can then go through a four-membered ring closure (3) to eliminate N<sub>2</sub> and generate the phosphinimine (4).<sup>52</sup>

The Staudinger reaction has applications in organic chemistry<sup>58-60</sup> and biology<sup>61</sup>, but the phosphinimine products are also desirable as ligands in coordination compounds.<sup>62</sup> Monodentate, anionic phosphinimides mimic the conical steric profile of cyclopentadienyl ligands and the resulting reactivity of phosphinimide complexes is similar to that of metallocenes (**Figure 1.8**).<sup>62</sup>

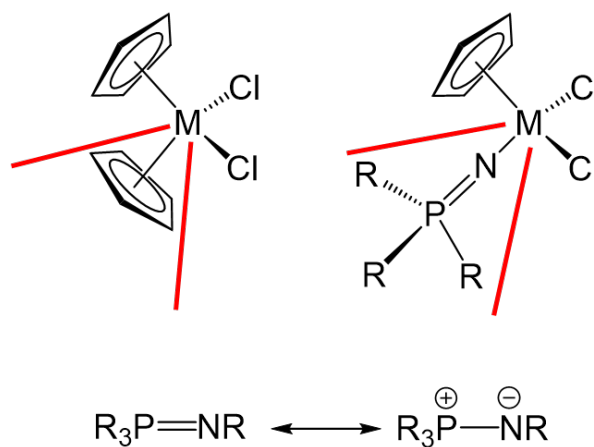


**Figure 1.8:** A comparison of the steric profile of a cyclopentadienyl ligand compared to a phosphinimide in a generic metallocene species. Also shown are the two major resonance forms of a phosphinimine.

Neutral phosphinimines have a polarized P=N bond and are best described as resonance hybrids between the two forms shown in **Figure 1.8**. Phosphinimines coordinate to metal ions via the lone pair on the sp<sup>2</sup> hybridized nitrogen, making them σ-donor ligands with minor π-acceptor properties.<sup>63</sup> Neutral monodentate phosphinimine fragments are often easily dissociated

from a metal center upon addition of stronger  $\sigma$ -donors, such as triphenylphosphine, triphenylphosphite, and 2,2'-bipyridine.<sup>64</sup> However, polydentate ligand scaffolds containing supplementary donor atoms to the phosphinimine moiety are capable of stabilizing a variety of metal ions, generating complexes utilized for a wide-range of applications.

Select examples of first-row transition metal complexes bearing phosphinimine containing ligand scaffolds are shown in **Figure 1.9**. A variety of chemical transformations can

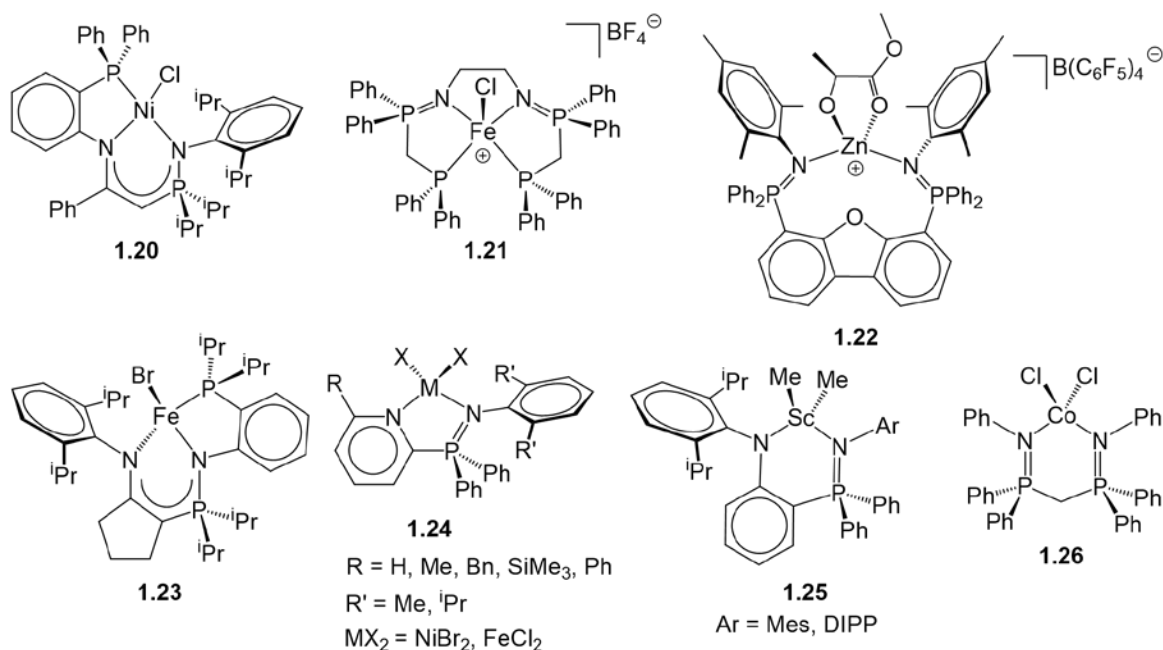


**Figure 1.9:** Examples of first-row transition metal complexes bearing phosphinimine containing ligands. **1.20** is used in Kumada cross-coupling reactions (ref 64). **1.21** displays transfer hydrogenation (ref 65). **1.22** is utilized in lactide polymerization (ref 66). **1.23** can be reduced to give a N<sub>2</sub> complex (ref 72). A variety of derivatives of **1.24** (ref 68) and **1.26** (ref 52) are ethylene polymerization catalysts. **1.25** is reported in ref 71.

be catalyzed by such complexes. Examples include coupling reactions,<sup>65</sup> transfer hydrogenation,<sup>66</sup> lactide polymerization,<sup>67</sup> and ethylene dimerization/polymerization.<sup>53, 68-70</sup>

While a variety of bidentate phosphinimine scaffolds coordinated to first-row transition metals have been reported,<sup>53, 68-69, 71-72</sup> studies regarding the reactivity of such complexes have focused on ethylene polymerization.<sup>53, 67-69</sup> The only literature reported example of small molecule

activation with a phosphinimine containing complex was reported by Masuda and coworkers with their tridentate iron species **1.23**.<sup>73</sup> Complex **1.23** can be reduced with potassium graphite to yield a bridging end-on dinitrogen complex (further discussion of this complex is provided in Chapter 2).

The previous section has established the utility of phosphinimine ligands in generating low-coordinate first-row transition-metal complexes. The mixed enamido-phosphinimine ligand scaffold, which is the focus of this thesis, was synthesized with the goal of coordination to first-row transition metals to generate paramagnetic complexes with applications in small molecule activation and catalysis. The characterization of paramagnetic complexes is often regarded as challenging because NMR spectroscopic characterization is less straightforward. The following section aims to explain the utility of some characterization techniques used in this thesis.

## **1.5 Characterization Techniques for Paramagnetic Complexes**

### **1.5.1 General Considerations**

One of the most important characterization technique used in the study of paramagnetic complexes is single-crystal X-ray crystallography because it is the only method to unambiguously determine the connectivity of atoms in a complex. As single-crystal X-ray crystallography is a commonly used technique in the physical and biological sciences,<sup>74</sup> an explanation of single-crystal X-ray crystallography will not be provided here. However, one shortcoming of X-ray crystallography is that the technique only determines the identity of the compound in the single-crystal that was analyzed. To address this issue, elemental analysis was performed on the bulk material to determine purity. Crystalline material was only used for elemental analysis if the compound in question was isolated as such. In instances where the sensitivity of the complex prevented accurate elemental analysis, high-resolution mass

spectrometry was performed to confirm the identity of the bulk material relative to the molecular structure determined by crystallography.

The above mentioned techniques are solid-state measurements. The paramagnetic complexes studied in this thesis were also analyzed in the solution-state using  $^1\text{H}$  NMR spectroscopy. While analysis is less straightforward in comparison to NMR characterization of diamagnetic compounds,  $^1\text{H}$  NMR spectroscopy is still a useful technique for the analysis of paramagnetic complexes.

### 1.5.2 The Paramagnetic $^1\text{H}$ NMR Experiment

In a typical  $^1\text{H}$  NMR experiment, a sample containing a molecule with  $^1\text{H}$  nuclei is placed in an external magnetic field.  $^1\text{H}$  nuclei have a nuclear spin quantum number ( $I$ ) of  $1/2$ , causing the energy level of each  $^1\text{H}$  nucleus in the sample to split according to the spin angular momentum quantum number ( $m$ ) when in the presence of an external magnetic field. These energy levels can take values of  $m = +1/2$  and  $-1/2$ , also referred to as spin-up ( $\alpha$ ) and spin-down ( $\beta$ ), respectively.<sup>75</sup> The population of  $^1\text{H}$  nuclei in the lower energy state ( $E_\alpha$ ) aligned with the external magnetic field will be slightly higher than the population in the higher energy level ( $E_\beta$ ) opposed to the external magnetic field.<sup>76</sup> The inherent magnetic moment of the  $^1\text{H}$  nucleus causes an induced magnetization vector within the sample due to the unequal populations of nuclei in the  $\alpha$ -state compared to the  $\beta$ -state (**Figure 1.10**). The Larmor frequency is the rate of

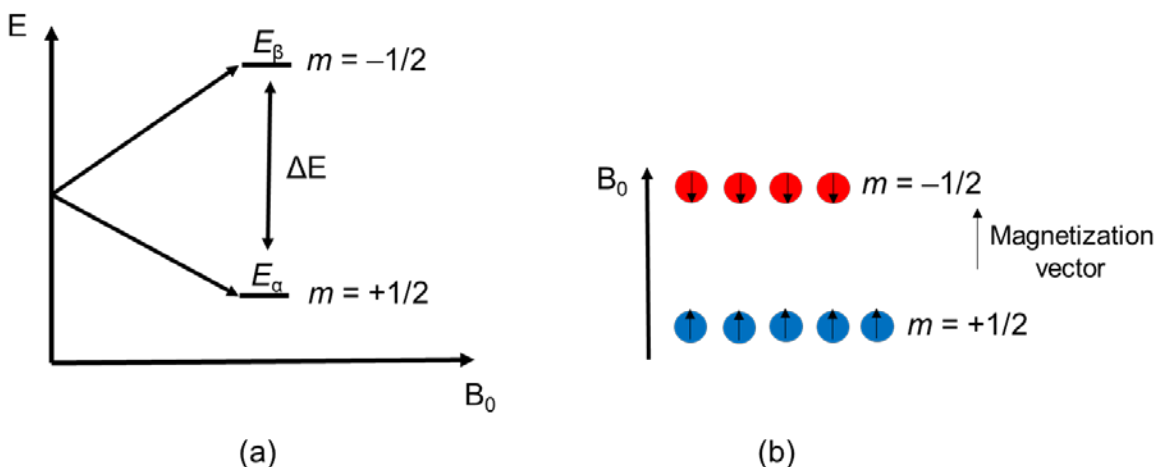


**Figure 1.10:** (a) The splitting of energy levels for a  $1/2$  spin nucleus in an external magnetic field. As the strength of the external magnetic field ( $B_0$ ) increases, the energy difference ( $\Delta E$ ) between the spin  $+1/2$  state and the spin  $-1/2$  state also increases. (b) The resulting population distribution of nuclei with the  $+1/2$  spin-state is slightly greater than the number of nuclei with the  $-1/2$  spin state, resulting in a net magnetization vector pointing in the same orientation as the external magnetic field.

precession of a nuclear magnetic moment in an external magnetic field.<sup>76</sup> When the sample is irradiated with a radiofrequency pulse equal to the Larmor frequency, the magnetization vector changes orientation. The change in precession of the magnetization vector as it realigns with the external magnetic field is detected and converted to a signal that is recorded during the NMR experiment.<sup>75</sup> Magnetic interactions through bonds between various NMR active nuclei in the molecule give rise to coupling effects and the chemical shift is affected by the electron density surrounding the nuclei in the molecule being analyzed.

The presence of an unpaired electron in a molecule significantly complicates the  $^1\text{H}$  NMR experiment described above. As was previously stated, the magnetic moment of the nucleus is the fundamental property underlying NMR spectroscopy. Electrons also have a magnetic moment and the absolute value is 658 times greater than that of a proton (which has the largest magnetic moment among the magnetic nuclei, except tritium).<sup>76</sup> The unpaired electrons in

a paramagnetic compound tend to align with an external magnetic field, resulting in an induced magnetic dipole which interacts with the magnetic nuclei in the compound. For the sake of simplicity, consider that the unpaired electrons in a paramagnetic compound are localized on a metal center, shown in **Figure 1.11**, rather than delocalized through the molecule in molecular orbitals. The magnetic dipole of the unpaired electron aligns with the external magnetic field  $B_0$ ,

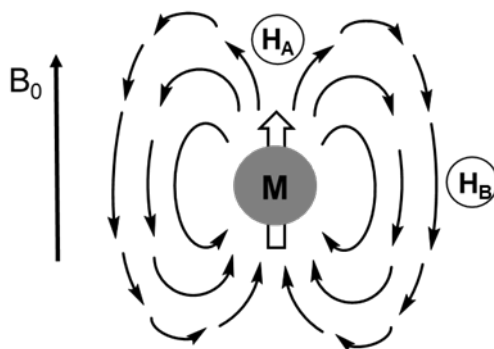


**Figure 1.11:** A paramagnetic metal  $M$  in an external magnetic field  $B_0$ . The magnetic dipole of the unpaired electron(s) orients along the external field, resulting in a dipolar magnetic field. Proton  $H_A$  is situated such that the external magnetic field and the dipolar magnetic field are additive, whereas  $H_B$  is located at a position where the dipolar magnetic field subtracts from the external magnetic field.

resulting in a dipolar magnetic field with field lines propagating from the metal center  $M$ . Two hydrogen nuclei that could be imagined to be part of a ligand scaffold coordinated to  $M$  are shown in **Figure 1.11**.  $H_A$  is located in a position where it would experience a dipolar field additive to the external field  $B_0$ , whereas  $H_B$  would experience a dipolar field that would subtract from the external field. The result is that proton  $H_A$  would experience an upfield shift in the resulting  $^1\text{H}$  NMR spectra, while  $H_B$  would experience a downfield shift. A weaker, but analogous effect is produced when diamagnetic aromatic compounds are placed in an external magnetic field. An induced ring current produces an internal magnetic field and nuclei positioned above the ring are shifted upfield, whereas nuclei on the sides of the ring are shifted downfield.

In the case of paramagnetic compounds, this through-space interaction is referred to as the pseudocontact or dipolar shift.<sup>76</sup> Thus, the spatial position of a hydrogen nuclei relative to the paramagnetic metal has a direct influence on the chemical shift value observed. The pseudocontact shift is responsible for the very large chemical shift ranges observed in NMR spectra of paramagnetic compounds. For example, mononuclear Fe(II) complexes typically give a range of chemical shifts from +150 to -200 ppm in <sup>1</sup>H NMR spectroscopy.<sup>16</sup> However, bimetallic species often give NMR spectra with narrower chemical shift ranges due to antiferromagnetic coupling between metals.<sup>16</sup> Antiferromagnetic coupling is the alignment of opposite electron spins, which effectively reduces the resulting dipolar field in a bimetallic complex.

Paramagnetism also has consequences on relaxation pathways during the NMR experiment. The large magnetic moment of an unpaired electron is strongly coupled to that of a magnetic nucleus and provides a mechanism for fast relaxation.<sup>77</sup> Electrons have very fast magnetic relaxation rates, typically on the scale of 10<sup>-7</sup> to 10<sup>-13</sup> seconds in contrast to the relaxation rates of <sup>1</sup>H nuclei that are on the order of seconds.<sup>77</sup> The fast magnetic relaxation of an unpaired electron causes magnetically coupled nuclei to also relax quickly, which results in signal broadening in the resulting NMR spectrum. The extent of broadening is highly dependent on the identity of the paramagnetic metal, the oxidation state, and electron configuration.<sup>77</sup> For example, <sup>1</sup>H NMR spectroscopy of samples containing high-spin Fe(II) and Co(II) typically feature signal broadening of 5-20 Hz for a proton 5 Å from the metal.<sup>77</sup> In contrast, high-spin Fe(III) can cause signals to broaden by 200-12,000 Hz.<sup>77</sup> As a consequence, all proton-proton or proton-heteroatom coupling information is lost in <sup>1</sup>H NMR spectroscopy of paramagnetic compounds.

Despite the challenges outlined above,  $^1\text{H}$  NMR spectroscopy is still a useful characterization technique in the analysis of paramagnetic complexes, especially of Fe(II) and Co(II). The issue of short nuclear relaxation times can cause a poor signal-to-noise ratio in the resulting NMR spectrum. Using short acquisition times allows for the sampling of a large amount of data, resulting in a better signal-to-noise ratio.<sup>78</sup> Collecting data in a large spectral window allows for the observation of paramagnetically shifted resonances, though baseline distortions in the spectrum can occur. Careful corrections to the baseline are necessary if integration values are to be recorded.

Due to the low symmetry of many of the iron complexes described in this thesis, unambiguous assignment of  $^1\text{H}$  resonances is not feasible. Low symmetry results in many unique  $^1\text{H}$  resonances, which are often of similar integration values. The lack of proton-proton coupling and the unintuitive chemical shifts observed from the pseudocontact shift with the paramagnetic metal also add to the challenge of signal assignment. However, in this thesis  $^1\text{H}$  NMR spectroscopy of paramagnetic complexes is used to compare the number of resonances expected based on the symmetry of the complex to the number of signals observed in the spectrum. The observation of fewer resonances than expected could indicate that the complex has higher symmetry in solution compared to that observed in the solid-state. Likewise, the observation of more signals than expected could indicate lower symmetry than that predicted in the solid-state, though it is more likely that an impurity is present in the sample.

The number of unpaired electrons in a paramagnetic species can be determined by magnetic susceptibility measurements. The following section will address a method for taking such a measurement in the solution-state.

### 1.5.3 Magnetic Susceptibility

The effective magnetic moment ( $\mu_{\text{eff}}$ ) provides a means to quantify the number of unpaired electrons in a transition metal complex. The  $\mu_{\text{eff}}$  value is derived from molar magnetic susceptibility ( $\chi_{\text{m}}$ ) and is expressed in Bohr magnetons ( $\mu_{\text{B}}$ ), where  $1\mu_{\text{B}}=9.27 \times 10^{-24}$  J/T.<sup>79</sup> The relationship between  $\mu_{\text{eff}}$  and  $\chi_{\text{m}}$  is provided in equation 1.1, where N is the Avogadro constant, k

$$\chi_{\text{m}} = \frac{N\mu_{\text{B}}^2}{3kT} \mu_{\text{eff}}^2 \quad \text{Eq 1.1}$$

is the Boltzmann constant, and T is temperature.<sup>80</sup> Rearrangement of equation 1.1 and evaluation of the coefficient in front of  $\mu_{\text{eff}}$  leads to the relation shown in equation 1.2. Magnetic

$$\mu_{\text{eff}} = \sqrt{(\chi_{\text{m}})(2.344 \times 10^3)} \quad \text{Eq 1.2}$$

susceptibility values presented in this thesis were only measured in the solution-state using the Evans method and <sup>1</sup>H NMR spectroscopy.<sup>81</sup> The Evans method is based on the principle that the chemical shift of a proton resonance in a <sup>1</sup>H NMR spectrum is dependent on the bulk susceptibility of the medium in which the molecule is present. Regarding how the Evans experiment is performed, a chosen NMR solvent is doped with a non-coordinating molecule to act as a reference in order to measure the shift in frequency for a known resonance (for example, the solvent system used in this work was 1 mol % cyclooctane in *d*<sub>6</sub>-benzene). A capillary tube is filled with this solvent and sealed. A solution containing the paramagnetic complex of interest is weighed out and dissolved in the Evans NMR solvent and is transferred into a standard NMR tube containing the capillary. A standard <sup>1</sup>H NMR spectrum is collected and a set of two signals per unique magnetic position in the reference molecule will be observed. One of the signals belongs to the reference molecule sealed in the capillary and the other signal, at a more downfield chemical shift, belongs to the same reference molecule in solution with the

paramagnetic species. This difference in the chemical shift is used to calculate  $\chi_m$  according to equation 1.3, where  $\delta\nu$  is the shift in frequency (Hz) for the reference molecule,  $\nu_0$  is the operating frequency of the spectrometer (Hz),  $c$  is concentration in g/mL of the paramagnetic

$$\chi_m = \frac{3(\delta\nu)}{4\pi(\nu_0)(c)} M_w \quad \text{Eq 1.3}$$

complex in the NMR solvent, and  $M_w$  is the molecular weight of the paramagnetic species.<sup>81-82</sup>

The  $3/4\pi$  term comes from the fact that the experiment is performed with the cylindrical sample axis (the NMR tube) being parallel to the magnetic field in the spectrometer (also known as the shape factor).<sup>82</sup>

The  $\mu_{\text{eff}}$  value from equation 1.2 can be used to approximate the number of unpaired electrons in the paramagnetic species according to the relationship shown in equation 1.4, where  $n$  is the number of unpaired electrons.<sup>79</sup> Note that equation 1.4 only serves as an approximation if

$$\mu_{(\text{spin only})} = \sqrt{n(n+2)}\mu_B \quad \text{Eq 1.4}$$

the primary contribution to the magnetic moment is from the spin angular momentum ( $S$ ) of the unpaired electrons.<sup>79</sup> Low-coordinate first-row transition metal complexes are often reported to have  $\mu_{\text{eff}}$  values higher than the spin-only predicted values. This effect is due to orbital angular momentum contributions caused by spin-orbit coupling between  $d$ -orbitals of different symmetry but similar energy.<sup>16</sup> For the compounds described in this thesis, the  $\mu_{\text{eff}}$  values are reported and compared to spin-only predicted values, as detailed analysis into orbital angular momentum contributions is not provided.

#### 1.5.4 Mössbauer Spectroscopy

Mössbauer spectroscopy was only performed on three iron complexes reported in this thesis. Nevertheless, a short description of the technique will be provided here, with a more detailed explanation for the relevant iron complexes provided in Chapter 2.3.2 and Chapter 4.3.

The Mössbauer effect is the emission and resonant absorption of nuclear  $\gamma$ -rays under conditions where nuclear recoil is negligible upon  $\gamma$ -ray emission and absorption.<sup>79</sup> Thus, Mössbauer spectroscopy is a solid-state technique, as the nuclei under investigation are held rigidly in a crystal lattice. The most commonly studied nucleus with Mössbauer spectroscopy is  $^{57}\text{Fe}$ , due to the availability of the radioactive  $^{57}\text{Co}$  source. The  $^{57}\text{Co}$  radioisotope undergoes radioactive decay to give the excited state of  $^{57}\text{Fe}$  that emits  $\gamma$ -radiation as it decays to the ground state nuclear energy level. By measuring absorbance of the incident  $\gamma$ -rays by  $^{57}\text{Fe}$  in the sample, the electronic environment of Fe nuclei can be probed.<sup>79</sup> Since it is not feasible to change the chemical environment of the  $^{57}\text{Co}$  source to influence the energy of  $\gamma$ -rays emitted, the  $^{57}\text{Co}$  source is instead moved at different velocities towards or away from the absorber, varying the energy of the emitted  $\gamma$ -rays through the Doppler effect. The velocity of movement required to cause maximum absorption relative to  $\alpha$ -Fe (the arbitrary zero for iron) is called the isomer shift of  $^{57}\text{Fe}$  and has units of mm/s.<sup>79</sup>

The isomer shift is a direct measure of the electron density at the  $^{57}\text{Fe}$  nucleus, providing information regarding oxidation state.<sup>79</sup> Due to the requirement that the electron density must be present at the nucleus to impact the isomer shift, only  $s$ -electrons directly effect this value. However, in the case of Fe nuclei involved in coordination compounds or ionic solids, the  $3d$ -electrons are expected to partially screen the nuclear charge from the  $4s$  electrons.<sup>83</sup> An increase in the number of  $3d$ -electrons at a  $^{57}\text{Fe}$  nucleus will cause enhanced screening that reduces  $s$ -

electron density at the nucleus, resulting in a more positive isomer shift value. It should be noted that explicit structural information cannot be extracted from the isomer shift value, though there is a trend for shorter ligand-iron bonds (via spin state, oxidation state, or coordination number) to result in lower isomer shift values.<sup>83</sup>

The Mössbauer spectra for  $^{57}\text{Fe}$  typically feature a doublet for each unique iron nucleus, the center of which is the isomer shift value. The peak separation within the doublet is due to electric quadrupole splitting. The nuclear excitation caused by absorption of  $\gamma$ -radiation causes a change in the nuclear spin-state from  $1/2$  to  $3/2$ .<sup>83</sup> In the presence of an electric field gradient, the nuclear excited state is split into two energy levels, thus causing two possible transitions to the ground-state. The splitting in energy is especially pronounced when a  $^{57}\text{Fe}$  atom has  $3d$  electronic structure with orbital angular momentum, making it possible to distinguish between low-spin and high-spin Fe complexes.<sup>83</sup> The electric quadrupole splitting is also sensitive to ligand charge and coordination geometry, though the precise consequence of these factors on the splitting value cannot be easily predicted.<sup>83</sup>

The above section provided an overview as to the types of characterization that were performed on paramagnetic species described in this thesis. The final section will now outline the content of each chapter in this work.

## 1.6 Scope of Thesis

The discussion in section 1.2 highlighted the influence that steric and electronic variations in the  $\beta$ -diketiminato ligand scaffold have on the reactivity of the resulting first-row transition metal complexes. It was proposed that since the electronic and steric factors of NacNac can be tuned for desirable outcomes in small molecule activation and catalysis, perhaps the utilization of a modular, unsymmetrical ligand scaffold would be beneficial for reactivity studies.

A bidentate enamido-phosphinimine scaffold was proposed, where the enamine-phosphine ligand precursor could be treated with various organic azides through the Staudinger reaction to generate a sterically unsymmetrical coordination environment (**Figure 1.12**). While bidentate phosphinimine containing ligand scaffolds on first-row transition metals have been used extensively as ethylene polymerization catalysts, small molecule activation with such systems is

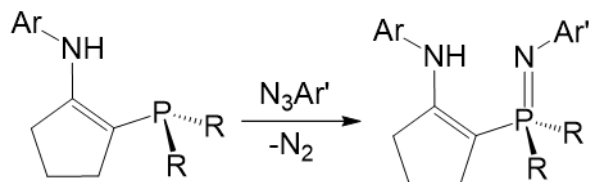


**Figure 1.12:** The use of different aryl azides in the Staudinger reaction allows for synthetic modularity in the generation of sterically unsymmetrical ligand scaffolds.

relatively unexplored.

Chapter 2 describes the synthesis of a number of sterically unsymmetrical enamine-phosphinimine ligand scaffolds and their coordination to iron. In addition to variation in the aryl group of the phosphinimine N-donor, the cyclopentyl ring of the ligand backbone was also substituted with an indene ring to study the effects of additional charge delocalization in the ligand backbone. A variety of low-coordinate Fe(II) bromide complexes were synthesized and their reduction chemistry, with the intent of forming dinitrogen complexes, was explored. Comparisons between the degree of dinitrogen activation in the enamido-phosphinimine iron dinitrogen complexes and  $\beta$ -diketiminate iron dinitrogen complexes are made. Additionally, a brief discussion into the synthesis of a dianionic indenyl enamido-phosphinimine ligand scaffold is provided.

The work presented in Chapter 3 focuses on the isolation of a low-coordinate iron hydride complex featuring a sterically encumbered enamido-phosphinimine ligand scaffold. The

insertion reactivity of the iron hydride species with unsaturated substrates such as 3-hexyne and azobenzene is analogous to the reactivity of  $\beta$ -diketiminato iron hydride complexes.

Interestingly, the enamido-phosphinimine iron hydride species can serve as a hydrodefluorination catalyst for perfluorinated aromatics. Comparisons are made to the hydrodefluorination reactivity of a literature reported  $\beta$ -diketiminato iron fluoride precatalyst and mechanistic proposals are put forth.

The contents of Chapter 4 deal with the isolation of a phosphazide intermediate in the Staudinger reaction used in the general ligand synthesis described in Chapter 2. The phosphazide intermediate is shown to be thermally stable at ambient conditions, and the enamine-phosphazide ligand scaffold was used in salt-metathesis reactions with  $\text{FeBr}_2(\text{THF})_2$  and  $\text{CoCl}_2(\text{Py})_4$ . The enamido-phosphazide iron bromide complex displays reactivity with potassium triethylborohydride to cleave the N-C(aryl) bond of the phosphazide moiety. Mechanistic studies that utilized deuteride labeling indicate that the ligand decomposition pathway occurred through a radical process.

Chapter 5 features preliminary results for phosphinimine complexes that may have useful catalytic applications and conclusions are drawn for the work presented in this thesis. Additionally, future directions for small molecule activation and catalysis are proposed based on the reactivity patterns documented in this thesis.

## Chapter 2: Iron Dinitrogen Complexes

### 2.1 Introduction

#### 2.1.1 Dinitrogen Activation

Nitrogen is an element critical for life, taking part in the structure of biomolecules such as DNA and polypeptides. However, in order for an organism to incorporate nitrogen into a biomolecule, reactive forms of nitrogen such as  $\text{NH}_3$  must first be synthesized from inert dinitrogen ( $\text{N}_2$ ). On an industrial scale, the chemical fixation of nitrogen is performed through the Haber-Bosch process, in which  $\text{H}_2$  and  $\text{N}_2$  are combined at  $500\text{ }^\circ\text{C}$  with a pressure of 200 bar to yield  $\text{NH}_3$ .<sup>84</sup> The importance of the Haber-Bosch process cannot be overstated. Often coined “bread from air,” synthetic ammonia production for use in agricultural fertilizers is estimated to feed 40% of the world’s population.<sup>85-86</sup> Critical to the practicality of the Haber-Bosch process is the Mittasch catalyst employed in the reactor, which is identified as promoted  $\alpha$ -Fe, formed from reduction of a fused mixture of  $\text{Fe}_3\text{O}_4$ ,  $\text{Al}_2\text{O}_3$  and  $\text{K}_2\text{O}$ .<sup>84, 87</sup> Mechanistic studies have shown that the rate limiting step for nitrogen fixation is the cleavage of chemisorbed  $\text{N}_2$  to form nitrides ( $\text{N}^{3-}$ ) on the surface of the Fe catalyst.<sup>88-89</sup> While exact details as to the number of iron atoms necessary for  $\text{N}_2$  dissociation has eluded investigation, informative comparisons can be drawn to biological nitrogen fixation, in which multiple iron sites within the nitrogen fixing metalloenzyme nitrogenase play an important role in catalytic ammonia production.

Nitrogenase catalytically convert  $\text{N}_2$ , electrons, and protons to  $\text{NH}_3$  and an equivalent of  $\text{H}_2$  through the consumption of 16 ATP molecules at standard temperature and pressures (equation 2.1). The most thoroughly studied form of the nitrogenase contains a MoFe protein



featuring the FeMo cofactor, the active site where nitrogen fixation occurs.<sup>90-92</sup> The structure of the FeMo cofactor is shown below in **Figure 2.1**.<sup>90, 93-95</sup> The exact mechanism for nitrogen

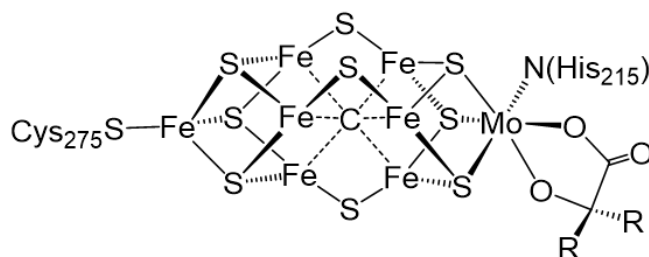


**Figure 2.1:** The Iron-Molybdenum cofactor found within the nitrogenase enzyme.

fixation at the FeMo cofactor is not yet understood, but is hypothesized to involve low-coordinate iron sites to aid in the coordination of N<sub>2</sub>.<sup>91, 96</sup> Further support for the importance of iron in biological nitrogen fixation can be seen in other forms of nitrogenase lacking molybdenum at the active site, such as the vanadium nitrogenase and the all iron nitrogenase, all of which catalyze ammonia synthesis, albeit with lower activity.<sup>97-98</sup>

Since the discovery of the first metal-dinitrogen complex [Ru(NH<sub>3</sub>)<sub>5</sub>(N<sub>2</sub>)]<sup>2+</sup> in 1965,<sup>99</sup> coordination chemists continue to strive towards a molecular catalytic system for the fixation of nitrogen. Interestingly, of the few catalytic systems that have been successfully developed, most reported examples require either molybdenum or iron centers for nitrogen functionalization (**Figure 2.2**).<sup>100-105</sup> In addition to the contributions from the Nishibayashi group<sup>103-105</sup> shown in **Figure 2.2**, they have also reported the catalytic formation of tris(trimethylsilyl)amine (N(SiMe<sub>3</sub>)<sub>3</sub>) from dinitrogen using both ferrocene and [Fe(CO)<sub>5</sub>] as catalysts.<sup>106</sup> A point of interest in all of the aforementioned systems is that the metals utilized for catalysis are the same metals comprising the molybdenum-iron cofactor of nitrogenase.

In addition to the aforementioned catalytic systems capable of nitrogen fixation, iron complexes bearing β-diketimate ligands have also been shown to coordinate and activate N<sub>2</sub>.

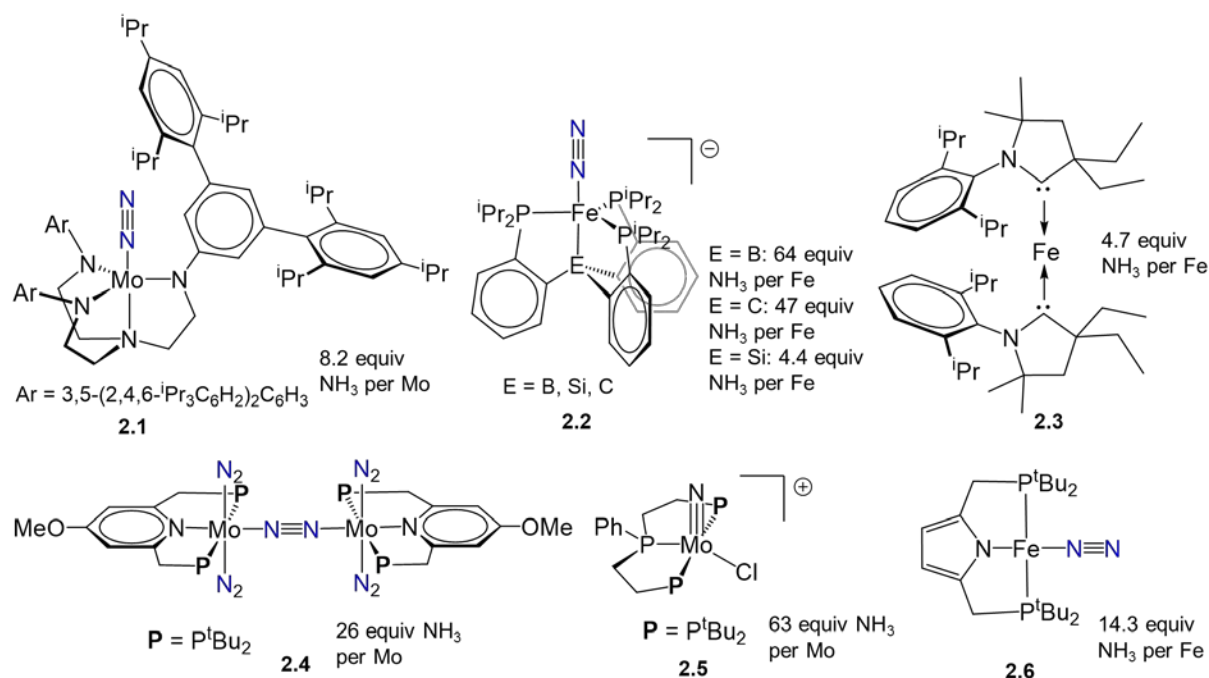


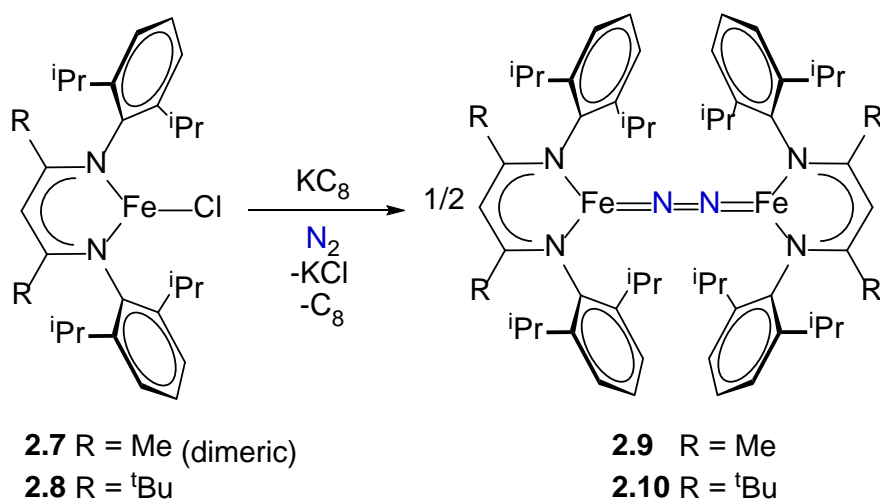
**Figure 2.2:** Catalytic systems capable of converting N<sub>2</sub> to NH<sub>3</sub>. **2.1** see ref 100. All three variations of **2.2** where E = B, Si, and C are reported in ref 101. **2.3** see ref 102. **2.4** see ref 103. **2.5** see ref 104. **2.6** see ref 105. The NH<sub>3</sub> equivalents shown are the highest single run values reported for each complex.

While there has yet to be a reported instance of catalytic dinitrogen functionalization from  $\beta$ -diketiminato iron dinitrogen complexes, such species are of fundamental interest for understanding the role of ligand sterics and stabilizing cations during the course of dinitrogen activation. This is the subject of the next section.

### 2.1.2 $\beta$ -diketiminato Iron Dinitrogen Complexes

Pioneering work on the synthesis and characterization of low-coordinate  $\beta$ -diketiminato iron dinitrogen complexes was performed by Holland and coworkers. Initial studies focused on the reduction of iron chloride complexes featuring  $\beta$ -diketiminato ligands decorated with bulky 2,6-diisopropylphenyl rings on the N-donors, with either methyl or *tert*-butyl groups in the backbone of the ligand. Both the methyl (**2.7**) and *tert*-butyl (**2.8**)  $\beta$ -diketiminato iron chloride complexes yield dimeric end-on bridging dinitrogen complexes upon reduction with potassium

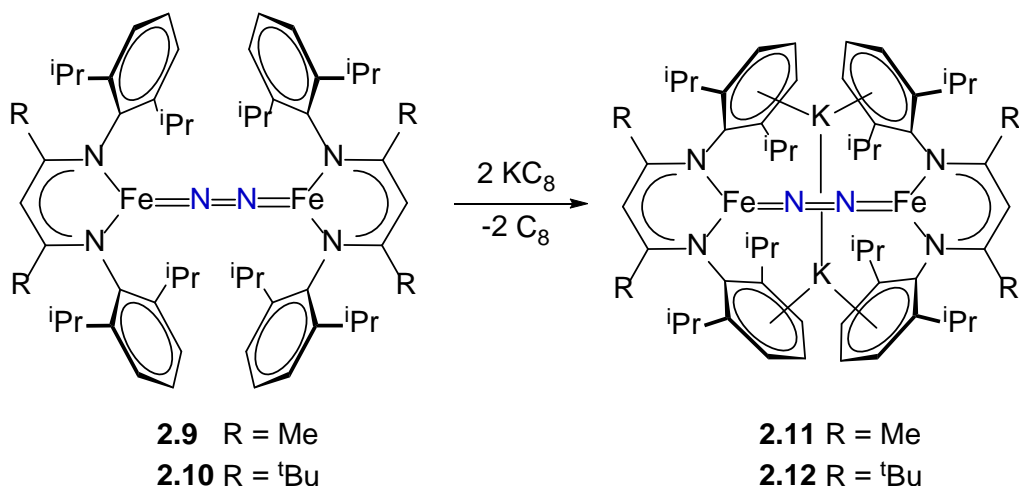
graphite (KC<sub>8</sub>) under an atmosphere of N<sub>2</sub> (**Scheme 2.1**).<sup>107</sup> Complex **2.9** has a coordinated N–N distance of 1.186(7) Å<sup>107</sup> and for **2.10** this bond length is slightly elongated at 1.192(6) Å.<sup>34</sup>



**Scheme 2.1:** Reduction of iron chloride complexes **2.7** and **2.8** with KC<sub>8</sub> in the presence of N<sub>2</sub> yields the bridging N<sub>2</sub> complexes **2.9** and **2.10**.

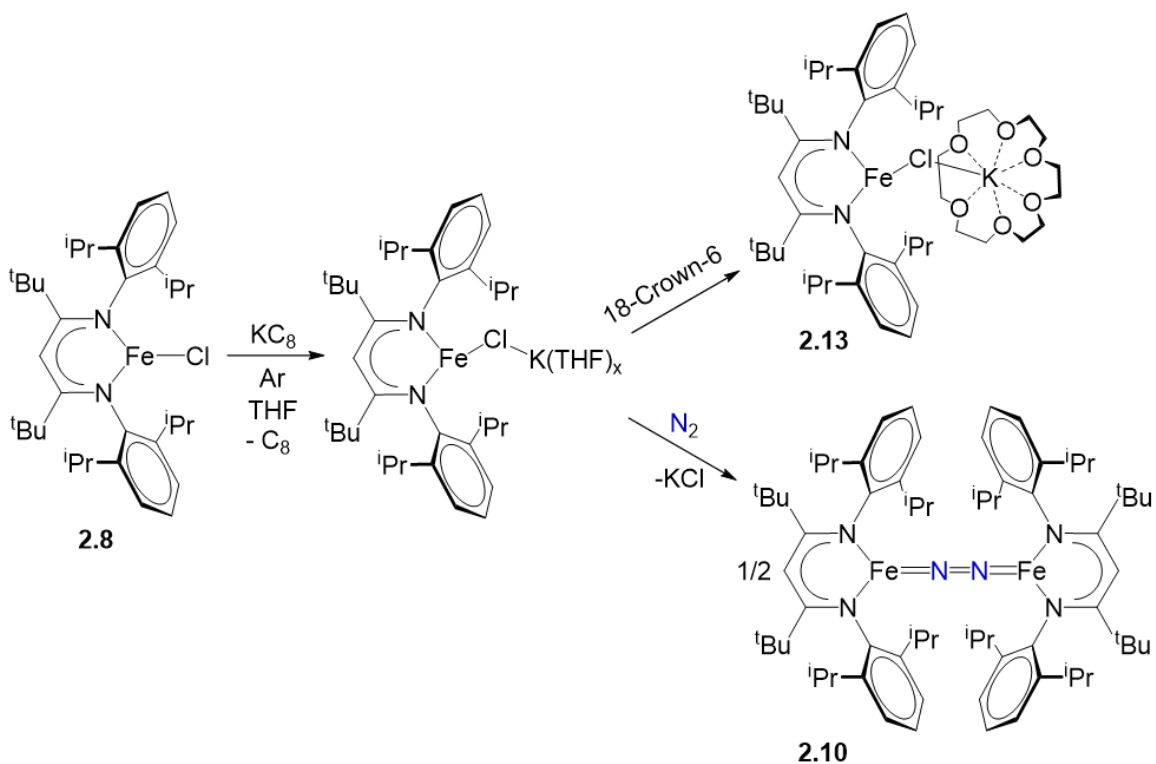
These N–N bond distances are longer than the triple bond of free N<sub>2</sub> (1.098 Å), but shorter than the N=N double bond (1.25 Å). However, Mössbauer data and computations provide support for the formulation of the coordinated dinitrogen existing as N<sub>2</sub><sup>2-</sup>, with both iron centers having Fe<sup>2+</sup> character.<sup>16</sup>

Further reduction of both **2.9** and **2.10** is possible by adding an additional equivalent of KC<sub>8</sub> per Fe (**Scheme 2.2**). Increased elongation of the N–N bond is observed, with a distance of 1.215(6) Å for **2.11** and 1.241(7) Å for **2.12**.<sup>34, 107</sup> The K<sup>+</sup> ion is also present within both structures, forming a critical interaction with the aryl rings of the ligand as well as with the coordinated N<sub>2</sub>; removal of K<sup>+</sup> from compounds **2.11** and **2.12** with 18-crown-6 leads to intractable product mixtures. Computational results indicate that the K<sup>+</sup> ion enhances the orbital interaction between the Fe based dπ orbitals and the π\* orbital of N<sub>2</sub>, which leads to further weakening of the N–N bond.<sup>107</sup>



**Scheme 2.2:** Reduction of the N<sub>2</sub> complexes **2.9** and **2.10** with KC<sub>8</sub> yields the further reduced N<sub>2</sub> complexes **2.11** and **2.12**.

Reduction of the three-coordinate iron chloride complex **2.8** under an argon atmosphere in the presence of 18-crown-6 allows for the isolation of **2.13** (Scheme 2.3). Exposure of the

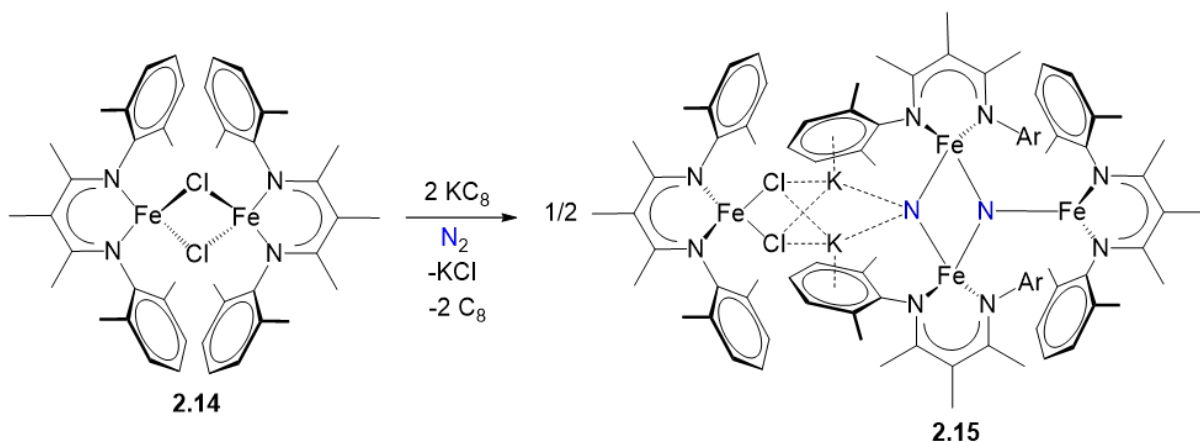


**Scheme 2.3:** Reduction of the  $\beta$ -diketiminato FeCl complex in the absence of N<sub>2</sub> leads to the formation of Fe(I) KCl adducts. If a crown ether is used to stabilize the generated KCl adduct, complex **2.13** can be isolated. Exposure of the KCl adducts to N<sub>2</sub> leads to the formation of **2.10**.

KCl adducts to  $N_2$  generates the  $N_2$  complex **2.10**, indicating that the Fe(I) adduct of KCl is formed prior to the coordination of  $N_2$ . This result will be of importance later in this chapter.

The  $N_2$  complexes **2.9** and **2.10** act as sources of Fe(I) and display reactivity patterns as such. For example, coordinated  $N_2$  is displaced and reduction of elemental sulfur<sup>45</sup>, carbon dioxide<sup>108</sup>, and acetophenone<sup>107</sup> occurs. Likewise, addition of stronger  $\pi$  acceptors than  $N_2$ , such as benzene<sup>107</sup>, carbon monoxide<sup>107</sup>, or alkynes<sup>109</sup>, leads to the irreversible displacement of  $N_2$  for the stronger  $\pi$  acid. However, attempts at the functionalization of the coordinated  $N_2$  by treatment with strong acid for both **2.9** and **2.10**, as well as with the doubly reduced species **2.11** and **2.12** failed to produce appreciable amounts of  $NH_3$ .<sup>107</sup>

In an attempt to further enhance the reactivity of low-coordinate iron  $\beta$ -diketiminate complexes, the steric demand of the ligand scaffold was decreased by replacing the isopropyl groups with methyl groups at the 2,6-positions of the aryl rings decorating the N-donors. When the bridging chloride species **2.14** was reduced with  $KC_8$  under an atmosphere of  $N_2$ , a surprising result was obtained in which the dinitrogen triple bond was completely cleaved, resulting in the formation of the four Fe, two nitride cluster **2.15**, stabilized by two  $K^+$  ions (Scheme 2.4).<sup>110</sup> The



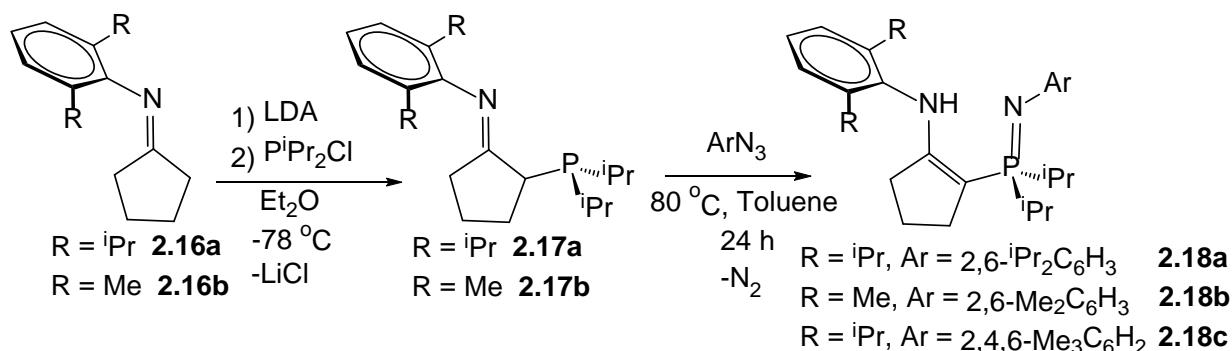
**Scheme 2.4:** Reduction of **2.14** with  $KC_8$  under an atmosphere of  $N_2$  leads to the formation of **2.15** in which  $N_2$  has been fully reduced to two  $N^{3-}$ .

enhanced reactivity observed during the reduction of **2.14** in comparison to the more sterically hindered iron chloride complexes **2.7** and **2.8** was suggested to result from the ability of multiple Fe centers to interact with N<sub>2</sub>, allowing for the six electron reduction of N<sub>2</sub> to two bridging nitrides.<sup>110</sup> The reduction observed in **2.15** is reversible. Upon subsequent treatment of **2.15** with strong  $\pi$  acids such as CO, isocyanide, and benzene, the two bridging nitrides reform the N<sub>2</sub> triple bond along with KCl and the Fe(I) complex of the  $\pi$  acid.<sup>111</sup> The presence of the alkali metal cation is critical for the formation of the observed cluster (an analogous cluster to **2.15** can be formed with Rb) and there is evidence that the alkali metal can steer the cooperation of multiple Fe atoms to reduce the N<sub>2</sub> triple bond.<sup>112</sup>

As can be seen from the above work, small changes in the steric environment of the  $\beta$ -diketiminate scaffold can result in large changes in reactivity towards N<sub>2</sub> activation. Inspired by the work of Holland and coworkers regarding the synthesis and reduction of low-coordinate iron complexes, the work presented in the remainder of Chapter 2 focuses on the synthesis and coordination chemistry of sterically and electronically unsymmetrical enamine-phosphinimine  $\beta$ -diketiminate mimics (outlined in Chapter 1), with iron dinitrogen complexes being the target compounds. In addition, attempts were made at synthesizing an indenyl ligand scaffold that could hold negative charge and coordinate K<sup>+</sup> ions, potentially leading to the self-assembly of iron-potassium-dinitrogen clusters.

## 2.2 Ligand Synthesis

The synthetic protocol for generating enamine-phosphinimine ligands featuring varying degrees of steric hindrance is shown in **Scheme 2.5**. The starting cyclopentylidene

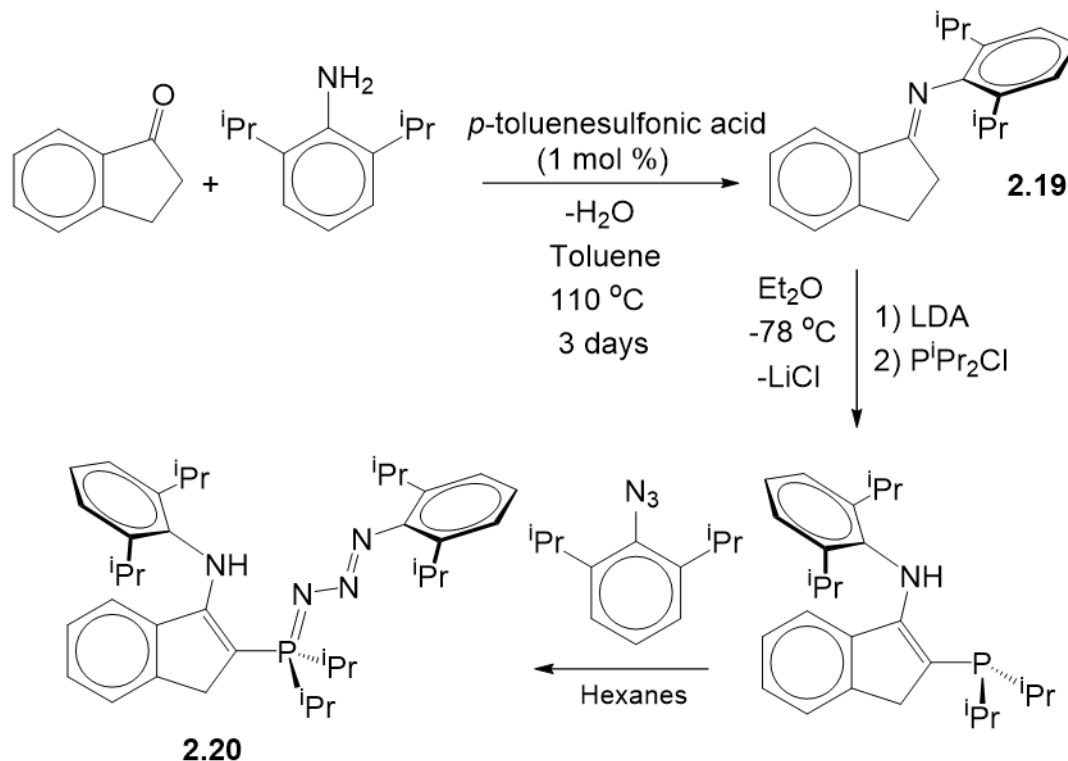


**Scheme 2.5:** General ligand synthesis for the preparation of the enamine-phosphinimine ligands **2.18a-c**.

imines **2.16a-b** and cyclopentylidene imine diisopropylphosphines **2.17a-b** have been previously reported in our laboratory and were synthesized according to the published procedure.<sup>56</sup> Upon treatment of **2.17a** and **2.17b** with the appropriate aryl azide and heating to 80 °C for 1-4 days, the desired enamine-phosphinimine moieties **2.18a**, [<sup>CY5</sup>NpN<sup>DIPP,DIPP</sup>]H, **2.18b**, [<sup>CY5</sup>NpN<sup>DMP,DMP</sup>]H, and **2.18c**, [<sup>CY5</sup>NpN<sup>DIPP,Mes</sup>]H were prepared in good yields; these aryl substituents on both the imine and the phosphinimine provide a range of steric effects that can enhance or lessen the difference between the unsymmetrical donors of these ligand precursors. Nomenclature for the naming of the above compounds follows where CY5 represents the cyclopentylidene linker and DIPP, DMP, and Mes are the imine substituents, 2,6-diisopropylphenyl, 2,6-dimethylphenyl, and 2,4,6-trimethylphenyl respectively. In the <sup>1</sup>H NMR spectra, **2.18a-c** have a characteristic downfield resonance for the enamine N-H proton found near δ 9, likely caused by hydrogen bonding with the phosphinimine nitrogen. The recently reported [NpNP<sup>*i*Pr</sup>]H system with a linked *ortho*-phenylene P<sup>*i*Pr</sup><sub>2</sub> on the phosphinimine donor displayed an identical chemical shift for the N-H resonance at δ 9.0 in the <sup>1</sup>H NMR spectrum in

addition to an observed hydrogen bond between the enamine N-H and phosphinimine moiety in the solid-state molecular structure.<sup>73</sup> The  $^{31}\text{P}\{^1\text{H}\}$  NMR spectra for **2.18a-c** are very similar to one another, with singlet resonances found between  $\delta$  19.6-18.6.

In addition to the cyclopentylidene based ligand scaffold described above, a scaffold containing an indene unit was synthesized (**Scheme 2.6**). Imine **2.19** was prepared in poor yields



**Scheme 2.6:** Synthesis for the indene ligand scaffold to the point where the enamine-phosphazide **2.20** was isolated.

from the condensation reaction between 1-indanone and 2,6-diisopropylaniline. The solid state molecular structure for **2.19** (**Figure 2.3**) confirms the formation of the C=N bond, as the distance of 1.276(1) Å is a typical length for a carbon-nitrogen double bond. **Figure 2.3** also

shows that the aryl group is oriented *trans* and perpendicular to the aromatic ring of the indene unit.

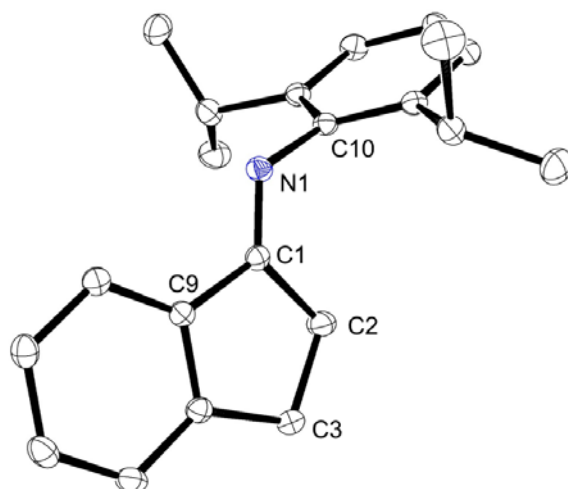


**Figure 2.3:** ORTEP drawing of the solid-state molecular structure of **2.19** (ellipsoids at 50% probability level). All hydrogen atoms have been omitted for clarity. Selected bond lengths (Å), angles (deg), and torsion angles (deg): C1-C2: 1.519(1), C1-N1: 1.276(1), N1-C10: 1.423(1), C1-N1-C10: 120.2(7), C9-C1-N1-C10: 6.2(7).

Deprotonation of **2.19** with lithium diisopropylamide, followed by a quench with chlorodiisopropylphosphine and subsequent addition of 2,6-diisopropylphenylazide resulted in the isolation of the enamine-phosphazide [<sup>IND</sup>NpN<sub>3</sub><sup>DIPP,DIPP</sup>]H **2.20** after recrystallization. Enamine-phosphazide **2.20** displays a signal in the <sup>31</sup>P{<sup>1</sup>H} NMR spectrum located at δ 51.9. The N-H resonance is shifted downfield at δ 11.6 due to a hydrogen bonding interaction with the triaza unit of the phosphazide. The solid-state molecular structure confirms the enamine-

phosphazide structure of **2.20**, as well as the hydrogen bonding interaction between the enamine hydrogen atom and the phosphinimine nitrogen atom (**Figure 2.4**).

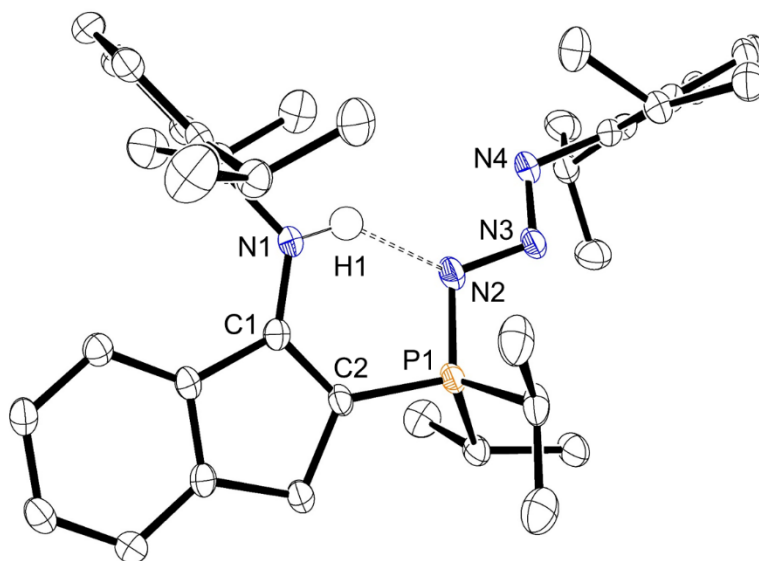
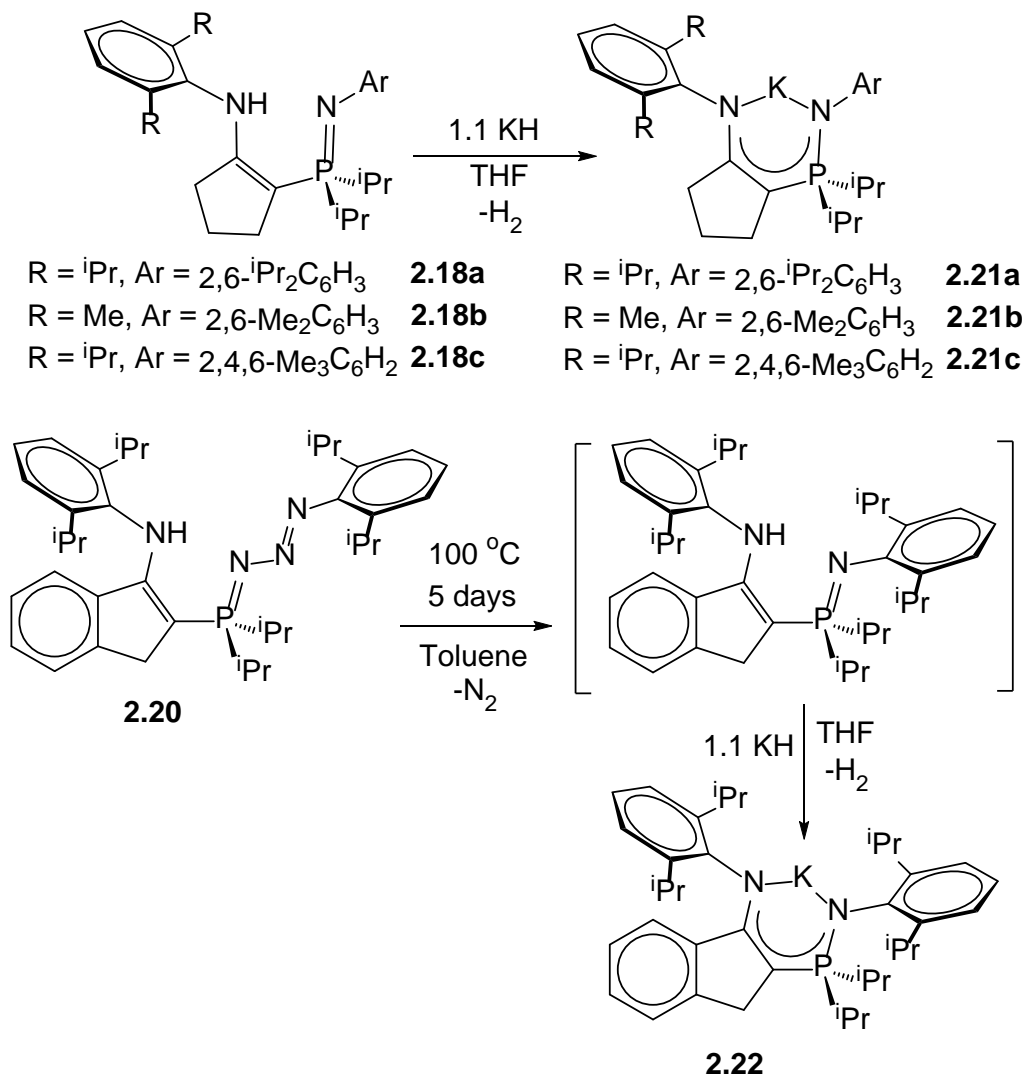


**Figure 2.4:** ORTEP drawing of the solid-state molecular structure of **2.20** (ellipsoids at 50% probability level). All hydrogen atoms except H1 have been omitted for clarity. H1 was located in the difference map. Selected bond lengths (Å), angles (deg), and torsion angles (deg): C1-C2: 1.379(3), C1-N1: 1.353(3), C2-P1: 1.761(2), P1-N2: 1.635(2), N2-N3: 1.369(2), N3-N4: 1.265(3), N1-H1: 0.880(2), N2-H1: 2.051(2), P1-N2-N3: 112.97(2), N2-N3-N4: 110.59(2), C1-C2-P1-N2: 21.0(2), P1-N2-N3-N4: 175.18(2).

The reaction of precursors **2.18a-c** with excess potassium hydride (KH) resulted in deprotonation to generate the corresponding potassium complexes **2.21a**,  $[\text{CY}^5\text{NpN}^{\text{DIPP,DIPP}}]\text{K}(\text{THF})_2$ , **2.21b**,  $[\text{CY}^5\text{NpN}^{\text{DMP,DMP}}]\text{K}(\text{THF})_{0.25}$ , and **2.22c**,  $[\text{CY}^5\text{NpN}^{\text{DIPP,Mes}}]\text{K}$ , as evidenced by the disappearance of the downfield N-H resonance in the  $^1\text{H}$  NMR spectra of the isolated salts. The  $^{31}\text{P}\{^1\text{H}\}$  NMR spectra for these potassium derivatives **2.21a-c** are shifted slightly upfield relative to the starting protonated ligand precursors. Heating **2.20** to 100 °C for 5 days followed by subsequent treatment with potassium hydride also resulted in the formation of the potassium complex  $[\text{INDNpN}^{\text{DIPP,DIPP}}]\text{K}$  **2.22**. Interestingly, the methylene protons of the indene ring are resistant to deprotonation. Using an excess of potassium hydride does not result



**Scheme 2.7:** Deprotonation with KH yields the corresponding potassium enamido-phosphinimine salts.

in the formation of a dianionic complex. Rather, only the enamine nitrogen is deprotonated. This is supported by the  $^1\text{H}$  NMR spectrum for **2.22**, in which the methylene protons are clearly observed as a singlet at  $\delta$  3.8 that integrates to 2 H but the downfield N-H resonance is absent. Additional support for the single deprotonation is seen in the solid-state molecular structure of **2.22**, shown below as a diethyl ether adduct in **Figure 2.5**. While KH is not basic enough to remove the methylene proton in the indene backbone of **2.22**, a stronger base is capable of performing the desired deprotonation (see Chapter 2.4). Having synthesized a wide range of

sterically diverse potassium enamido-phosphinimine salts, the generation of low-coordinate Fe(II) complexes was pursued.

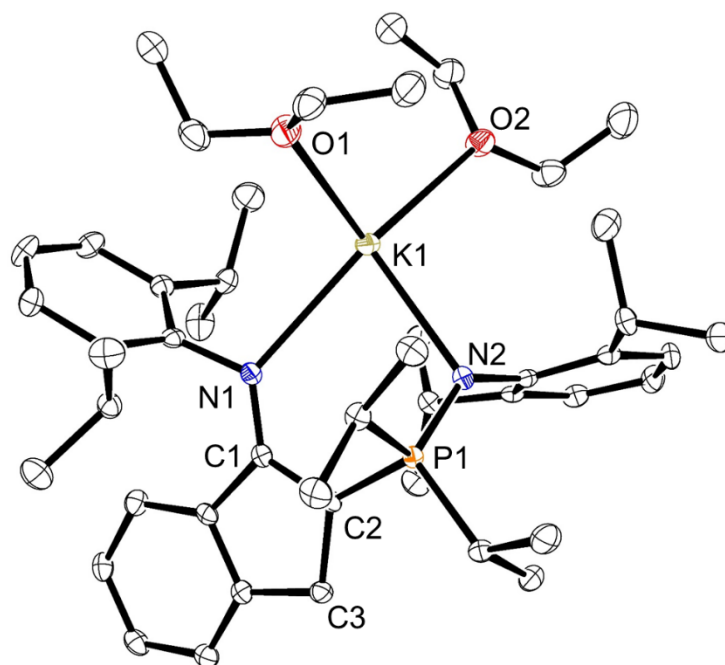


**Figure 2.5:** ORTEP drawing of the solid-state molecular structure of **2.22** (ellipsoids at 50% probability level). All hydrogen atoms have been omitted for clarity. Selected bond lengths (Å), angles (deg), and torsion angles (deg): C1-N1: 1.342(3), C1-C2: 1.406(3), C2-C3: 1.519(3), C2-P1: 1.763(3), P1-N2: 1.596(2), N1-K1: 2.820(2), N2-K1: 2.714(2), K1-O1: 2.717(2), K1-O2: 2.832(2), C2-C1-N1: 126.2(2), N1-K1-N2: 77.9(6), C2-P1-N2-K1: 58.1(2).

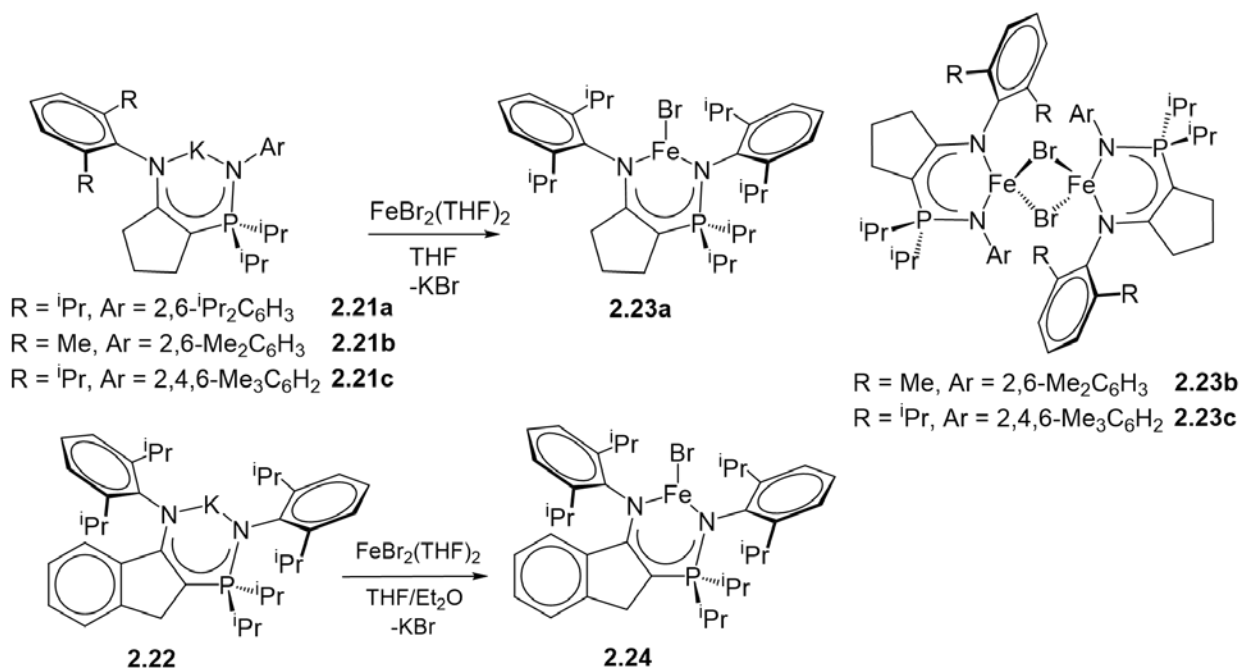
## 2.3 Synthesis of Iron Dinitrogen Complexes

### 2.3.1 Synthesis of Low-Coordinate Iron Bromide Complexes

Treatment of the potassium salts **2.21a-c** and **2.22** with  $\text{FeBr}_2(\text{THF})_2$  in THF provided the iron(II) bromide complexes **2.23a**,  $[\text{CY}^5\text{NpN}^{\text{DIPP,DIPP}}]\text{FeBr}$ , **2.23b**,  $([\text{CY}^5\text{NpN}^{\text{DMP,DMP}}]\text{FeBr})_2$ , **2.23c**,  $([\text{CY}^5\text{NpN}^{\text{DIPP,Mes}}]\text{FeBr})_2$ , and **2.24**,  $[\text{INDNpN}^{\text{DIPP,DIPP}}]\text{FeBr}$  in moderate to good yield as crystalline yellow or orange solids (**Scheme 2.8**). These complexes are paramagnetic and show high-spin room temperature magnetic moments as measured by the Evans method in  $\text{C}_6\text{D}_6$ .

While the magnetic moment for **2.23a** and **2.24** is normal for high spin ( $\mu_{\text{eff}} = 5.3 \mu_{\text{B}}$  and  $5.2 \mu_{\text{B}}$

respectively, measured in  $C_6D_6$ ), complexes **2.23b** and **2.23c** display lower magnetic moment values at 4.2 and 4.0  $\mu_B$ , respectively; these lower values are discussed below.



**Scheme 2.8:** The salt metathesis reactions between the potassium salts **2.21a-c** and **2.22** with  $FeBr_2(THF)_2$ .

There is a drastic difference in the solubility of complex **2.23c** in comparison to **2.23a**, **2.23b**, and **2.24**. Whereas **2.23c** is only soluble in THF and  $CH_2Cl_2$ , **2.23a**, **2.23b**, and **2.24** are soluble in THF,  $CH_2Cl_2$  and aromatic solvents. **Figures 2.6** and **2.7** contrast the effects of the deuterated solvent on the resulting  $^1H$  NMR spectra for **2.23a** and **2.23c**, respectively. For example, the spectra for **2.23a** (**Figure 2.6**) in  $d_8$ -THF,  $CD_2Cl_2$  and  $C_6D_6$  are similar, with moderate shifts in select resonances. In contrast, completely different spectra are observed for **2.23c** (**Figure 2.7**), where sharp, well-resolved signals are obtained in  $d_8$ -THF and very broad resonances result from using  $C_6D_6$  as the NMR solvent. Interestingly, the  $^1H$  NMR spectrum of **2.23c** in  $CD_2Cl_2$  is different from the spectra collected in  $d_8$ -THF. This difference could be attributed to the fact that  $d_8$ -THF can coordinate to the iron center, disrupting the symmetry of

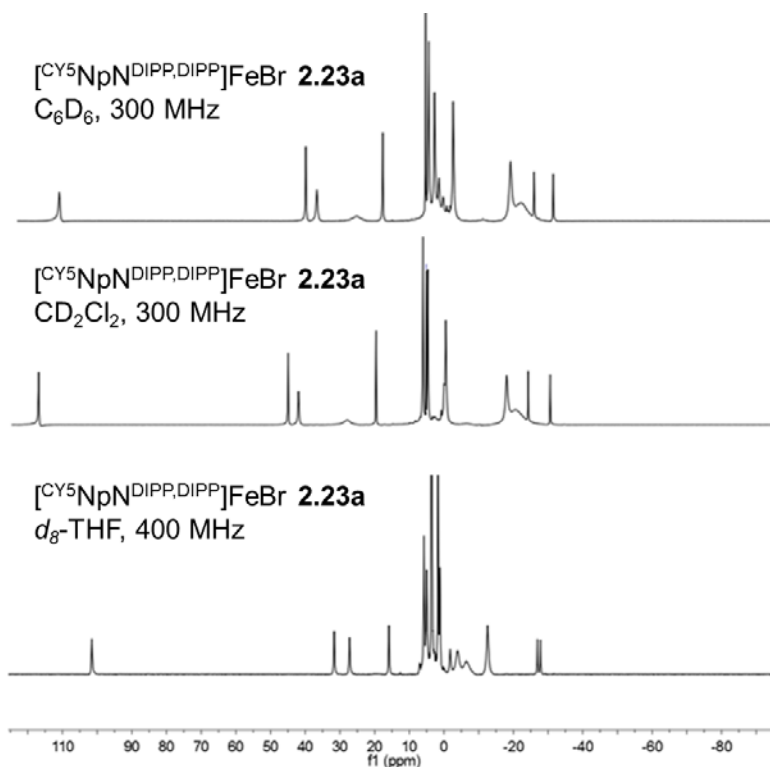


**Figure 2.6:**  $^1\text{H}$  NMR spectra for  $[\text{CY}^5\text{NpN}^{\text{DIPP,DIPP}}]\text{FeBr}$  **2.23a** in  $d_6$ -benzene (top),  $d_2$ -DCM (middle), and  $d_8$ -THF (bottom).

the solubilized complex in comparison to when  $\text{CD}_2\text{Cl}_2$  is used as the solvent. It is also possible (and supported by the solid-state structures shown below) that complex **2.23c** is solubilized in a dimeric form when  $\text{CD}_2\text{Cl}_2$  is used as the solvent, but dissociates into monomers in  $d_8$ -THF, resulting in different  $^1\text{H}$  NMR spectra, as the magnetic environment present between monomeric and dimeric iron species will be drastically different. This observation also explains the lower magnetic moments measured in solution for the less sterically crowded complexes in  $\text{C}_6\text{D}_6$ , as they are likely solubilized as dimers and thus experience weak anti-ferromagnetic coupling across the bridging bromide ligands via superexchange pathways.<sup>113-115</sup>

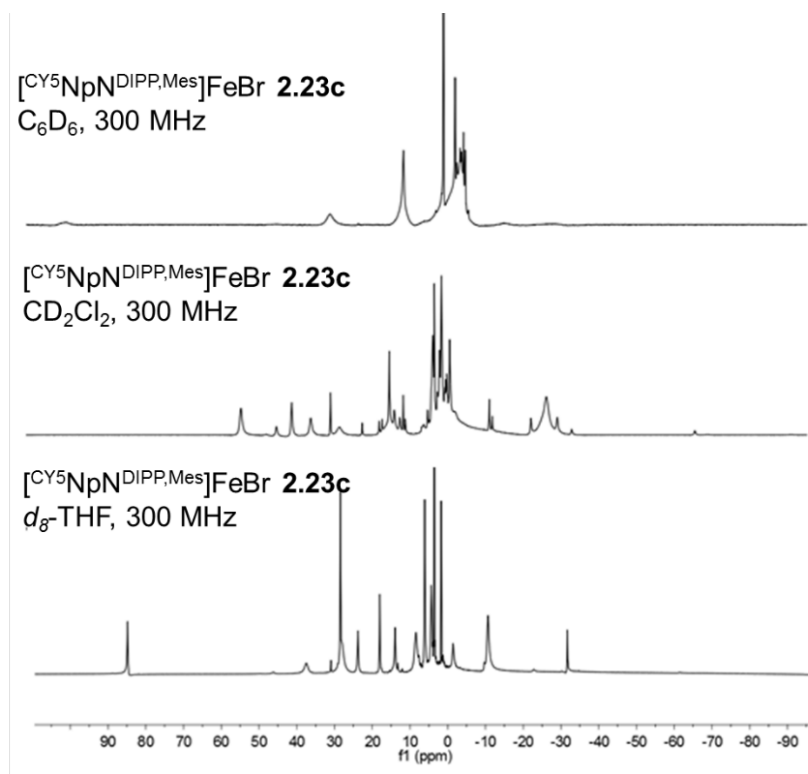


**Figure 2.7:**  $^1\text{H}$  NMR spectra for  $[\text{CY5NpN}^{\text{DIPP,Mes}}]\text{FeBr}$  **2.23c** in  $d_6$ -benzene (top),  $d_2$ -DCM, (middle) and  $d_8$ -THF (bottom).

A comparison of the  $^1\text{H}$  NMR spectra for complexes **2.23a-c** in  $d_8$ -THF is provided in **Figure 2.8**. Each of the three complexes is  $C_s$  symmetric, even considering the potential for **2.23b** and **2.23c** to be dimeric in solution. The expected 16 resonances based on unique proton environments are observed for complexes **2.23b** and **2.23c**, but only 13 of 16 signals are observed for **2.23a**; the difference between observed and expected signals may be due to signal overlap, as the integration value obtained for the sum of the resonances equals the expected 54 protons counted for the ligand backbone of **2.23a**. The number of expected signals is determined by considering that each of the complexes contains a horizontal mirror plane. Definitive signal assignments were not made for any of these complexes due to the number of unique proton environments with similar integration values; for example, complexes **2.23a-c** each contain three different methylene ( $\text{CH}_2$ ) environments in the cyclopentenyl ring, as well as the 3,5-positions of

the aryl rings that each integrate to 2 protons, none of which can be unequivocally identified. Nevertheless, informative comparisons can be drawn between the spectra in **Figure 2.8**. For

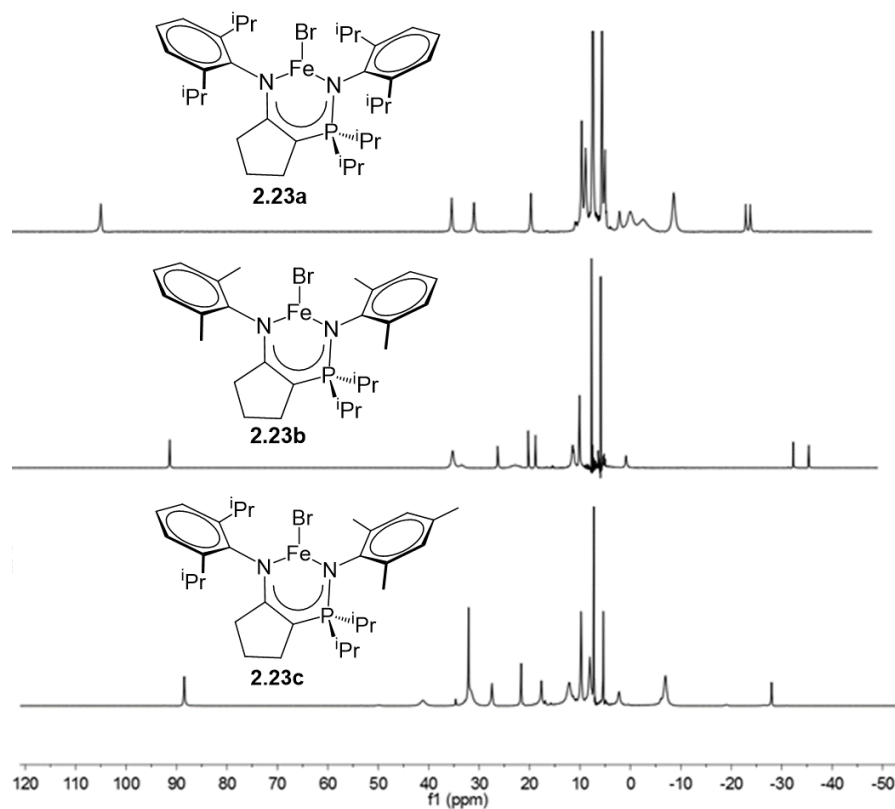


**Figure 2.8:**  $^1\text{H}$  NMR spectra for **2.23a** (top), **2.23b** (middle), and **2.23c** (bottom) (400 MHz,  $d_8$ -THF, 298 K).

example, the slightly broadened resonances located at  $\delta$  -12.6 and -10.6 in **2.23a** and **2.23c** respectively, integrate to 6 protons. The spectrum for complex **2.23b** does not display a corresponding resonance in this region, suggesting that the signals belong to a set of methyl protons present on the aryl isopropyl groups. The very downfield signal at  $\delta$  109.6 in **2.23a** is assigned to one of the methylene units of the cyclopentylidene ring as it integrates to 2 protons and corresponds to a similar peak at  $\delta$  88.0 in complex **2.23b**, which does not contain any aryl isopropyl methine protons; **2.23c** shows a similar peak at  $\delta$  84.8 that integrates to 2 protons. Complex **2.24**, not shown in **Figure 2.8**, has its own unique resonances at  $\delta$  15.9 and 208.4 when

compared to the similar 2,6-diisopropylphenyl decorated complex **2.23a**. The signal at  $\delta$  208.4 likely belongs to the methylene position of the indene ring, as this position would have a different chemical environment compared to the cyclopentylidene analog.

The solid-state molecular structure for **2.23a** is shown in **Figure 2.9**. A comparison between the structure of **2.23a** and the  $\beta$ -diketiminato iron chloride complex,<sup>26</sup> [<sup>t</sup>BuNacNac<sup>DIPP</sup>]<sub>2</sub>FeCl (**2.8** from the introduction **2.1.2**), provides some insight as to the steric hindrance imparted to the iron center through the use of the enamido-phosphinimine ligand. If the C6-N1-C1 angle of **2.23a** is compared to the analogous C-N-C angle in [<sup>t</sup>BuNacNac<sup>DIPP</sup>]<sub>2</sub>FeCl, the degree that the N-donor aryl groups are forced towards the Fe in these two complexes can be quantified. In the symmetric [<sup>t</sup>BuNacNac<sup>DIPP</sup>]<sub>2</sub>FeCl complex, the C-N-C angle is 128.4(2)°, while

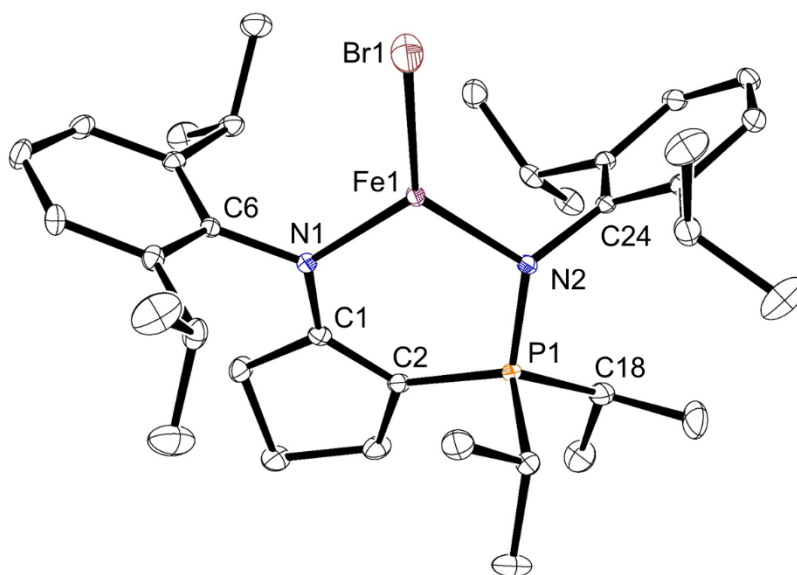


**Figure 2.9:** ORTEP drawing of the solid-state molecular structure of **2.23a** (ellipsoids at 50% probability level). All hydrogen atoms have been omitted for clarity. Selected bond lengths (Å), angles (deg), and torsion angles (deg): C1-N1: 1.359(4), C1-C2: 1.382(4), C2-P1: 1.771(3), C18-P1: 1.858(4), P1-N2: 1.637(2), N1-Fe1: 1.943(2), N2-Fe1: 1.956(3), Fe1-Br1: 2.3290(6), C2-C1-N1: 129.6(3), N1-Fe1-Br1: 125.35(8), N2-Fe1-Br1: 129.93(7), N1-Fe1-N2: 104.72(10), C1-N1-C6: 118.8(2), P1-N2-C24: 125.9(2), C1-C2-P1-N2: 28.3(3).

for **2.23a** shallower angles are measured of  $118.8(2)^\circ$  for C1-N1-C6 and  $125.9(2)^\circ$  for P1-N2-C24; the larger angle centered on the phosphinimine nitrogen N2 compared to N1 can be rationalized by the steric crowding present with the isopropyl groups on phosphorus. However, this steric effect is not as great as that observed for the *tert*-butyl groups in  $[\text{tBuNacNac}^{\text{DIPP}}]\text{FeCl}$ . The N1-Fe1-N2 bite angle in **2.23a** is  $104.72(10)^\circ$ , which is larger than the  $96.35(11)^\circ$  angle reported for  $[\text{tBuNacNac}^{\text{DIPP}}]\text{FeCl}$ , and implies more access to the central iron in the former. The C1-C2 bond length of  $1.382(4) \text{ \AA}$  is longer than the  $1.34 \text{ \AA}$  bond distance observed for C=C bonds, but shorter than the C-C bond length of  $1.403(3) \text{ \AA}$  observed in  $[\text{tBuNacNac}^{\text{DIPP}}]\text{FeCl}$ . However, the C1-N1 distance in **2.23a** of  $1.359(4) \text{ \AA}$  is similar to the analogous C-N distance of  $1.346(3) \text{ \AA}$  in  $[\text{tBuNacNac}^{\text{DIPP}}]\text{FeCl}$ . Also of note is the significant shortening of the C2-P1 bond distance to  $1.771(3) \text{ \AA}$  in comparison to the phosphorus-isopropyl carbon (C18-P1) single bond distance of  $1.858(4) \text{ \AA}$ , indicating that there is double bond character between phosphorus and the carbon in the cyclopentylidene ring. These effects indicate that there is charge delocalization within the ligand framework of the electronically asymmetric bidentate ligand. Single crystals were also grown for  $[\text{INDNpN}^{\text{DIPP,DIPP}}]\text{FeBr}$  **2.24** but the X-ray diffraction data was not of sufficient quality to accurately determine bonding metrics. Nonetheless, the solid-state structure showing connectivity is displayed in **Figure 2.10**.

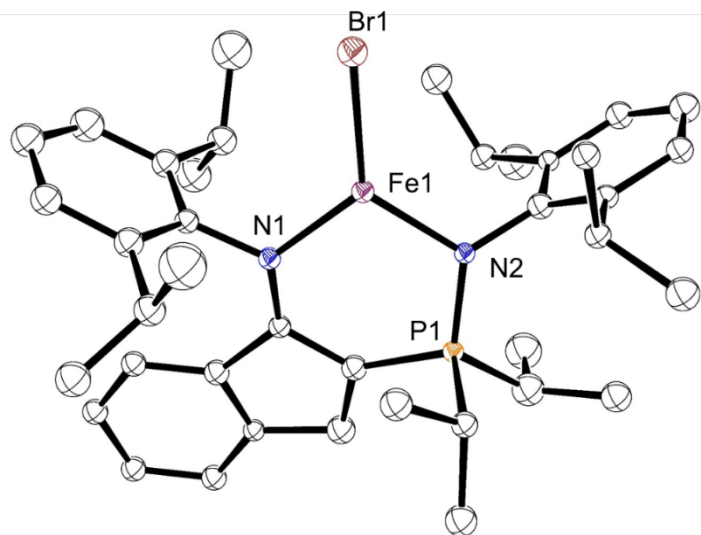


**Figure 2.10:** ORTEP drawing of the solid-state molecular structure of **2.24**. All atoms are isotropically refined due to poor data quality. Hydrogen atoms and the co-crystallized toluene molecule have been omitted for clarity.

In contrast to **2.23a** and **2.24**, complexes **2.23b** and **2.23c** are dimeric in the solid-state. The substitution of 2,6-diisopropylphenyl with 2,4,6-trimethylphenyl on the phosphinimine nitrogen donor is a sufficient change in steric bulk to change the geometry at the Fe center from trigonal planar in **2.23a** to distorted tetrahedral with bridging bromides for **2.23c** (shown in **Figure 2.11**) in the solid-state. The difference in sterics is best quantified through a comparison of the P1-N2-C24 bond angles between **2.23a** and **2.23c**, which is  $5.6^\circ$  larger in the former complex. This larger bond angle likely results from the steric interaction between the isopropyl groups present on the phosphorus and the isopropyl groups located on the N-Aryl of the phosphinimine moiety. However, comparison to the analogous angle P1-N2-C20 of **2.23b** measuring  $126.0(5)^\circ$  (**Figure 2.12**), which features methyl groups in the 2,6-positions of the aryl ring, indicates that steric repulsion between the phosphorus isopropyl units and the aryl 2,6-positions is not the dominating steric factor. Rather, the *para* methyl present in the mesityl group

of **2.23c** likely forces a shallower P1-N2-C24 angle through steric interaction with the adjacent aryl group within the dimeric structure of the bridging complex.

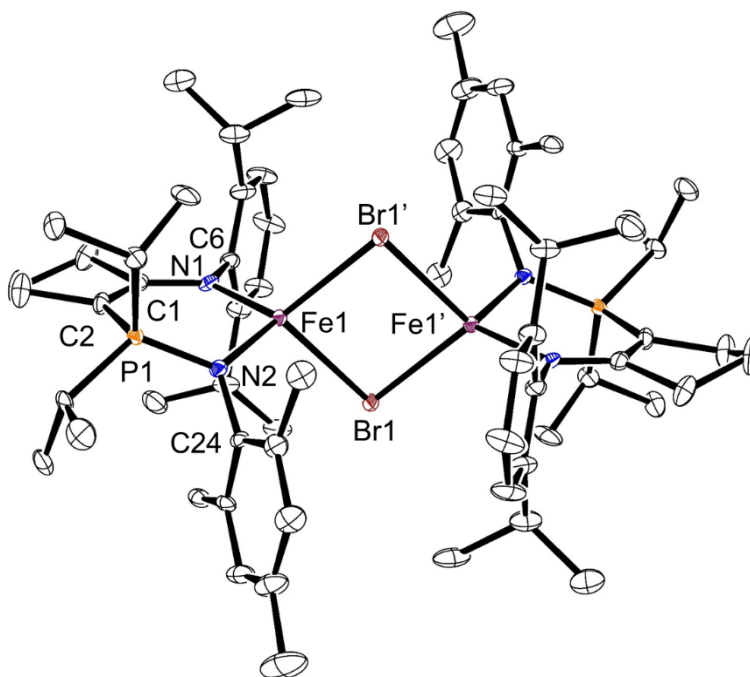


**Figure 2.11:** ORTEP drawing of the solid-state molecular structure of **2.23c** (ellipsoids at 50% probability level). All hydrogen atoms have been omitted for clarity. Selected bond lengths (Å), angles (deg), and torsion angles (deg): C1-N1: 1.355(8), C1-C2: 1.368(9), C2-P1: 1.764(7), P1-N2: 1.627(5), N1-Fe1: 1.986(5), N2-Fe1: 1.999(5), Fe1-Br1: 2.5390(13), Fe1-Br1': 2.5232(12), Fe1-Fe1': 3.5984(17), C1-N1-C6: 117.6(5), P1-N2-C24: 120.3(4), N1-Fe1-N2: 103.6(2), Br1-Fe1-Br1': 89.40(3), N1-Fe1-Br1: 116.43(14), N1-Fe1-Br1': 121.23(15), N2-Fe1-Br1: 109.54(14), N2-Fe1-Br1': 116.43(15), C1-C2-P1-N2: 22.5(7).

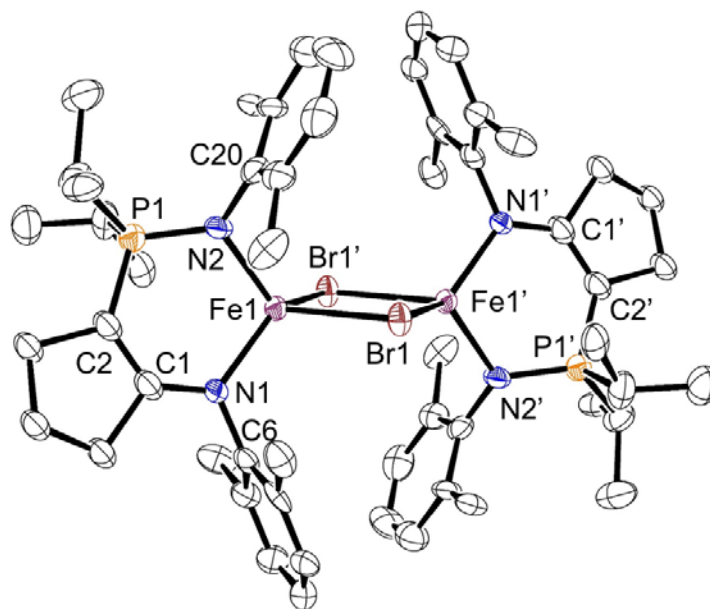


**Figure 2.12:** ORTEP drawing of the solid-state molecular structure of **2.23b** (ellipsoids at 50% probability level). All hydrogen atoms have been omitted for clarity. Selected bond lengths (Å), angles (deg), and torsion angles (deg): C1-N1: 1.339(9), C1-C2: 1.358(11), C2-P1: 1.753(8), P1-N2: 1.645(6), N1-Fe1: 1.988(6), N2-Fe1: 2.009(6), Fe1-Br1: 2.5361(13), Fe1-Br1': 2.5415(13), Fe1-Fe1': 3.614(2), C1-N1-C6: 117.9(6), P1-N2-C20: 126.0(5), N1-Fe1-N2: 102.4(2), Br1-Fe1-Br1': 89.25(4), N1-Fe1-Br1: 112.08(17), N1-Fe1-Br1': 122.32(17), N2-Fe1-Br1: 114.42(18), N2-Fe1-Br1': 116.61(18), C1-C2-P1-N2: 25.8(9).

### 2.3.2 Reduction Chemistry

A number of reducing agents were screened in an attempt to convert the iron bromide complexes **2.23a-c** into the corresponding dinitrogen complexes. While sodium amalgam and magnesium were unsuccessful in performing the desired conversion, performing the reduction with  $\text{KC}_8$  in hexanes successfully reduced the iron center to Fe(I), causing loss of KBr and coordination of  $\text{N}_2$ . However, it was observed in the paramagnetic  $^1\text{H}$  NMR spectra that reduction of complex **2.23c** proceeded much more cleanly than the reduction of **2.23a**, which produced an overly complicated paramagnetic  $^1\text{H}$  NMR spectrum. Nonetheless, X-ray

crystallography performed on a crystal picked from the product mixture obtained from the reduction of **2.23a** confirmed that one of the products is the desired dinitrogen complex **2.25a**, shown in **Figure 2.13**. The degree of N<sub>2</sub> activation in **2.25a** can be estimated by the observed

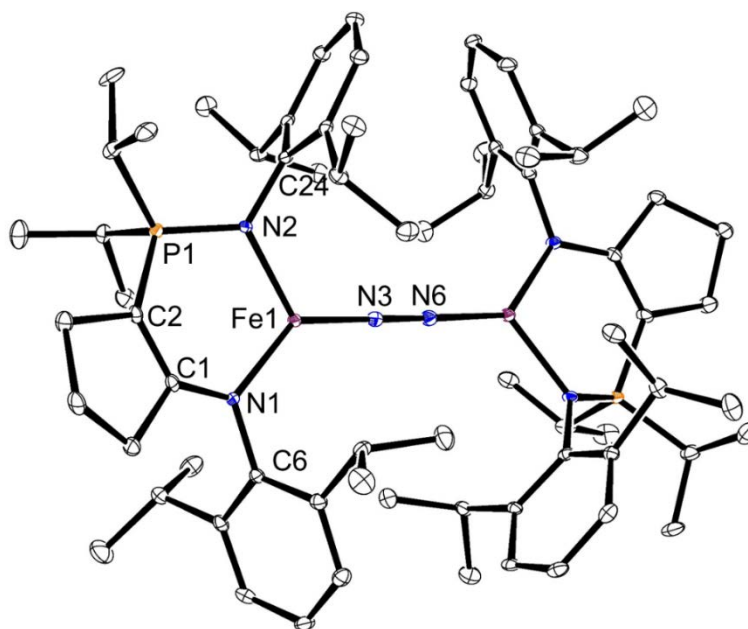


**Figure 2.13:** ORTEP drawing of the solid-state molecular structure of **2.25a** (ellipsoids at 50% probability level). All hydrogen atoms have been omitted for clarity. Selected bond lengths (Å), angles (deg), and torsion angles (deg): N3-N6: 1.186(3), C1-C2: 1.373(3), C1-N1: 1.355(3), C2-P1: 1.758(2), P1-N2: 1.6230(19), N1-Fe1: 1.9640(18), N2-Fe1: 1.9866(18), Fe1-N3: 1.776(2), N1-Fe1-N2: 103.52(8), N1-Fe1-N3: 135.07(8), N2-Fe1-N3: 121.30(8), Fe1-N3-N6: 178.11(19), C1-N1-C6: 117.26(18), P1-N2-C24: 123.14(15), N2-P1-C2-C1: 35.2(2)

N–N bond length in the coordinated N<sub>2</sub> unit, which is 1.186(3) Å (compared to 1.098 Å for free N<sub>2</sub>). This value is similar to that observed in ([<sup>t</sup>BuNacNac<sup>DIPP</sup>]Fe)<sub>2</sub>(μ-N<sub>2</sub>) (**2.10** from introduction 2.1.2), with an N–N bond length of 1.182(5) Å<sup>107</sup>, and to the N–N bond length in ([NpNP<sup>i</sup>Pr]Fe)<sub>2</sub>(μ-N<sub>2</sub>) of 1.186(6) Å.<sup>73</sup> As all of these complexes feature similar levels of N<sub>2</sub> activation, it appears that the ligand scaffold in **2.25a** provides a similar electronic environment for iron when compared to the aforementioned diiron dinitrogen β-diketimate complex and to

$([\text{NpNP}^{\text{iPr}}]\text{Fe})_2(\mu\text{-N}_2)$ , at least as measured by the N–N bond lengths. In all cases, the observed N–N bond distances are slightly longer than an  $\text{N}\equiv\text{N}$  triple bond but shorter than  $\text{N}=\text{N}$  double bonds.

In an attempt to elucidate the structure of the impurity produced alongside dinitrogen complex **2.25a**, reduction of complex **2.23a** was performed using  $\text{KC}_8$  under vacuum. After workup of the reaction mixture, it was determined through a comparison of the paramagnetic  $^1\text{H}$  NMR spectra that the resonances in the product obtained from reduction under vacuum (complex **2.26**) matched many of the impurity resonances present from the reduction under  $\text{N}_2$  (**Figure 2.14**). The solid-state molecular structure for **2.26** (**Figure 2.15**) indicates that a ligand rearrangement has occurred in which the  $\text{P}=\text{N}$  bond has been cleaved, resulting in the formation

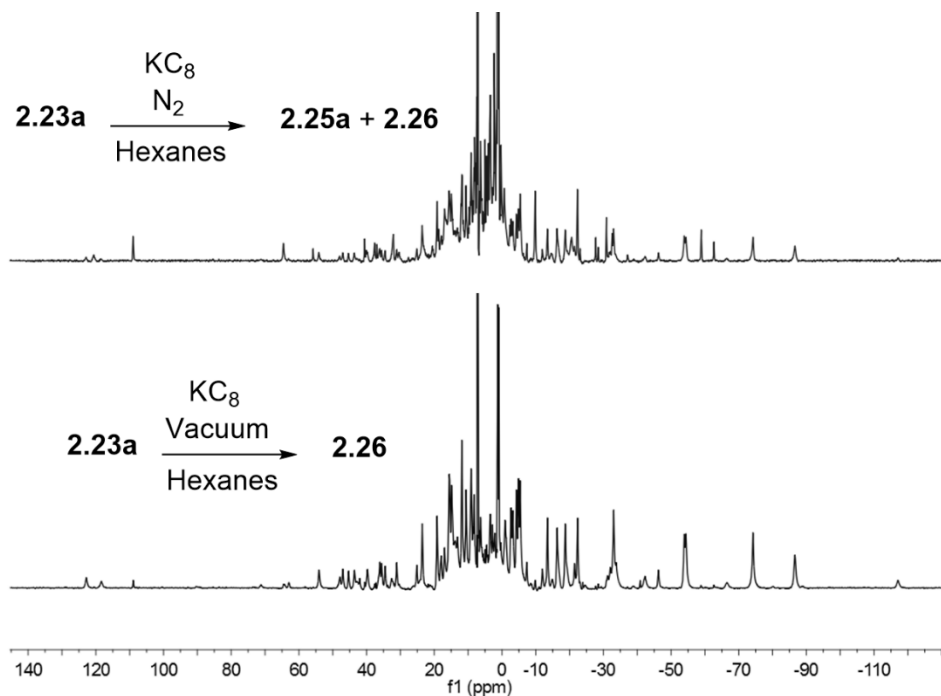


**Figure 2.14:**  $^1\text{H}$  NMR spectra for the mixture of products obtained from the reduction of  $[\text{CYPNpN}^{\text{DIPP,DIPP}}]\text{FeBr}$  **2.23a** with  $\text{KC}_8$  in the presence of  $\text{N}_2$  (top spectrum) and the reduction of **2.23a** under vacuum to give exclusively  $[\text{CYPNpN}]\text{Fe}(\mu\text{-N-DIPP})\text{Fe}[\text{NP}^{\text{CYP}}]$  **2.26** (bottom) (300 MHz,  $d_6$ -benzene, 298 K).

of a bridging imido between two Fe(II) centers. While the connectivity of **2.26** can be determined unambiguously, accurate bond parameters could not be obtained due to high disorder within the crystal.

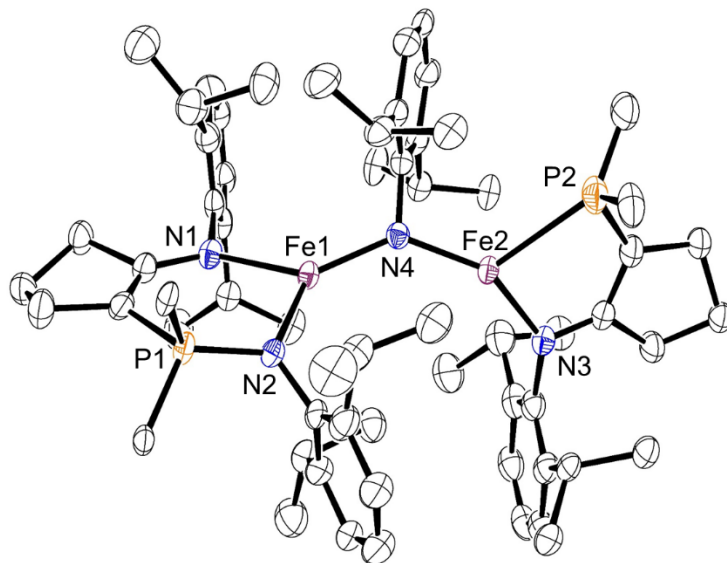
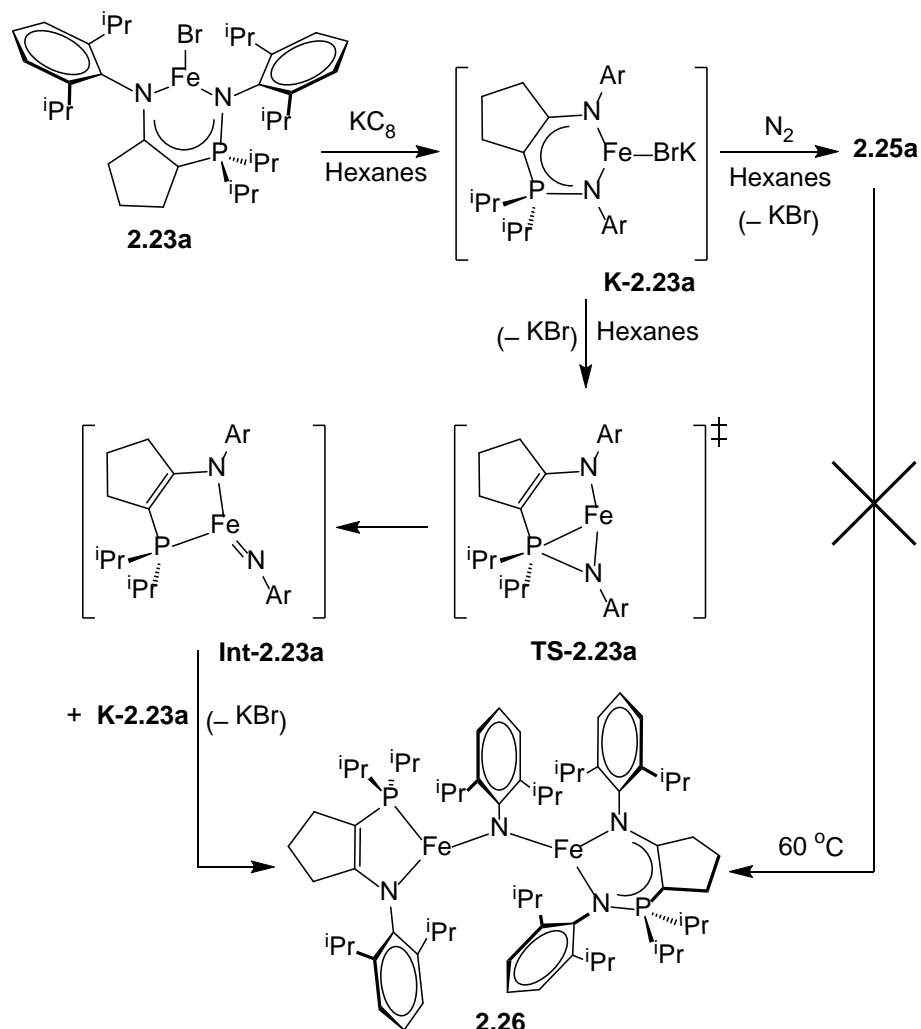


**Figure 2.15:** ORTEP drawing of the solid-state molecular structure of **2.26** (ellipsoids at 35% probability level). All hydrogen atoms and the isopropyl methyl carbons on P1 and P2 have been omitted for clarity. See text for lack of bond metrics.

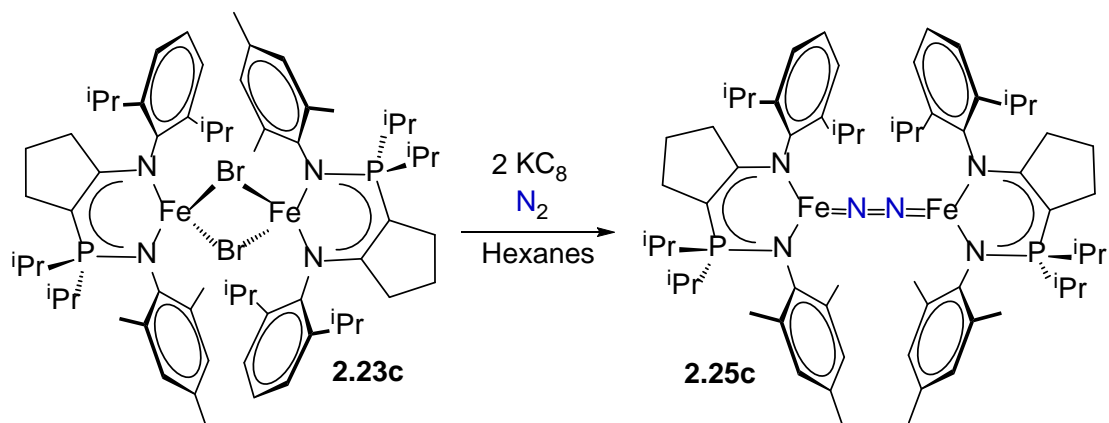
A possible mechanism for the formation of **2.26** is shown in **Scheme 2.9**. Presumably performing the reduction of **2.23a** in the presence of  $N_2$  or under vacuum leads to an Fe(I) intermediate, which could be the  $[^{CY5}NpN^{DIPP,DIPP}]FeBrK$  complex (**K-2.23a**) similar to that previously described for  $[^{tBu}NacNac^{DIPP}]FeClK(18\text{-crown-}6)$  (complex **2.13** shown in **Scheme 2.3** of the introduction 2.1.2).<sup>107</sup> In the absence of  $N_2$ , this Fe(I) intermediate could insert into the P=N bond, forming the transient Fe(III) imido species, **Int-2.23a**, via an  $\eta^2\text{-P=NAr}$  interaction with the Fe(I) center shown as **TS-2.23a**. The further reaction of **Int-2.23a** with another Fe(I) intermediate, such as **K-2.23a** in solution, would generate the imido-bridged species **2.26**. In the presence of  $N_2$ , competition between dinitrogen coordination and reduction of the P=N bond



**Scheme 2.9:** Proposed mechanism for the formation of complex **2.26**.

with the Fe(I) intermediate occurs, causing the formation of both products. Attempts to generate **2.26** directly from the dinitrogen complex **2.25a** by heating the product mixture containing the two species to  $60^\circ\text{C}$  did not lead to the further production of the imido bridged product. It appears that once  $\text{N}_2$  is coordinated to generate **2.25a**, it is stable to this particular ligand rearrangement.

As mentioned previously, the reduction of complex **2.23c** proceeds cleanly to the formation of the dinitrogen complex **2.25c** (Scheme 2.10). Crystals of **2.25c** feature co-



**Scheme 2.10:** Reduction of **2.23c** with  $\text{KC}_8$  under an atmosphere of  $\text{N}_2$  leads to formation of **2.25c**.

crystallized disordered *n*-pentane in the unit cell, which could not be modeled accurately (**Figure 2.16**). The N–N bond length of 1.183(6) Å for the coordinated  $\text{N}_2$  does not vary significantly

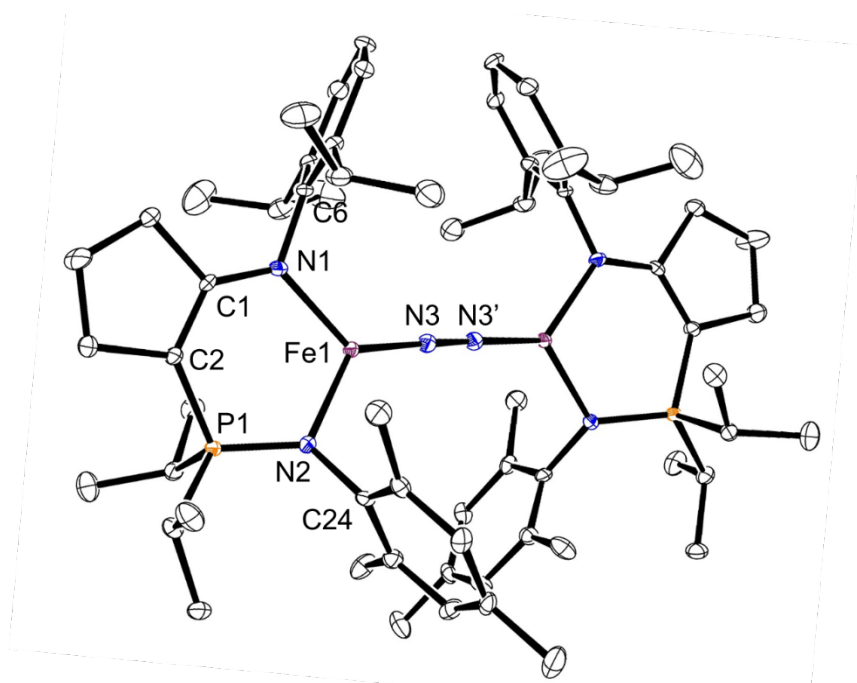
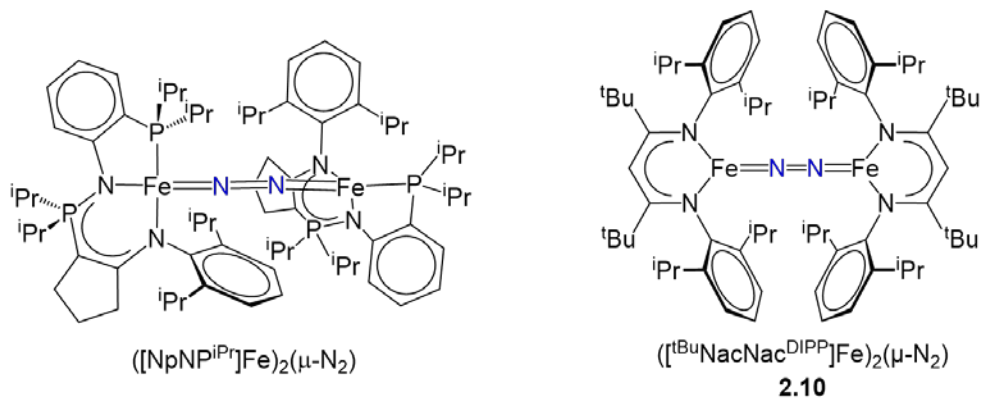


**Figure 2.16:** ORTEP drawing of the solid-state molecular structure of **2.25c** (ellipsoids at 50% probability level). All hydrogen atoms have been omitted for clarity. Selected bond lengths (Å), angles (deg), and torsion angles (deg): N3–N3': 1.183(6), C1–C2: 1.380(5), C1–N1: 1.348(4), C2–P1: 1.764(4), P1–N2: 1.616(3), Fe1–N1: 1.967(3), Fe1–N2: 1.963(3), Fe1–N3: 1.764(3), N1–Fe1–N2: 102.86(13), N2–Fe1–N3: 127.58(14), N1–Fe1–N3: 129.21(14), Fe1–N3–N3': 177.3(4), C1–N1–C6: 120.7(3), P1–N2–C24: 128.1(2), C1–C2–P1–N2: 27.0(4).

from the lengths observed for **2.25a**,  $([\text{NpNP}^{\text{iPr}}]\text{Fe})_2(\mu\text{-N}_2)$ , and  $([\text{t}^{\text{Bu}}\text{NacNac}^{\text{DIPP}}]\text{Fe})_2(\mu\text{-N}_2)$  **2.10**. This trend holds true for the vast majority of the geometric parameters for the above iron complexes, with the only major exception being the ligand bite angle about the reduced iron center. The ligand bite angles between complexes **2.25a** and **2.25c** are similar at  $103.52(8)^\circ$  and  $102.86(13)^\circ$  respectively. However, the N-Fe-N bite angles observed in the dinitrogen complexes  $([\text{NpNP}^{\text{iPr}}]\text{Fe})_2(\mu\text{-N}_2)$  and  $([\text{t}^{\text{Bu}}\text{NacNac}^{\text{DIPP}}]\text{Fe})_2(\mu\text{-N}_2)$  **2.10** are more shallow at  $99.19(14)^\circ$  and  $96.0(2)^\circ$  respectively. A further point of comparison is the Fe-N<sub>2</sub> bond length, which is similar for **2.25a**, **2.25c**, and  $([\text{t}^{\text{Bu}}\text{NacNac}^{\text{DIPP}}]\text{Fe})_2(\mu\text{-N}_2)$ , but is significantly elongated in the case of  $([\text{NpNP}^{\text{iPr}}]\text{Fe})_2(\mu\text{-N}_2)$ . These differences are summarized in **Table 2.1**. An interesting feature of

**Table 2.1:** Comparison of Bond Distances and Angles Obtained From Various Fe-N<sub>2</sub> Complexes

	<b>2.25a</b>	<b>2.25c</b>	$([\text{NpNP}^{\text{iPr}}]\text{Fe})_2(\mu\text{-N}_2)$	$([\text{t}^{\text{Bu}}\text{NacNac}^{\text{DIPP}}]\text{Fe})_2(\mu\text{-N}_2)$
N <sub>2</sub> length (Å)	1.186(3)	1.183(6)	1.186(6)	1.182(5)
P=N length (Å)	1.623(2)	1.616(3)	1.622(5)	-
Fe-N <sub>2</sub> length (Å)	1.776(2)	1.764(3)	1.812(4)	1.770(5)
N-Fe-N bite angle (°)	103.52(8)	102.86(13)	99.19(14)	96.0(2)



**2.25c** in comparison to **2.25a** is that **2.25c** crystallizes with the phosphinimine units “*cis*” to each other, while **2.25a** crystallizes in the “*trans*” orientation. Heating **2.25c** under vacuum in *d*<sub>8</sub>-toluene or *d*<sub>8</sub>-THF in the presence of KBr did not lead to the formation of a bridging imido species analogous to **2.26**. In addition, performing the reduction of **2.23c** under vacuum and

carrying out the subsequent workup under an N<sub>2</sub> atmosphere led to the clean formation of **2.25c** (Figure 2.17). It appears that the energetic barrier for the reduction of the P=N bond is

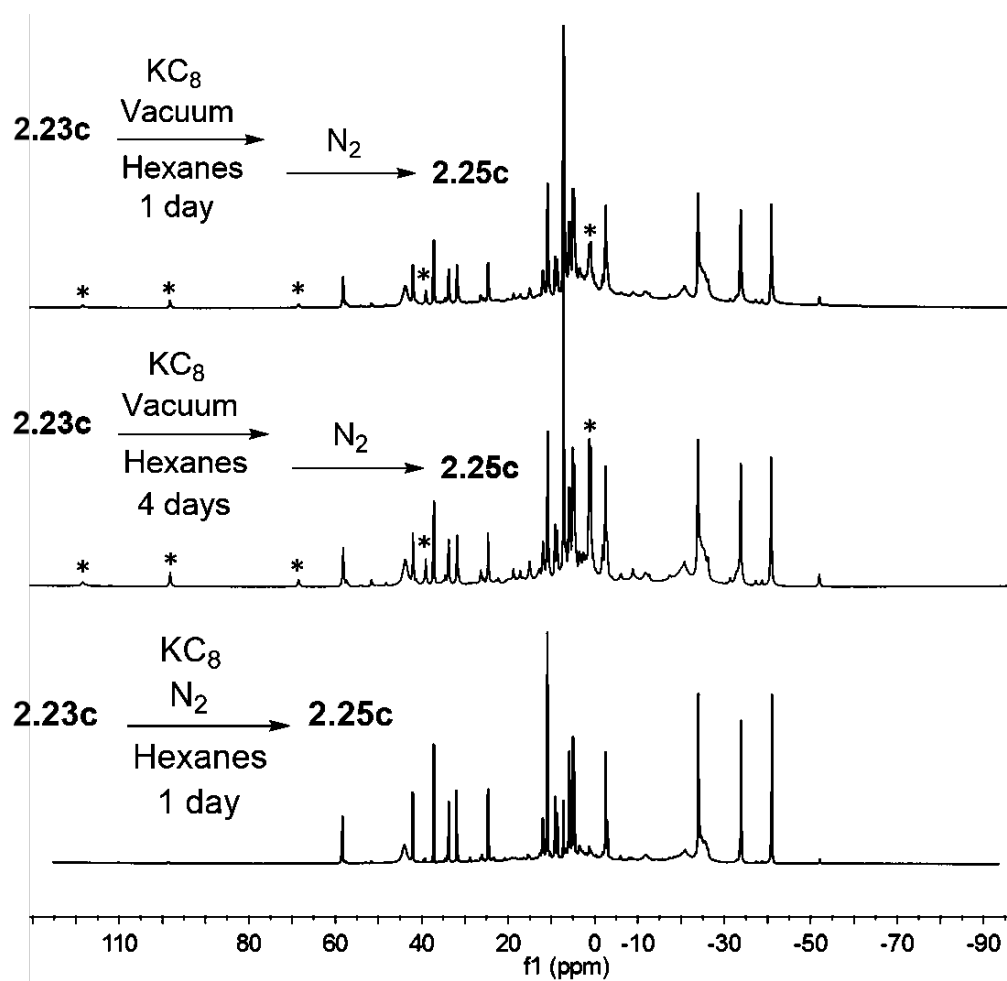


**Figure 2.17:** <sup>1</sup>H NMR spectra for the reduction of **2.23c** under vacuum for 1 day, followed by exposure to N<sub>2</sub> (top spectrum), the reduction of **2.23c** under vacuum for 4 days, followed by exposure to N<sub>2</sub> (middle), and the spectrum for [(<sup>CYP</sup>NpN<sup>DIPP,Mes</sup>)Fe]<sub>2</sub>(μ-N<sub>2</sub>) **2.25c** produced from the reduction of **2.23c** under an atmosphere of N<sub>2</sub> (bottom). Impurities denoted with (\*) (300 MHz, *d*<sub>6</sub>-benzene, 298 K).

substantially higher for reduced **2.23c** in comparison to reduced **2.23a**. This result can be rationalized by the difference in sterics between the two species. The increased steric bulk of **2.23a** in comparison to **2.23c** likely destabilizes the LFeBrK intermediate described in **Scheme 2.9**, leading to loss of KBr and competition between N<sub>2</sub> coordination and ligand based P=N bond

reduction. In the case of complex **2.23c**, the reduced steric bulk resulting from the substitution of the phosphinimine 2,6-diisopropylphenyl group to a mesityl group stabilizes the intermediate LFeBrK complex, even in the absence of dinitrogen.

Zero-field Mössbauer spectroscopy was performed on  $[(^{CYP}NpN^{DIPP,Mes})Fe]_2(\mu-N_2)$  **2.25c** to elucidate the electronic environment at the Fe center. The observed spectrum featured a quadrupole doublet with an isomer shift ( $\delta$ ) of 0.56 mm/s and a quadrupole splitting ( $\Delta E_Q$ ) of 1.14 mm/s (**Figure 2.18**). Both the isomer shift and quadrupole splitting values are lower than

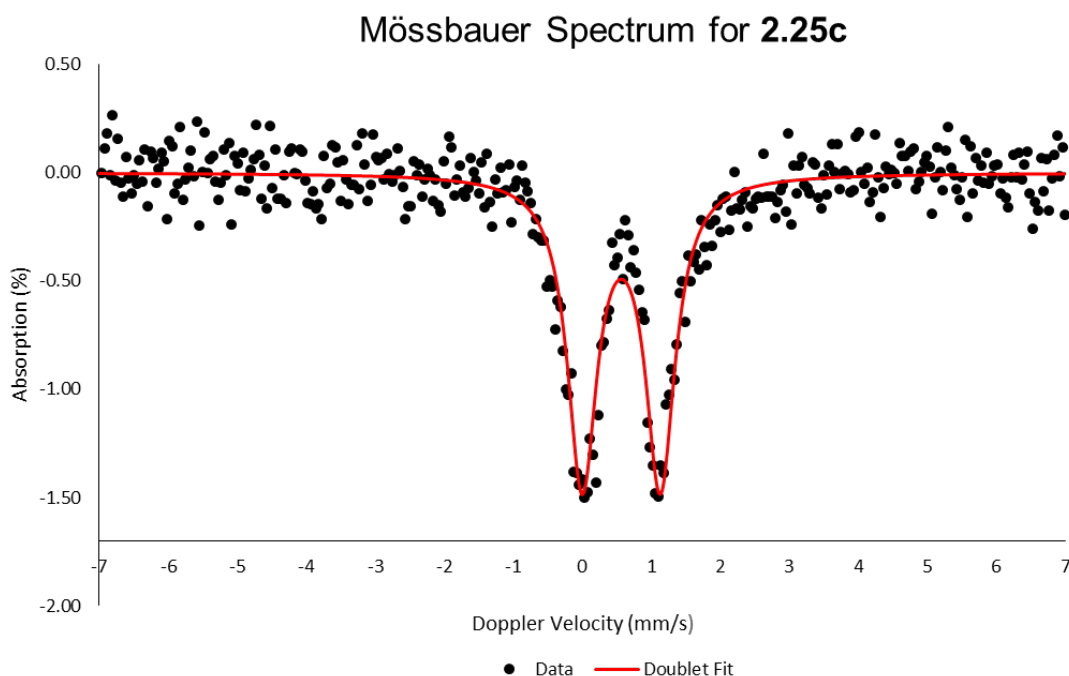


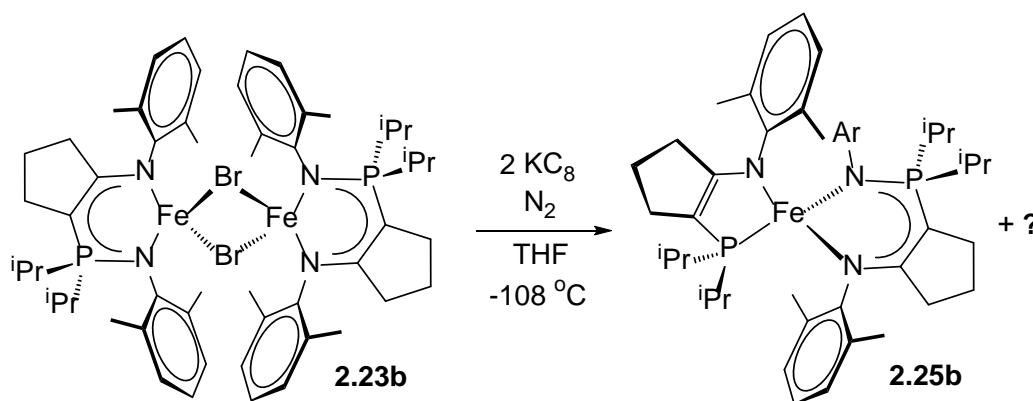
**Figure 2.18:** Zero-field  $^{57}Fe$  Mössbauer spectra for powdered samples of  $[(^{CYP}NpN^{DIPP,Mes})Fe]_2(\mu-N_2)$  **2.25c** obtained at 295 K. The parameters used for the fit of **2.25c** (red line) were an isomer shift of ( $\delta$ ) 0.56 mm/sec and a quadrupole splitting ( $\Delta E_Q$ ) of 1.14 mm/sec.

those observed in similar systems, such as  $[(^{Me}NacNac)^{DIPP}Fe]_2(\mu-N_2)$  (complex **2.9** from introduction **2.1.2**) ( $\delta = 0.62$  mm/s,  $\Delta E_Q = 1.41$  mm/s)<sup>116</sup> and the recently reported  $[(NpNP^{iPr})Fe]_2(\mu-N_2)$  ( $\delta = 0.73$  mm/s,  $\Delta E_Q = 1.83$  mm/s)<sup>73</sup>. It should be noted that direct comparison of the isomer shift values to the  $[(NpNP^{iPr})Fe]_2(\mu-N_2)$  system is tenuous as the Fe

center is 4-coordinate, which will contribute to a higher  $\delta$  compared to the 3-coordinate examples.<sup>117</sup> Generally, for complexes with similar ligand environments and spin states, the isomer shift value increases with decreasing oxidation state.<sup>117</sup> However, for low-valent Fe centers ( $\text{Fe}^0$ ,  $\text{Fe}^{\text{I}}$ ), isomer shift values have been reported vary insignificantly from analogous  $\text{Fe}^{\text{II}}$  compounds.<sup>118</sup> This fact makes the comparison of  $\delta$  for **2.25c** to  $[(^{\text{Me}}\text{NacNac})^{\text{DIPP}}\text{Fe}]_2(\mu\text{-N}_2)$  less straightforward. A potential method for analyzing isomer shifts is to analyze the bonding interactions at the iron center, because a decrease in  $\delta$  (as observed for **2.25c**) could indicate that stronger back-bonding interactions between Fe and the ligand scaffold have occurred, an effect observed for low-coordinate iron-alumatrane dinitrogen complexes.<sup>119</sup> This in turn would lead to an increase in 4s electron density, causing a smaller  $\delta$  value. However, it does not appear as though electron density on Fe in **2.25c** is being transferred to a greater extent through back-bonding interactions with the ligand framework when compared to  $[(^{\text{Me}}\text{NacNac})^{\text{DIPP}}\text{Fe}]_2(\mu\text{-N}_2)$  because the bond metrics between Fe, the N-donor atoms, and coordinated  $\text{N}_2$  do not vary significantly between the two complexes. Nevertheless, the similarity in  $\delta$  for **2.25c** to the well-established  $[(^{\text{Me}}\text{NacNac})^{\text{DIPP}}\text{Fe}]_2(\mu\text{-N}_2)$  system supports the assignment of an oxidation state of  $\text{Fe}^{\text{II}}$ , with the dinitrogen unit being reduced to  $\text{N}_2^{2-}$ . Lastly, the difference in  $\Delta E_{\text{Q}}$  between **2.25c** and  $[(^{\text{Me}}\text{NacNac})^{\text{DIPP}}\text{Fe}]_2(\mu\text{-N}_2)$  may be due to the differences in the ligand bite angles between the two complexes. It has been reported that an increase in the distortion of the coordination environment for high-spin Fe(II) causes an increase in the quadrupole splitting value.<sup>120</sup> Complex **2.25c** has a ligand bite angle of  $102.86(13)^\circ$ , closer to the ideal  $120^\circ$  for a trigonal planar complex compared to the  $97.6(1)^\circ$  angle observed for  $[(^{\text{Me}}\text{NacNac})^{\text{DIPP}}\text{Fe}]_2(\mu\text{-N}_2)$ .<sup>107</sup> Thus, a lower  $\Delta E_{\text{Q}}$  of 1.14 mm/s is observed for **2.25c** in comparison to the  $\Delta E_{\text{Q}}$  of 1.41 mm/s for  $[(^{\text{Me}}\text{NacNac})^{\text{DIPP}}\text{Fe}]_2(\mu\text{-N}_2)$ .

Attempts were made to functionalize the coordinated N<sub>2</sub> in complex **2.25c** to NH<sub>3</sub>. Reacting a catalytic amount of **2.25c** with an excess of KC<sub>8</sub> and [H(Et<sub>2</sub>O)<sub>2</sub>]<sup>+</sup>[[3,5-(CF<sub>3</sub>)<sub>2</sub>C<sub>6</sub>H<sub>3</sub>]<sub>4</sub>B]<sup>-</sup> at -78° C did not lead to the production of measurable amounts of NH<sub>3</sub> (determined via the indophenol method).<sup>121</sup> This is an unsurprising result, as there have been no reported examples to date of the functionalization of N<sub>2</sub> when it is coordinated in an end-on bridging mode.

The iron bromide complex **2.23b** was synthesized with the goal of replicating the reactivity observed for the least sterically encumbered β-diketiminato iron derivative reported by the Holland lab (complex **2.14** from introduction 2.1.2). Reduction of **2.14** under an atmosphere of N<sub>2</sub> results in cleaving the dinitrogen triple bond, yielding a cluster complex containing bridging nitrides derived from N<sub>2</sub> (complex **2.15**, **Scheme 2.4**). Unfortunately, reduction of **2.23b** under an N<sub>2</sub> atmosphere with KC<sub>8</sub> in thawing THF led to a product mixture containing a heteroleptic Fe(II) complex containing both enamido-phosphine and enamido-phosphinimine ligands **2.25b** (**Scheme 2.11**). X-ray crystallography was performed on a crystal picked out of



**Scheme 2.11:** Reduction of **2.23b** leads to a mixture of products, one of which is **2.25b**, as characterized by X-ray crystallography.

the product mixture, allowing for the identification of **2.25b**, shown in **Figure 2.19**. The P=N

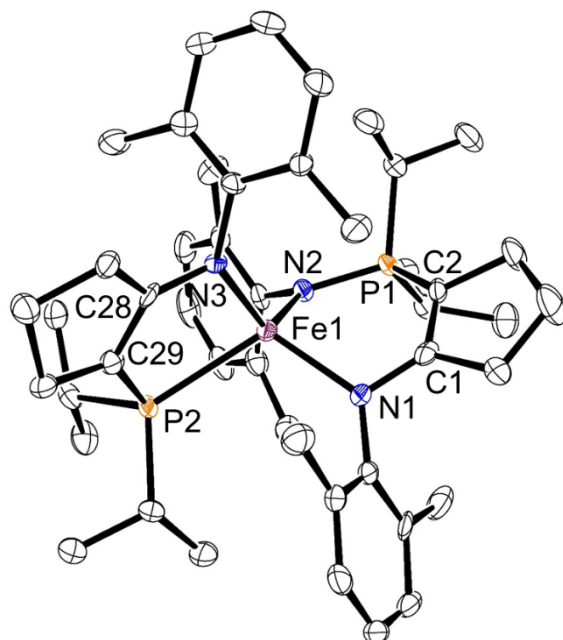
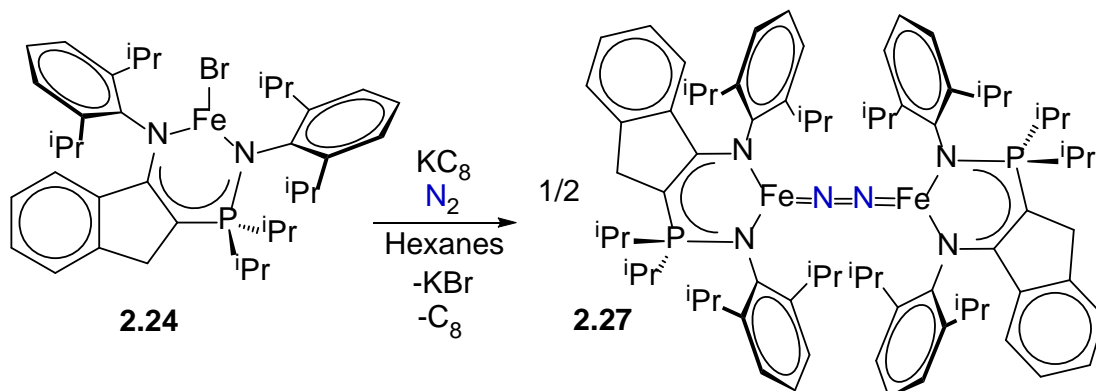


**Figure 2.19:** ORTEP drawing of the solid-state molecular structure of **2.25b** (ellipsoids at 50% probability level). All hydrogen atoms have been omitted for clarity. Selected bond lengths (Å) and angles (deg): C1-N1: 1.368(5), C1-C2: 1.374(6), C2-P1: 1.747(5), P1-N2: 1.628(4), C28-N3: 1.359(5), C28-C29: 1.381(5), P2-C29: 1.772(4), N1-Fe1: 2.052(3), N2-Fe1: 2.023(4), N3-Fe1: 2.017(3), P2-Fe1: 2.4981(12), N1-Fe1-N2: 98.37(14), N2-Fe1-N3: 122.76(14), N1-Fe1-P2: 111.93(9), N3-Fe1-P2: 86.07(10).

bond of one of the ligands has again been cleaved, similar to **2.26**. The identity of the other species produced in this specific reaction was not determined. Additionally, performing the reduction at ambient temperature led to an intractable product mixture. Thus, this specific system was abandoned.

Reduction of **2.24**, the iron bromide complex featuring an indene based ligand scaffold, with  $\text{KC}_8$  led to the isolation of the bridging  $\text{N}_2$  complex **2.27** (**Scheme 2.12**). However, reproducibility of the synthesis of **2.27** was challenging and a relatively clean paramagnetic  $^1\text{H}$  NMR was only recorded once. The irreproducibility of the reduction shown in **Scheme 2.12** is likely due to the same side reaction resulting in the cleavage of the phosphinimine bond shown in **Scheme 2.9**. Single crystals of **2.27** were isolated from this reaction mixture and the solid-state

molecular structure is shown in **Figure 2.20**. The degree of N<sub>2</sub> activation observed in **2.27**, as determined by the N–N bond length of 1.193(4) Å, varies insignificantly from the dinitrogen complexes **2.25a** and **2.25c**.



**Scheme 2.12:** Treatment of **2.24** with KC<sub>8</sub> under an atmosphere of N<sub>2</sub> leads to the isolation of **2.27**.

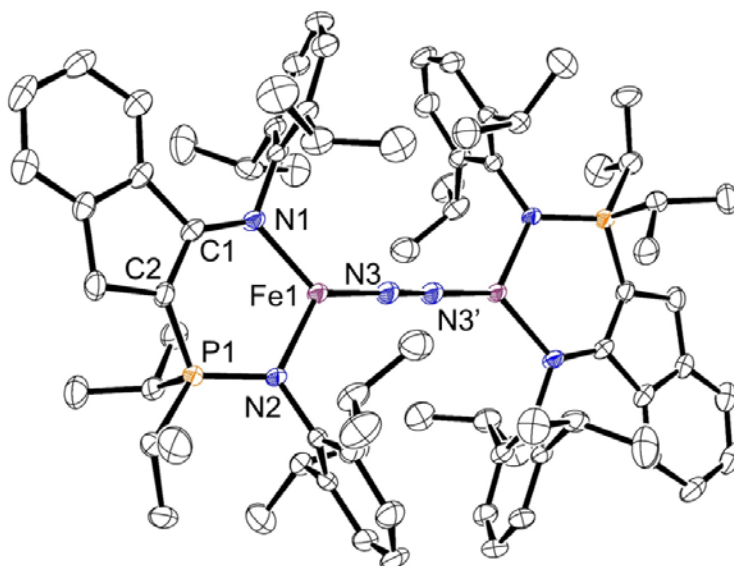


**Figure 2.20:** ORTEP drawing of the solid-state molecular structure of **2.27** (ellipsoids at 50% probability level). All hydrogen atoms have been omitted for clarity. Selected bond lengths (Å) and angles (deg): N3–N3': 1.193(4), Fe1–N3: 1.776(2), Fe1–N1: 1.972(2), Fe1–N2: 1.984(2), C1–N1: 1.354(3), C1–C2: 1.393(4), C2–P1: 1.759(3), P1–N2: 1.621(2), N1–Fe1–N2: 103.88(8), Fe1–N3–N3': 1.9(3).

The indene ligand scaffold was synthesized with the sole interest of deprotonating the  $\beta$ -methylene position to generate an anionic charge in the ligand backbone. The rationale behind this transformation was to impart more electron density on the low-coordinate Fe center of a  $N_2$  complex, perhaps adding electron density to the  $d\pi-N_2 \pi^*$  orbital interaction. This could aid in  $N_2$  activation, with the potential of further weakening of the dinitrogen triple bond beyond what is typically observed for bridging iron dinitrogen complexes. To perform the desired deprotonation, dinitrogen complex **2.27** was treated with *n*-butyllithium at  $-78^\circ\text{C}$  to provide a product with the  $^1\text{H}$  NMR spectrum shown in **Figure 2.21**. The 18  $^1\text{H}$  resonances observed for **2.27** collapse

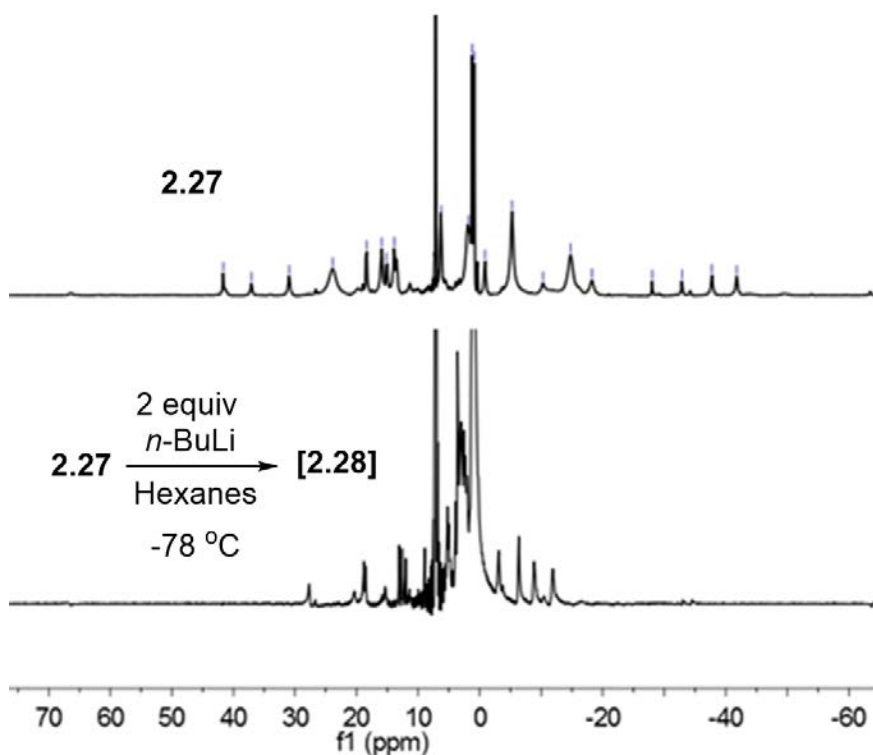


**Figure 2.21:** A comparison of the  $^1\text{H}$  NMR spectra obtained for **2.27** (top spectrum) and for the product obtained from treatment of **2.27** with *n*-butyllithium (bottom spectrum). (300 MHz,  $d_6$ -benzene, 298 K).

closer to the diamagnetic region, indicating that a reaction occurred. Numerous attempts at growing crystals of the suspected deprotonation product [**2.28**] failed, and thus, definitive proof

as to its structure is lacking (as indicated by the brackets surrounding **[2.28]**). An attempt was made at the deprotonation of **2.27** with benzyl potassium, but an intractable product mixture formed. Nonetheless, the question still remained as to whether the dianionic charge that could exist in the supposed structure of **[2.28]**, shown in **Figure 2.22**, would lead to enhanced N<sub>2</sub>

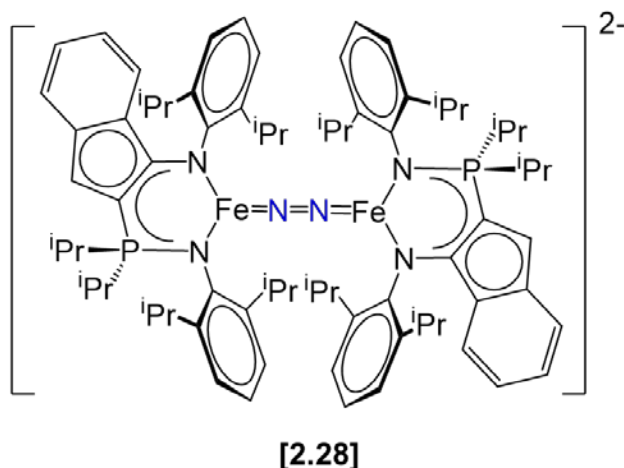


**Figure 2.22:** The predicted identity for complex **[2.28]**. The lithium cations are omitted from the above structure, as they are from the DFT calculations to follow.

activation. To address this question, Density Functional Theory (DFT) analyses were performed on complexes **2.27** and **[2.28]** to examine the differences in charge distribution and molecular orbital structure between the two complexes.

### 2.3.3 DFT Analysis

Two questions were put forth to answer with DFT analysis. First, how does the charge distribution differ between the neutral indene complex **2.27** and the putative dianionic indenyl complex **[2.28]**? Would dianionic **[2.28]** have significantly more negative charge delocalized on the nitrogen atoms of coordinated N<sub>2</sub>? Second, how do the molecular orbitals (MOs) involved with N<sub>2</sub> coordination compare between **2.27** and **[2.28]**? Starting from the solid-state molecular structure of **2.27** obtained from X-ray crystallography, geometry optimization was performed

using the UB3LYP functional and the TZV basis set, with  $S = 3$  (multiplicity = 7). Natural Bond Order (NBO) calculations were then performed on the geometry optimized structure in order to use Natural Population Analysis (NPA) to examine charge distribution. From the geometry optimized structure of **2.27**, one hydrogen atom was removed from the  $\beta$ -methylene position to convert it to a  $\beta$ -methine environment. Geometry optimization was performed on the new *in silico* generated structure of [**2.28**] with a -2 charge present on the complex, omitting the presence of lithium cations. Following geometry optimization, an NBO calculation was performed on [**2.28**] to again analyze NPA results.

The differences in charge distribution between **2.27** and [**2.28**] are shown below in **Figure 2.23** and **Table 2.2** summarizes the numerical differences in charge distribution. As can be seen from the NPA results, there is an insignificant difference in the charge distribution

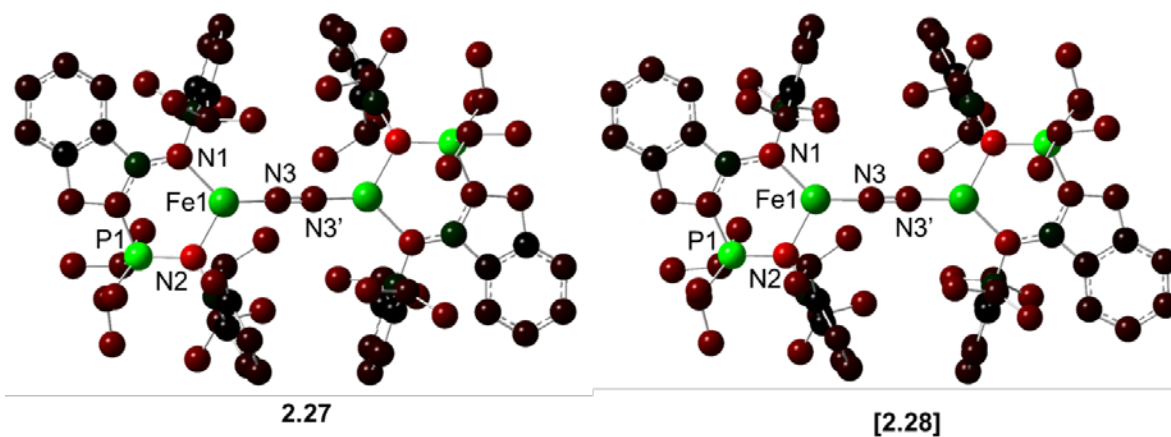


**Figure 2.23:** Visualization of Natural Population Analysis results showing charge distribution within **2.27** and [**2.28**]. Intensity of color indicates magnitude of charge, where green indicates positive charge, red indicates negative charge, and black indicates neutral charge. The numerical values associated with the atoms in **Figure 2.23** are summarized in **Table 2.2**.

between **2.27** and [**2.28**]. More importantly, the amount of negative charge calculated to exist on the nitrogen of coordinated  $N_2$  is only slightly greater for [**2.28**] with a value of -0.508 relative to

**Table 2.2:** Select Calculated Bond Distances and Atomic Charges

Atomic Charges	<b>2.27</b>	<b>[2.28]</b>
Fe1	1.202	1.170
N1	-0.752	-0.822
N2	-1.132	-1.124
N3	-0.486	-0.508
P1	1.606	1.615
Calculated Bond Distances	<b>2.27</b>	<b>[2.28]</b>
N3-N3'	1.214	1.221
Fe1-N3	1.815	1.824

the -0.486 for complex **2.27**. Additionally, a comparison of the N<sub>2</sub> bond length between **2.27** (1.214 Å) and **[2.28]** (1.221 Å) from the calculated geometry optimized structures indicates that the degree of enhanced N<sub>2</sub> activation resulting from the negative charge placed on the indenyl ring of **[2.28]** is small. Somewhat counter to the slightly increased N<sub>2</sub> bond length for **[2.28]** in comparison to **2.27** is the longer Fe–N bond distance to N<sub>2</sub> of 1.824 Å for **[2.28]** in comparison to the corresponding distance of 1.815 Å for **2.27**. This trend runs counter to the prediction that increased contribution to the dπ–N<sub>2</sub> π\* interaction would increase the N–N bond distance in coordinated N<sub>2</sub> while simultaneously decreasing the distance between iron and N<sub>2</sub>. Nonetheless, from the calculated bond metrics and the NPA charge distribution results, it appears that the anionic charge located at the indenyl rings of **[2.28]** would contribute insignificantly to the degree of N<sub>2</sub> activation in comparison to the neutral complex **2.27**.

Examination of the α MO diagrams resulting from the geometry optimization calculations performed on **2.27** and **[2.28]** provides further evidence that the anionic charge present in **[2.28]** does not contribute to an enhanced dπ–N<sub>2</sub> π\* interaction. The MOs associated with the overlap between the dπ–N<sub>2</sub> π\* are shown in **Figure 2.24**, images **a** and **b** for **2.27** and **[2.28]**,

respectively. There does not appear to be overlap between the anionic indenyl ring and the  $d\pi-N_2$   $\pi^*$  interaction for **[2.28]**, which supports the NPA calculations that only marginally more

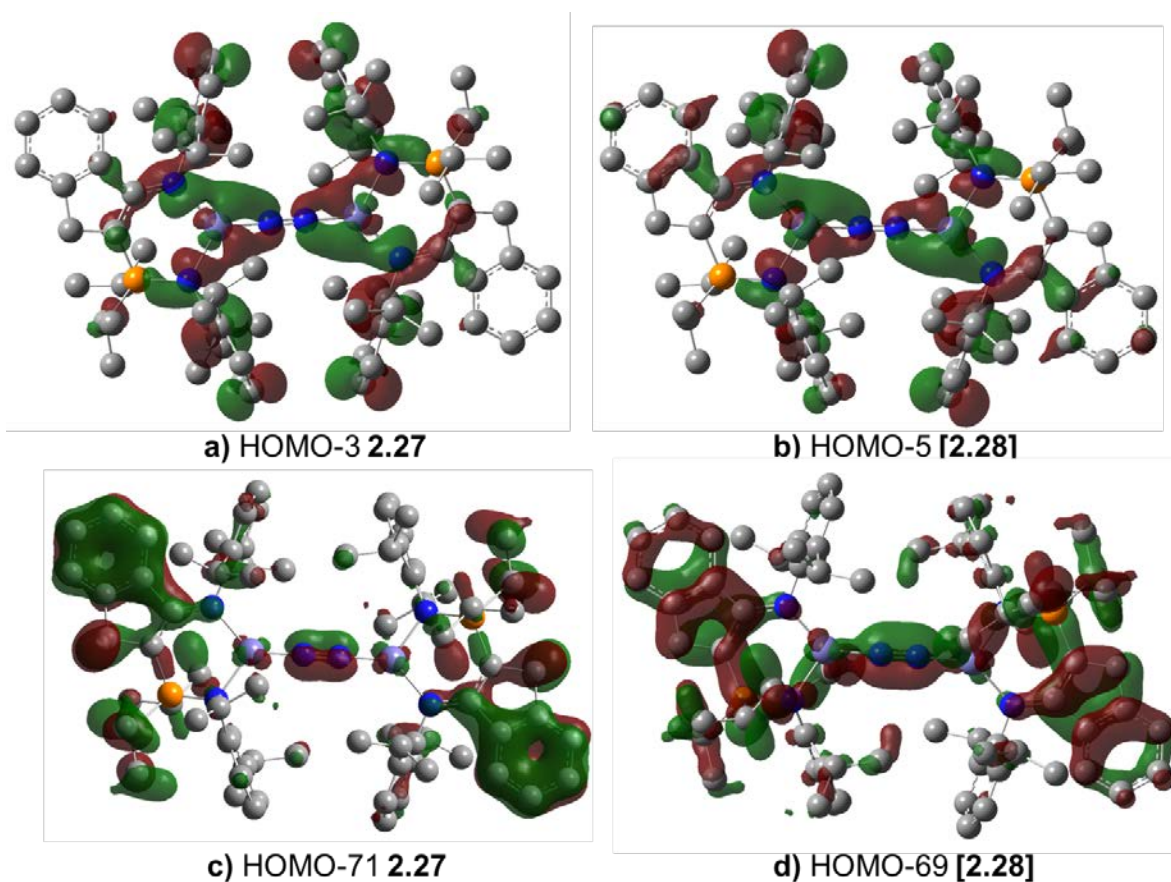


**Figure 2.24:** Alpha molecular orbitals for the  $d\pi-N_2$   $\pi^*$  interaction in **2.27** (a) and **[2.28]** (b). The molecular orbitals associated with the overlap between the aromatic system of the ligand backbone and the  $\pi$  orbital of  $N_2$  are shown in (c) for **2.27** and (d) for **[2.28]**.

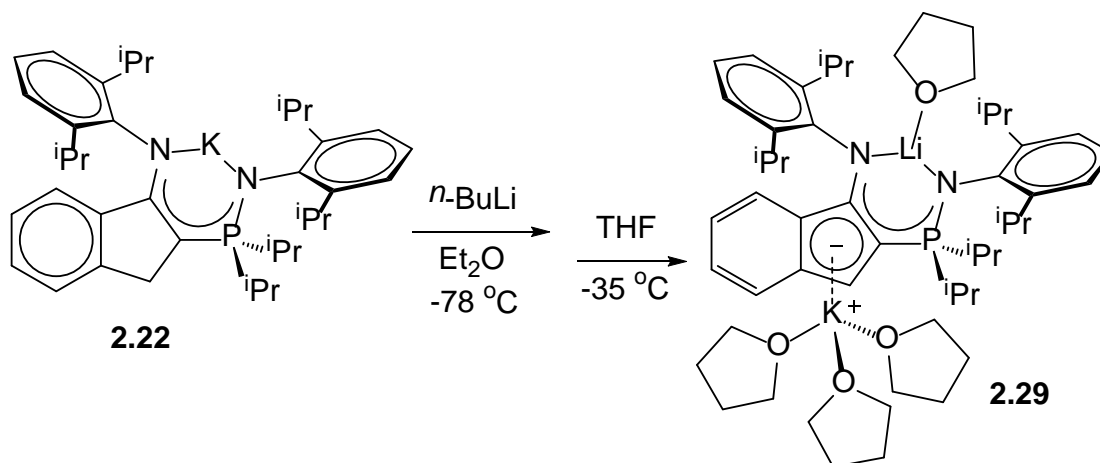
negative charge is delocalized on the coordinated  $N_2$  of **[2.28]** in comparison to **2.27**. The only calculated MOs in which the indene rings of **2.27** and the anionic indenyl rings of **[2.28]** are in phase with the orbitals of  $N_2$  are found in images **c** and **d**. For the MOs displayed in **c** and **d**, the interaction appears to be between the aromatic system of the indene and indenyl rings and the  $\pi$  orbital of  $N_2$ . More overlap is observed in the case of **[2.28]** in comparison to **2.27**. This qualitative analysis of select MO diagrams supports the charge distribution analysis performed

earlier, in that the anionic charge present in [2.28] was unlikely to contribute significantly to the weakening of the coordinated N<sub>2</sub> triple bond.

Though full characterization of [2.28] was not performed, the question still remained as to whether the indene scaffold could be deprotonated to generate a dianionic ligand system. To simplify characterization, the deprotonation of the potassium complex [INDNpN<sup>DIPP,DIPP</sup>]K 2.22 was performed with *n*-butyllithium.

#### 2.4 Dianionic Indenyl Ligand and Coordination Attempts

Treatment of a diethyl ether solution of 2.22 with a hexane solution of *n*-butyllithium at -78 °C, followed by recrystallization from THF at -35 °C led to the isolation of purple 2.29 (Scheme 2.13). X-ray quality single crystals grown from the cooled THF solution of 2.29



**Scheme 2.13:** Deprotonation of 2.22 with *n*-butyllithium yields the dianionic ligand salt 2.29.

allowed for the determination of the solid-state molecular structure, shown in **Figure 2.25**. An interesting feature observed in the solid-state structure of 2.29 is the migration of the K<sup>+</sup> cation from the coordination pocket located between the N-donor groups to an η<sup>5</sup>-interaction with the anionic indenyl ring. The driving force for cation exchange is likely due to stronger bond enthalpies between lithium and the negatively charged N-donors, as Li<sup>+</sup> is a harder cation than

$K^+$ . Further aiding in the cation exchange is the ability for  $K^+$  to form strong cation-arene interactions.<sup>122-123</sup> The bond metrics for C1–C2 (1.439(4) Å) and C2–C3 (1.443(4) Å) are between the range for carbon-carbon double and single bonds, indicating the negative charge of the indenyl ring is delocalized throughout the aromatic system.

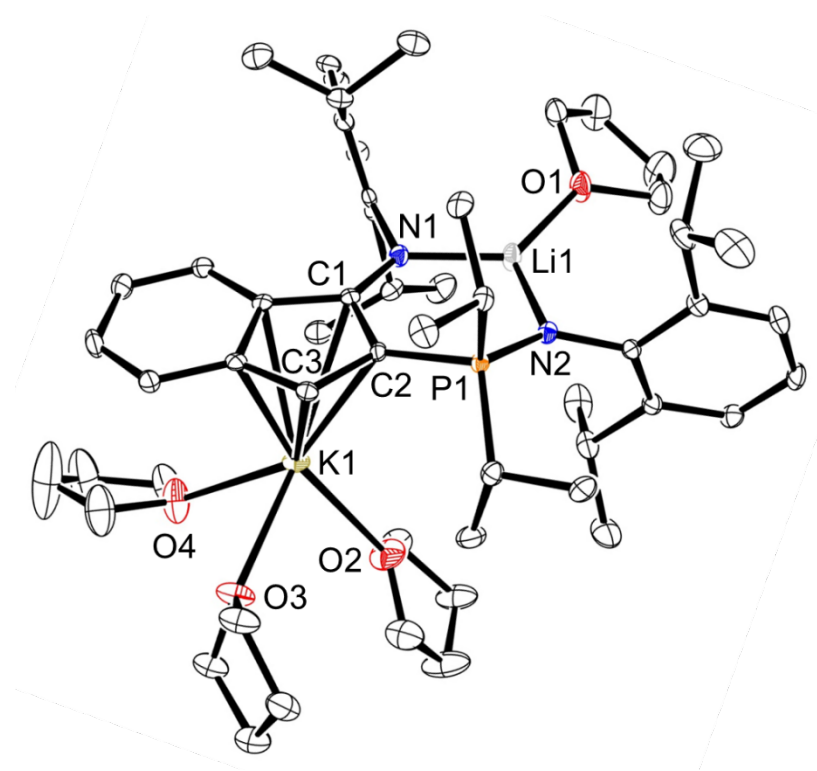


**Figure 2.25:** ORTEP drawing of the solid-state molecular structure of **2.29** (ellipsoids at 50% probability level). All hydrogen atoms have been omitted for clarity. Selected bond lengths (Å), and angles (deg): C1–C2: 1.439(4), C1–N1: 1.372(4), C2–C3: 1.443(4), C2–P1: 1.763(3), P1–N2: 1.595(3), N1–Li1: 1.884(6), N2–Li1: 1.947(7), Li1–O1: 1.929(6), C1–K1: 3.109(3), C2–K1: 3.163(3), C3–K1: 3.066(3), K1–O2: 2.715(3), and N1–Li1–N2: 109.5(3).

The dianionic ligand salt **2.29** is only soluble in highly polar solvents. A comparison between the  $^1H$  and  $^{31}P\{^1H\}$  NMR spectra between **2.22** and **2.29** show a number of differences. The  $^{31}P\{^1H\}$  NMR spectrum of **2.29** shows a singlet at  $\delta$  33.1, a downfield shift relative to the  $^{31}P\{^1H\}$  chemical shift of  $\delta$  15.9 observed for **2.22**. An informative comparison can also be made upon inspection of the  $^1H$  NMR spectra. The  $^1H$  NMR spectrum for  $[^{IND}NpN^{DIPP,DIPP}]K$  **2.22**

contains a singlet at  $\delta$  3.8 with an integration value of 2H for the methylene resonance of the indene backbone. In contrast, this resonance is missing in the  $^1\text{H}$  NMR spectrum for dianionic **2.29** and the corresponding methine proton now displays a chemical shift of  $\delta$  5.4 with an integration value of 1H. The differences in the  $^1\text{H}$  spectra for **2.22** and **2.29** are depicted in **Figure 2.26**.

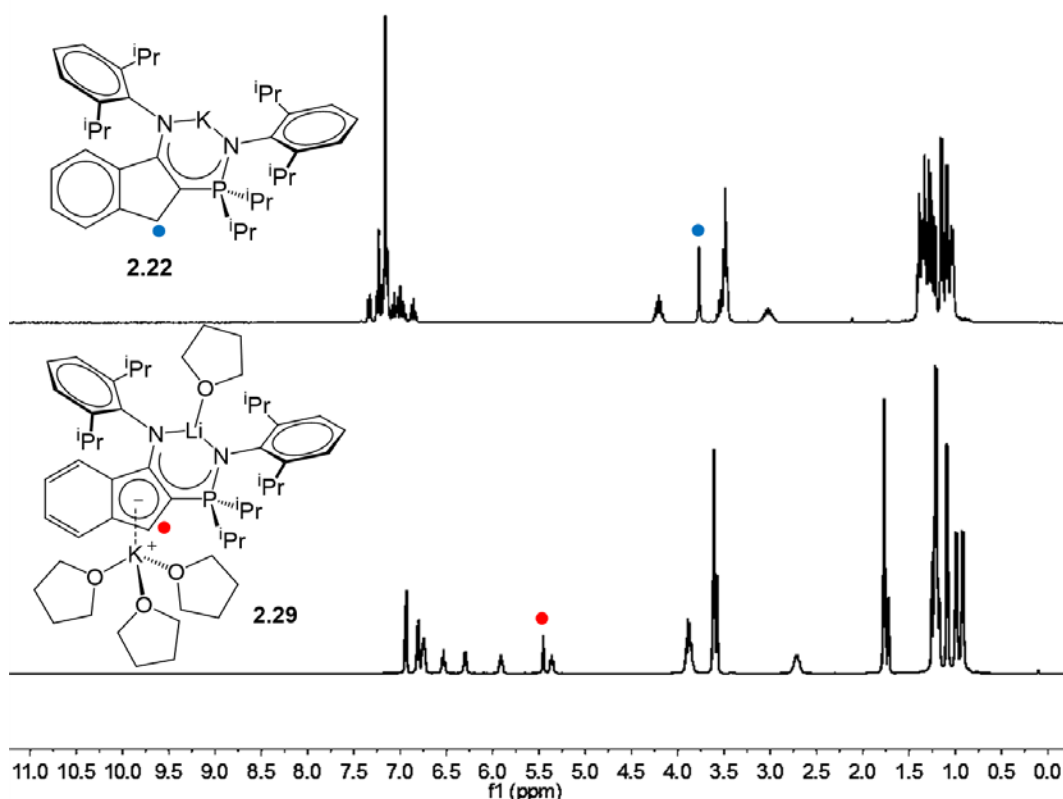


**Figure 2.26:**  $^1\text{H}$  NMR comparison between **2.22** (top spectrum) (400 MHz,  $d_6$ -benzene, 298 K) and **2.29** (bottom spectrum) (400 MHz,  $d_8$ -THF, 298 K).

Numerous salt metathesis reactions were attempted between **2.29** and various early and late metal precursors. However, in almost all cases the formation of numerous products occurred. Even when steric bulk was imparted to the metal precursor being used (for example, using early metal precursors featuring pentamethylcyclopentadienyl as a co-ligand), at least two products were observed when monitored by  $^{31}\text{P}\{^1\text{H}\}$  NMR spectroscopy. The only attempted reaction

found to yield one product by  $^{31}\text{P}\{^1\text{H}\}$  NMR spectroscopy was the addition of orange trichloro(pentamethylcyclopentadienyl)titanium (IV) ( $\text{Cp}^*\text{TiCl}_3$ ) to purple **2.29** in the presence of magnesium metal to yield a blue product **[2.30]** with a  $^{31}\text{P}\{^1\text{H}\}$  signal at  $\delta$  26.6. A comparison of the  $^1\text{H}$  NMR spectra between **2.29** and **[2.30]** is shown in **Figure 2.27**. Performing this

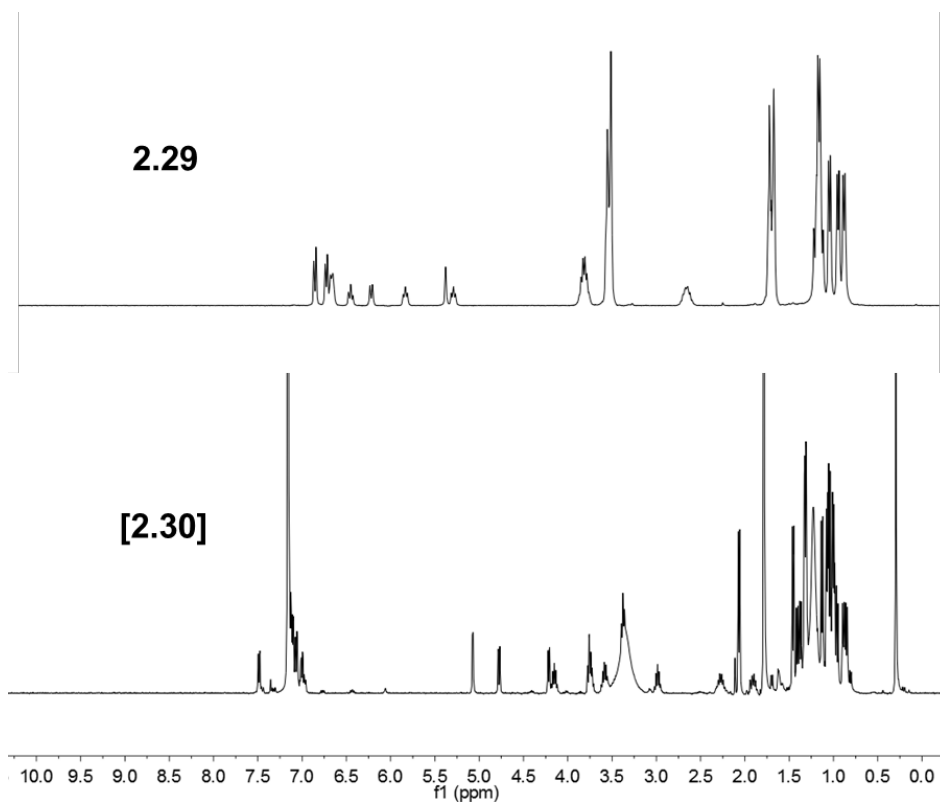


**Figure 2.27:**  $^1\text{H}$  NMR comparison between **2.29** (top spectrum) (400 MHz,  $d_8$ -THF, 298 K) and **[2.30]** (bottom spectrum) (400 MHz,  $d_6$ -benzene, 298 K).

reaction in the absence of magnesium, even at  $-78$   $^\circ\text{C}$ , yielded a brown product mixture with three  $^{31}\text{P}\{^1\text{H}\}$  resonances at  $\delta$  3.6, 16.3, and 54.1. Compound **[2.30]** is thermally sensitive, gradually decomposing if not kept at  $-35$   $^\circ\text{C}$ . Unfortunately, X-ray quality crystals of **[2.30]** remained elusive.

A possible cause for the formation of multiple products observed in the aforementioned reactions attempted with **2.29** was elucidated from the salt metathesis reaction of **2.29** with

FeBr<sub>2</sub>(THF)<sub>2</sub>. The observation that the reaction of **2.29** with both one or two equivalents of FeBr<sub>2</sub>(THF)<sub>2</sub> yielded the same diamagnetic product, **2.31**, with a <sup>31</sup>P{<sup>1</sup>H} chemical shift of δ 2.8 spurred further investigation. X-ray diffraction analysis of single crystals grown from an *n*-pentane solution cooled to -35 °C provided the structure shown in **Figure 2.28**. Examination of

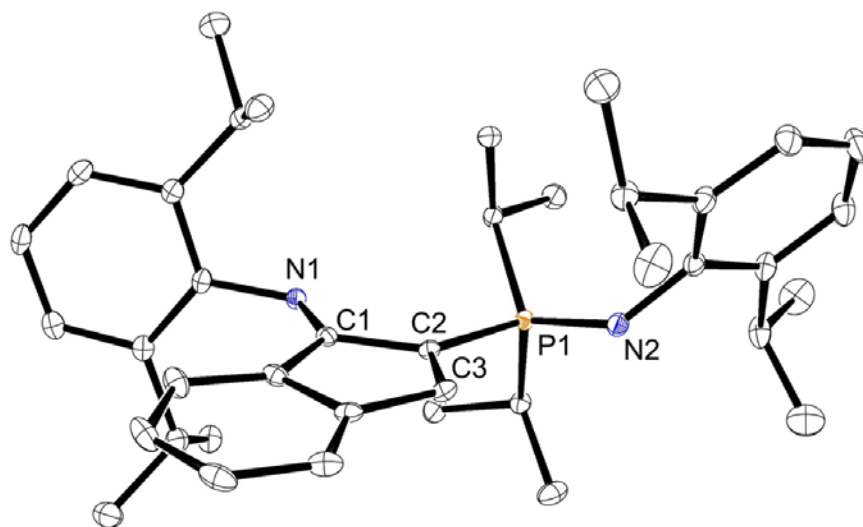
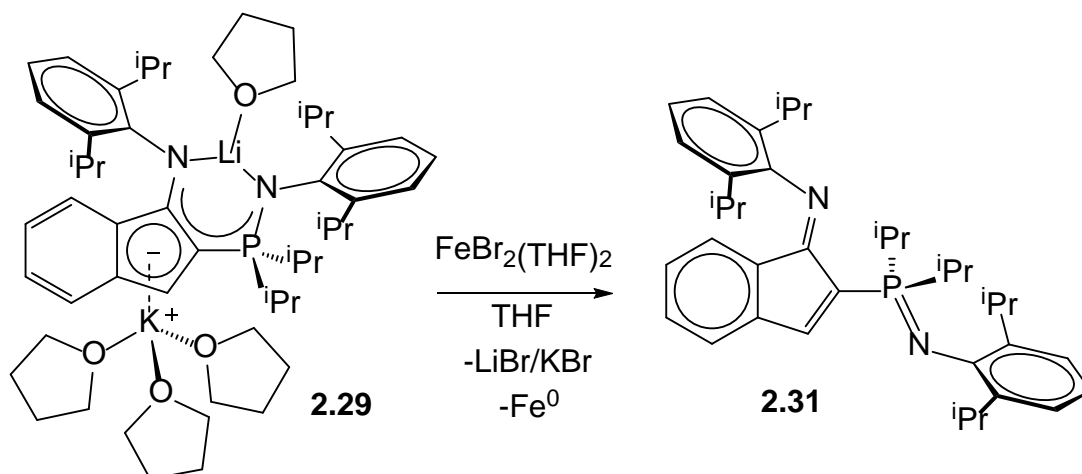


**Figure 2.28:** ORTEP drawing of the solid-state molecular structure of **2.31** (ellipsoids at 50% probability level). All hydrogen atoms have been omitted for clarity. Selected bond lengths (Å), and angles (deg): C1-N1: 1.282(2), C1-C2: 1.499(2), C2-C3: 1.350(2), C2-P1: 1.812(2), P1-N2: 1.557(1), N1-C1-C2: 123.16(14), C1-C2-P1: 131.25(12).

the bond metrics shows that a double bond has formed between C2–C3 with a distance of 1.350(2) Å and the C1–N2 bond distance of 1.282(2) Å is consistent with an imine C=N double bond. Thus, it is likely that **2.29** was oxidized to form **2.31**, with concurrent formation of LiBr, KBr, and Fe<sup>0</sup> (**Scheme 2.14**). The ability of **2.29** to reduce metal precursors is a likely explanation for the formation of multiple products in other salt metathesis reactions.

Reconsideration of the reaction to generate [**2.30**], the addition of magnesium likely caused the pre-emptive reduction of the Cp\*TiCl<sub>3</sub> starting material, which allowed for salt metathesis with **2.29** rather than competitive oxidation of **2.29**. Based on the <sup>31</sup>P{<sup>1</sup>H} chemical shift for [**2.30**] of



**Scheme 2.14:** Oxidation of **2.29** by  $\text{FeBr}_2(\text{THF})_2$  to yield **2.31**.

$\delta$  26.6 in comparison to **2.29** ( $\delta$  33.1) and **2.31** ( $\delta$  2.8), it is likely that the anionic indenyl fragment is still present in [**2.30**] and oxidation of the ligand scaffold had not occurred.

It is difficult to reconcile the highly reductive nature of the dianionic ligand scaffold present in **2.29** with the computational results indicating that the anionic charge in the supposed  $\text{N}_2$  complex [**2.28**] does not contribute substantially to enhanced  $\text{N}_2$  activation. Perhaps since the deprotonation to generate [**2.28**] was performed on the already reduced  $\text{N}_2$  complex **2.27**, it results in the localization of the negative charge in the indenyl ring system. Performing cyclic voltammetry could potentially have been an informative exercise on the reducing capabilities of [**2.28**] and **2.29**. However, this was not attempted.

## 2.5 Conclusions

Low-coordinate Fe(II) bromide complexes were successfully synthesized featuring mixed donor enamido-phosphinimine ligands with varying degrees of steric hindrance. Reduction of the Fe(II) bromide complex containing a ligand scaffold with 2,6-diisopropylphenyl and mesityl on the N-donor atoms (**2.23c**) successfully resulted in the clean production of a  $\mu\text{-N}_2$  complex with moderate activation of the  $\text{N}_2$  triple bond (**2.25c**). However, reduction of the other low-

coordinate Fe(II) bromide complexes investigated in this work led to mixtures of products, where in one case cleavage of the ligand P=N bond to form a bridging imido unit was observed.

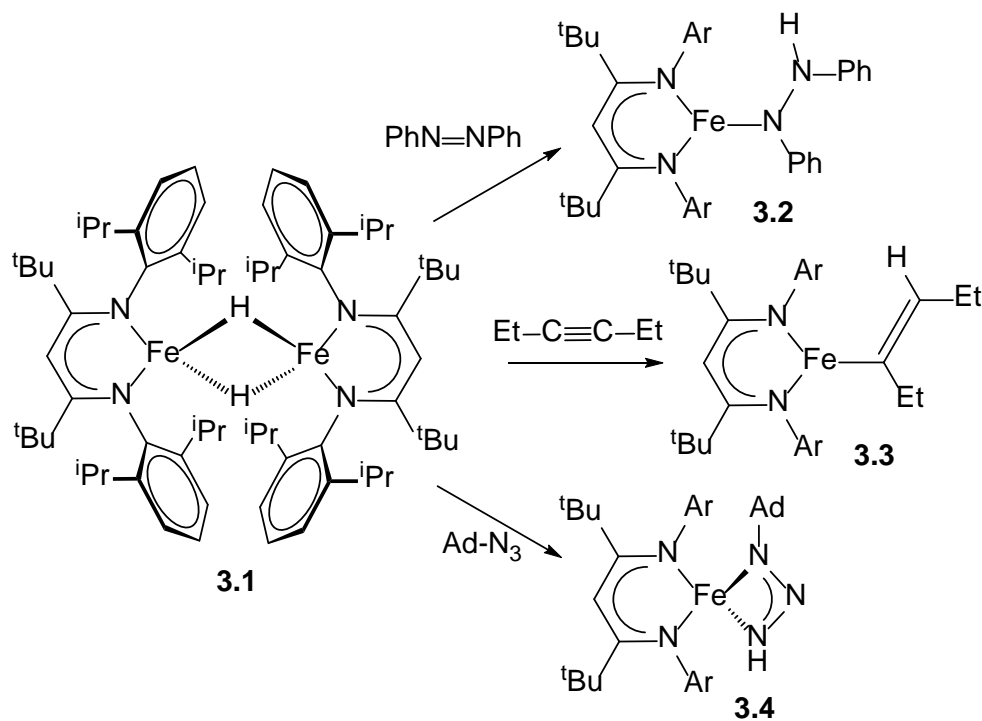
Comparison of low-coordinate iron dinitrogen complexes indicated that changing the electronics of the donor atoms coordinated to iron does not influence the degree of activation of the dinitrogen triple bond, since all of the N–N bond lengths observed are effectively identical.

Additionally, DFT calculations indicate that additional negative charge located in an anionic indenyl ligand scaffold would not contribute significantly to enhanced N<sub>2</sub> activation in a bridging diiron dinitrogen complex ([**2.26**]). Unfortunately, due to issues of reproducibility, studying the effect of a potassium-N<sub>2</sub> interaction with the indenyl scaffold was not pursued.

## Chapter 3: Iron Hydride Complexes

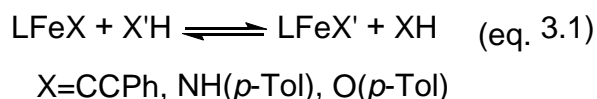
### 3.1 Introduction

The reactivity patterns of low-coordinate first-row transition metal complexes are well documented with regards to small molecule activation and catalytic processes.<sup>28, 102, 124-128</sup> Of particular interest is the family of variously substituted  $\beta$ -diketiminato iron hydrides.<sup>128-131</sup> These complexes are highly reactive species, with the ability to undergo insertion processes, for example, hydride insertion into the nitrogen-nitrogen double bond of azobenzene<sup>132</sup>, the carbon-carbon triple bond of alkynes<sup>130, 132</sup>, and into the azido group of 1-azidoadamantane (**Scheme 3.1**).<sup>130</sup> However, the utilization of low-coordinate iron hydrides as catalyst precursors has been limited. As discussed by Holland and coworkers, the Fe–H bond in low-coordinate species is



**Scheme 3.1:** The dimeric  $\beta$ -diketiminato iron hydride **3.1** inserts into unsaturated substrates. Insertion into azobenzene yields the hydrazido complex **3.2** (ref 132). Reaction with 3-hexyne gives complex **3.3** (ref 132) and reaction with 1-azidoadamantane yields the triazenido species **3.4** (ref 130).

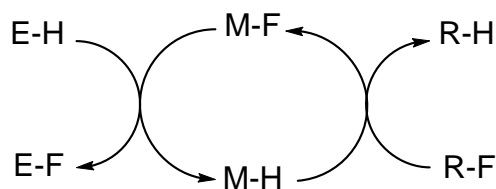
unstable, leading to insertion reactions favoring the formation of stronger Fe–X bonds (X = C, N, O).<sup>16</sup> An extension of this property is the trend for iron to preferentially form bonds to more electronegative elements, with C < N < O (equation 3.1).<sup>133</sup> Considering the enthalpic driving



force for the breakage of Fe–H bonds and the consequent formation of stronger Fe–X bonds, a natural extension of this reactivity is the use of iron hydrides to cleave strong C–F bonds, resulting in the subsequent formation of Fe–F bonds. Such reactivity could be harnessed in a catalytic cycle for hydrodefluorination (HDF).

The cleavage of C–F bonds is an active area of chemical research. Fluorinated organics have become ubiquitous in pharmaceuticals and agrochemicals due to their useful chemical properties and the stability.<sup>134-135</sup> However, the stability of fluorinated organics also presents an environmental challenge, as fluorinated species persist in the biosphere.<sup>136</sup> Thus, removing fluorine atoms via catalytic HDF for remediation purposes is an important area of research.

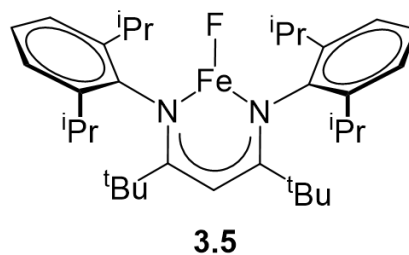
Late transition-metals are attractive for catalytic HDF due to the relatively weak M–F bond, which facilitates turnover of the catalytic cycle upon reaction with a hydride source (**Scheme 3.2**).<sup>137</sup> This reactivity stands in contrast to the utilization of early transition metal



**Scheme 3.2:** General HDF catalytic cycle involving a metal hydride/fluoride couple.

complexes in which the formation of a prohibitively strong M–F bond often prevents applications in catalysis.<sup>138-140</sup> The majority of homogenous HDF catalysts utilize the precious

late-metal Rh.<sup>141-143</sup> Though there are some examples of HDF catalysis with the relatively abundant metal Ni,<sup>144-148</sup> there is only one reported example in the literature of iron catalyzed HDF.<sup>149</sup> The three-coordinate  $\beta$ -diketiminato iron fluoride complex (**3.5** in **Figure 3.1**) defluorinates fluorinated aromatic substrates in the presence of triethylsilane (Et<sub>3</sub>SiH).<sup>149</sup>



Substrate	Conditions	Product Distribution	TON
C <sub>6</sub> F <sub>6</sub>	45 °C, 4 days	C <sub>6</sub> HF <sub>5</sub> (50%)	2.5
C <sub>5</sub> F <sub>5</sub> N	45 °C, 4 days	<i>p</i> -C <sub>5</sub> HF <sub>4</sub> N (71%)	3.6
C <sub>6</sub> F <sub>5</sub> CF <sub>3</sub>	45 °C, 12 h	<i>p</i> -C <sub>6</sub> HF <sub>4</sub> CF <sub>3</sub> (90%)	4.5

**Figure 3.1:** Select examples of catalytic hydrodefluorination (HDF) reported for iron(II) fluoride  $\beta$ -diketiminato complex **3.5**. Each reaction was performed in d<sub>8</sub>-THF using 20 mol% of catalyst. Triethylsilane was used as a hydride source.

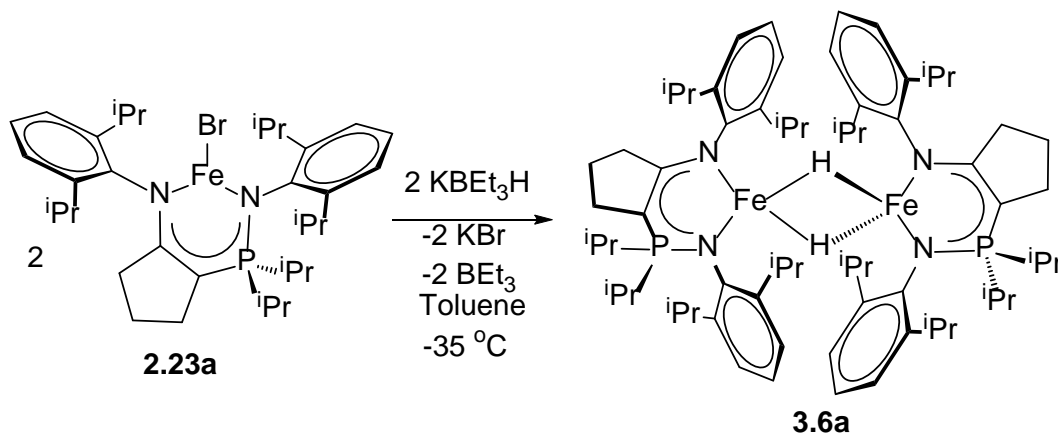
However, conversions are low and the propensity for catalyst decomposition made mechanistic investigations difficult.<sup>149</sup> Interestingly, utilization of the hydride species **3.1** as a precatalyst leads to lower HDF activity.<sup>149</sup> Thus, we sought to investigate whether an electronic variation to the low-coordinate environment present in **3.1** and **3.5** would allow for enhanced stability of the catalytically active species in HDF.

The contents of the following chapter describe the synthesis and characterization of a low-coordinate, paramagnetic iron hydride complex bearing the electronically asymmetric enamido-phosphinimine (NpN) ligand scaffold described in Chapter 2. In addition, select examples of insertion reactions with multiply bonded substrates are described. The most surprising reactivity observed was the direct reaction of the NpN iron hydride complex with C<sub>6</sub>F<sub>6</sub>

to generate the corresponding low-coordinate iron fluoride complex. Consequently, the NpN iron hydride complex performs HDF catalysis of fluorinated aromatics at low loadings and displays relatively high TON for the monodefluorination of pentafluoropyridine (C<sub>5</sub>F<sub>5</sub>N).

### 3.2 Synthesis of Low-Coordinate Iron Hydride Complexes

Treatment of the three-coordinate iron (II) bromide complex (<sup>CY5</sup>NpN<sup>DIPP,DIPP</sup>)FeBr **2.23a** with potassium triethylborohydride (KBET<sub>3</sub>H) served as a convenient synthetic route for the synthesis of the desired low-coordinate iron hydride complexes [(<sup>CY5</sup>NpN<sup>DIPP,DIPP</sup>)FeH]<sub>2</sub> **3.6a**, shown in **Scheme 3.3**. Single crystals of **3.6a** were grown from a toluene solution of the product



**Scheme 3.3:** Treatment of the iron bromide complex **2.23a** with KBET<sub>3</sub>H at -35 °C affords the dimeric iron hydride **3.6a**.

cooled to -35 °C. The solid-state molecular structure for **3.6a** is shown in **Figure 3.2**. The bridging hydrides in **3.6a** were located in the difference density map and were freely refined without constraining the Fe–H bond distance. In comparison to the most closely related NacNac complex [(<sup>t</sup>BuNacNac<sup>DIPP</sup>)FeH]<sub>2</sub> **3.1**, the distance between the two iron centers in **3.6a** is longer (2.6762(4) Å) in contrast to the distance of 2.624(2) Å for **3.1**. This is a surprising result, as the aryl rings in **3.1** experience more steric interaction with the *tert*-butyl groups in the backbone of

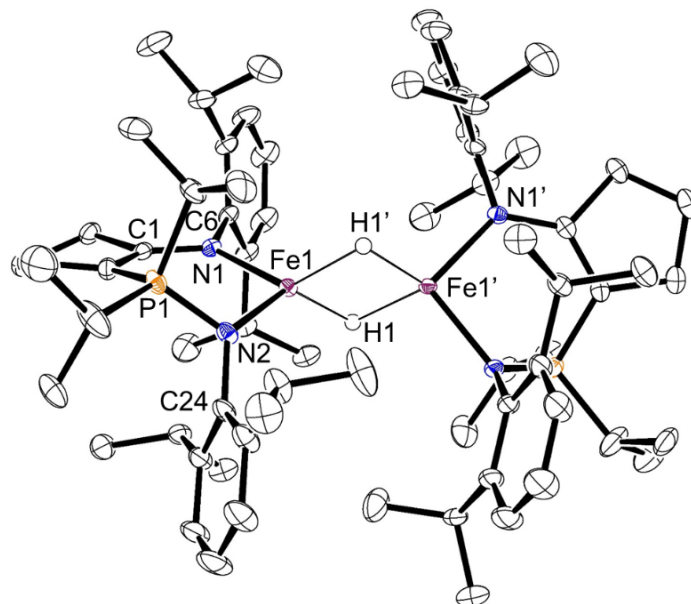


**Figure 3.2:** ORTEP drawing of the solid-state molecular structure of **3.6a** (ellipsoids at 50% probability level). All hydrogen atoms except those bonded to iron have been omitted for clarity. Selected bond lengths (Å), angles (deg), and torsion angles (deg): Fe1-H1: 1.713(19), Fe1-H1':1.789(17), Fe1-Fe1': 2.6762(4), N1-Fe1: 2.0461(9), N2-Fe1: 2.0455(9), H1-Fe1-H1': 48.4(7), N1-Fe1-N2: 99.60(4), C1-N1-C6: 115.66(9), P1-N2-C24: 119.63(8), N1-Fe1-Fe1'-N1': 37.17(8).

NacNac in comparison to the sterics present in the ligand backbone of **3.6a**. This effect is quantified by the C-N-C angle where the aryl rings present on the N-donors are forced towards the Fe center, which for **3.1** has an average value of  $121.3(6)^\circ$ .<sup>132</sup> The two corresponding angles for **3.6a** are C1-N1-C6: 115.66(9) and P1-N2-C24: 119.63(8). Based on this analysis of ligand sterics, it can be rationalized that the elongated distance between the iron centers in **3.6a** in comparison to  $[(^t\text{BuNacNac}^{\text{DIPP}})\text{FeH}]_2$  is likely electronic in nature.

The  $^1\text{H}$  NMR spectra of **3.6a** in  $d_6$ -benzene and  $d_8$ -THF are virtually identical at 25 °C (**Figure 3.3**) indicating that the structure of **3.6a** in both solvents is the same. This suggests that the dimer is retained in solution, given the tendency for THF to coordinate to low-coordinate derivatives. Any dimer-monomer equilibrium would likely be perturbed in going from non-polar

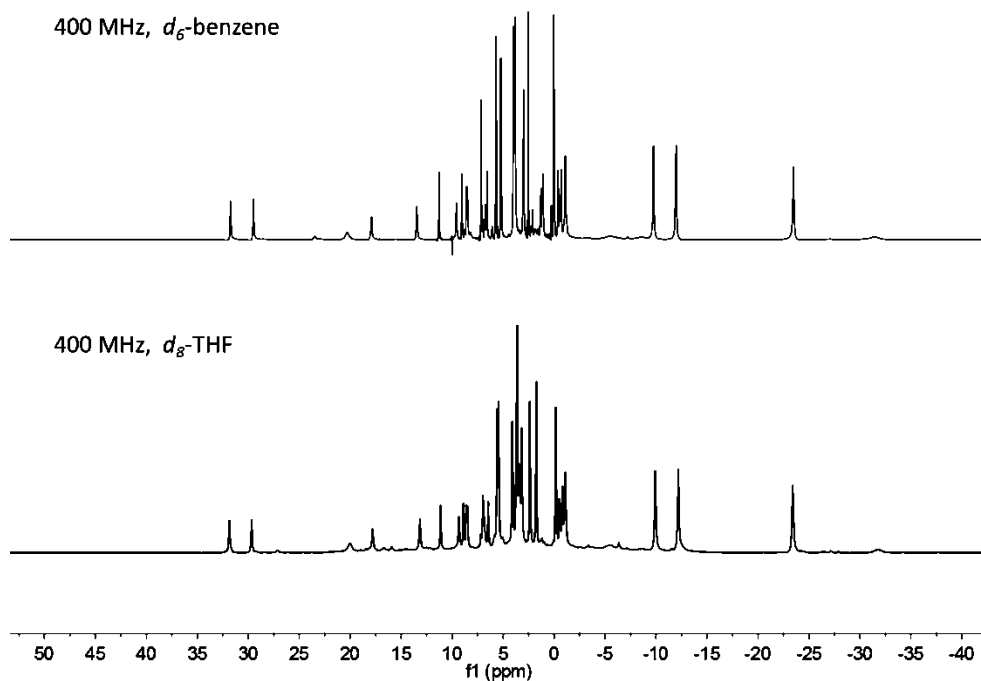


**Figure 3.3:**  $^1\text{H}$  NMR spectra for **3.6a** in  $d_6$ -benzene (top) and  $d_8$ -THF (bottom). Both spectra were collected at 400 MHz at 25 °C.

benzene to THF. In addition, the complexity of the spectrum (approximately 30 unique resonances) is consistent with a  $C_1$  symmetric dimer (if the structure **3.6a** displays in the solid-state is retained in solution). A  $C_s$  symmetric monomer would only display 16 resonances in the  $^1\text{H}$  NMR spectrum. The hydrides are not observed due to the extremely rapid relaxation experienced during the NMR experiment resulting from being directly bonded to the iron center.<sup>150</sup> Additional evidence for the dimeric structure of **3.6a** is the low solution magnetic moment of  $4.2 \mu_B$  measured by the Evans method, indicating strong anti-ferromagnetic coupling of the normally high-spin Fe(II) centers in the dimer. Similarly low magnetic values have been reported for **3.1** at 25 °C.<sup>132</sup>

The synthesis of **3.6a** must be performed at -35 °C in order to prevent a side reaction with the triethylborane by-product. When **2.23a** is treated with  $\text{KBET}_3\text{H}$  at 25 °C and the reaction

mixture is left to stir for 15 minutes, the resulting  $^1\text{H}$  NMR spectrum obtained for the product mixture contains 52 resonances. X-ray diffraction of single crystals picked from a diethyl ether solution of the product mixture cooled to  $-35\text{ }^\circ\text{C}$  provided the structure of the iron dihydridoborate complex **3.7** (Figure 3.4). The formation of **3.7** follows from the reaction of

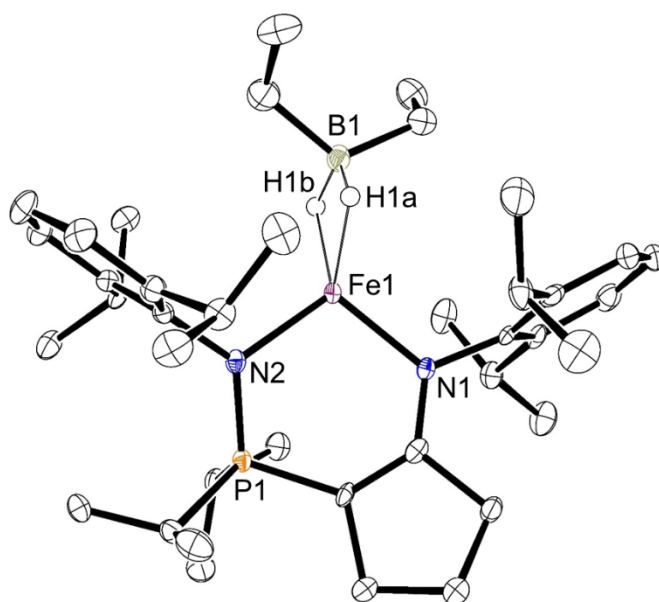
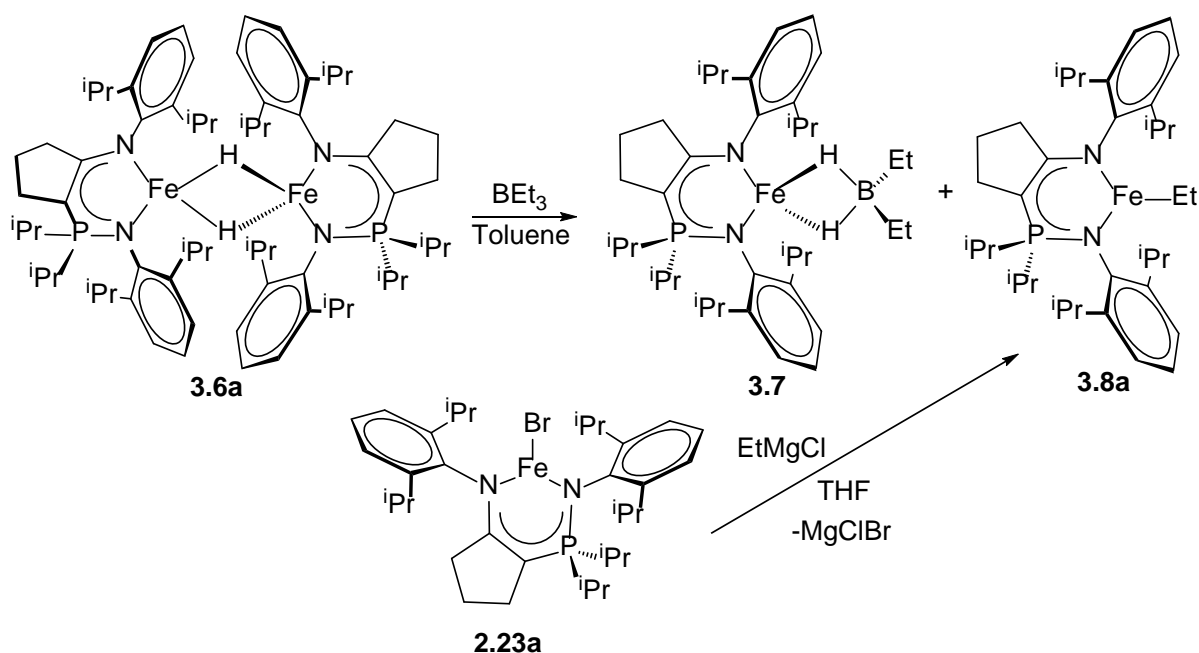


**Figure 3.4:** ORTEP drawing of the solid-state molecular structure of **3.7** (ellipsoids at 50% probability level). All hydrogen atoms except those bonded to iron have been omitted for clarity. Selected bond lengths ( $\text{\AA}$ ) and angles (deg): Fe1-N1: 1.952(2), Fe1-N2: 1.971(2), P1-N2: 1.632(2), Fe1-H1a: 1.81(3), Fe1-H1b: 1.66(3), N1-Fe1-N2: 105.26(9), and H1a-Fe1-H1b: 59.8(14).

**3.6a** with the by-product triethylborane produced in the hydride metathesis reaction, additionally producing the 3-coordinate iron ethyl complex **3.8a** (Scheme 3.4). Analogous reactivity is well-established for the reaction between  $[(^t\text{BuNacNac}^{\text{DIPP}})\text{FeH}]_2$  **3.1** and triethylborane.<sup>151</sup> In order to confirm that the iron ethyl species **3.8a** was produced concurrently with complex **3.7**, the 3-



**Scheme 3.4:** The dimeric iron hydride complex **3.6a** reacts with triethylborane to give the dihydridoborate species **3.7** and the three-coordinate iron ethyl complex **3.8a**. The iron ethyl complex **3.8a** can be independently synthesized through treatment of **2.23a** with a THF solution of  $\text{EtMgCl}$ .

coordinate iron bromide complex **2.23a** was treated with a THF solution of ethylmagnesium chloride for  $^1\text{H}$  NMR spectral comparison of independently synthesized **3.8a** and the product mixture from which single crystals of **3.7** were grown. Indeed, resonances consistent with **3.6a** and **3.8a** were observed in the  $^1\text{H}$  NMR spectrum for the product mixture yielding **3.7** (**Figure 3.5**). The solid-state molecular structure of the iron ethyl complex **3.8a** is shown in **Figure 3.6**. Additionally, pure **3.6a** and triethylborane were heated to  $60\text{ }^\circ\text{C}$  with the intent of cleanly producing **3.7** and **3.8a**. This serves as a demonstration that potential impurities in the  $\text{KBEt}_3\text{H}$  did not lead to the initially observed formation of **3.7**. Comparison of the  $^1\text{H}$  NMR spectra for independently synthesized **3.8a** with the reaction of hydride **3.6a** and triethylborane at  $60\text{ }^\circ\text{C}$

clearly shows that **3.6a** does react to form the ethyl complex **3.8a**, with the unassigned resonances likely belonging to **3.7** (Figure 3.7).

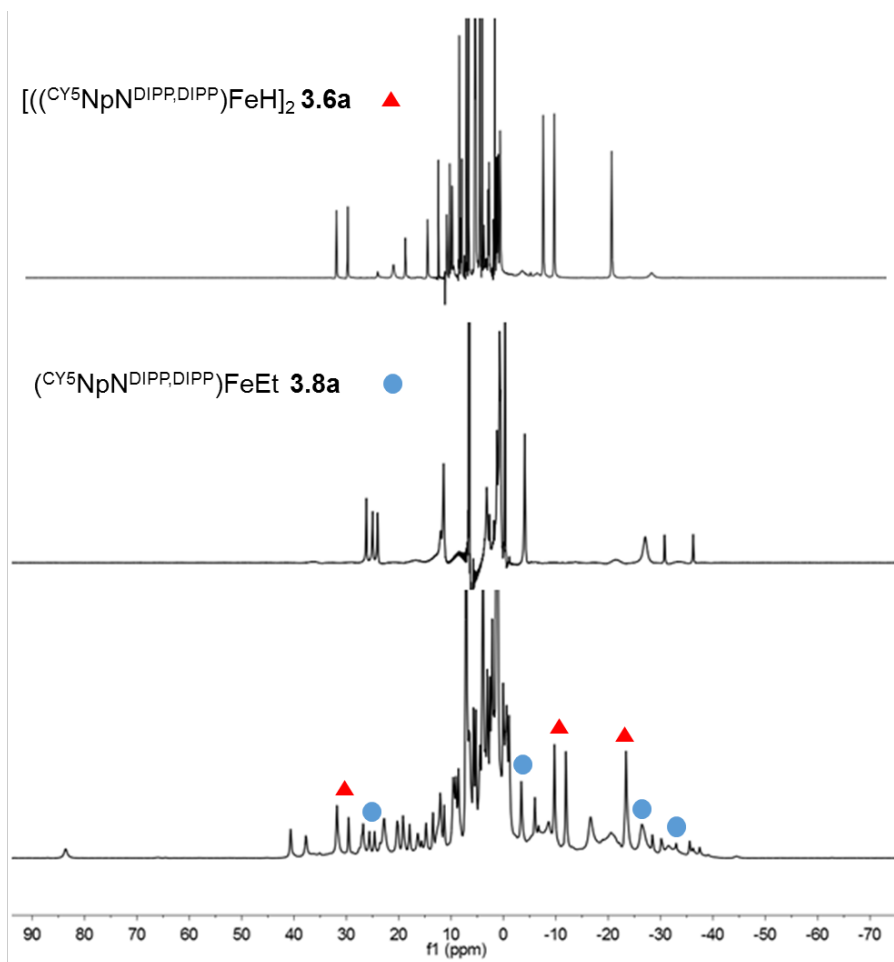


**Figure 3.5:** <sup>1</sup>H NMR spectra for **3.6a** (top), **3.8a** (middle), and the product mixture from which single crystals of **3.7** were grown (bottom). Red triangles for **3.6a** and blue circles for **3.8a** are used to mark discernable signals belonging to their respective compounds in the complicated product mixture shown in the bottom spectrum. All spectra recorded at 300 MHz in *d*<sub>6</sub>-benzene at 25 °C.

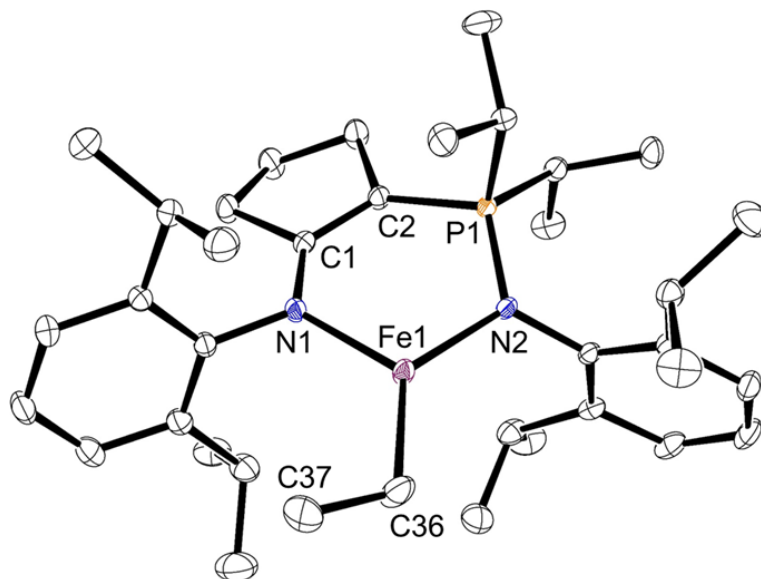


**Figure 3.6:** ORTEP drawing of the solid-state molecular structure of **3.8a** (ellipsoids at 50% probability level). All hydrogen atoms have been omitted for clarity. Selected bond lengths (Å) and angles (deg): Fe1-N1: 1.9860(10), Fe1-N2: 2.0072(9), C1-N1: 1.3524(14), C1-C2: 1.3853(15), C2-P1: 1.7564(11), P1-N2: 1.6314(9), Fe1-C36: 2.052(5), C36-C37: 1.481(10), N1-Fe1-N2: 103.44(4), and C37-C36-Fe1: 116.9(4).

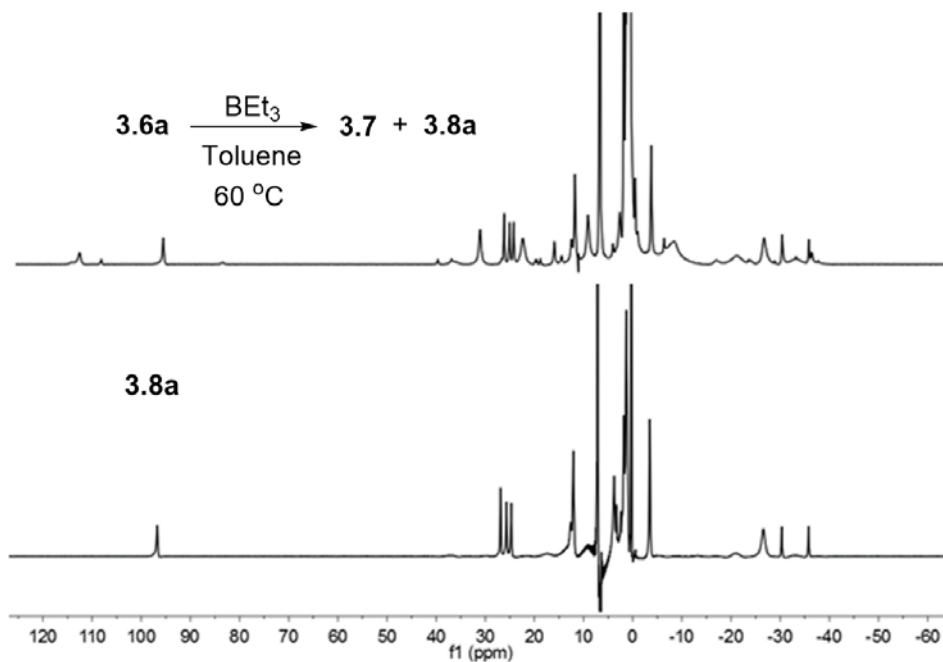
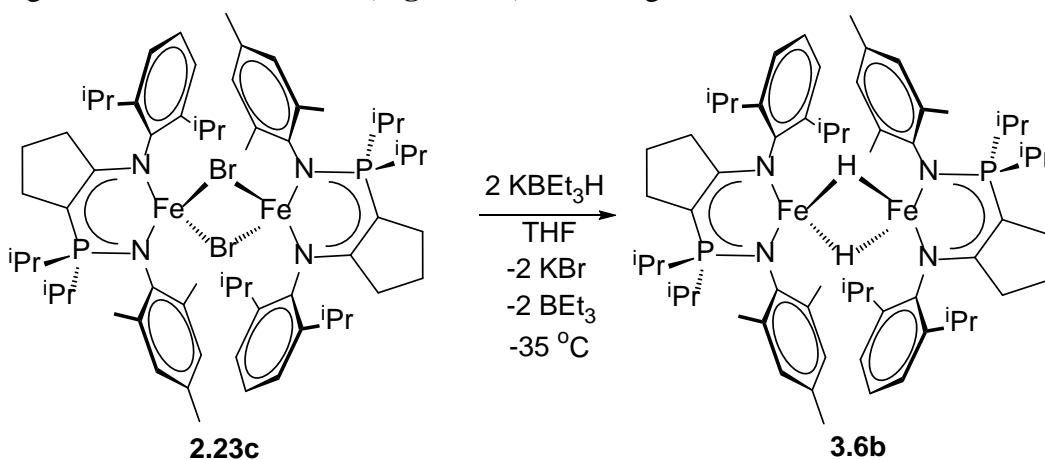


**Figure 3.7:** The  $^1\text{H}$  NMR spectrum for the reaction of **3.6a** with  $\text{BEt}_3$  at  $60\text{ }^\circ\text{C}$  for 2h (300 MHz,  $d_8$ -toluene,  $25\text{ }^\circ\text{C}$ ) compared to the  $^1\text{H}$  NMR spectrum for **3.8a** (300 MHz,  $d_6$ -benzene,  $25\text{ }^\circ\text{C}$ ).

Preparation of the sterically unsymmetrical low-coordinate iron hydride

$[(^{CY5}NpN^{DIPP,Mes})FeH]_2$  **3.6b** was attempted through the same methodology used to synthesize **3.6a** (Scheme 3.5). However, similar  $^1H$  NMR spectra for the product mixtures were observed when the hydride metathesis reaction with  $KBET_3H$  was performed rapidly at  $-35\text{ }^\circ C$  compared to an overnight reaction time at  $25\text{ }^\circ C$  (Figure 3.8). Puzzling features observed in both of these



**Scheme 3.5:** The reaction of **2.23c** with  $KBET_3H$  for the attempted synthesis of the dimeric iron hydride complex **3.6b**.

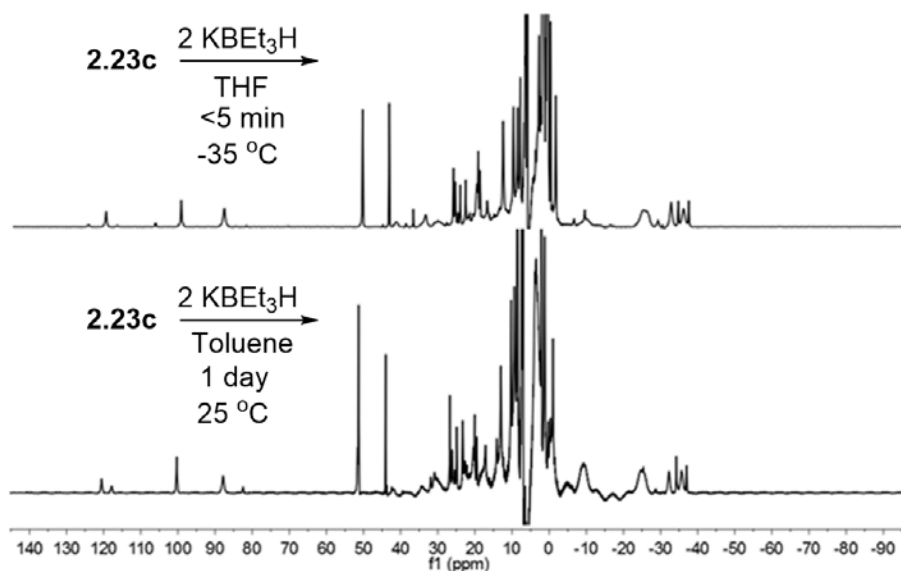


**Figure 3.8:**  $^1H$  NMR spectra for the reaction of **2.23c** with  $KBET_3H$  at  $-35\text{ }^\circ C$  with a reaction time under 5 minutes (300 MHz,  $d_8$ -toluene,  $25\text{ }^\circ C$ ), and the reaction of **2.23c** with  $KBET_3H$  at  $25\text{ }^\circ C$  with an overnight reaction time (300 MHz,  $d_6$ -benzene,  $25\text{ }^\circ C$ ).

spectra were the downfield resonances located in the range of  $\delta$  120 – 90. Such downfield shifted resonances are a common spectral feature for monomeric paramagnetic species, whereas dimeric species commonly feature narrower  $\delta$  ranges, similar to complex **3.6a** and the diiron dinitrogen complex **2.25c** described in Chapter 2. To confirm whether the side reaction between **3.6b** and triethylborane had occurred, even during short reaction times at  $-35\text{ }^{\circ}\text{C}$ , the iron ethyl complex ( $\text{CY}^5\text{NpN}^{\text{DIPP,MeS}}$ )FeEt **3.8b** was synthesized for the purpose of  $^1\text{H}$  NMR spectral comparison (**Figure 3.9**). Complex **3.8b** was prepared under similar conditions to the synthesis of **3.8a** and

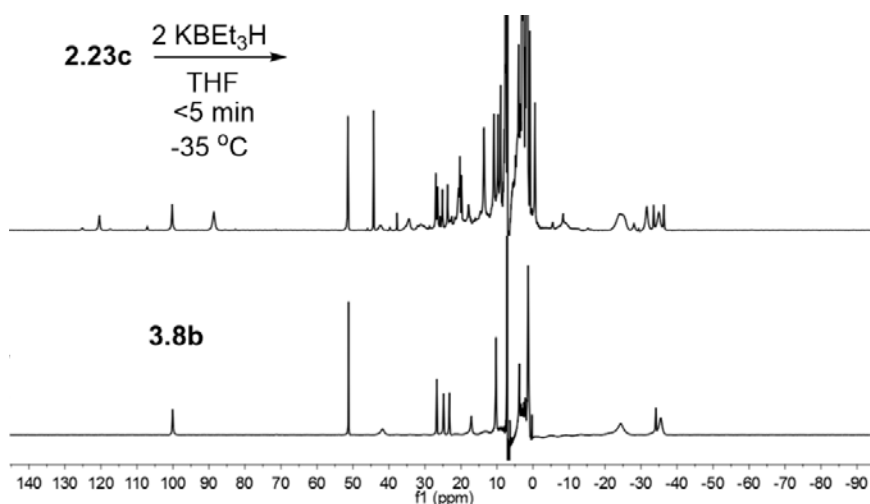


**Figure 3.9:**  $^1\text{H}$  NMR spectra for the reaction of **2.23c** with  $\text{KBET}_3\text{H}$  at  $-35\text{ }^{\circ}\text{C}$  with a reaction time under 5 minutes (300 MHz,  $d_8$ -toluene,  $25\text{ }^{\circ}\text{C}$ ) in comparison to the iron ethyl complex **3.8b** (300 MHz,  $d_6$ -benzene,  $25\text{ }^{\circ}\text{C}$ ). The presence of complex **3.8b** is observed in the product mixture obtained from the reaction of **2.23c** with  $\text{KBET}_3\text{H}$ .

the solid-state molecular structure of **3.8b** is shown in **Figure 3.10**. Inspection of **Figure 3.9** indicates a reaction between the transiently formed hydride complex **3.6b** and triethylborane had occurred because the resonances corresponding to the ethyl complex **3.8b** are observed in the product mixture. Surprisingly, crystals of the hydride complex **3.6b** were isolated from a toluene solution of the product mixture cooled to  $-35\text{ }^{\circ}\text{C}$  (solid-state molecular structure shown in **Figure 3.11**). While select crystals of **3.6b** could be isolated, synthesizing bulk quantities of **3.6b**

through hydride metathesis was not feasible. Thus, further reactivity studies were pursued with the more sterically-hindered iron hydride **3.6a**.

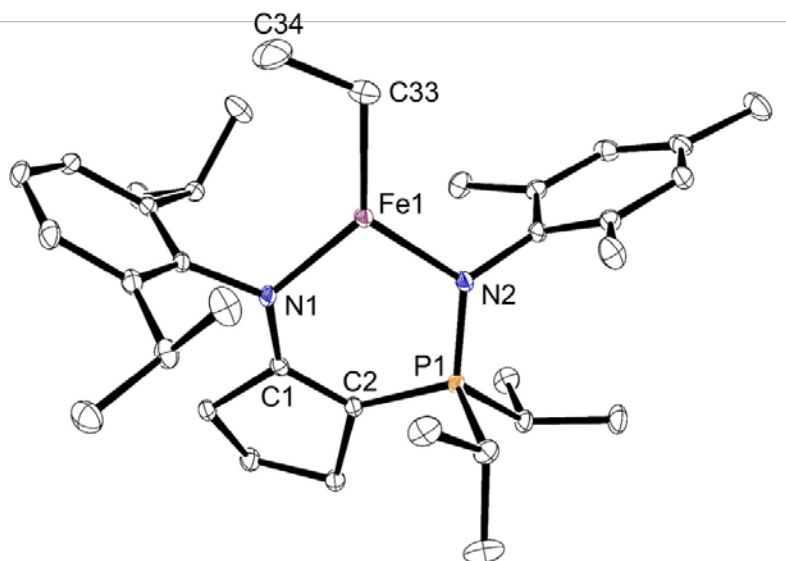


**Figure 3.10:** ORTEP drawing of the solid-state molecular structure of **3.8b** (ellipsoids at 50% probability level). All hydrogen atoms have been omitted for clarity. Selected bond lengths (Å) and angles (deg): Fe1-N1: 1.9783(10), Fe1-N2: 1.9952(10), C1-N1: 1.3524(13), C1-C2: 1.3857(15), C2-P1: 1.7527(11), P1-N2: 1.6299(10), Fe1-C33: 2.0343(12), C33-C34: 1.5396(19), N1-Fe1-N2: 101.43(4), and C34-C33-Fe1: 116.99(9).

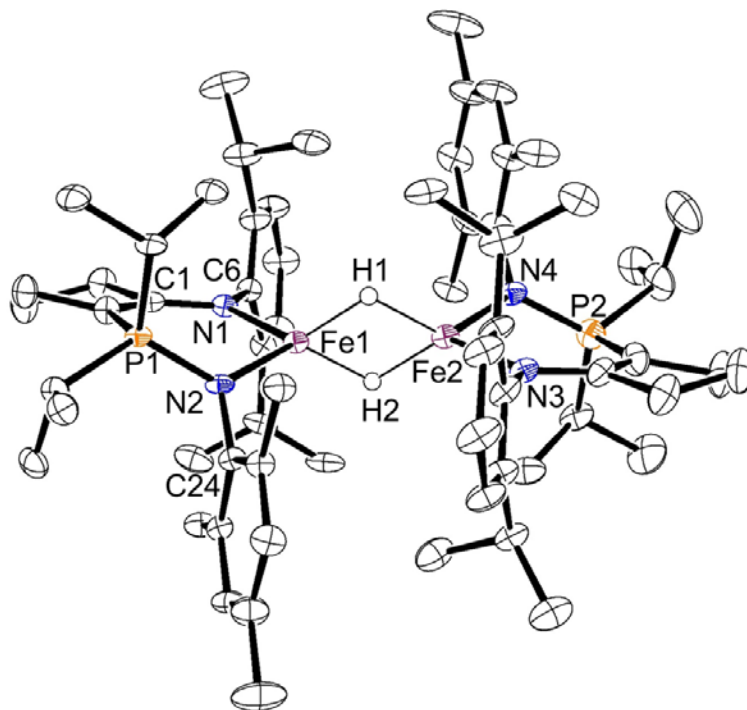
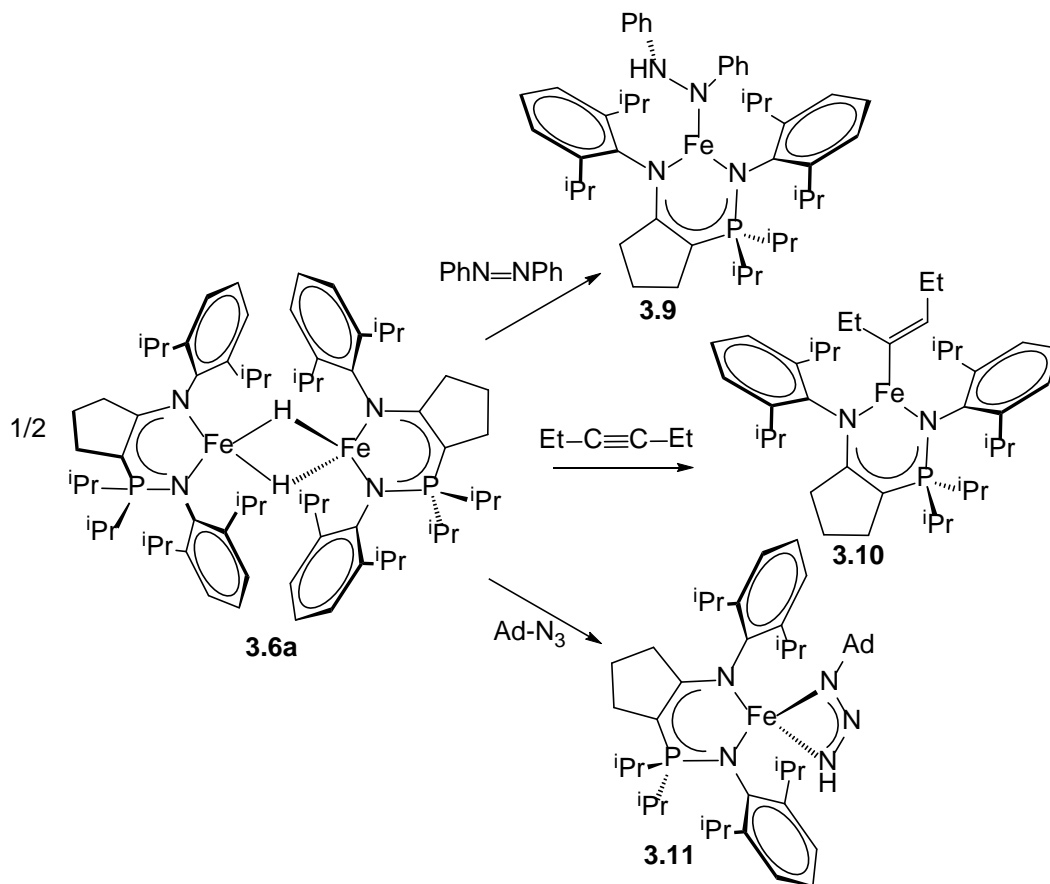


**Figure 3.11:** ORTEP drawing of the solid-state molecular structure of **3.6b** (ellipsoids at 50% probability level). All hydrogen atoms except those bonded to iron have been omitted for clarity. Selected bond lengths (Å), angles (deg), and torsion angles (deg): Fe1-H1: 1.61(2), Fe1-H2:1.60(2), Fe1-Fe2: 2.6447(10), N1-Fe1: 2.016(4), N2-Fe1: 2.012(4), H1-Fe1-H2: 69.5(12), Fe1-H1-Fe2: 98.1(1), N1-Fe1-N2: 99.39(15), C1-N1-C6: 114.9(4), P1-N2-C24: 121.7(3), N1-Fe1-Fe2-N4: 0.2(2).

### 3.3 Hydride Insertion Reactivity

To compare the reactivity of hydride complex **3.6a** with the reactivity displayed by the  $\beta$ -diketiminato iron hydride **3.1**, complex **3.6a** was treated with a selection of substrates containing multiple bond character (**Scheme 3.6**). In each case, the postulated insertion product was formed



**Scheme 3.6:** Insertion products isolated from the reaction of the iron hydride complex **3.6a** with azobenzene (**3.9**), 3-hexyne (**3.10**), and 1-azidoadamantane (**3.11**).

with few differences in the structure of the resulting complex in comparison to the iron  $\beta$ -diketiminato analogues.<sup>130, 132</sup> For example, the solid-state molecular structure for the hydrazido complex **3.9** is shown below in **Figure 3.12** and displays a nearly identical N–N bond length (1.429(5) Å) to the hydrazido N–N bond in **3.2** (1.423(2) Å).<sup>132</sup>

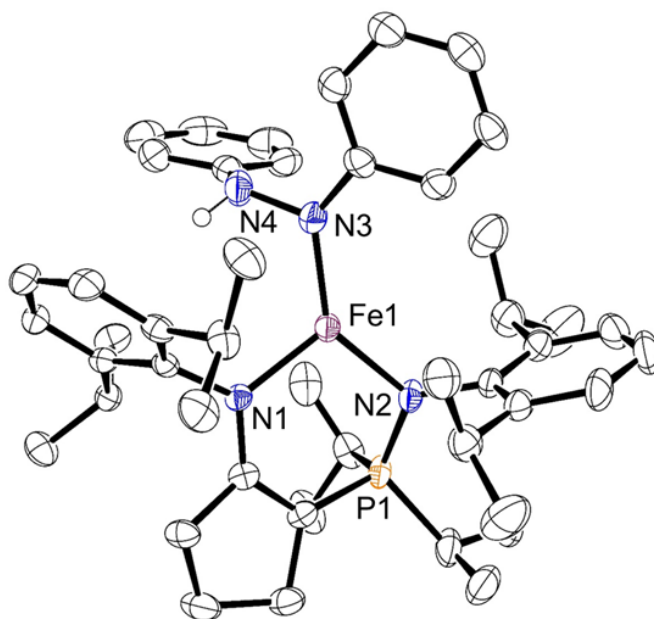


**Figure 3.12:** ORTEP drawing of the solid-state molecular structure of **3.9** (ellipsoids at 50% probability level). All hydrogen atoms except those bonded to N have been omitted for clarity. Selected bond lengths (Å) and angles (deg): Fe1-N1: 1.973(3), Fe1-N2: 1.990(3), N3-N4: 1.429(5), Fe1-N3: 1.934(3), P1-N2: 1.644(4), N1-Fe1-N2: 104.46(14), and Fe1-N3-N4: 115.7(3).

The hydrazido complex **3.9** is  $C_1$  symmetric in the solution state, giving a  $^1\text{H}$  NMR spectrum with 33 resonances when collected in  $d_6$ -benzene. The asymmetry of **3.9** in solution is likely caused by hindered rotation about the Fe–N (hydrazido) bond, as observed for the analogous  $\beta$ -diketiminato hydrazido complex **3.2**.<sup>132</sup> Heating a benzene solution of complex **3.9** to 50 °C resulted in the clean formation of a new paramagnetic species **3.12** over the course of 24 hours (**Figure 3.13**). Single crystals of **3.12** were grown from a hexanes solution cooled to -35 °C and the solid-state molecular structure displaying connectivity is shown in **Figure 3.14**. Complex **3.12** features an anilido ligand derived from the coordinated hydrazido of **3.9**, indicating that the N–N bond was cleaved at elevated temperature with the presumed production of half an equivalent of azobenzene (**Scheme 3.7**). An analogous reaction has been reported when the NacNac iron hydrazido complex **3.2** is heated to 80 °C for 3 hours.<sup>132</sup>

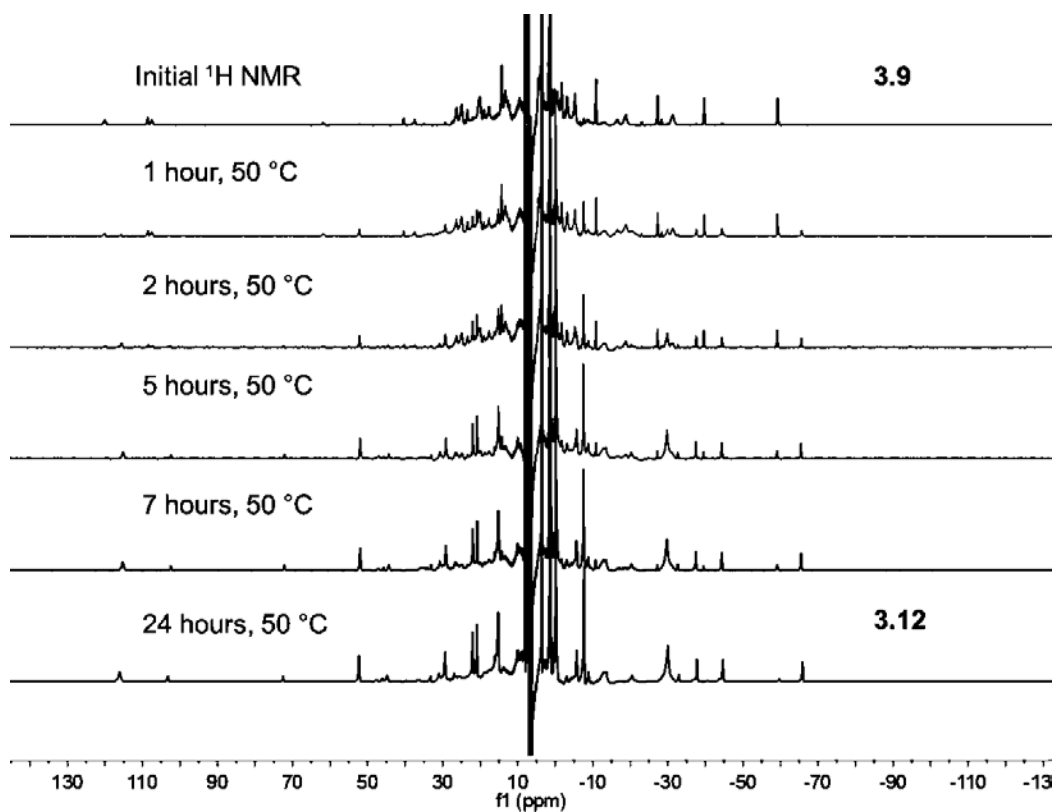


**Figure 3.13:** <sup>1</sup>H NMR spectra for complex **3.9** heated to 50 °C over the course of 24 hours. Conversion is nearly complete after 7 hours of heating to 50 °C. The new paramagnetic species formed is the anilido complex **3.12** (*d*<sub>6</sub>-benzene, 300 MHz, 25 °C).

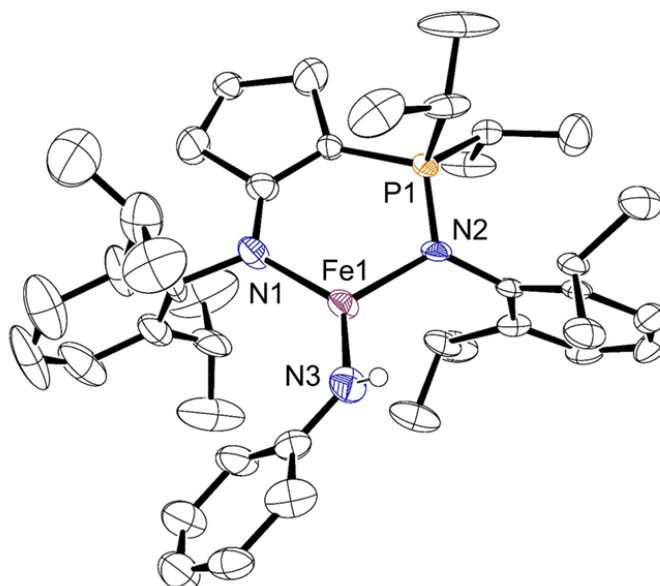
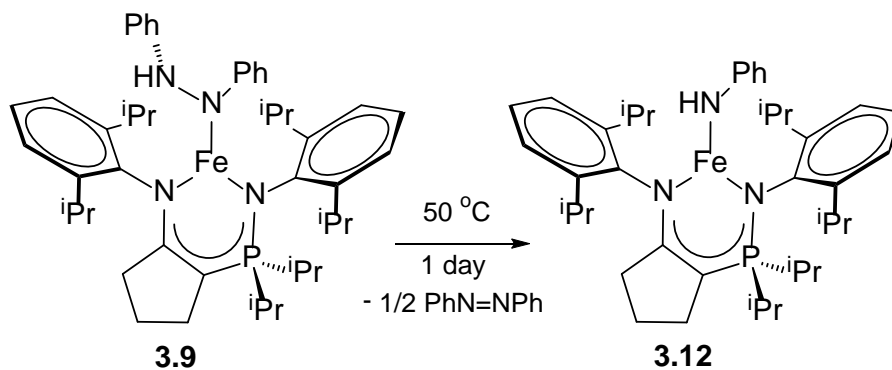


**Figure 3.14:** ORTEP drawing of the solid-state molecular structure of **3.12** (ellipsoids at 50% probability level). All hydrogen atoms except those bonded to N have been omitted for clarity. Due to the poor quality of the data, bonding metrics will not be described. Nonetheless, the connectivity can be determined unambiguously.



**Scheme 3.7:** Thermolysis of the N–N bond of the hydrazido ligand leads to the formation of the anilido complex **3.12**, with the putative formation of half an equivalent of azobenzene.

The reaction of **3.6a** with 3-hexyne gives the *cis* alkene complex **3.10**. The solid-state molecular structure of **3.10** is depicted in **Figure 3.15**, providing evidence for the conversion of

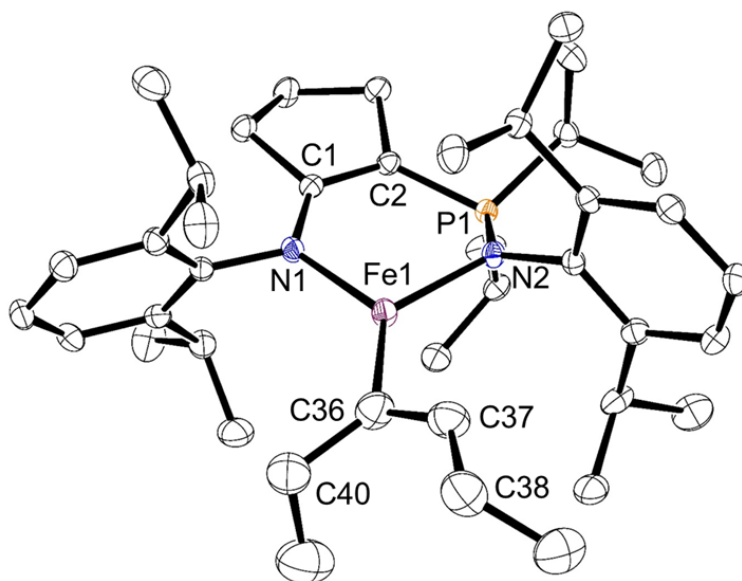


**Figure 3.15:** ORTEP drawing of the solid-state molecular structure of **3.10** (ellipsoids at 50% probability level). All hydrogen atoms have been omitted for clarity. Selected bond lengths (Å) and angles (deg): Fe1-N1: 1.9807(16), Fe1-N2: 2.0081(16), Fe1-C36: 2.016(2), C1-C2: 1.387(3), C1-N1: 1.355(2), C2-P1: 1.7605(19), P1-N2: 1.6295(16), C36-C40: 1.526(4), C36-C37: 1.369(4), C37-C38: 1.502(3), N1-Fe1-N2: 102.02(6), C36-Fe1-N1: 130.40(8), C36-Fe1-N2: 127.31(9), C36-C37-C38: 129.6(2) and C40-C36-C37: 120.0(2).

the alkyne to the alkene through analysis of the bonding metrics. The bond length between C36-C37 of 1.369(4) Å corresponds to an elongated C=C bond, and the bond angle for C40-C36-C37 of 120.0(2)° corroborates the assignment of a  $sp^2$  hybridization for C36. Interestingly, the C36-C37-C38 angle of 129.6(2)° is larger than the ideal 120° bond angle for a  $sp^2$  hybridized carbon, but this may be due to the steric interaction of the alkyl chain bonded to C37 with the 2,6-diisopropylphenyl group of the ligand. The  $^1\text{H}$  NMR spectrum for **3.10** contains 18 signals, indicating that rotation of the 3-hexene unit around the Fe1-C36 bond is rapid on the NMR timescale.<sup>130</sup>

The solid-state molecular structure for complex **3.11**, the product from hydride insertion into 1-azidoadamantane, is shown in **Figure 3.16**. The triazenido moiety is coordinated through the nitrogen atoms N5 and N3, with a torsion angle of 165.70(12) $^{\circ}$  indicating the non-

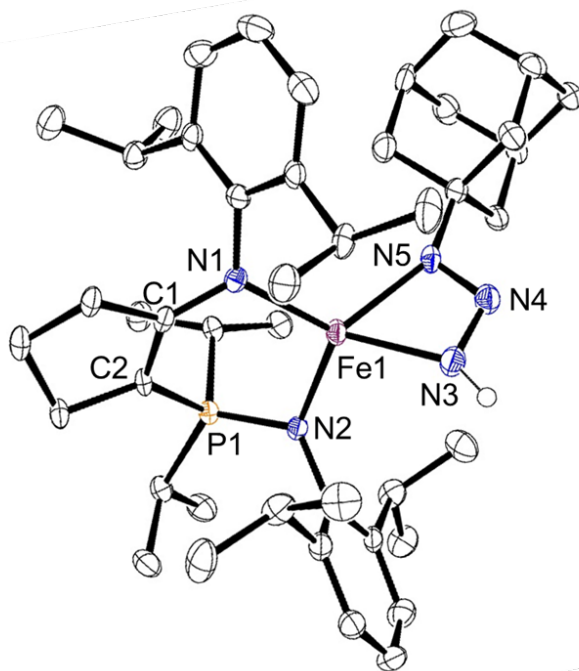


**Figure 3.16:** ORTEP drawing of the solid-state molecular structure of **3.11** (ellipsoids at 50% probability level). All hydrogen atoms except those bonded to N have been omitted for clarity. Selected bond lengths ( $\text{\AA}$ ) and angles (deg): Fe1-N1: 2.0170(16), Fe1-N2: 2.0273(17), C1-C2: 1.376(3), C1-N1: 1.369(2), C2-P1: 1.770(2), P1-N2: 1.6263(16), Fe1-N3: 2.1060(17), Fe1-N5: 2.0901(17), N3-N4: 1.321(3), N4-N5: 1.296(2), N1-Fe1-N2: 104.95(7), N3-Fe1-N5: 60.30(7), N3-N4-N5: 107.26(16), and C1-N1-Fe1-N4: 165.70(12).

perpendicular orientation of the triazenido group. The bond lengths within the triazenido moiety are consistent with those reported for the  $\beta$ -diketiminato complex ( $^t\text{BuNacNac}^{\text{DIPP}}\text{Fe}(\eta^2\text{-HNNNAd})$  **3.4**.<sup>130</sup> Another similarity between **3.11** and the NacNac complex **3.4** is the higher symmetry in solution (determined by  $^1\text{H}$  NMR spectroscopy) than predicted from the solid-state molecular structure. For example, **3.4** is  $C_s$  symmetric in the solid-state but displays  $C_{2v}$  symmetry in solution.<sup>130</sup> This effect is rationalized by the rapid isomerization of the triazenido

ligand through hemilability and re-coordination on the NMR timescale.<sup>130</sup> Complex **3.11** is C<sub>1</sub> symmetric if the solid-state molecular structure is retained in solution and would be expected to give 34 resonances. However, **3.11** displays higher symmetry in solution, as only 24 resonances are observed. Thus, the same hemilability and subsequent re-coordination of the triazenido ligand reported for **3.4** also applies to **3.11**. Heating **3.11** overnight at 80 °C causes a color change from green to yellow-orange and quantitative conversion to a new paramagnetic species [**3.13**] as determined by <sup>1</sup>H NMR spectroscopy (**Figure 3.17**). The β-diketiminato triazenido

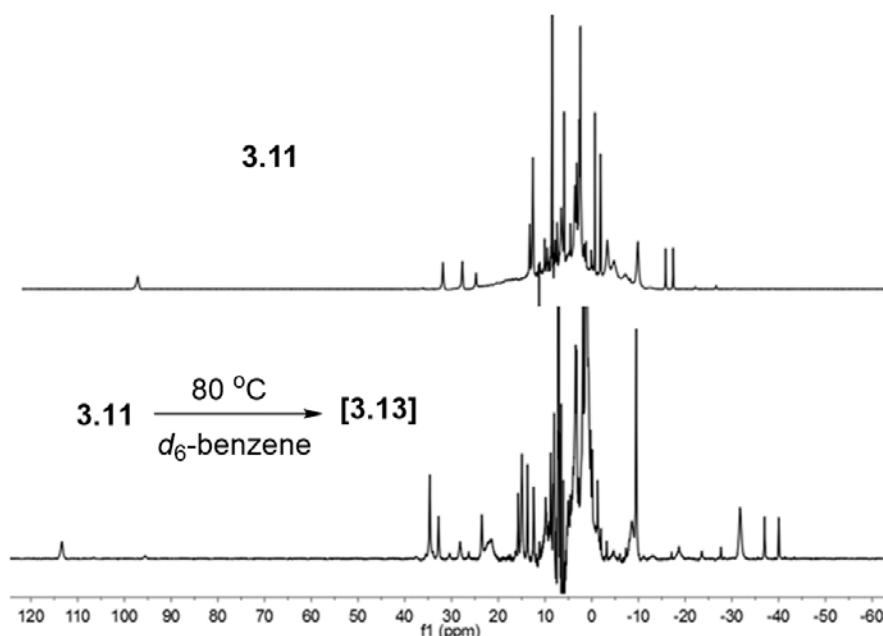
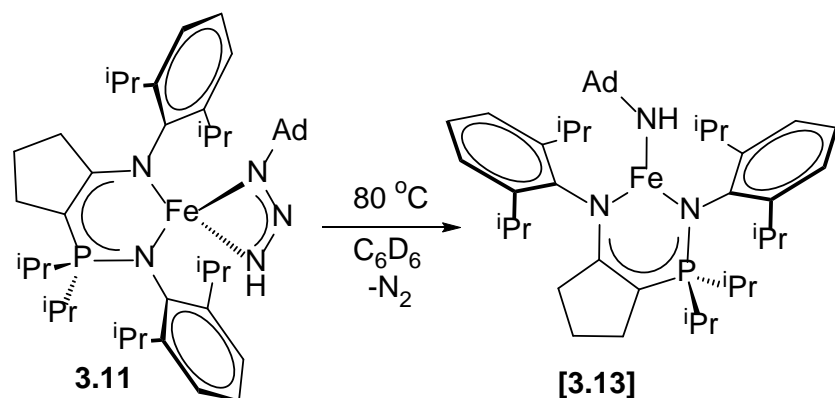


**Figure 3.17:** <sup>1</sup>H NMR spectra for complex **3.11** in comparison to [**3.13**], the product formed from heating **3.11** to 80 °C for 3 days (*d*<sub>6</sub>-benzene, 300 MHz, 25 °C).

complex **3.4** expels N<sub>2</sub> and forms (t<sup>Bu</sup>NacNac<sup>DIPP</sup>)FeNHAd when heated to 80 °C for 5 hours.<sup>130</sup>

By analogy, [**3.13**] is likely the amido species (CY<sup>5</sup>NpN<sup>DIPP,DIPP</sup>)FeNHAd (**Scheme 3.8**).



**Scheme 3.8:** Heating **3.11** to 80 °C results in the quantitative conversion to the likely amido species [**3.13**].

The stoichiometric reactivity of **3.6a** towards select unsaturated substrates was identical to that observed for the  $\beta$ -diketimate hydride complex **3.1**. However, application of the unsymmetrical ligand environment present in **3.6a** to showcase an advantage over the symmetric low-coordinate environment imparted by the  $\beta$ -diketimate scaffold was desirable. Small changes in the electronic or steric features of a complex can have large implications for catalytic activity.<sup>152-157</sup> Thus, an investigation was pursued regarding the HDF catalytic activity of the electronically asymmetric complex **3.6a** in comparison to the  $\beta$ -diketimate system (hydride complex **3.1** and the fluoride complex **3.5**).

### 3.4 Catalytic Hydrodefluorination

#### 3.4.1 HDF Utilizing Low-Coordinate Iron Hydride Precatalysts

As discussed in the introduction, the only reported example of iron catalyzed hydrodefluorination utilizes the low-coordinate iron fluoride  $\beta$ -diketimate complex (<sup>t</sup>BuNacNac<sup>DIPP</sup>)FeF **3.5**.<sup>149</sup> Presumably, these HDF reactions operate via formation of a low-coordinate transient iron-hydride species, which upon interaction with a fluorinated aromatic compound, regenerates the iron fluoride species. However, in the  $\beta$ -diketimate system there is no direct reaction between the hydride **3.1** and C<sub>6</sub>F<sub>6</sub> or octafluorotoluene (C<sub>6</sub>F<sub>5</sub>CF<sub>3</sub>) even when

heated to 120 °C in  $d_6$ -benzene or  $d_8$ -THF. Interestingly, in the presence of  $\text{Et}_3\text{SiH}$ , heating **3.1** with  $\text{C}_6\text{F}_6$  or  $\text{C}_6\text{F}_5\text{CF}_3$  does result in the catalytic production of mono-defluorinated products, though conversions are lower than when catalysis is performed with the iron fluoride **3.5** as the precatalyst.<sup>149</sup>

Considering the lack of reactivity the  $\beta$ -diketiminato iron hydride **3.1** displayed towards fluorinated organics, the electronically asymmetric iron hydride **3.6a** was investigated for different reactivity. Gratifyingly, a reaction occurred in  $d_8$ -THF between **3.6a** and  $\text{C}_6\text{F}_6$ , with the formation of  $\text{C}_6\text{F}_5\text{H}$  observed by  $^{19}\text{F}$  NMR spectroscopy. The production of  $\text{C}_6\text{F}_5\text{H}$  was observed in 15 minutes when the reaction mixture is heated to 70 °C (**Figure 3.18**), though decomposition of the iron containing product also occurs at this temperature as observed by  $^1\text{H}$  NMR spectroscopy. If **3.6a** reacts directly with  $\text{C}_6\text{F}_6$  to generate  $\text{C}_6\text{F}_5\text{H}$ , it follows that the concurrent

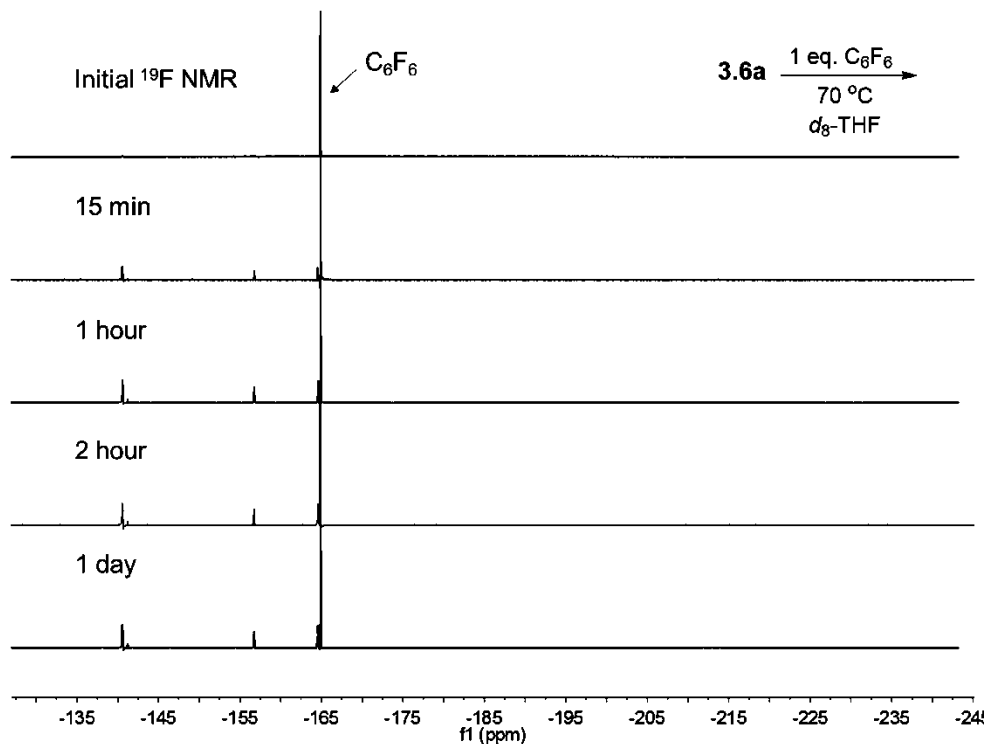
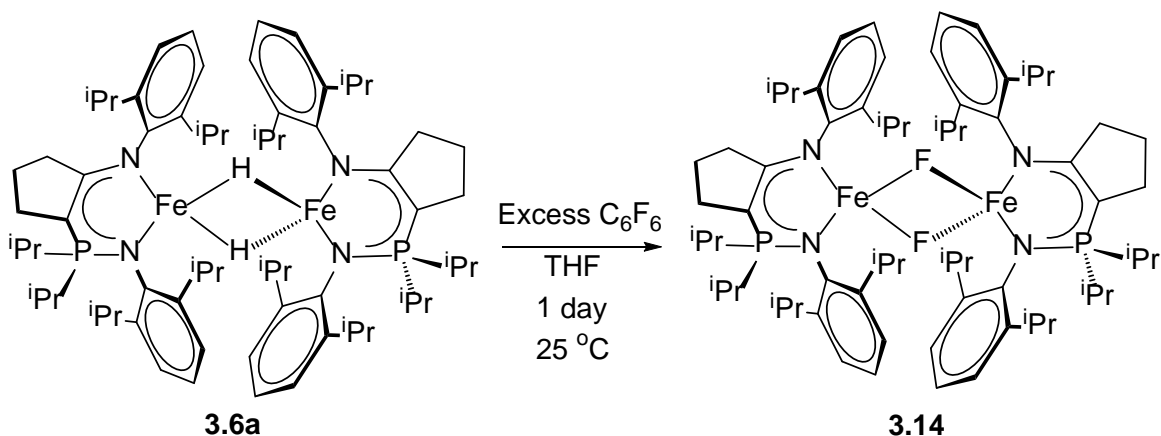


**Figure 3.18:**  $^{19}\text{F}$  NMR spectra for the stoichiometric reaction of **3.6a** with  $\text{C}_6\text{F}_6$  at 70 °C in  $d_8$ -THF.  $^{19}\text{F}$  NMR spectra were collected after 15 minutes, 1 hour, 2 hours, and 1 day ( $d_8$ -THF, 282 MHz, 25 °C).

formation of an iron fluoride species occurs. Reaction of **3.6a** with excess  $C_6F_6$  in THF overnight at room temperature afforded the isolation of the dimeric iron fluoride complex

$[(^{CY5}NpN^{DIPP,DIPP})FeF]_2$  **3.14** (Scheme 3.9). The use of THF as the solvent is crucial for this reaction; Attempting the reaction in diethyl ether or aromatic solvents failed to facilitate a reaction between **3.6a** and  $C_6F_6$ .



**Scheme 3.9:** The reaction of **3.6a** with excess  $C_6F_6$  in THF afforded the dimeric iron(II) fluoride complex **3.14**.

The solid-state molecular structure for **3.14** is shown in **Figure 3.19**. The dimeric nature of **3.14** is somewhat surprising because this enamine-phosphiminine ligand scaffold was used to isolate the three-coordinate iron bromide complex **2.23a**. A comparison of the angle between the nitrogen donors and the 2,6-diisopropylphenyl ring is used to quantify the difference in sterics between similar complexes. The  $C1-N1-C6$  ( $114.3(5)^\circ$ ) and  $P1-N2-C24$  ( $123.1(4)^\circ$ ) angles of **3.14** are shallower than the analogous angles found in **2.23a** of  $118.8(2)^\circ$  and  $125.9(2)^\circ$ , respectively. Thus, a degree of flexibility exists in the enamido-phosphinimine ligand scaffold that is absent in the  $\beta$ -diketiminato systems. The  $C-N-C$  angles of  $127.95(13)^\circ$  found between the imine nitrogen and the aryl rings in the three-coordinate ( $^{tBu}NacNac^{DIPP}$ )FeF complex **3.5** provide enough steric hindrance to force the trigonal planar geometry at the iron center. A less sterically

hindered iron(II) fluoride complex featuring a  $\beta$ -diketiminate with methyl groups in the ligand backbone is reported to adopt a dimeric structure very similar to **3.14**. The  $[(^{\text{Me}}\text{NacNac}^{\text{DIPP}})\text{FeF}]_2$  complex features C-N-C angles of  $119.92(18)^\circ$  and  $117.32(18)^\circ$  and a Fe-Fe distance of  $3.0831(6) \text{ \AA}$ .<sup>149</sup> It is rationalized that the steric bulk imparted by the enamido-phosphinimine scaffold in **3.6a** and **3.14** is greater than the methyl substituted NacNac ligand, but is less sterically hindered than the *tert*-butyl NacNac scaffold.

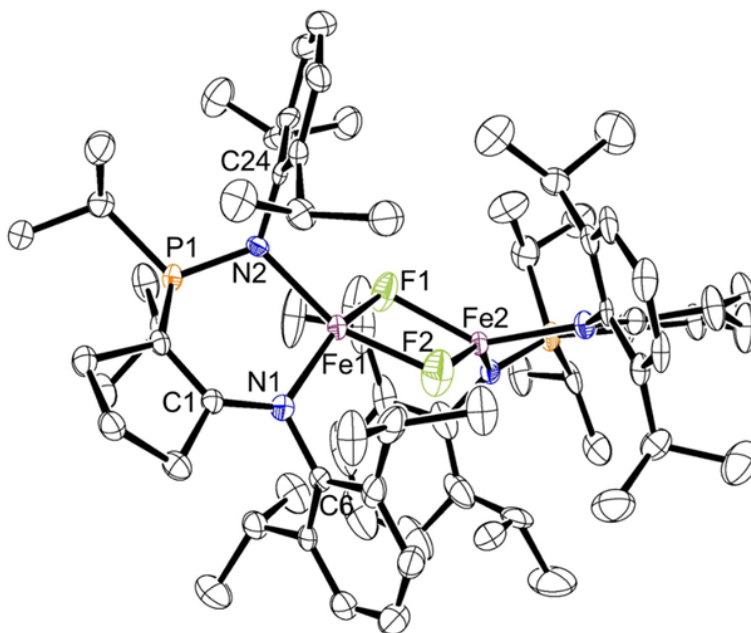


**Figure 3.19:** ORTEP drawing of the solid-state molecular structure of **3.14** (ellipsoids at 50% probability level). All hydrogen atoms have been omitted for clarity. Selected bond lengths ( $\text{\AA}$ ) and angles (deg): Fe1-N1: 2.055(5), Fe1-N2: 2.058(5), Fe1-F1: 2.033(4), Fe1-F2: 1.990(4), Fe1-Fe2: 3.1457(14), N1-Fe1-N2: 96.5(2), F1-Fe1-F2: 77.08(16), Fe1-F1-Fe2: 101.5(2), C1-N1-C6: 114.3(5), and P1-N2-C24: 123.1(4) .

The  $^1\text{H}$  NMR spectrum for **3.14** contains 30 resonances, indicating that it exists as a dimer in solution. However, in contrast to other dimeric species reported in this thesis, the spectral window is more indicative of a monomeric species (with an extremely downfield shifted resonance at  $\delta$  109.1). Fluoride ligands in bridged species have been shown to allow weak

antiferromagnetic exchange between paramagnetic metal centers.<sup>158-159</sup> Thus, the weak antiferromagnetism observed for dimeric **3.14** is likely a result of the bridging fluoride ligands. In agreement with this assessment is the relatively high solution magnetic moment of  $6.2 \mu_B$  per dimer, which is the same solution magnetic moment reported for dimeric  $[(^{\text{Me}}\text{NacNac}^{\text{DIPP}})\text{FeF}]_2$ .<sup>149</sup>

With reactivity between **3.6a** and  $\text{C}_6\text{F}_6$  established, catalytic HDF was investigated with the addition of  $\text{Et}_3\text{SiH}$  to the reaction mixture. Utilizing a catalyst loading of 0.05 mole equivalents of **3.6a** (calculated per monomer) relative to equimolar amounts of  $\text{C}_6\text{F}_6$  and  $\text{Et}_3\text{SiH}$ , catalytic monodefluorination occurred in  $d_8$ -THF at  $50^\circ\text{C}$ . A marginally higher TON of 4.2 was achieved under a shorter time period (2 days) relative to the HDF catalysis reported with the  $(^{\text{tBu}}\text{NacNac}^{\text{DIPP}})\text{FeF}$  **3.5** precatalyst with the same substrates (TON = 2.5, 4 days).<sup>149</sup> Complex **3.6a** also performs the monodefluorination of 1,3,5-trifluorobenzene ( $\text{C}_6\text{F}_3\text{H}_3$ ), though the TON is only 1.2 after 5 days at  $70^\circ\text{C}$ . Interestingly, precatalyst **3.6a** displays a higher tolerance to silane choice compared to the  $\beta$ -diketiminato iron fluoride system, which is reported to decompose at room temperature in the presence of silanes other than  $\text{Et}_3\text{SiH}$ , such as triethoxysilane ( $\text{EtO}_3\text{SiH}$ ) and triphenylsilane ( $\text{Ph}_3\text{SiH}$ ).<sup>149</sup> Both  $\text{Ph}_3\text{SiH}$  and butylsilane ( $n\text{-BuSiH}_3$ ) can be utilized in the HDF of  $\text{C}_6\text{F}_6$ , albeit with lower conversions after a 2 day reaction period relative to using  $\text{Et}_3\text{SiH}$  as the fluoride acceptor (TON = 3 with  $\text{Ph}_3\text{SiH}$  and TON = 2.4 with  $n\text{-BuSiH}_3$ ).

The greatest difference in reactivity between **3.6a** and **3.5** occurs in the HDF of  $\text{C}_5\text{F}_5\text{N}$ . After 3 days at  $50^\circ\text{C}$  in  $d_8$ -THF,  $\text{C}_5\text{F}_5\text{N}$  was quantitatively converted to  $p\text{-C}_5\text{HF}_4\text{N}$  in the presence of **3.6a** when  $\text{Et}_3\text{SiH}$  was used as the fluoride acceptor (**Figure 3.20**). Higher TON's were achieved with lower catalyst loadings; for example, using 0.01 molar equivalents of **3.6a**

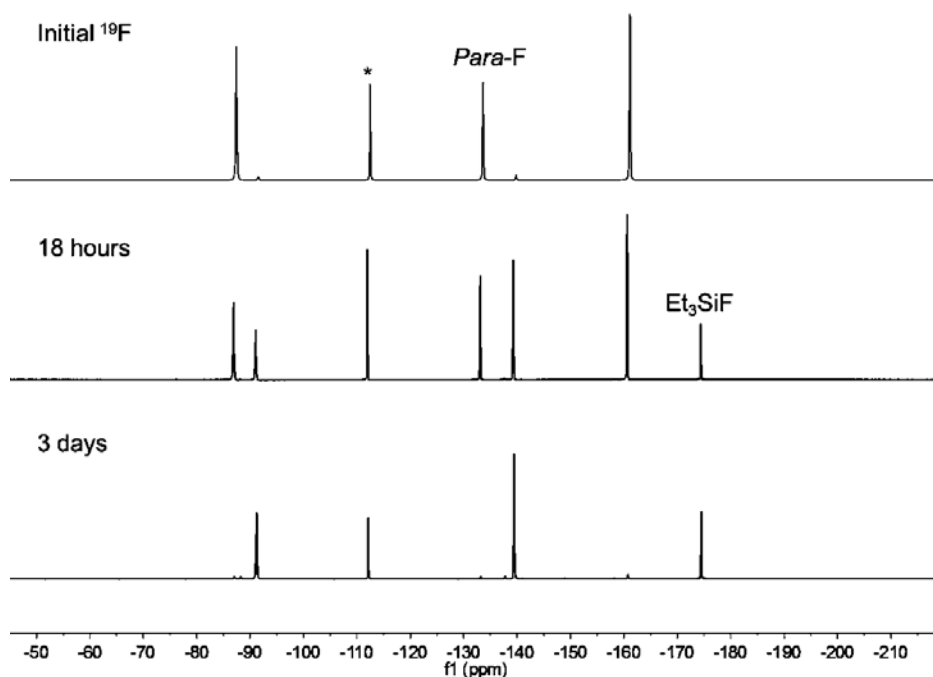


**Figure 3.20:**  $^{19}\text{F}$  NMR for the catalytic HDF of pentafluoropyridine ( $\text{C}_5\text{F}_5\text{N}$ ) using  $\text{Et}_3\text{SiH}$  as the fluoride trap and 5 mol% of **3.6a** as the precatalyst ( $d_8$ -THF,  $50^\circ\text{C}$ ). After 18 hours, the appearance of the ortho and meta  $^{19}\text{F}$  resonances belonging to 2,3,5,6-tetrafluoropyridine ( $p\text{-C}_5\text{HF}_4\text{N}$ ), along the  $^{19}\text{F}$  resonance for  $\text{Et}_3\text{SiF}$  are observed. After 3 days, the resonance belonging to the para-F of  $\text{C}_5\text{F}_5\text{N}$  is no longer observed, indicating complete consumption of  $\text{C}_5\text{F}_5\text{N}$ . Fluorobenzene was used as the internal standard and is denoted with \*.

relative to  $\text{C}_5\text{F}_5\text{N}$  and  $\text{Et}_3\text{SiH}$  and heating the reaction mixture for 1 week resulted in 50% conversion to  $p\text{-C}_5\text{HF}_4\text{N}$  (TON = 50). This is a drastic difference in reactivity relative to **3.5**, which is reported to have a TON of 3.6 for the HDF of  $\text{C}_5\text{F}_5\text{N}$  after 4 days at  $45^\circ\text{C}$ . The dependence of catalytic activity on solvent choice demonstrates a similarity between **3.6a** and **3.5**. For example, attempted HDF of  $\text{C}_6\text{F}_6$  in  $d_6$ -benzene resulted in zero production of  $\text{C}_6\text{F}_5\text{H}$  with precatalyst **3.6a** and marginal production in the case of **3.5** (TON = 0.3).<sup>149</sup> The use of  $d_6$ -benzene as the solvent in the HDF of  $\text{C}_5\text{F}_5\text{N}$  with **3.6a** suppressed the TON to 11.2 in contrast to the full conversion observed when  $d_8$ -THF was the solvent. Thus, it is hypothesized that in both

systems the presence of a coordinating solvent is necessary for breaking up dimeric species during catalysis or stabilizing catalytic intermediates.

The observation that the donor molecule THF increased the catalytic activity of **3.6a** towards HDF spurred the investigation into the addition of other donors to the HDF of C<sub>6</sub>F<sub>6</sub> in the presence of Et<sub>3</sub>SiH. The addition of triphenylphosphine caused a marginally higher TON (5.4 with PPh<sub>3</sub> relative to TON = 4.2 without PPh<sub>3</sub>), though the <sup>1</sup>H NMR spectrum of the iron containing resting state indicates that the phosphine is dissociated. Interestingly, the addition of 4-dimethylaminopyridine (DMAP) to the reaction mixture or the use of *d*<sub>5</sub>-pyridine as the solvent entirely arrests HDF catalysis. It is reasonable to suggest that the presence of a weakly coordinating ligand aids in breaking apart the iron hydride dimer and facilitates reactivity, but

**Table 3.1:** Hydrodefluorination Results Utilizing the Iron(II) Hydride Complex **3.6a** in Comparison to the Catalytic Activity of the β-diketiminato Iron(II) Fluoride Catalyst **3.5**<sup>149</sup>

Precatalyst	Substrate	Reagent	Solvent	Conditions	TON
<b>3.6a</b> (5 mol%)	C <sub>6</sub> F <sub>6</sub>	Et <sub>3</sub> SiH	<i>d</i> <sub>8</sub> -THF	50 °C/ 2 days	4.2
<b>3.6a</b> (5 mol%)	C <sub>5</sub> F <sub>5</sub> N	Et <sub>3</sub> SiH	<i>d</i> <sub>8</sub> -THF	50 °C/ 3 days	20
<b>3.6a</b> (1 mol%)	C <sub>5</sub> F <sub>5</sub> N	Et <sub>3</sub> SiH	<i>d</i> <sub>8</sub> -THF	50 °C/ 7 days	50
<b>3.6a</b> (5 mol%)	C <sub>3</sub> F <sub>3</sub> H <sub>3</sub>	Et <sub>3</sub> SiH	<i>d</i> <sub>8</sub> -THF	70 °C/ 5 days	1.2
<b>3.6a</b> (5 mol%)	C <sub>6</sub> F <sub>6</sub>	Et <sub>3</sub> SiH	C <sub>6</sub> D <sub>6</sub>	50 °C/ 2 days	0
<b>3.6a</b> (5 mol%)	C <sub>6</sub> F <sub>6</sub>	Et <sub>3</sub> SiH	<i>d</i> <sub>5</sub> -pyridine	50 °C/ 2 days	0
<b>3.6a</b> (5 mol%)	C <sub>5</sub> F <sub>5</sub> N	Et <sub>3</sub> SiH	C <sub>6</sub> D <sub>6</sub>	50 °C/ 3 days	11.2
<b>3.6a</b> (5 mol%)	C <sub>6</sub> F <sub>6</sub>	<i>n</i> -BuSiH <sub>3</sub>	<i>d</i> <sub>8</sub> -THF	50 °C/ 2 days	2.4
<b>3.6a</b> (5 mol%)	C <sub>6</sub> F <sub>6</sub>	Ph <sub>3</sub> SiH	<i>d</i> <sub>8</sub> -THF	50 °C/ 2 days	3
<b>3.6a</b> (5 mol%)	C <sub>6</sub> F <sub>6</sub>	Et <sub>3</sub> SiH, DMAP	<i>d</i> <sub>8</sub> -THF	50 °C/ 2 days	1.2
<b>3.6a</b> (5 mol%)	C <sub>6</sub> F <sub>6</sub>	Et <sub>3</sub> SiH, PPh <sub>3</sub>	<i>d</i> <sub>8</sub> -THF	50 °C /2 days	5.4
<b>3.5</b> (20 mol%)	C <sub>6</sub> F <sub>6</sub>	Et <sub>3</sub> SiH	<i>d</i> <sub>8</sub> -THF	45 °C/ 4 days	2.5
<b>3.5</b> (20 mol%)	C <sub>6</sub> F <sub>6</sub>	Et <sub>3</sub> SiH	C <sub>6</sub> D <sub>6</sub>	45 °C/ 4 days	0.3
<b>3.5</b> (20 mol%)	C <sub>5</sub> F <sub>5</sub> N	Et <sub>3</sub> SiH	<i>d</i> <sub>8</sub> -THF	45 °C/ 4 days	3.6

too strong of a donor inhibits catalysis, likely through occupation of coordination sites necessary for reactivity. A summary of the catalysis results discussed above are shown in **Table 3.1**.

As solvent choice plays an important role in HDF catalysis, we postulated the structure of the operative species as the monomeric form of **3.6a** and sought to detect this species at higher temperatures. Heating a  $d_8$ -THF solution of **3.6a** to 60 °C only afforded small changes in the  $^1\text{H}$  NMR spectrum (**Figure 3.21**). Upon close inspection of the  $^1\text{H}$  NMR spectrum at 60 °C, a new

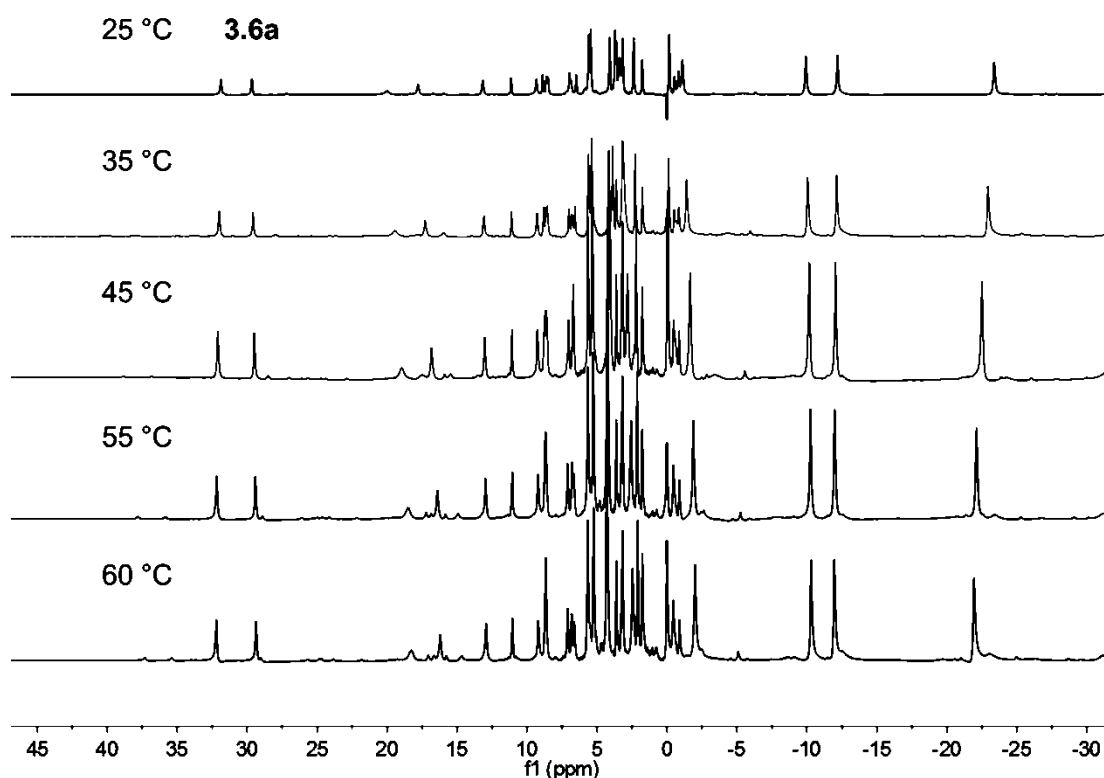


**Figure 3.21:** Stacked variable temperature for a  $d_8$ -THF solution of the dimeric iron hydride **3.6a**. There is not an appreciable difference in the spectra across the various temperatures recorded. Spectra collected at 400 MHz.

set of resonances at  $\delta$  37.3 and 35.4 are apparent. Cooling the NMR sample from 60 °C to 25 °C resulted in the disappearance of these two signals (**Figure 3.22**). These results suggest that at elevated temperature, dimeric **3.6a** may exist in equilibrium with its monomeric form.

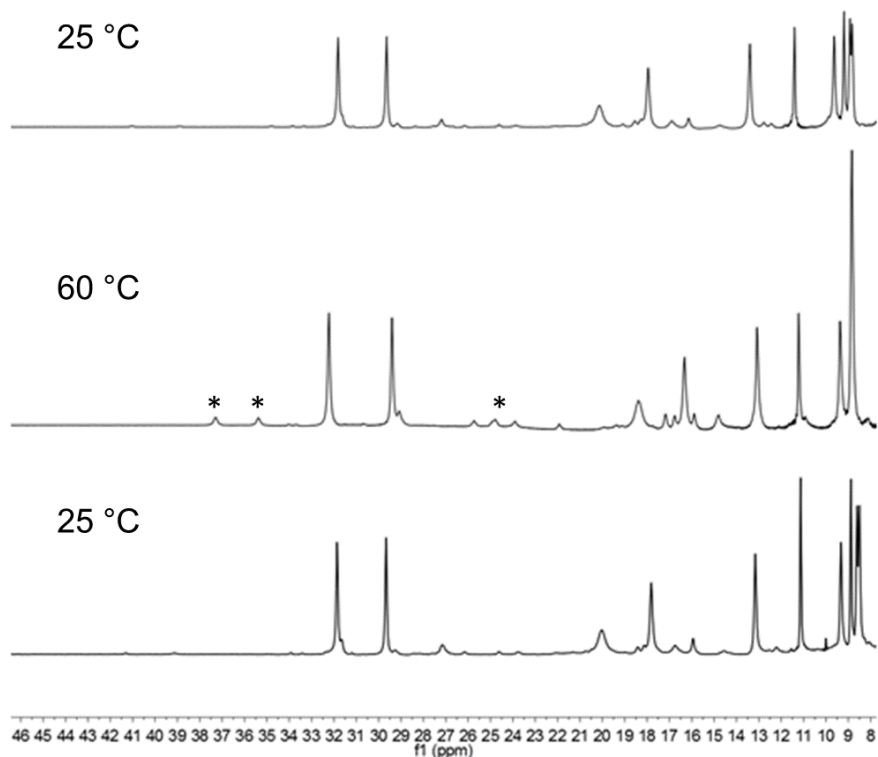


**Figure 3.22:** Stacked variable temperature for a  $d_8$ -THF solution of the dimeric iron hydride **3.6a**. This zoomed-in region shows a new set of resonances that appear at  $\delta$  37.3 and 35.4 at 60 °C, designated with “\*”. These same signals disappear upon cooling the NMR sample to 25 °C. Spectra collected at 400 MHz.

Having established **3.6a** as a precatalyst for HDF, the activity of the dimeric iron fluoride **3.14** was investigated. Unfortunately, employing the same conditions used for the HDF of  $C_6F_6$  with **3.6a** does not result in catalysis when starting with 5 mol % of **3.14** (TON = 0.8). The inactivity of **3.14** in comparison to **3.6a** is somewhat puzzling, and stands in contrast to the reactivity observed for the  $\beta$ -diketiminato system.<sup>149</sup> We suggest these differences arise from distinct solution state equilibria for the dissociation of dimeric species in THF. Further support for this hypothesis is illustrated by the lack of HDF activity reported for the dimeric  $\beta$ -diketiminato iron fluoride [ $(^{Me}NacNac^{DIPP})FeF$ ]<sub>2</sub>.<sup>149</sup>

The following section offers an examination of the reaction kinetics and  $^1\text{H}$  NMR spectra collected during catalysis in order to provide insight into potential mechanistic pathways during HDF.

### 3.4.2 Mechanistic Considerations

A series of kinetic experiments were performed for the HDF of pentafluoropyridine at  $50\text{ }^\circ\text{C}$  using precatalyst **3.6a** and  $\text{Et}_3\text{SiH}$  as the fluoride acceptor (**Table 3.2** and **Figure 3.23**).

**Table 3.2:** Parameters for Kinetic Investigation of  $\text{C}_5\text{F}_5\text{N}$  HDF

Entry	$[\text{Et}_3\text{SiH}]$ (M)	$[\text{C}_5\text{F}_5\text{N}]$ (M)	<b>[3.6a]</b> (M)	Rate ( $10^{-7}\text{ M s}^{-1}$ )
Reference	0.11	0.11	$5.5 \times 10^{-3}$	1.6(1)
[silane] $\times 2$	0.22	0.11	$5.5 \times 10^{-3}$	3.2(2)
[catalyst] $\times 2$	0.11	0.11	0.011	3.5(2)
[PyF] $\times 2$	0.11	0.22	$5.5 \times 10^{-3}$	1.8(1)
[silane] $\times 4$	0.44	0.11	$5.5 \times 10^{-3}$	6.7(3)

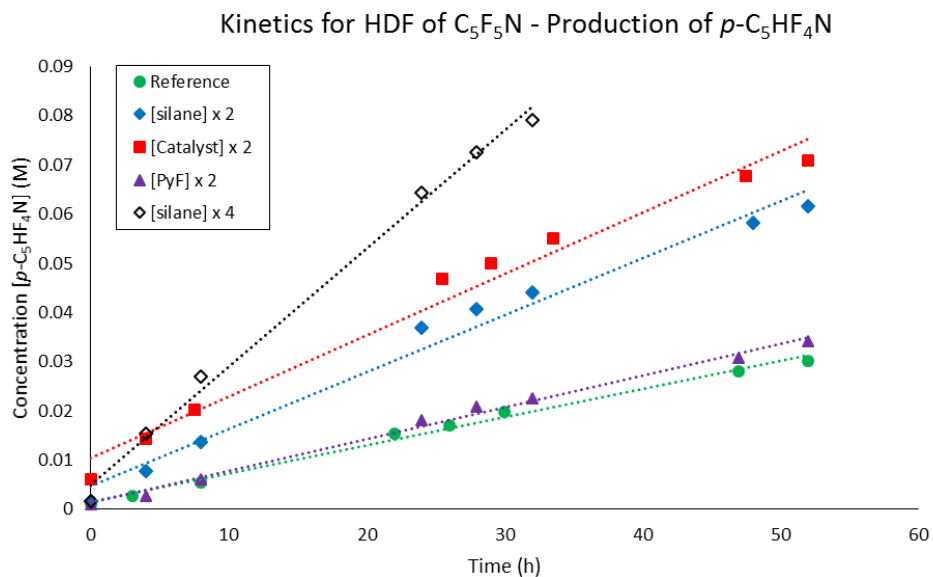


**Figure 3.23:** Progress of HDF for pentafluoropyridine showing the changes in rate due to changes in substrate concentration relative to a reference experiment with  $[\text{silane}] = [\text{PyF}] = 0.11\text{ M}$ ,  $[\text{Fe}] = 5.5 \times 10^{-3}\text{ M}$  using  $d_8\text{-THF}$  at  $50\text{ }^\circ\text{C}$ .

The production of 2,3,5,6-tetrafluoropyridine and fluorotriethylsilane was monitored by quantitative  $^{19}\text{F}$  NMR spectroscopy over the courses of two days. Due to the relative stability of the iron hydride precatalyst, the course of the reaction could be monitored over this time frame as the rate of reaction remained relatively constant. From a comparison of the reaction rates for the various kinetic runs, it can be seen that the reaction is first-order with respect to both the iron hydride **3.6a** (monomer) and  $\text{Et}_3\text{SiH}$  but is zero order with respect to pentafluoropyridine. The general rate law is shown in equation 3.2:

$$d[p\text{-C}_5\text{HF}_4\text{N}]/dt = k[\text{Et}_3\text{SiH}]^1[\mathbf{3.6a}]^1[\text{C}_5\text{F}_5\text{N}]^0 \quad (3.2)$$

The second order rate constant obtained from this equation is  $k = 2.8(1) \times 10^{-4} \text{ s}^{-1}\text{M}^{-1}$ . The rate law observed for HDF of  $\text{C}_5\text{F}_5\text{N}$  using **3.6a** is identical to that reported by Holland and coworkers for the hydrodefluorination of octafluorotoluene using the  $(^t\text{BuNacNac}^{\text{DIPP}})\text{FeF}$  catalyst **3.5**.<sup>149</sup> Interestingly, the initial amount of  $p\text{-C}_5\text{HF}_4\text{N}$  produced at  $t = 0$  for  $[\text{Fe}] \times 2$  is double that of the reference trial, whereas initial production of  $\text{Et}_3\text{SiF}$  for both the reference trial and  $[\text{Fe}] \times 2$  is zero. This observation is in agreement with the derived rate law, in which the iron hydride **3.6a** quickly reacts with  $\text{C}_5\text{F}_5\text{N}$  and the rate-determining step in catalysis involves silane.

Examination of the  $^1\text{H}$  NMR spectra collected during the various catalytic trials provides insight into the identity of the paramagnetic resting state. As seen in **Figure 3.24**, the paramagnetic species observed during each of the HDF catalytic trials remains unchanged regardless of the fluorinated substrate or silane utilized. The  $^1\text{H}$  NMR spectrum obtained from the trial using  $n\text{-BuSiH}_3$  as the fluoride acceptor did contain additional resonances not observed in the trials using  $\text{Et}_3\text{SiH}$  or  $\text{Ph}_3\text{SiH}$ , but the major species present is consistent with that observed in the other trials. Likewise, the same paramagnetic species is present in both the HDF

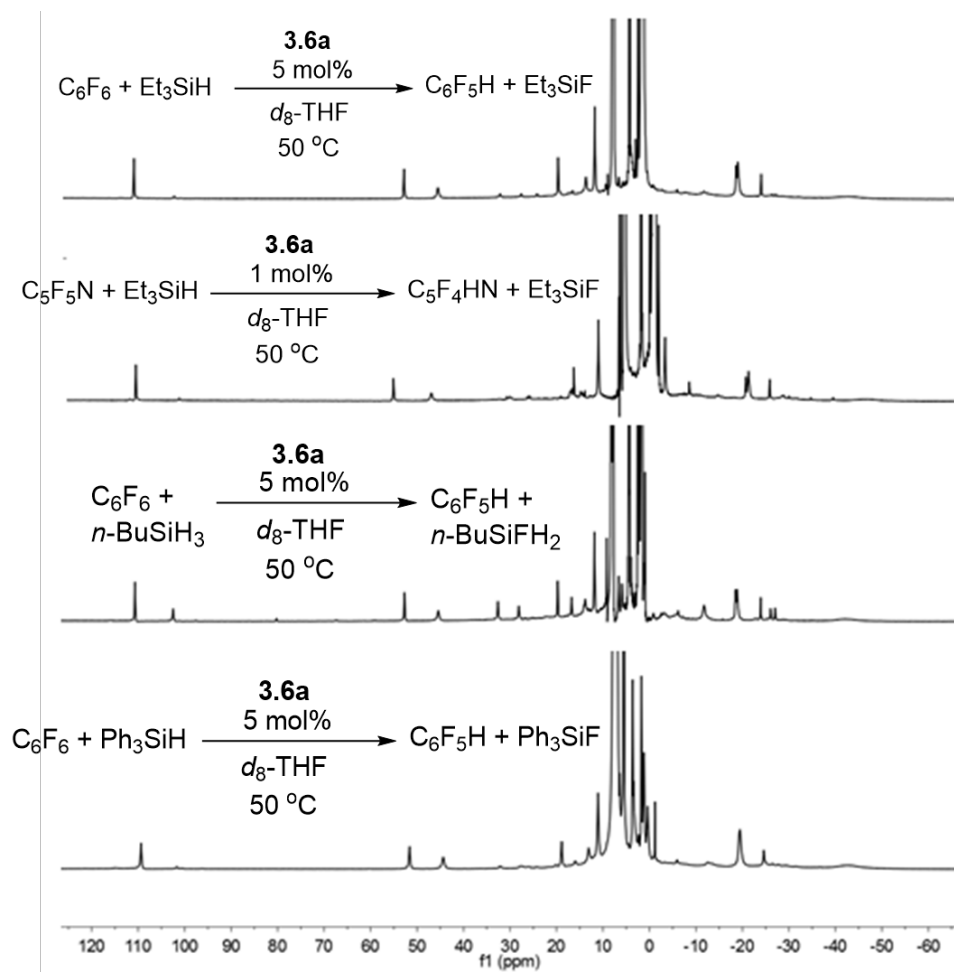


**Figure 3.24:** A comparison of the  $^1\text{H}$  NMR spectra collected at the final time points of various HDF catalytic runs using different substrates. With the exception of the trial utilizing  $n\text{-BuSiH}_3$  as the fluoride acceptor, all observed resonances are consistent between trials. This indicates that the HDF catalytic resting state is independent of the fluorinated substrate. All spectra collected in  $d_8\text{-THF}$  at 300 MHz at 25  $^\circ\text{C}$ .

catalysis for  $\text{C}_6\text{F}_6$  and  $\text{C}_5\text{F}_5\text{N}$ , indicating that the resting state does not have the fluorinated substrate coordinated to iron. As neither the identity of the fluorinated substrate nor the silane changes the paramagnetic resting state, we hypothesized that the resting state species is the iron fluoride complex **3.14**. However, comparison of the  $^1\text{H}$  NMR spectra for **3.6a**, **3.14**, and the

resting states obtained from HDF of  $C_6F_6$  with  $Et_3SiH$  utilizing **3.6a** and **3.14** as precatalysts rules out either **3.6a** and **3.14** as the resting state (**Figure 3.25**).

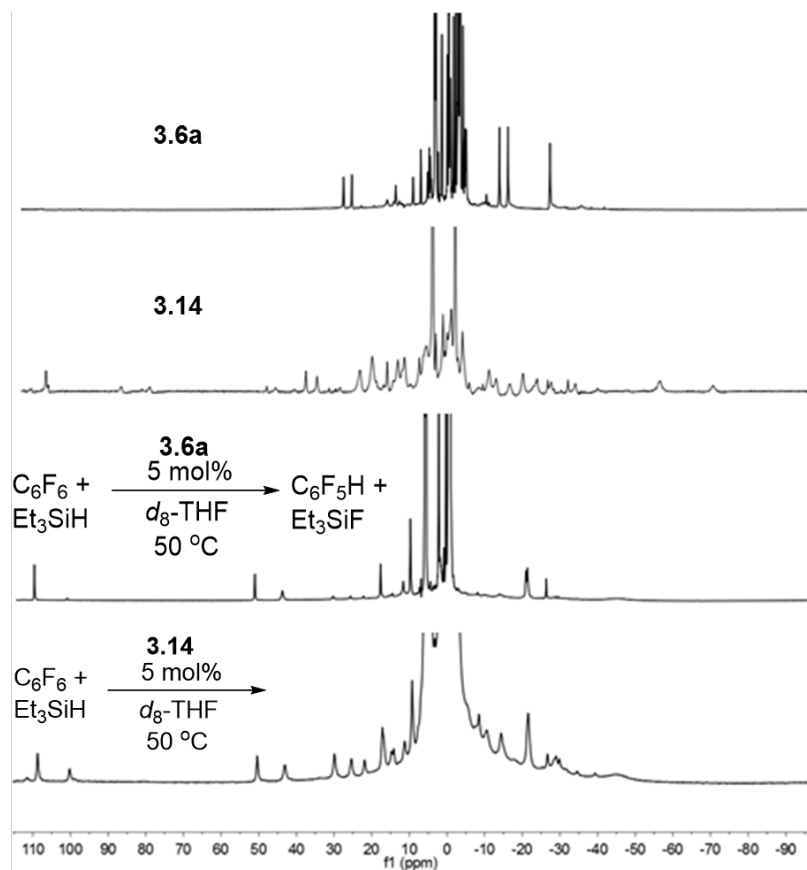


**Figure 3.25:** A comparison of the  $^1H$  NMR spectra for **3.6a**, **3.14**, and the final time points for the HDF catalytic runs (2 days) using **3.6a** and **3.14** as precatalysts. The resting state during catalysis is not the hydride species **3.6a**, nor apparently the fluoride species **3.14**. Spectra collected in  $d_8$ -THF at 300 MHz at 25 °C.

Interestingly, stepwise progression of HDF can be observed through sequential addition of reagents, seen in **Figure 3.26**. When one equivalent of  $C_6F_6$  was added to a  $d_8$ -THF solution of **3.6a** and heated to 50 °C for 1 day, nearly quantitative consumption of **3.6a** was achieved with concurrent formation of the catalytic resting state, as observed by  $^1H$  NMR spectroscopy. As only **3.6a** and  $C_6F_6$  were present to react, this observation refutes the results presented in **Figure**

**3.25.** The addition of one equivalent of  $\text{Et}_3\text{SiH}$  to this solution followed by heating to  $50\text{ }^\circ\text{C}$  for an additional day allows for the partial conversion of the catalytic resting state back to **3.6a**.

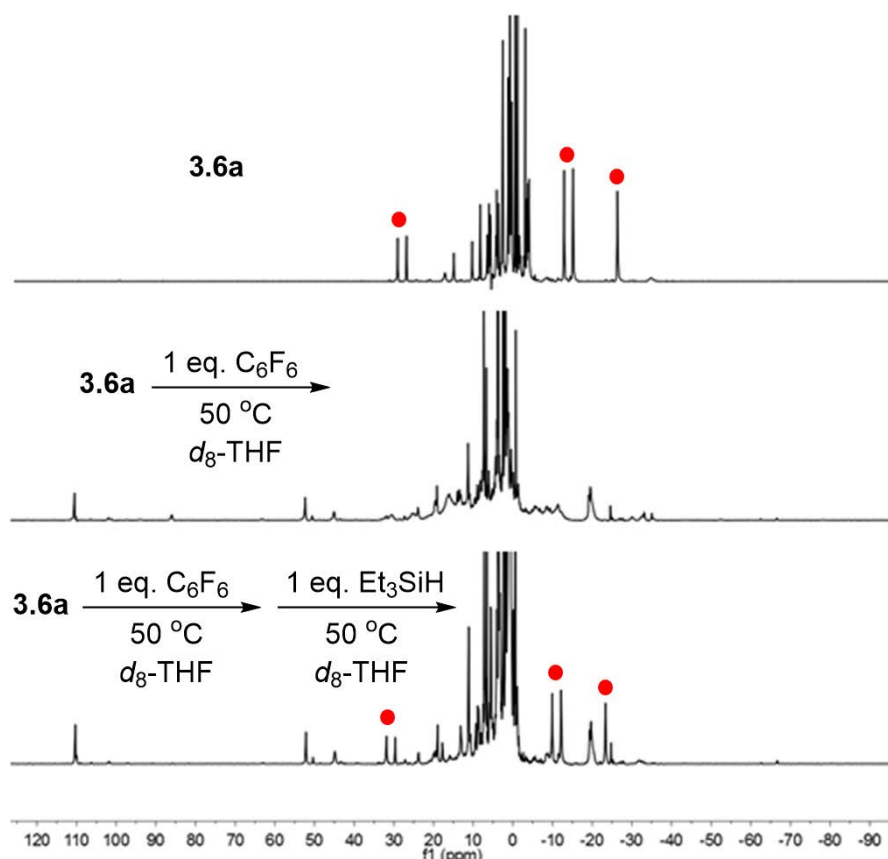
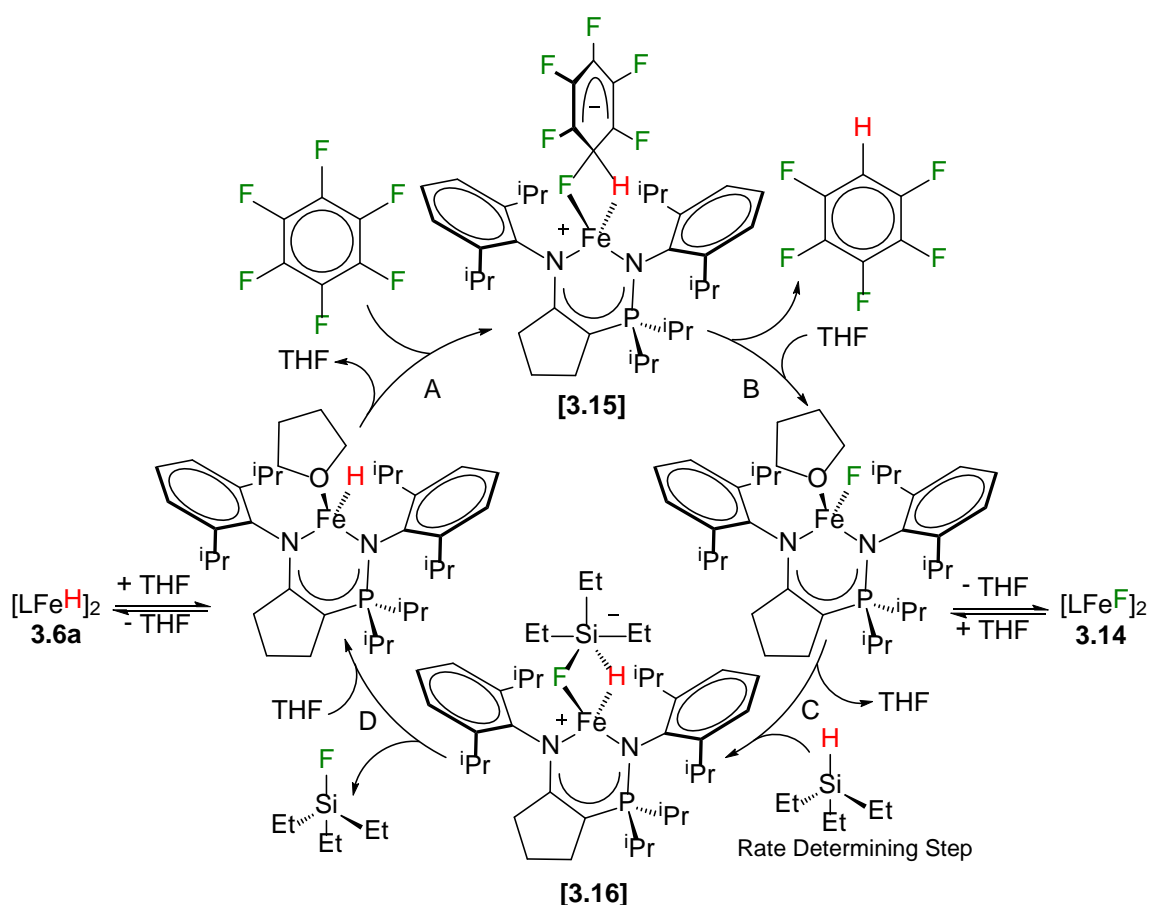


**Figure 3.26:**  $^1\text{H}$  NMR spectra for **3.6a** (top spectrum), the reaction between **3.6a** and  $\text{C}_6\text{F}_6$  (middle spectrum), and following reaction with  $\text{Et}_3\text{SiH}$  (bottom spectrum). Resonances belonging to the hydride **3.6a** are observed following the reaction with  $\text{Et}_3\text{SiH}$  are denoted with red circles. All spectra collected in  $d_8$ -THF at 300 MHz at  $25\text{ }^\circ\text{C}$ .

From the above  $^1\text{H}$  NMR spectroscopic observations and kinetics data, a proposed catalytic cycle is shown in **Scheme 3.10**. Although **Scheme 3.10** shows the HDF of  $\text{C}_6\text{F}_6$  with  $\text{Et}_3\text{SiH}$  as the fluoride acceptor, analogous cycles could be imagined for other fluorinated aromatics and silanes. An initial step in the cycle is the cleavage of dimeric **3.6a** into monomers, likely via the coordination and dissociation of THF. This process only occurs at elevated temperatures (recall **Figure 3.3** and **Figure 3.22**) and it is likely that dissociation of THF from

the monomeric species precedes nucleophilic attack. As shown previously in **Figure 3.23**, the reaction rate is independent of the concentration of  $C_5F_5N$ . The same zero-order dependence on the concentration of  $C_6F_5CF_3$  towards the reaction rate was reported by Holland and coworkers



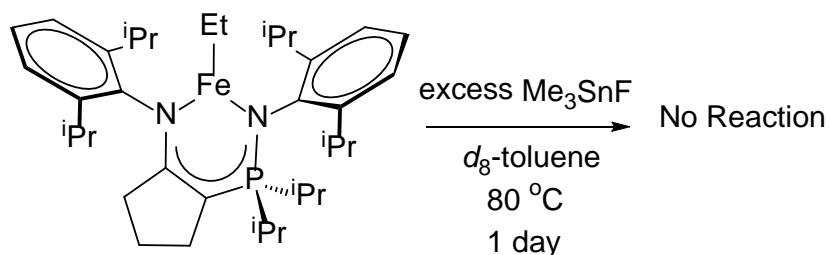
**Scheme 3.10:** A proposed catalytic cycle for HDF of  $C_6F_6$  with  $Et_3SiH$  as the fluoride acceptor.

with their iron fluoride precatalyst **3.5**.<sup>149</sup> It follows that step (A), the nucleophilic attack of the hydride on the fluorinated aromatic, is rapid. The observation by  $^{19}F$  NMR spectroscopy that defluorinated aromatics are produced before the formation of fluorosilane indicates that Meisenheimer species **[3.15]** is transient and step (B) is fast. The reaction rate showed a first order dependence on silane and iron concentration, similar to the  $\beta$ -diketimate system.<sup>149</sup> This dependence would indicate that monomeric **3.14** is the catalytic resting state and the reaction

with silane (C) is the rate determining step. While this is reported to be the case for the  $\beta$ -diketimate system, with the detection of **3.5** during HDF by  $^1\text{H}$  NMR spectroscopy,<sup>149</sup> it is inconsistent with the  $^1\text{H}$  NMR data for the enamido-phosphinimine system. The results presented in **Figure 3.26** rule out species [**3.16**] as the resting state, which indicates that step (D) is also rapid. Thus, additional confirmation regarding the identity of **3.14** and its dissociation in solution is necessary before definitive claims regarding the nature of the catalytic resting state can be made.

### 3.5 Attempts at an Alternate Synthesis for Iron(II) Fluoride Complexes

The conflicting  $^1\text{H}$  NMR data for **3.14** and the catalytic resting state is difficult to reconcile. Numerous attempts at the synthesis of **3.14** from direct treatment of **3.6a** with  $\text{C}_6\text{F}_6$  yielded similar inconsistent results. An alternate approach to the synthesis of **3.14** is through the transmetallation reaction between an iron(II) alkyl complex and an organotin fluoride. The attempted reaction between trimethyltin fluoride ( $\text{Me}_3\text{SnF}$ ) and the iron ethyl complex **3.8a** failed to form a new paramagnetic product (**Scheme 3.11**). A synthetic challenge



**Scheme 3.11:** The attempted transmetallation of **3.8a** with  $\text{Me}_3\text{SnF}$ .

encountered in the above reaction is the extreme insolubility of  $\text{Me}_3\text{SnF}$ , which is attributed to its polymeric nature in the solid state.<sup>160</sup> In fact,  $\text{Me}_3\text{SnF}$  is reportedly soluble in hot alcohols exclusively.<sup>160</sup> This observation is counter to the reported synthesis of the  $\beta$ -diketimate iron fluoride **3.5**, which is synthesized from the reaction of a NacNac iron methyl complex with

Me<sub>3</sub>SnF in toluene at 80 °C overnight.<sup>149</sup> The transmetallation process likely occurs on the surface of the solid Me<sub>3</sub>SnF, and perhaps the increased steric hindrance of the ethyl group in **3.8a** inhibits reactivity in comparison to the methyl group of the β-diketiminato complex. Future work for the preparations of enamido-phosphinimine iron(II) fluorides should investigate the reaction of a methyl analogue to **3.8a** with Me<sub>3</sub>SnF or perhaps the use of monomeric organotin fluorides, such as trimesityltin fluoride.<sup>161</sup> Alternatively, treatment of the iron bromide complex **2.23a** with silver(I) fluoride (AgF) may result in isolable **3.14**. This is a reported strategy for the synthesis of a Co(III) fluoride complex starting from a Co(III) iodide precursor.<sup>162</sup>

### 3.6 Conclusions

A dimeric iron(II) hydride species **3.6a** bearing the enamido-phosphinimine ligand scaffold was successfully synthesized by the treatment of the iron bromide complex **2.23a** with KBEt<sub>3</sub>H. However, the attempted synthesis of the less sterically hindered iron(II) hydride **3.6b** was less successful due to the high reactivity of **3.6b** towards the simultaneously produced BEt<sub>3</sub> by-product. Complex **3.6a** reacted with the unsaturated substrates azobenzene, 3-hexyne, and 1-azidoadamantane to yield the expected insertion products. Surprisingly, **3.6a** displayed reactivity towards the fluorinated aromatic compounds C<sub>6</sub>F<sub>6</sub> and C<sub>5</sub>F<sub>5</sub>N. Single crystals of the iron fluoride complex **3.14** were isolated from the reaction of **3.6a** with C<sub>6</sub>F<sub>6</sub>. This result stands in contrast to the lack of reactivity the β-diketiminato iron hydride systems display towards fluorinated aromatics. HDF catalysis was performed using 5 mol % loadings of precatalyst **3.6a** and a variety of silanes can act as fluoride acceptors without catalyst decomposition. The highest TON of 50 was observed for the HDF of C<sub>5</sub>F<sub>5</sub>N (1 mol % loading **3.6a**). Kinetic experiments highlighted the stability of the active catalytic species, as reaction rates were relatively linear over the course of 50 hours. The general rate law for HDF of C<sub>5</sub>F<sub>5</sub>N with the **3.6a** precatalyst

was in agreement with the rate law for HDF catalysis of  $C_6F_5CF_3$  reported for the  $\beta$ -diketiminato iron fluoride system. Both systems display a first order dependence on silane concentration, indicating that the reaction of a low-coordinate iron fluoride with silane is the rate-determining step in HDF. However, the  $^1H$  NMR spectra obtained for the catalytic resting states across multiple trials does not agree with the spectrum for **3.14**, making a definitive claim as to the identity of the resting state difficult. Future work should aim at an alternate synthesis of **3.14** to confirm its identity as the catalytic resting state. Likewise, further analysis of the HDF reaction using in situ ReactIR<sup>163</sup> could confirm the presence of an iron fluoride species. The possibilities for improvements to catalytic rate and turnover are numerous and could potentially be achieved through further steric modification of the enamido-phosphinimine scaffold.

## Chapter 4: Enamido-Phosphazide Complexes of Iron and Cobalt

### 4.1 Introduction

As discussed in **Chapter 1**, the Staudinger reaction is a convenient route for the synthesis of phosphinimines from phosphines and organic azides.<sup>51</sup> During the course of the Staudinger reaction, a phosphazide intermediate is formed that undergoes a four-membered ring transition state in order to expel N<sub>2</sub> and form a bond between phosphorus and the distal nitrogen atom of the organic azide.<sup>51-52</sup> Under particular constraints, the phosphazide intermediate can be trapped, usually through the use of sterically hindered phosphines and/or azides.<sup>57, 164-166</sup> Other methods for trapping the phosphazide intermediate employ electronic stabilization,<sup>167</sup> coordination to a metal center<sup>168-170</sup> or a Lewis acid,<sup>171-172</sup> and the presence of hydrogen bonding.<sup>173</sup>

Transition metal complexes featuring phosphazide ligands are rare, with the few reported examples shown in **Figure 4.1**. The phosphazide ligands in the nickel and iron complexes **4.1**

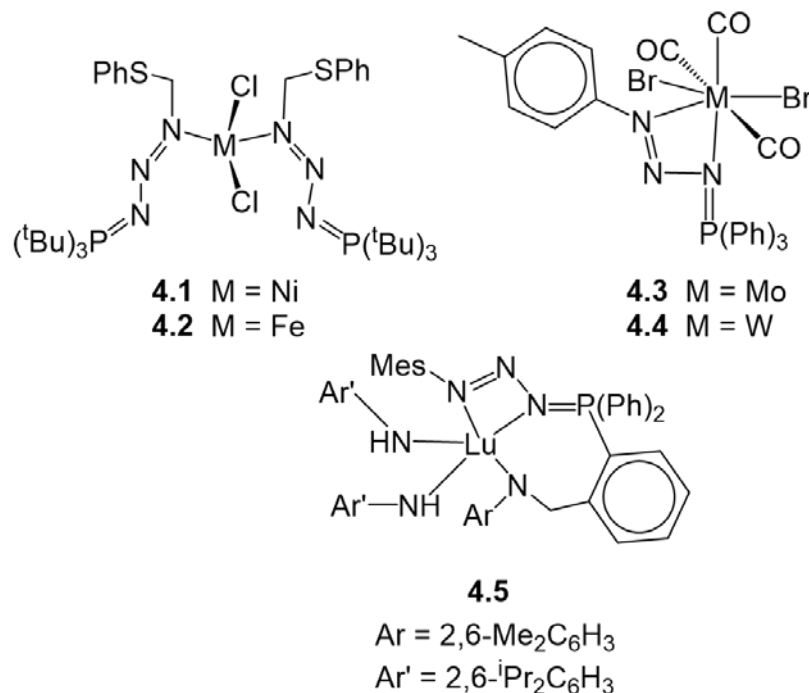


**Figure 4.1:** The only literature reported transition metal phosphazide complexes. **4.1** and **4.2** see ref. 169. **4.3** and **4.4** see ref 168. **4.5** see ref. 174.

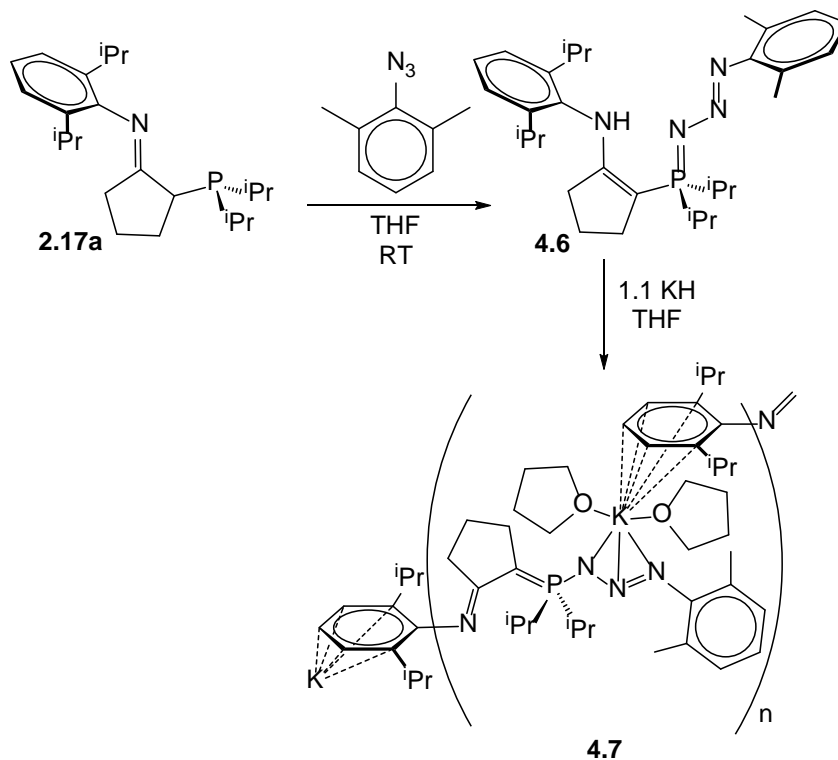
and **4.2** act as monodentate donors, with the distal nitrogen of the phosphazide coordinated to the metal. Steric hindrance at the phosphorus has been invoked as the governing feature that forces the phosphazides in **4.1** and **4.2** to coordinate in a  $\kappa^1$  bonding mode.<sup>169</sup> In contrast, the molybdenum, tungsten, and lutetium complexes **4.3**, **4.4**, and **4.5**, respectively, feature the phosphazide in a  $\kappa^3$  coordination mode.<sup>168, 174</sup> The reactivity of the above phosphazide complexes is unreported, with only **4.5** being used in catalysis for the formation of 1,2,3-triazoles from the cycloaddition of organic azides with alkynes.<sup>174</sup>

During the course of the enamine-phosphinimine ligand synthesis reported in Chapter 2, it was observed that enamine-phosphazide species could be stabilized and isolated. Due to the unexplored reactivity of transition metal phosphazide complexes, the coordination chemistry and subsequent reactivity of enamido-phosphazide complexes of iron and cobalt was investigated.

## 4.2 Enamido-Phosphazide Synthesis

Similar to the general ligand synthesis described in Chapter 2.2.1, imine-phosphine **2.17a** was treated with 2,6-dimethylphenylazide at ambient temperature to generate the enamine-phosphazide **4.6** (Scheme 4.1). Compound **4.6** displays solution state properties reminiscent of the enamine-phosphazide **2.20** described in Chapter 2.2.1. Most notably the presence of a  $^{31}\text{P}\{^1\text{H}\}$  NMR chemical shift of  $\delta$  50.9, as well as an N-H resonance in the  $^1\text{H}\{^{31}\text{P}\}$  NMR spectrum located at  $\delta$ 10.9. The solid-state molecular structure of **4.6** (Figure 4.2) confirms the presence of the phosphazide moiety. The phosphazide is in the *s-trans* geometry, likely due to the bulk of the aryl unit and the isopropyl substituents at the phosphorus center. In addition, the presence of the hydrogen bond between the enamine N-H and N2 of the triaza unit likely adds to the stability of the phosphazide; the distance between H1 and N2 is 2.046(16) Å. Also consistent

with the enamine-phosphazide formalism are the short C1–C2 (1.3668(13) Å), P1–N2 (1.6393(9) Å), and N3–N4 (1.2665(11) Å) bond lengths, which are best described as double bonds.



**Scheme 4.1:** Synthetic scheme for the formation of the enamine-phosphazide **4.6** and its deprotonation with KH to form the polymeric ligand potassium salt **4.7**.

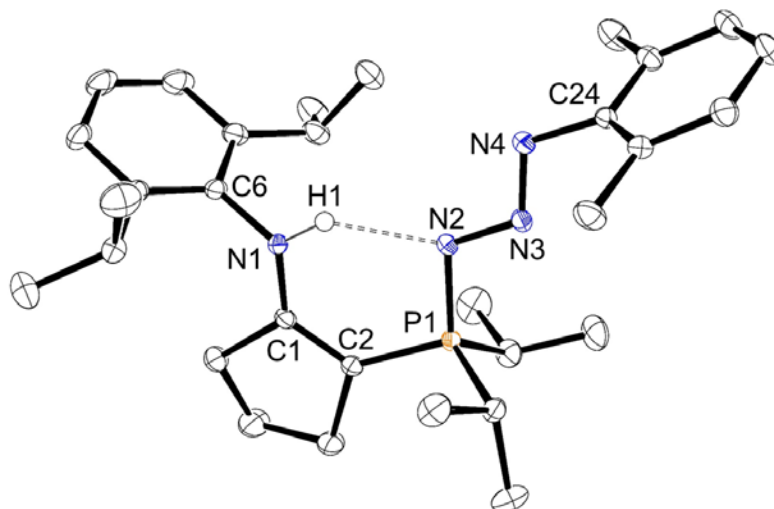


**Figure 4.2:** ORTEP drawing of the solid-state molecular structure of **4.6** (ellipsoids at 50% probability level). All hydrogen atoms except for H1 have been omitted for clarity. H1 was located in the difference map. Selected bond lengths (Å) and angles (deg): N1-C1: 1.3657(12), C1-C2: 1.3668(13), C2-P1: 1.7540(10), P1-N2: 1.6393(9), N2-N3: 1.3583(11), N3-N4: 1.2665(11), H1...N2: 2.046(16), C1-N1-C6: 122.10(8), N1-C1-C2: 128.07(9), C2-P1-N2: 105.37(4), P1-N2-N3: 110.29(6), N2-N3-N4: 112.92(8), N3-N4-C24: 111.18(8).

Enamine-phosphazide **4.6** was deprotonated by KH in THF to generate the potassium salt **4.7**. Complex **4.7** displays a singlet resonance at  $\delta$  44.2 in the  $^{31}\text{P}\{^1\text{H}\}$  NMR spectrum, only slightly upfield-shifted from the starting phosphazide at  $\delta$  50.9. The N-H resonance at  $\delta$  10.9 observed for **4.6** is absent in the  $^1\text{H}\{^{31}\text{P}\}$  NMR spectrum for **4.7**. Analysis of **4.7** by X-ray diffraction revealed that the  $\text{K}^+$  ion binds in a  $\kappa^3$  fashion to the triaza portion of the molecule, as shown in **Figure 4.3**. The X-ray structure also indicates that **4.7** is polymeric in the solid-state. However, the solubility of **4.7** in aromatic solvents suggests loss of this intermolecular interaction in solution. Conjugation in **4.7** is localized between N1-C1-C2, as the bond lengths for N1-C1 (1.320(3) Å) and C1-C2 (1.405(3) Å) are between single and double bonds. In addition, the bond metrics between P1-N2, N2-N3, and N3-N4 are consistent with the neutral phosphazide **4.6**, indicating that conjugation is absent in this portion of the molecule.

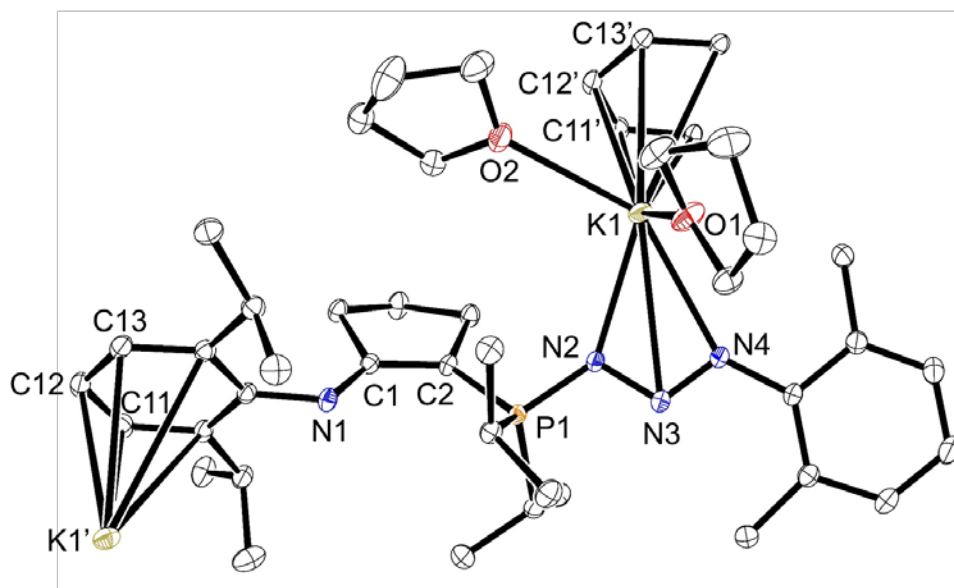


**Figure 4.3:** ORTEP drawing of the solid-state molecular structure of **4.7** (ellipsoids at 50% probability level). All hydrogen atoms have been omitted for clarity. Selected bond length (Å), angles (deg), and torsion angles (deg): K1-N2: 2.715(2), K1-N3: 3.288(2), K1-N4: 2.860(2), K1-O1: 2.675(2), K1-O2: 2.860(2), K1-C13': 3.228(3), K1-C12': 3.107(3), K1-C11': 3.257(3), N1-C1: 1.320(3), C1-C2: 1.405(3), C2-P1: 1.729(2), P1-N2: 1.660(2), N2-N3: 1.342(3), N3-N4: 1.276(3), P1-N2-N3: 112.5(2), N2-N3-N4: 111.3(2), N1-C1-C2-P1: 0.8(4), C1-C2-P1-N2: 149.2(2), P1-N2-N3-N4: 6.6(2).

Having successfully deprotonated the enamide-phosphazide ligand scaffold, investigations into the coordination chemistry of the anionic enamido-phosphazide **4.7** with iron and cobalt was pursued.

### 4.3 Synthesis of an Iron(II) Phosphazide Complex and Hydride Metathesis Reactivity

The salt metathesis reaction of **4.7** with  $\text{FeBr}_2(\text{THF})_2$  results in the clean formation of the corresponding adduct **4.8**. The solid-state structure for **4.8** clearly shows that the enamido-phosphazide ligand scaffold coordinates in a bidentate mode, with only the  $\alpha$ -nitrogen (N2) of the triaza unit bound to Fe (**Figure 4.4**). The geometry at the Fe(II) center is tetrahedral with both Fe–N bond distances nearly identical at 2.04 Å. The combination of a proximal enamido to the phosphazide unit generates a six-membered chelate ring geometry. Iron complex **4.8** is

paramagnetic with  $\mu_{\text{eff}}=4.8 \mu_{\text{B}}$  (4 unpaired electrons) based on the Evans method and 12 resonances are observed in the  $^1\text{H}$  NMR spectrum. Based on the relatively low number of  $^1\text{H}$  NMR resonances observed, **4.8** is likely fluxional in solution.

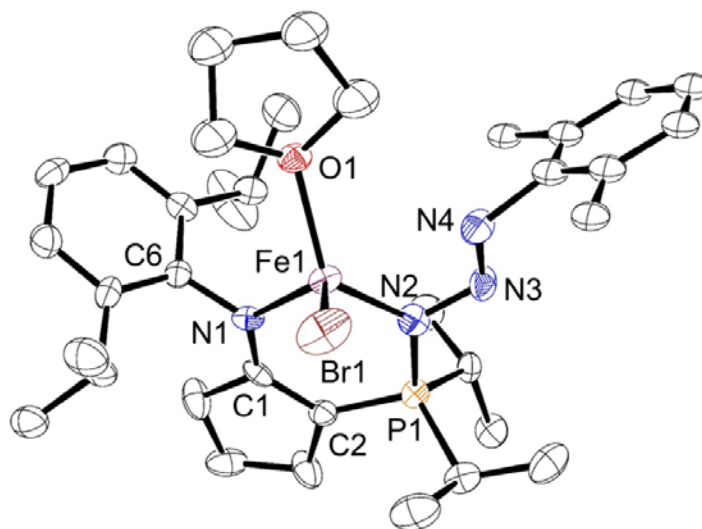
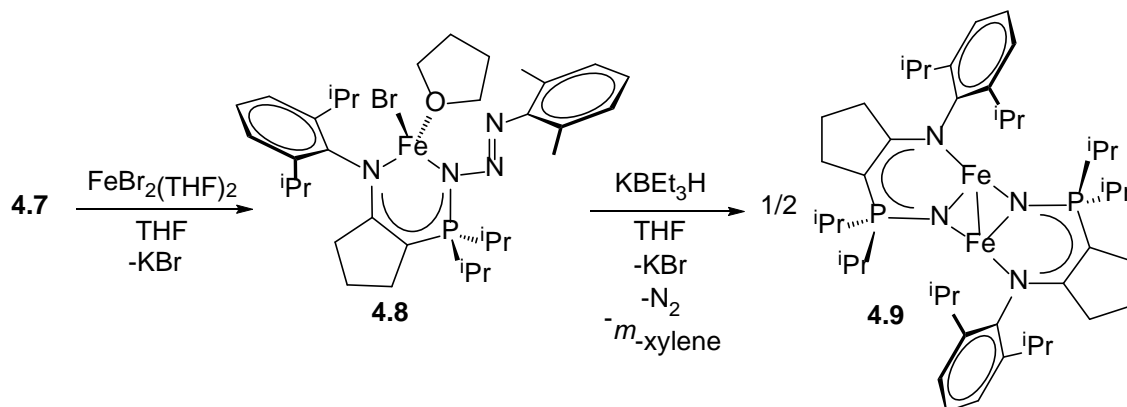


**Figure 4.4:** ORTEP drawing of the solid-state molecular structure of **4.8** (ellipsoids at 50% probability level). All hydrogen atoms have been omitted for clarity. Selected bond length ( $\text{\AA}$ ) and angles (deg): Fe1-N1: 2.032(7), Fe1-N2: 2.039(7), Fe1-Br1: 2.417(2), Fe1-O1: 2.122(5), N1-C1: 1.348(10), C1-C2: 1.398(12), C2-P1: 1.726(9), P1-N2: 1.660(7), N2-N3: 1.354(9), N3-N4: 1.285(9), N1-Fe1-N2: 89.7(3), N1-Fe1-Br1: 121.5(2), N2-Fe1-Br1: 115.2(2), C1-N1-C6: 116.8(7), N1-C1-C2: 128.3(8), C1-C2-P1: 128.1(6), P1-N2-N3: 114.3(6), N2-N3-N4: 108.9(7).

Complex **4.8** was treated with  $\text{KBET}_3\text{H}$  to investigate if dimeric hydride species analogous to those reported in Chapter 3 could be isolated with the phosphazide ligand scaffold. The addition of a THF solution of  $\text{KBET}_3\text{H}$  to a THF solution of **4.8** resulted in an immediate color change of the solution from orange to dark brown, with the new paramagnetic iron complex **4.9** isolated in low yields (**Scheme 4.2**). The new species **4.9** can also be obtained through using toluene as the reaction solvent, though yields are lower than in THF solution. The solid-state structure of **4.9**, as shown in **Figure 4.5**, indicates that the product of the reaction with

$\text{KBET}_3\text{H}$  is a dimeric species with bridging phosphinimido units. The Fe–Fe distance of 2.4996(9) Å is close to the single bond Fe–Fe value of 2.48 Å,<sup>175</sup> indicating that **4.9** contains a Fe–Fe bond.



**Scheme 4.2:** Iron complex **4.8** is synthesized through the salt metathesis reaction between the ligand potassium salt **4.7** with  $\text{FeBr}_2(\text{THF})_2$ . The reaction of **4.8** with  $\text{KBET}_3\text{H}$  yields the dimeric phosphinimido complex **4.9**.

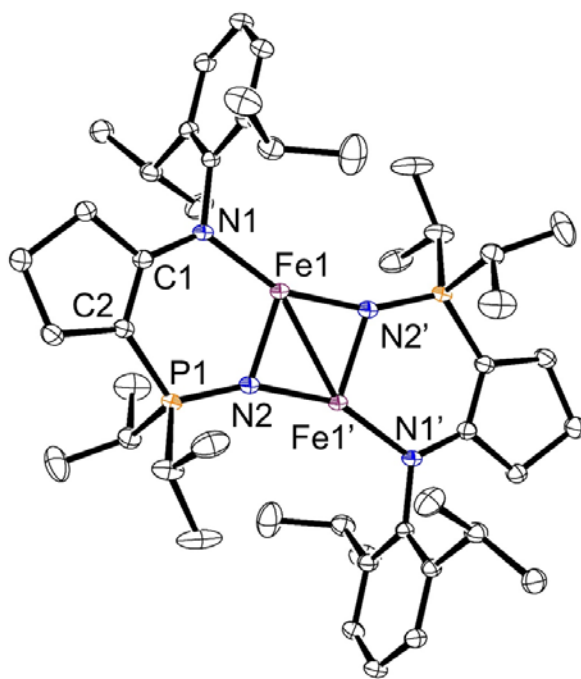


**Figure 4.5:** ORTEP drawing of the solid-state molecular structure of **4.9** (ellipsoids at 50% probability level). All hydrogen atoms have been omitted for clarity. Selected bond length (Å) and angles (deg): Fe1–N1: 1.9303(13), Fe1–N2: 1.9247(13), Fe1–N2': 1.8678(14), Fe1–Fe1': 2.4996(9), N1–C1: 1.3578(17), C1–C2: 1.3809(17), C2–P1: 1.7654(14), P1–N2: 1.5847(13), N1–Fe1–N2: 107.11(5), Fe1–N2–Fe1': 82.44(5), N2–Fe1–N2': 97.55(5), C2–P1–N2: 113.94(7).

The solution state behavior of **4.9** is also indicative of a Fe–Fe bond. First, the measured magnetic moment in solution for the dimer is  $3.1 \mu_B$ , which is consistent with two high spin Fe(II) centers that are strongly antiferromagnetically coupled. Second, the  $^1\text{H}$  NMR spectrum has a very narrow spectral width in which the 10 resonances for **4.9** fall between  $\delta$  12.3 and -3.0, while still containing features supporting the presence of a paramagnetic species, such as lack of proton-proton coupling. As has been reported elsewhere in this thesis, dimeric paramagnetic species are typically represented by  $^1\text{H}$  NMR spectra in which the spectral window for the paramagnetically shifted resonances is narrower than monomeric paramagnetic species. Complex **4.9** has the narrowest  $^1\text{H}$  NMR spectrum of any paramagnetic compound reported in this thesis, providing further support for the strong antiferromagnetic coupling that exists through the presence of the Fe–Fe bond.

During the course of the conversion of **4.8** to **4.9**, the phosphazide unit of the ligand scaffold in **4.8** is converted into a phosphinimido moiety in **4.9** through loss of  $\text{N}_2$  and *m*-xylene ( $1,3\text{-Me}_2\text{C}_6\text{H}_4$ ). When the reaction was performed with  $\text{KBET}_3\text{D}$  as a deuteride source in protio-THF, no deuterium incorporated into xylene was observed (though  $\text{D}_2$  gas was detected by  $^2\text{H}$  NMR spectroscopy) (**Figure 4.6**). However, when the reaction was performed in  $d_8$ -THF with

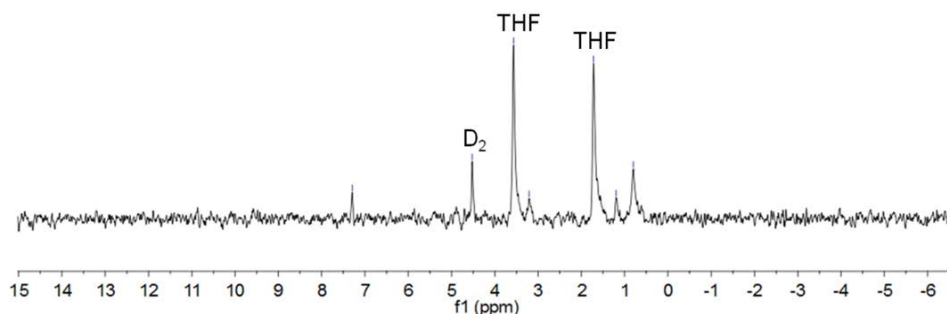


**Figure 4.6:**  $^2\text{H}$  NMR spectrum for the reaction of complex **4.8** with  $\text{KBET}_3\text{D}$  in a sealed J. Young tube with protio-THF as the solvent.  $\text{D}_2$  is observed at  $\delta$  4.52. The natural abundance of  $^2\text{H}$  in THF gave the observed THF signals (400 MHz, THF, 298 K).

$\text{KBEt}_3\text{H}$ , 2- $d_1$ -xylene was generated as confirmed by GC-MS and  $^{13}\text{C}\{^1\text{H}\}$  spectroscopy (**Figure 4.7** and **Figure 4.8**, respectively). On the basis of these two experiments (**Scheme 4.3**), a direct

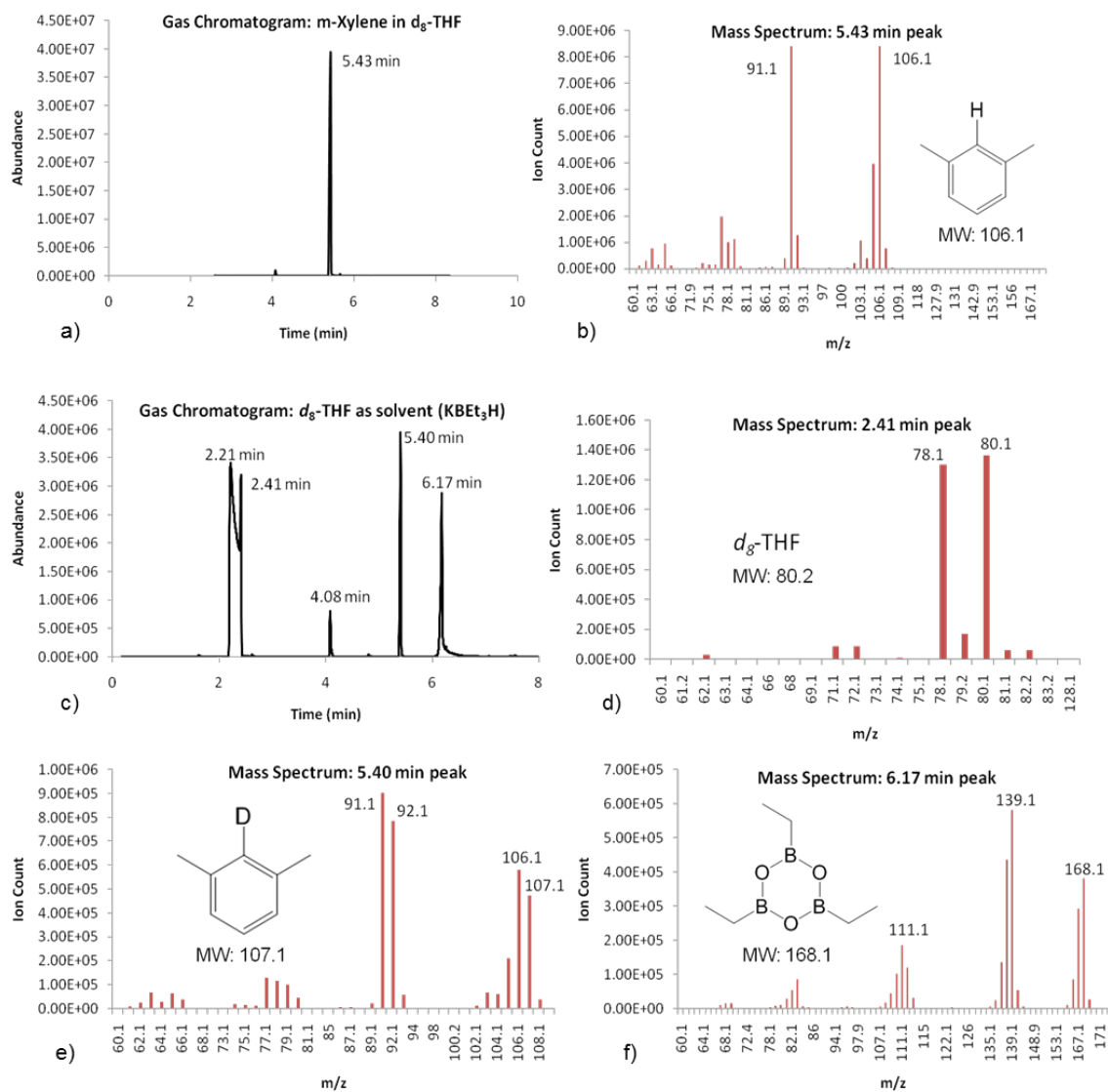


**Figure 4.7:** Gas chromatogram (a) and corresponding mass spectrum (b) obtained from a sample of authentic  $m$ -xylene dissolved in  $d_8$ -THF to act as a control. Gas chromatogram (c) and corresponding mass spectra obtained from the volatiles isolated from the reaction of complex **4.8** with  $\text{KBEt}_3\text{H}$  in  $d_8$ -THF. The peak at 5.40 minutes in the GC corresponds to 2- $d_1$ -xylene. Note the signal intensity of the mass peak 107.1 for  $m$ -xylene (e) to that found in (b). The species observed at 6.17 minutes in the GC is from triethylborane (a by-product of the reaction) having reacted with water vapor in air. The observed mass spectrum (f) matches the predicted spectrum for 2,4,6-triethylboroxin.

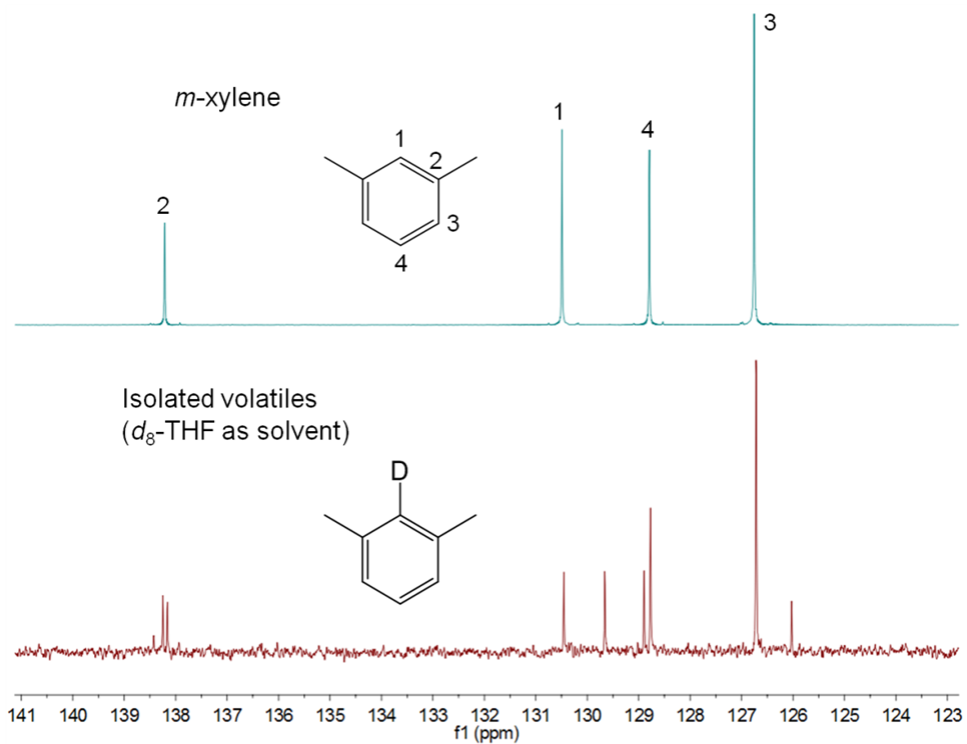
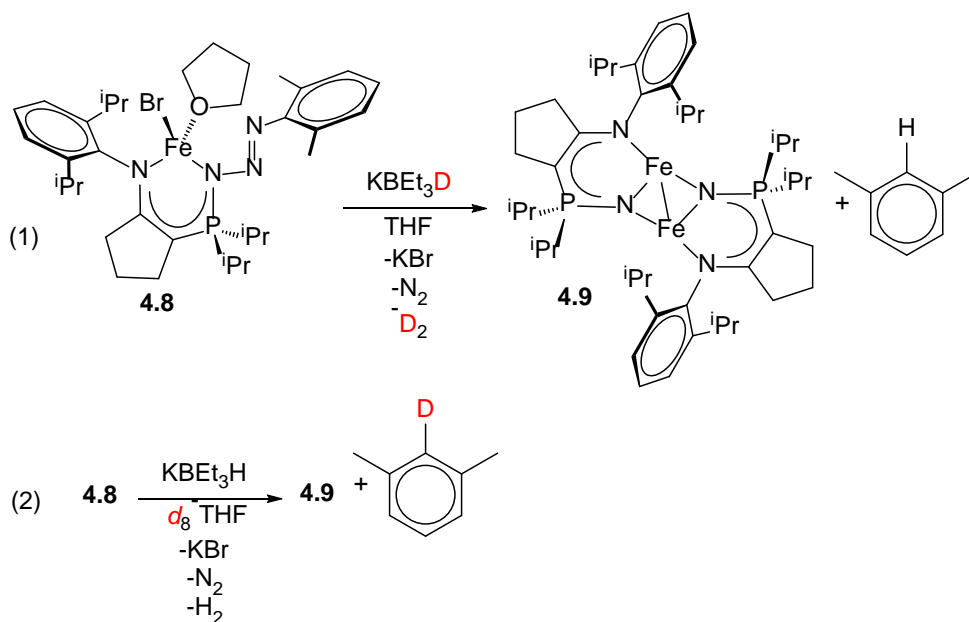


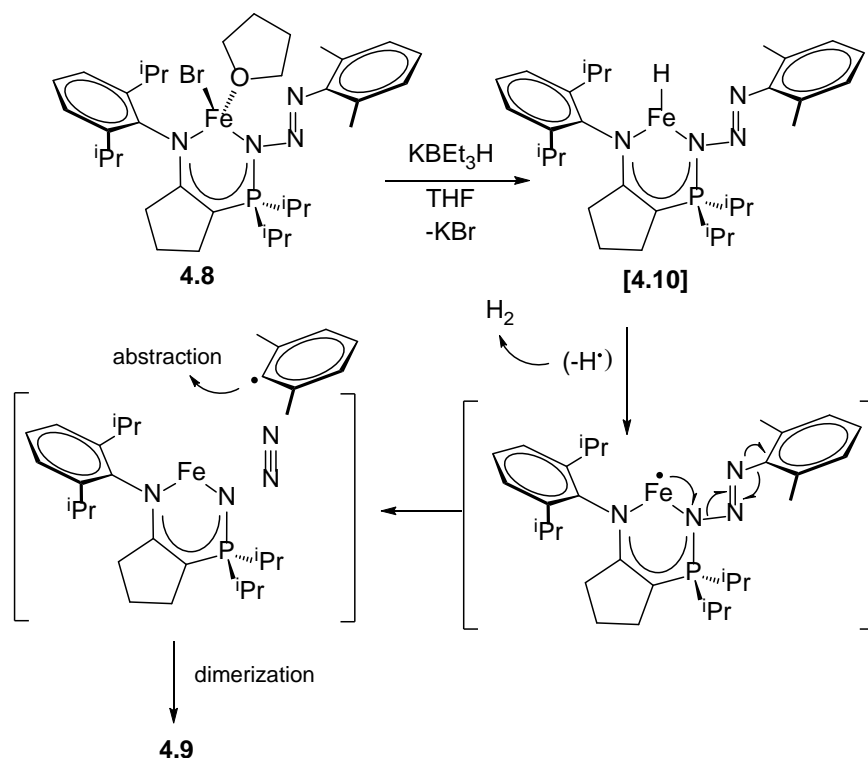
**Figure 4.8:**  $^{13}\text{C}\{^1\text{H}\}$  NMR (aromatic region) comparison of *m*-xylene (top) to the isolated volatiles ( $d_8$ -THF as solvent) from the radical trapping experiment (bottom) (**Scheme 4.3** in text). The  $^1\text{H}$ - $^{13}\text{C}$  HSQC of *m*-xylene was used to confirm deuterium incorporation (1:1:1 triplet) at carbon position 1 in  $1-d_1$ -2,6- $\text{Me}_2\text{C}_6\text{H}_3$  (400 MHz,  $d_8$ -THF, 298 K).



**Scheme 4.3:** The two deuterium labeling experiments used to propose the reaction mechanism for the conversion of **4.8** to **4.9**. Analysis of the products formed from the reaction of **4.8** with  $\text{KBET}_3\text{D}$  in proteo-THF by  $^2\text{H}$  NMR spectroscopy and GC/MS indicated that deuterium was not incorporated into *m*-xylene, but rather was lost as  $\text{D}_2$  (Reaction 1). Treatment of **4.8** with  $\text{KBET}_3\text{H}$  in  $d_8$ -THF yielded 1- $d_1$ -2,6- $\text{Me}_2\text{C}_6\text{H}_3$ , as observed by  $^{13}\text{C}\{^1\text{H}\}$  NMR spectroscopy and GC/MS (Reaction 2).

reaction between the hydride and the C–N bond of the coordinated phosphazide unit, or even intramolecular H-transfer from the Fe center to the ipso carbon of the arylazido unit, can be ruled out. Instead, it appears as though a radical process generates an aryl radical at the 2-position of xylene, which subsequently abstracts a hydrogen or a deuterium from the solvent. One possible process is shown in **Scheme 4.4**, which involves the formation of the putative hydride [**4.10**], followed by elimination of  $\text{H}^\bullet$ , detected as  $\text{H}_2$  (or  $\text{D}_2$  for the reaction with  $\text{KBET}_3\text{D}$ ). Although [**4.10**] is shown as mononuclear, a dinuclear hydride bridged complex might facilitate  $\text{H}_2$  formation by combination of 2  $\text{H}^\bullet$ . A one-electron cascade then starts with a Fe(I) center and results in the generation of  $\text{N}_2$  and xylanyl radical and the subsequent H or D abstraction from the proteo or deuterio solvent, producing *m*-xylene or 2- $d_1$ -xylene, respectively. Alternatively, the

ArNN<sup>•</sup> radical may eliminate first, which then goes on to form Ar<sup>•</sup> and N<sub>2</sub>.<sup>176</sup> Once formed, the sterically unencumbered imine-phosphinimido Fe(II) complex dimerizes to form **4.9**.



**Scheme 4.4:** A possible radical pathway leading to the conversion of the phosphinimido complex **4.9** from the phosphazide complex **4.8** upon reaction with the hydride reagent  $\text{KBEt}_3\text{H}$ .

A comparison between the electronic environments present at the Fe center in **4.8** to **4.9** was carried out with zero-field  $^{57}\text{Fe}$  Mössbauer spectroscopy (**Figure 4.9**). The tetrahedral Fe(II) phosphazide complex **4.8** has an isomer shift of  $\delta = 0.92$  mm/s and quadrupole splitting  $\Delta E_Q = 2.40$  mm/s. The observed isomer shift value of 0.92 mm/s is similar to the isomer shift value for a wide range of reported tetrahedral Fe(II) complexes that typically have an average value of 0.88 mm/s.<sup>177-178</sup> The dimeric species **4.9** has a lower  $\delta$  value of 0.34 mm/s and a  $\Delta E_Q$  value of 1.26 mm/s. The low isomer shift value for **4.9** is consistent with other literature reported species featuring low-coordinate Fe, which typically have a  $\delta$  range between 0.18-0.65.<sup>179-181</sup> However,

the ligand environment in these species varies significantly, making a direct comparison with **4.9** difficult.

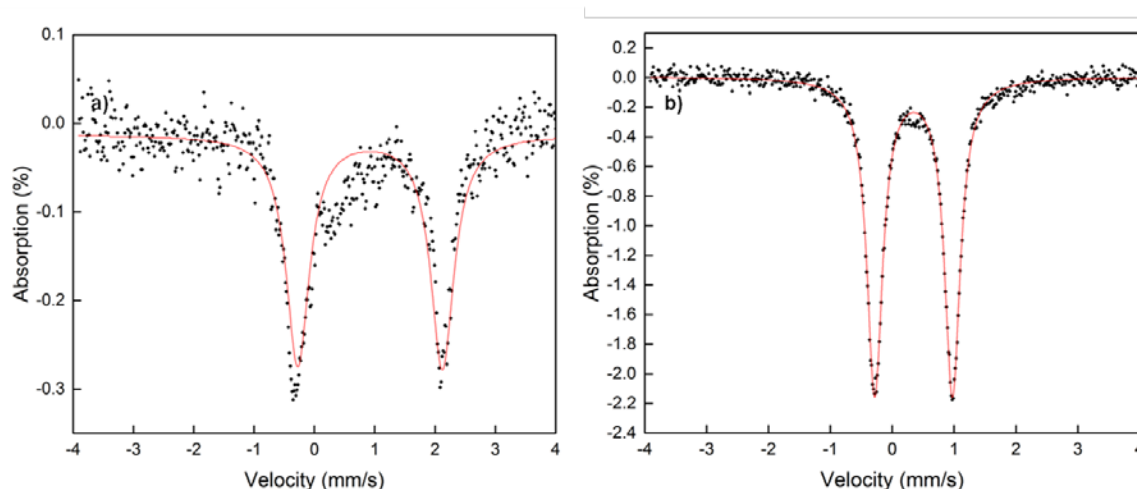


**Figure 4.9:**  $^{57}\text{Fe}$  Mössbauer spectra for powdered samples obtained at 295 K. Complex **4.8** (a); dimeric species **4.9** (b). Solid red lines correspond to simulated data. The spectrum of **4.8** was fit as a quadrupole doublet with  $\delta = 0.92 \text{ mms}^{-1}$  and  $\Delta E_{\text{q}} = 2.40 \text{ mms}^{-1}$ . The signal intensity for **4.8** is consistently weak, even after over 10 days collection due to a poor recoil-free fraction. The symmetric dimer **4.9** can be fit as a single quadrupole doublet with  $\delta = 0.34 \text{ mms}^{-1}$  and  $\Delta E_{\text{q}} = 1.26 \text{ mms}^{-1}$  for the equivalent iron centers.

The unexpected reactivity of the phosphazide complex **4.8** with  $\text{KBET}_3\text{H}$  begged the question whether other base metal phosphazide complexes could be synthesized and if arrival at similar species with metal-metal bonds could be achieved. Thus, attention was focused on the coordination of cobalt to the phosphazide ligand **4.6**.

#### 4.4 Cobalt Enamido-Phosphazide Complexes

The salt metathesis reaction between the phosphazide potassium salt **4.7** and the pyridine adduct of cobalt(II) chloride,  $\text{CoCl}_2(\text{Py})_4$ , afforded highly crystalline, green cobalt phosphazide complex **4.11**. X-ray quality single crystals of **4.11** were grown from a THF solution cooled to  $-35 \text{ }^\circ\text{C}$  and the solid-state molecular structure shown in **Figure 4.10** confirms coordination of the phosphazide to cobalt. The bond metrics present in the ligand scaffold are nearly identical to

those observed for the Fe analogue **4.8**, though the contacts of N1-Co1 (1.9845(17) Å) and N2-Co1 (1.9899(18) Å) are shorter than the corresponding bond distances to iron, Fe1-N1 (2.032(7) Å) and Fe1-N2 (2.039(7) Å). In addition, the bite angle for N1-Co1-N2 of 98.30(7)° is larger than that observed for **4.8**, which has an N1-Fe1-N2 bite angle of 89.7(3)°.

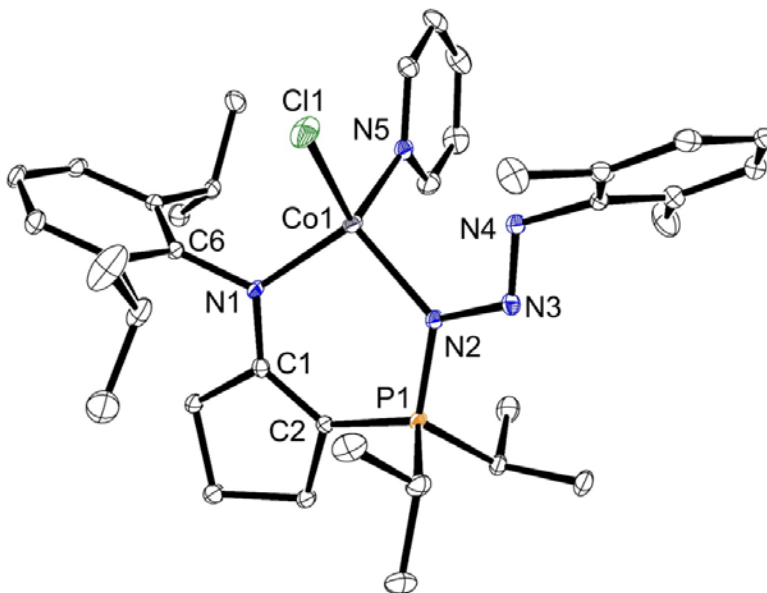


**Figure 4.10:** ORTEP drawing of the solid-state molecular structure of **4.11** (ellipsoids at 50% probability level). All hydrogen atoms have been omitted for clarity. Selected bond length (Å) and angles (deg): Co1-N1: 1.9845(17), Co1-N2: 1.9899(18), Co1-N5: 2.052(2), Co1-Cl1: 2.2439(7), C1-N1: 1.343(3), C1-C2: 1.391(3), C2-P1: 1.730(2), P1-N2: 1.6523(17), N2-N3: 1.373(2), N3-N4: 1.259(2), N1-Co1-N2: 98.30(7), Cl1-Co1-N5: 105.34(6), N1-Co1-Cl1: 107.87(6), N2-Co1-N5: 114.20(7), N2-N3-N4: 109.76(17), C1-N1-C6: 117.29(17).

The solution state behavior of **4.11** is drastically different from **4.8**. The  $^1\text{H}$  NMR spectrum for **4.11** shows 24 resonances, indicating the lack of a plane of symmetry through the complex. However, in order to observe 24 unique signals there must be free rotation at both the coordinated pyridine and the 2,6-dimethylphenyl of the phosphazide. The lack of symmetry in solution for **4.11** in comparison to **4.8** is likely caused by the donor strength of pyridine in comparison to THF. The coordinated THF observed in the solid-state structure for **4.8** un-

coordinates in solution and symmetrizes **4.8**, whereas this does not occur with the coordinated pyridine in **4.11**. An attempt was made at the synthesis of a cobalt phosphazide complex using  $\text{CoCl}_2$  in THF instead of the  $\text{CoCl}_2(\text{Py})_4$  starting material. The observed  $^1\text{H}$  NMR spectrum closely resembled the spectrum collected for the fluxional Fe phosphazide complex **4.8** and a comparison of the  $^1\text{H}$  NMR spectra for **4.8**, **4.11**, and **[4.12]** is shown in **Figure 4.11**.

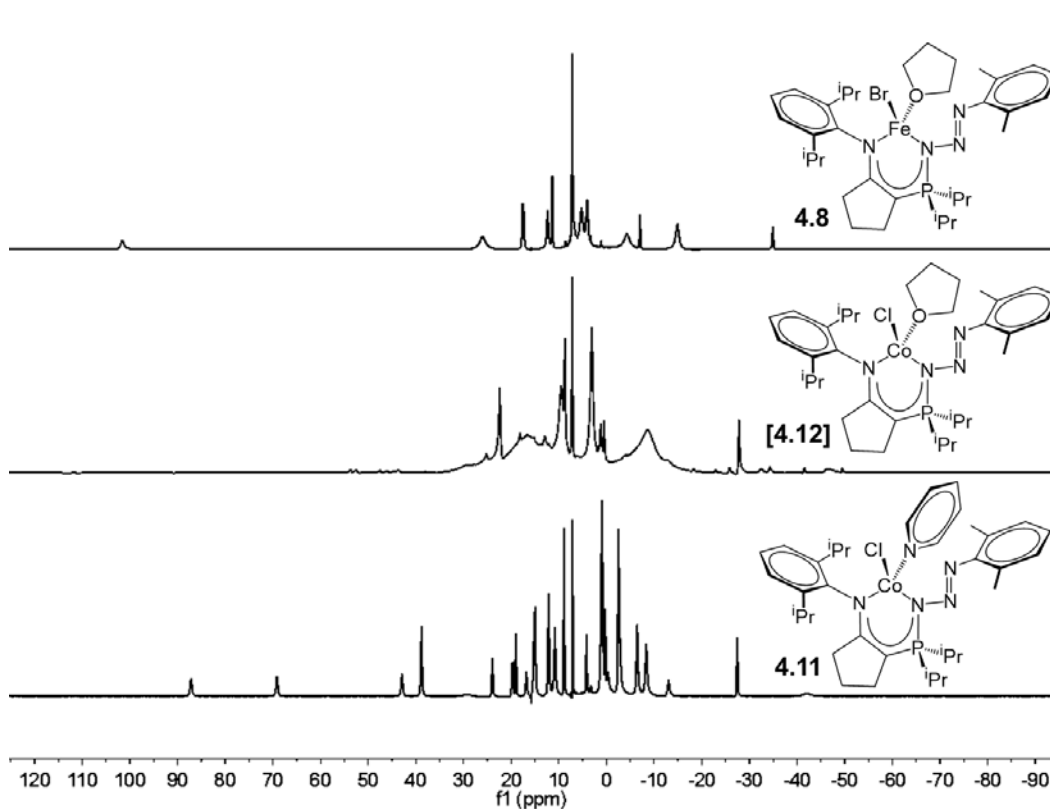


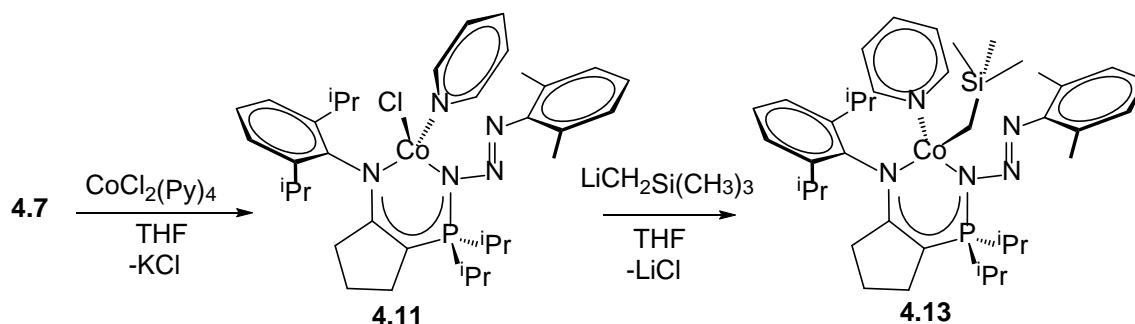
**Figure 4.11:** A comparison of the  $^1\text{H}$  NMR spectra for the iron phosphazide complex **4.8** (top spectrum), the putative cobalt phosphazide THF complex **[4.12]** (middle) and the cobalt phosphazide pyridine complex **4.11** (bottom). All spectra collected at 300 MHz in  $d_6$ -benzene at 298 K.

Unfortunately, single crystals of the putative Co phosphazide THF adduct **[4.12]** could not be obtained. Thus, definitive proof as to the identity of **[4.12]** was lacking and reactivity with the pyridine adduct **4.11** was pursued.

The reaction between **4.11** and  $\text{KBET}_3\text{H}$  in toluene led to an immediate color change of the solution from dark green to brown. The  $^1\text{H}$  NMR spectrum obtained for the product mixture

is that of an intractable product mixture, with 64 resonances observed. Attempts at growing single crystals of a species from this product mixture using the same solvent system employed to grow crystals of **4.9** (*n*-pentane/toluene at - 35 °C) failed to provide material suitable for X-ray diffraction. Thus, this specific research avenue was abandoned.

Due to the ability of the iron phosphazide complex **4.8** to undergo radical reactivity to generate **4.9**, cobalt alkyl phosphazide complexes were synthesized to probe their stability. It was predicted that homolytic bond cleavage would occur between Co–C,<sup>182</sup> generating a Co(I) species that could undergo a radical cascade similar to what is shown in **Scheme 4.3**. The cobalt phosphazide complex **4.11** was treated with (trimethylsilyl)methyl lithium in THF to generate the alkyl complex **4.13** (**Scheme 4.5**). Complex **4.13** is highly crystalline, and the solid state



**Scheme 4.5:** Treatment of the ligand potassium salt **4.7** with  $\text{CoCl}_2(\text{Py})_4$  leads to the isolation of the cobalt phosphazide complex **4.11**. The cobalt alkyl species **4.13** is synthesized from the reaction of **4.11** with  $\text{LiCH}_2\text{Si}(\text{Me})_3$ .

molecular structure is shown in **Figure 4.12**. The bond metrics described in the caption for **Figure 4.12** are in agreement the bond lengths and angles observed in the solid-state structure for complex **4.11** and the Co1–C37 bond length of 2.046(8) Å is comparable to the tetrahedral Co(II)-carbon bond length of 2.066(3) Å for the literature reported  $\text{Co}(\text{CH}_2\text{CMe}_2\text{Ph})_2(\text{Py})_2$ .<sup>183</sup> The solution state behavior for **4.13** is somewhat puzzling in comparison to **4.11**. Both complexes have measured magnetic moments in agreement with tetrahedral Co(II) as determined by the Evans method ( $\mu_{\text{eff}} = 4.0 \mu_{\text{B}}$  for **4.11** and  $4.5 \mu_{\text{B}}$  for **4.13**), but the <sup>1</sup>H NMR spectra are

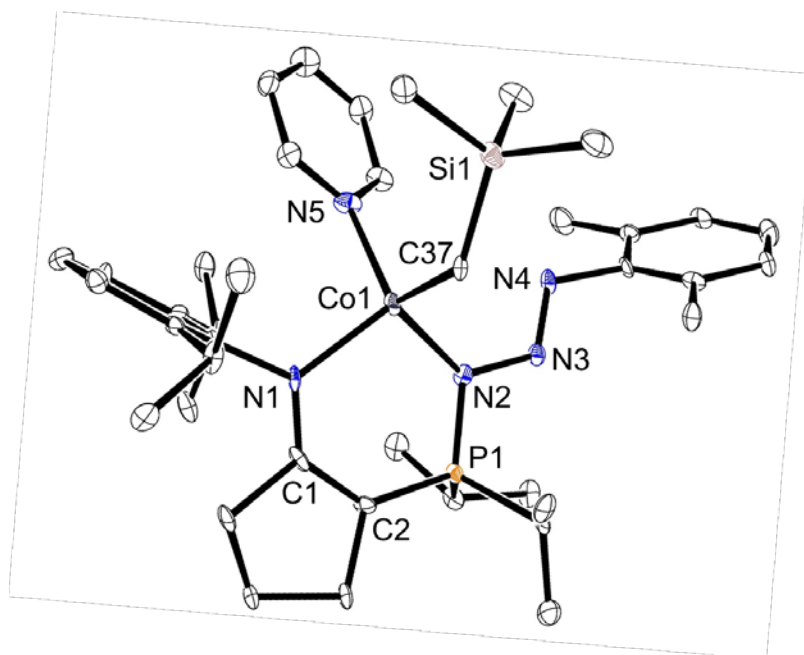


**Figure 4.12:** ORTEP drawing of the solid-state molecular structure of **4.13** (ellipsoids at 50% probability level). All hydrogen atoms have been omitted for clarity. Selected bond length (Å) and angles (deg): Co1-N1: 2.008(7), Co1-N2: 2.016(7), Co1-N5: 2.066(7), Co1-C37: 2.046(8), N1-C1: 1.320(11), C1-C2: 1.389(12), C2-P1: 1.728(8), P1-N2: 1.664(7), N2-N3: 1.382(9), N3-N4: 1.256(9), C37-Si1: 1.835(8), N1-Co1-N2: 97.2(3), N2-N3-N4: 113.7(6), N1-Co1-N5: 102.5(3), N2-Co1-N5: 116.7(3), N5-Co1-C37: 109.2(3).

dissimilar. As stated previously, the  $^1\text{H}$  NMR spectrum for **4.11** contains 24 resonances due to a lack of symmetry in the complex. In contrast, the  $^1\text{H}$  NMR spectrum for **4.13** only displays 18 apparent resonances. The signals observed in the spectrum for **4.13** are very broad, especially in the region between  $\delta$  18.4 and -4.7 (**Figure 4.13**). The overlap of resonances in this region may be the reason behind the apparent higher symmetry of **4.13** in solution. Additionally, the higher symmetry of **4.13** in solution may be due to enhanced lability of the coordinated pyridine due to the electronic and steric factors present in the alkyl complex **4.13** in comparison to **4.11**.

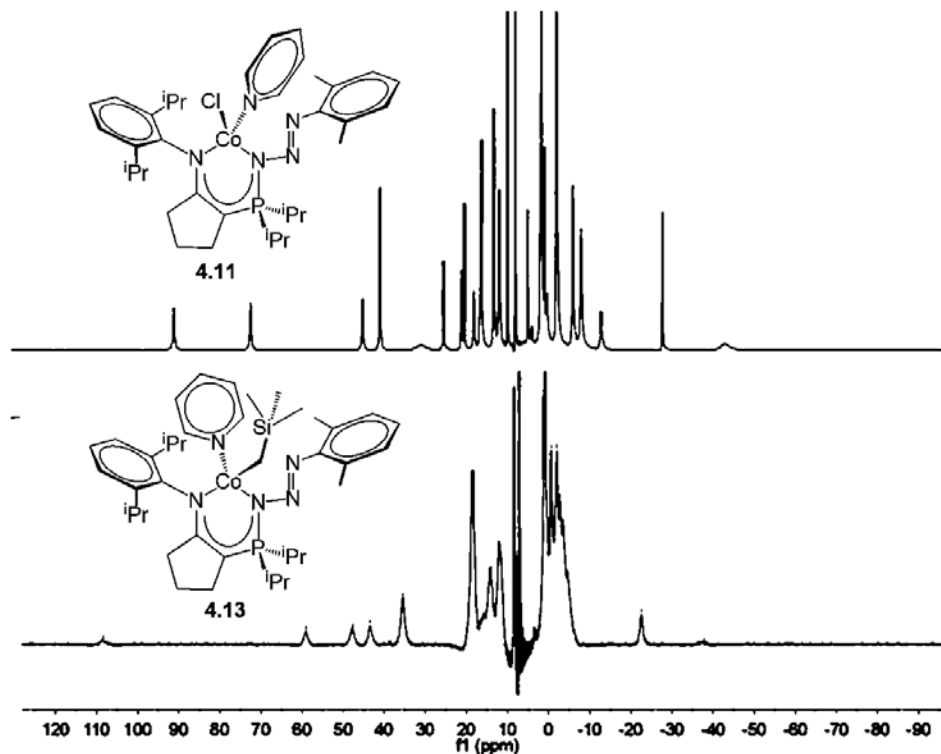


**Figure 4.13:** A comparison of the  $^1\text{H}$  NMR spectra obtained for **4.11** (top spectrum) and **4.13** (bottom spectrum). Both spectra collected at 300 MHz in  $d_6$ -benzene at 298 K.

Further reactivity with the cobalt alkyl complex **4.13** was not heavily investigated.

Complex **4.13** does not react with  $\text{H}_2$  and attempts at the hydrogenation of benzophenone, even in the presence of  $[\text{H}(\text{Et}_2\text{O})_2]^+[[3,5-(\text{CF}_3)_2\text{C}_6\text{H}_3]_4\text{B}]^-$  ( $\text{HBAr}^{\text{F}}$ ), failed. The addition of  $\text{HBAr}^{\text{F}}$  to the attempted hydrogenation reaction was rationalized by the observation that certain cobalt alkyl complexes have been shown to act as hydrogenation catalysts only after the ligand scaffold has been protonated with  $\text{HBAr}^{\text{F}}$ .<sup>155</sup> However, **4.13** reacts stoichiometrically with  $\text{HBAr}^{\text{F}}$  to give a new paramagnetic species as monitored by  $^1\text{H}$  NMR spectroscopy, but X-ray quality single crystals were not isolated for this species.

Future investigations into the reactivity of complex **4.13** could focus on its oxidation. Oxidation of  $\text{Co}(\text{II})$  to  $\text{Co}(\text{III})$  may cause the  $\text{Co}-\text{C}$  bond to undergo homolysis, generating a

Co(II) radical and an alkyl radical.<sup>182, 184</sup> The Co(II) radical could convert the phosphazide to a phosphinimido moiety through a radical cascade process as shown previously in **Scheme 4.3**. This could potentially serve as a route to dimeric cobalt species with a Co–Co bond, similar to that observed with the iron dimer **4.9**. Irradiation of **4.13** with UV light may also elicit Co–C bond homolysis.

#### **4.5 Conclusions**

This chapter highlighted the isolation of thermally stable phosphazide ligand scaffolds for the coordination to Fe(II) and Co(II). A surprising aspect of the reactivity displayed by the iron phosphazide complex is the hydride induced conversion of the phosphazide unit into a phosphinimido moiety without the intermediacy of a phosphinimine. Deuterium labeling experiments are consistent with this transformation being a radical process. While the phosphazide moiety can act as a ligand, there is also potential for phosphazides to act as precursors to phosphinimido units. The reactivity observed for iron with  $\text{KBET}_3\text{H}$  could not be extended to cobalt phosphazide complexes. Future work with cobalt phosphazide species could focus on cobalt-alkyl bond homolysis for the generation of cobalt based radicals, potentially facilitating the conversion of the ligand phosphazide into a phosphinimido.

## Chapter 5: Thesis Overview and Future Directions

### 5.1 Overview

This thesis outlined the synthesis and reactivity of unsymmetrical enamido-phosphinimine complexes of iron and their comparison to established  $\beta$ -diketiminato systems, especially focusing on the ability to change the electronics and sterics in the former. Three-coordinate and dimeric iron(II) bromide complexes **2.23a-c** and **2.24** served as synthetic precursors for further reactivity. The contents of Chapter 2 were primarily concerned with the reduction chemistry of complexes **2.23a-c** and **2.24** in the synthesis of iron dinitrogen complexes. The observation that less-steric hindrance in  $\beta$ -diketiminato iron complexes resulted in enhanced reactivity towards dinitrogen was an inspiration for the chosen ligand modifications pursued in this thesis. Systematic variations in the unsymmetrical steric profile of the enamido-phosphinimine scaffold were made with the intent of determining the steric threshold at which enhanced reactivity towards dinitrogen would occur. End-on bridging diiron dinitrogen complexes **2.25a**, **2.25c**, and **2.27** were successfully isolated from the reduction of **2.23a**, **2.23c** and **2.24**, respectively. The bond metrics obtained from the solid-state molecular structures indicate an insignificant difference in the degree of  $N_2$  activation in comparison to the end-on bridging NacNac analogues. In addition, only the synthesis of  $N_2$  complex **2.25c** was achievable without the concurrent formation of side-products. The side-product formed during the reduction of **2.23a** was identified through a separate experiment in which **2.23a** was reduced under vacuum, affording the bridging imido complex **2.26**. Isolation of **2.26** led to the conclusion that, in certain cases, the phosphinimine bond is susceptible to cleavage, likely through a reactive Fe(I) intermediate. Interestingly, the reduction of **2.23c** under vacuum did not lead to ligand P=N

bond cleavage and exposure of the putative Fe(I)BrK adduct to an atmosphere of N<sub>2</sub> allowed for the clean formation of **2.25c**.

An indene based ligand scaffold was synthesized with the intent of generating low-coordinate iron complexes that could subsequently be deprotonated at the indene ring to give an anionic indenyl backbone. The rationale was that enhanced activation of coordinated N<sub>2</sub> might be achieved if the negative charge delocalized in the indenyl ring contributed to the Fe–N<sub>2</sub> backbonding interaction. Unfortunately, single-crystals of the desired indenyl dinitrogen complex [**2.28**] were not isolated and DFT calculations suggested insignificant activation of the coordinated N<sub>2</sub>. An alternate application of the indenyl scaffold was in the attempted synthesis of heterobimetallic complexes. The dianionic indenyl scaffold was prepared as a mixed potassium-lithium salt **2.29**, but its oxidation potential made salt metathesis reactions difficult. To conclude Chapter 2, the results suggest the phosphinimine moiety is not suitable for reduction chemistry, given the propensity for P=N bond cleavage.

Chapter 3 described the reactivity of enamido-phosphinimine iron hydride complexes. Treatment of the dimeric hydride **3.6a** with azobenzene, 3-hexyne, and 1-azidoadamantane led to the formation of the expected insertion products. However, unprecedented reactivity of the iron hydride **3.6a** with hexafluorobenzene afforded the iron fluoride complex **3.14**. Catalytic HDF was performed using 5 mol % loading of precatalyst **3.6a** in the presence of fluorinated aromatics and silanes. The highest TON (50) was achieved for the HDF of pentafluoropyridine, outperforming the only literature reported iron based HDF catalyst by an order of magnitude. Surprisingly, the fluoride complex **3.14** did not act as a precatalyst for HDF. Kinetic data for the HDF reaction with **3.6a** support the rate law established for the β-diketimate Fe(II) fluoride system. The utility of **3.6a** as a precatalyst for HDF suggests that the enamido-phosphinimine

ligand scaffold is useful for stabilizing catalytically active species. Investigations into other catalytic processes with enamido-phosphinimine complexes may prove worthwhile.

Enamine-phosphazide species can be isolated during the course of the Staudinger reaction and Chapter 4 illustrated the coordination of an enamido-phosphazide ligand on Fe(II) and Co(II). Tetrahedral complexes of Fe(II) (**4.8**) and Co(II) (**4.11** and **4.13**) were isolated and unprecedented reactivity with  $\text{KBET}_3\text{H}$  was observed in the case of complex **4.8**. Hydride metathesis with **4.8** ultimately led to the formation of the phosphinimido complex **4.9**, which features an Fe–Fe bond. Labeling studies indicated that the C–N bond cleavage of the aryl phosphazide likely occurred through a radical pathway. Exploration into the reactivity of other base metal phosphazide complexes would likely yield additional surprising results.

## 5.2 Future Directions

### 5.2.1 Alternative Synthesis of Reactive Low-Coordinate Hydrides

Work presented in Chapter 3 highlighted the enhanced reactivity of the enamido-phosphinimine iron(II) hydride complex **3.6a** towards HDF catalysis in comparison to the analogous  $\beta$ -diketiminato iron hydride **3.1**. We propose that dimeric complex **3.6a** must first dissociate into three-coordinate monomeric iron hydrides in order to react with a perfluorinated aromatic substrate. If the equilibrium between dimeric and monomeric iron hydride species in solution can be shifted towards the monomeric form, enhanced reactivity would likely ensue. This could afford a HDF catalyst capable of reacting with partially fluorinated aromatics, perhaps at temperatures lower than 50 °C. One of the simplest methods for affecting the propensity towards dimerization would be a variation in ligand sterics. The modularity of the enamine-phosphinimine ligand synthesis would make the screening of sterically unsymmetrical scaffolds facile through the use of different organic azides in the Staudinger reaction.

Results presented in Chapter 3 illustrated that the hydride metathesis reactions between  $\text{KBET}_3\text{H}$  and the iron bromide complexes **2.23a** and **2.23c** produced iron ethyl and iron dihydridoborate complexes as side-products. Similar reactivity is reported for the  $\beta$ -diketiminato iron hydrides and mechanistic investigations performed by the Holland group indicate that the rate-determining transition state for B-C bond cleavage is the attack of a ring-opened iron hydride species on  $\text{BEt}_3$ .<sup>151</sup> This result has implications for the attempted synthesis of less sterically hindered iron hydrides and likely rules out hydride metathesis with  $\text{KBET}_3\text{H}$  as a synthetic protocol because the by-product borane would rapidly react with the desired hydride.

An interesting conclusion can be drawn about the attempted synthesis of the iron hydride **3.6b**. As the iron ethyl species **3.8b** was clearly formed when the hydride metathesis reaction between **2.23b** and  $\text{KBET}_3\text{H}$  was performed rapidly at  $-35\text{ }^\circ\text{C}$ , it is likely that the transiently formed iron hydride **3.6b** predominates as the monomeric form in solution. Though apparently less sterically encumbered than the **3.6a** analogue, the *para*-methyl of the mesityl group on the N-donor of the phosphininimine likely destabilizes the hydride dimer due to the close proximity of the two iron centers (**Figure 5.1**). Thus, to prevent the side reaction of a monomeric iron

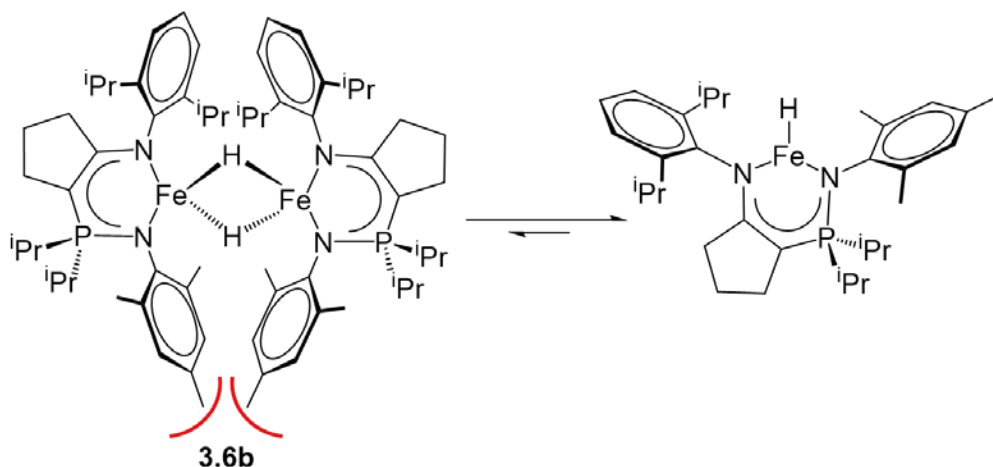
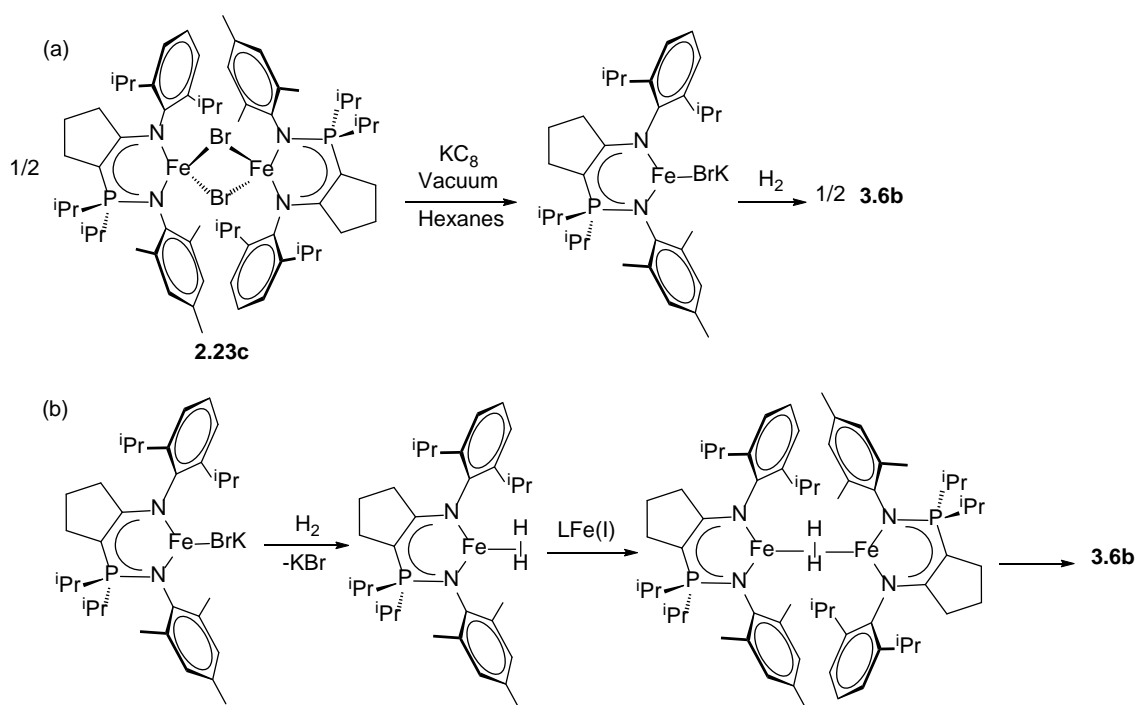


**Figure 5.1:** Steric interaction between the *para* methyl groups of the mesityl moiety likely destabilizes the dimeric form of **3.6b** in solution, resulting in a higher concentration of the monomeric species.

hydride of type **3.6b** with  $\text{BEt}_3$ , an alternate method for the synthesis of **3.6b** that does not utilize  $\text{KBET}_3\text{H}$  is required.

The utilization of a reduced Fe(I) species is proposed for the production of **3.6b**. In Chapter 2, results were provided showing reduction of **2.23c** under vacuum led to the stable, putative Fe(I)BrK adduct. Exposure of Fe(I)BrK to an atmosphere of  $\text{N}_2$  led to the clean formation of the  $\text{N}_2$  complex **2.25c**. By analogy, reduction of **2.23c** under vacuum, followed by exposure to an atmosphere of  $\text{H}_2$  may afford **3.6b** through a dinuclear oxidative addition process



**Scheme 5.1:** (a) The proposed synthesis of **3.6b** through reduction of **2.23c** and exposure to an atmosphere of  $\text{H}_2$ . (b) A possible mechanism for the process of binuclear oxidative addition of  $\text{H}_2$  via an Fe(I) intermediate.

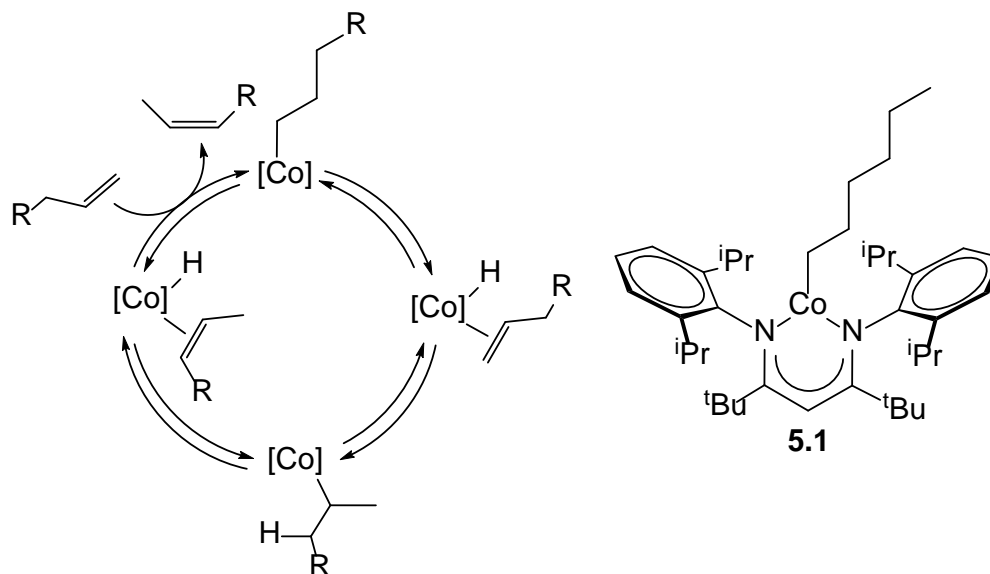
**(Scheme 5.1).** The oxidative addition of  $\text{H}_2$  by a Fe(I)  $\beta$ -diketiminate complex is a reported process.<sup>150</sup> Thus, the method outlined above is suitable for the generation of highly reactive low-coordinate hydrides, provided the particular ligand scaffold under investigation is stable to reduction.

## 5.2.2 Further Investigations into Catalysis

Given the increased HDF catalytic activity displayed by **3.6a** in comparison to the analogous  $\beta$ -diketiminate iron hydride, other comparisons to catalytic systems utilizing low-coordinate base-metal precatalysts should be investigated. Two catalytic processes suitable for further investigation with enamido-phosphinimine complexes are described herein.

### 5.2.2.1 Alkene Isomerization

The isomerization of terminal alkenes to internal alkenes is a well-studied catalytic process.<sup>185-190</sup> Catalytic systems have been developed for *E*-selective<sup>191-195</sup> and *Z*-selective<sup>196-198</sup> isomerization of alkenes. An inherent challenge in the development of a *Z*-selective isomerization catalyst is that *Z*-alkenes are thermodynamically less stable than the *E*-isomer. One of the few *Z*-selective isomerization catalysts of terminal alkenes to 2-alkenes is a  $\beta$ -diketiminate Co(II) *n*-hexyl complex **5.1**.<sup>197</sup> This catalyst operates via the alkyl mechanism, which occurs through sequential  $\beta$ -hydride elimination and [1,2]-insertion (**Scheme 5.2**). The high selectivity



**Scheme 5.2:** Complex **5.1** catalyzes the isomerization of terminal alkenes to the internal *Z*-isomer through an alkyl mechanism (shown to the left).

(12:1 *Z* to *E* isomer for certain substrates) is attributed to the steric influence of the ancillary ligand. DFT studies investigating the barrier to  $\beta$ -hydride elimination for **5.1** indicate that the transition state has a square-planar geometry.<sup>199</sup> This is critical to understanding the selectivity of the isomerization process, as the two rotamers that could form in the transition state will experience different degrees of steric interaction with the 2,6-diisopropylphenyl groups.<sup>197</sup> This effect is depicted in **Figure 5.2**, where the *Z*-rotamer orients the alkyl groups of the incipient

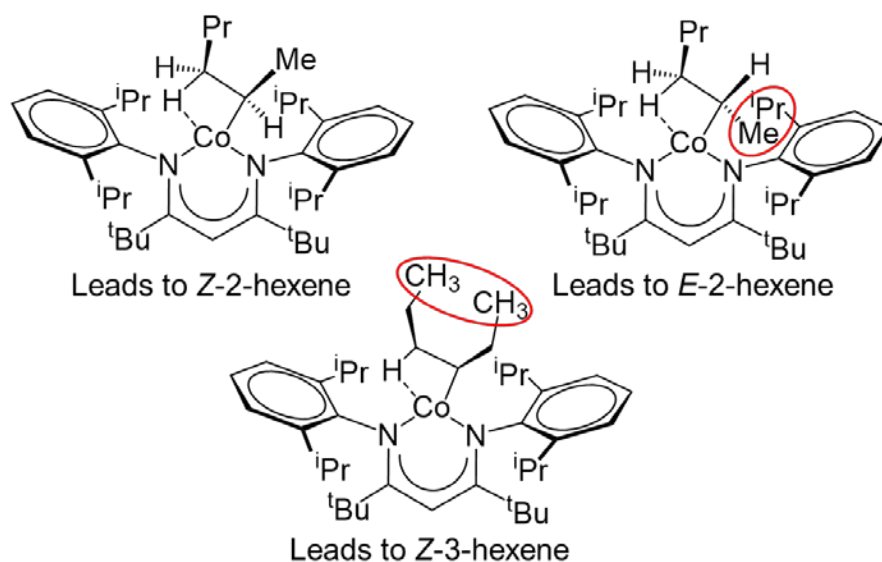


**Figure 5.2:** A depiction of the steric influence affecting the isomerization of terminal alkenes to internal alkenes. Steric interaction with the NacNac scaffold prohibits the formation of the square planar transition state for *E*-2-hexene and *Z*-3-hexene.

alkene between the bulky isopropyl groups of the ligand. In contrast, there is significantly higher steric interaction between the methyl group and the ligand scaffold in *E*-rotamer. Likewise, the regioselectivity of the **5.1** catalyst is due to a steric effect. There is no production of *Z*-3-hexene from the isomerization of 1-hexene due to the steric clash between the ethyl arms that are forced together by the ligand scaffold. Attempts at alkene isomerization using less sterically hindered

cobalt  $\beta$ -diketiminato catalysts are reported to result in neither regioselectivity nor stereoselectivity.<sup>197</sup>

In consideration of the model shown in **Figure 5.2**, the use of a sterically unsymmetrical enamido-phosphinimine scaffold may have implications for the selectivity of alkene isomerization. For example, consider the hypothetical enamido-phosphinimine cobalt complex **[5.2]** and the potential transition state it would undergo in the formation of *Z*-3-hexene (**Figure 5.3**). The enamido-phosphinimine scaffold is capable of flexibility, as determined by the

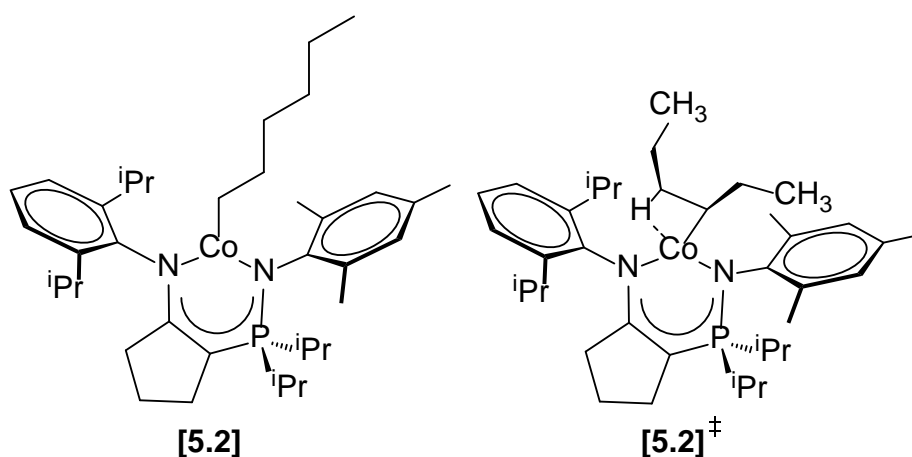
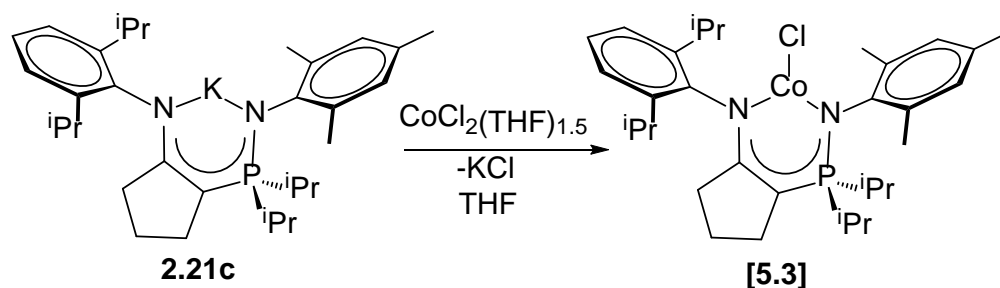


**Figure 5.3:** A hypothetical cobalt *n*-hexyl complex **[5.2]** and the implications of ligand sterics on the *Z*-3-hexene square planar transition state **[5.2]‡**.

dihedral angle of 20-30° between the carbons in the cyclopentylidene ring and the phosphinimine moiety (see structures in Chapter 2 for examples). This flexibility may be of benefit during chain-walking processes, resulting in less steric strain in a hypothetical *Z*-3-hexene transition state **[5.2]‡**. Complex **[5.2]** may give different regioselectivity in comparison to **5.1**. However, it remains to be determined if the mesityl group in **[5.2]** is sufficiently hindered to selectively yield *Z*-alkenes.

A preliminary reaction to access **[5.2]** was performed through the synthesis of the cobalt chloride complex **[5.3]** (**Scheme 5.3**). While single crystals suitable for X-ray diffraction remain

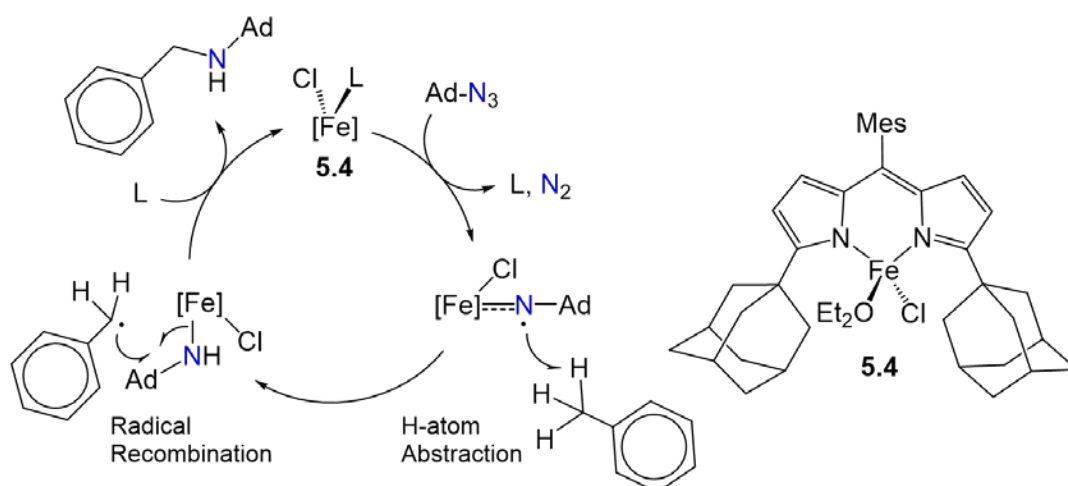


**Scheme 5.3:** Salt metathesis reaction between **2.21c** and  $\text{CoCl}_2(\text{THF})_{1.5}$  yields the low-coordinate cobalt complex **[5.3]**.

elusive, the  $^1\text{H}$  NMR spectrum of **[5.3]** showed paramagnetically shifted signals, indicating that the ligand was successfully coordinated to cobalt. However, the  $^1\text{H}$  NMR spectrum is inconclusive, as only 8 resonances of the expected 14 were observed when the spectrum was collected in  $d_8$ -THF. Further characterization of **[5.3]** and the synthesis of its alkyl derivatives is the next step towards the investigation of enamido-phosphinimine complexes as viable alkene isomerization catalysts.

### 5.2.2.2 C–H Bond Activation

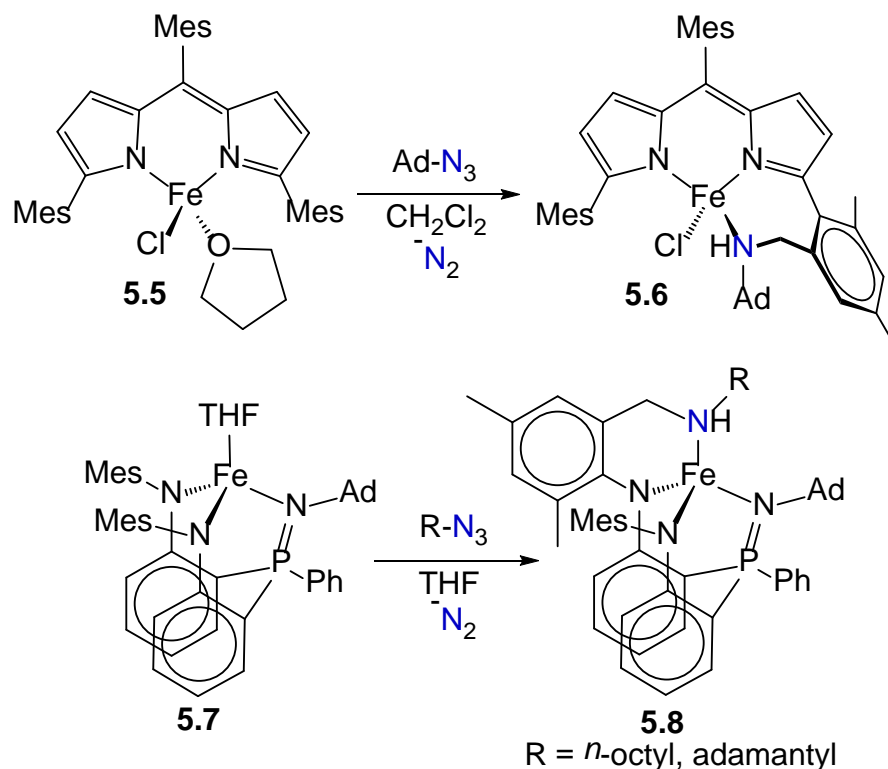
The functionalization of unactivated C–H bonds is a significant chemical challenge. However, there is value in studying C–H bond activation as this transformation could make possible the production of commodity chemicals from simple hydrocarbon feedstocks.<sup>200</sup> One strategy for C–H bond activation is to use metal-ligand multiple bonds, such as oxo<sup>201-204</sup> and imido<sup>127, 205-207</sup> species, to facilitate H-atom transfer processes. For example, transient high-spin Fe imido complexes, generated in situ from organic azides, delocalize significant radical character to the N-atom of the imido ligand, making H-atom abstraction from olefin and aromatic substrates possible.<sup>127, 208</sup> A subsequent radical recombination process allows for the formation of a C–N bond, forming an amine product. An example of a dipyrinato iron imido species that performs intermolecular C–H bond activation of toluene is shown in **Scheme 5.4**.<sup>127</sup>



**Scheme 5.4:** Complex **5.4** catalyzes the amination of toluene.

Judicious design of the ancillary ligand is critical for the intermolecular process to occur, as competitive intramolecular C–H bond activation with the ligand scaffold is a potential side-reaction. The installation of flanking adamantyl groups prevents deleterious C–H bond activation that could result with moieties containing weaker C–H bonds. Some examples of iron imido complexes that perform intramolecular C–H bond activation with their ligand scaffolds are shown in **Scheme 5.5**. In contrast to complex **5.4**, the mesityl substituted dipyrinato iron complex **5.5** undergoes intramolecular C–H bond activation upon exposure to 1-azidoadamantane to yield the tethered amine species **5.6**.<sup>209</sup> Likewise, treatment of the tripodal bis(anilido)phosphinimine complex **5.7** with organic azides yields the tethered amine complex **5.8**.<sup>210</sup>

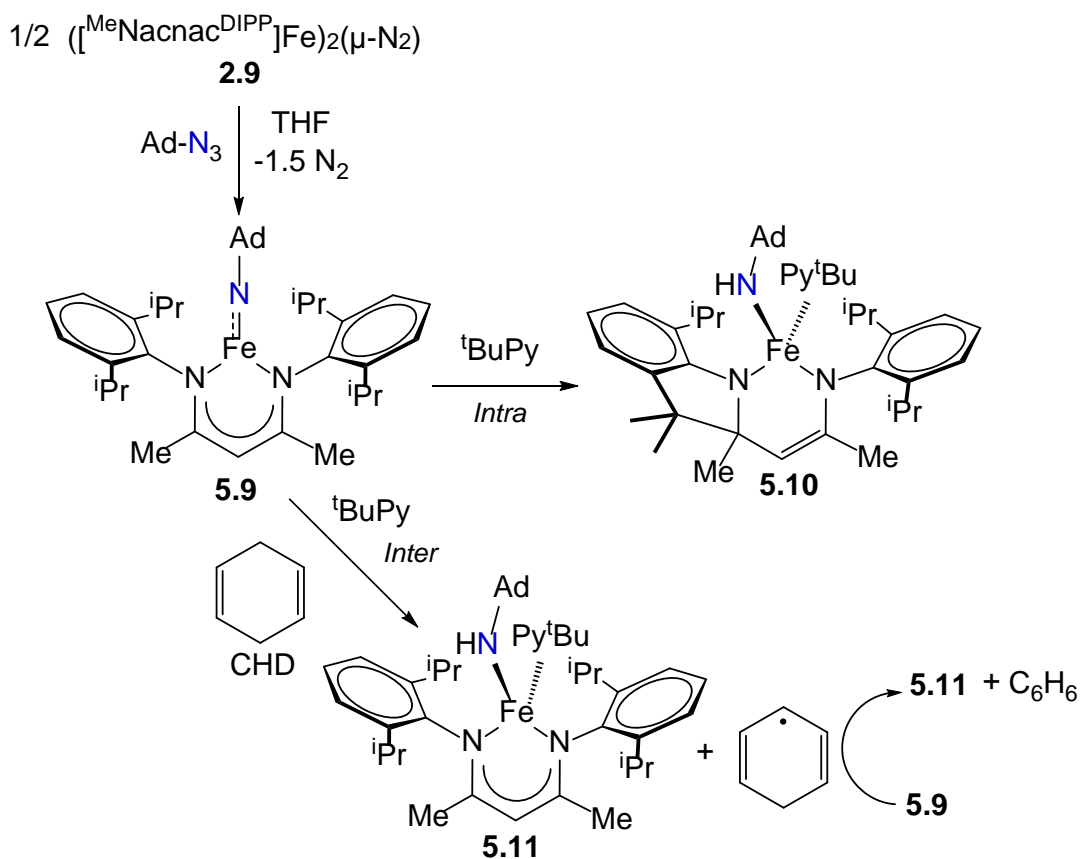
The coordination number of the iron imido complex influences its ability to perform H-atom abstraction. Addition of 1-azidoadamantane to the N<sub>2</sub>-complex **2.9** in THF affords the isolable three-coordinate iron(III) imido complex **5.9**<sup>211</sup> (**Scheme 5.6**). However, intramolecular



**Scheme 5.5:** Some examples of intramolecular C–H bond activation from transient iron imido species.

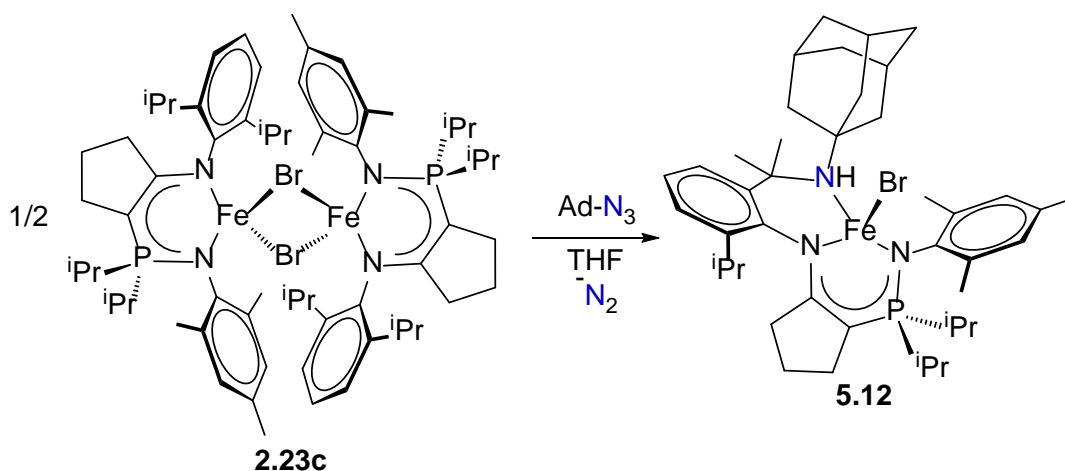
H-atom abstraction occurs upon addition of 4-*tert*-butylpyridine (*t*BuPy) to **5.9**, causing an intramolecular C–C coupling to form **5.10**. The increase in coordination number of iron from three to four coordinate is responsible for the enhanced reactivity of the imido moiety. While the intramolecular C–H bond activation of the  $\beta$ -diketiminato scaffold is rapid, the intermolecular process does occur in the presence of weak C–H bonds, such as those found in 1,4-cyclohexadiene (CHD) to give the Fe(II) amido complex **5.11**.<sup>207, 212</sup> The rate of H-atom abstraction was shown to depend on the steric accessibility of the substrate C–H bond to the imido nitrogen.<sup>207</sup> Subsequent modification to the  $\beta$ -diketiminato scaffold incorporated 2,4,6-tri(phenyl)phenyl moieties to the N-donors that greatly enhanced the stability and reactivity of the resulting iron imido species relative to **5.9**.<sup>213</sup> The above examples of iron dipyrinato and  $\beta$ -diketiminato complexes illustrate the importance of ligand modification for stabilizing iron imido

species. Thus, it would be of interest to apply sterically unsymmetrical enamido-phosphinimine iron complexes towards C–H bond activation.



**Scheme 5.6:** Treatment of the  $\beta$ -diketiminate iron  $\text{N}_2$  complex **2.9** with 1-azidoadamantane gives the three-coordinate imido complex **5.9**. Addition of  $^t\text{BuPy}$  causes intramolecular H-atom abstraction in the absence of weak C–H bonds, yielding **5.10**. In the presence of substrates containing weak C–H bonds, intermolecular H-atom abstraction is possible.

A synthetic methodology similar to that employed for generating transient imido species with the dipyrinato system was utilized for forming an iron imido with the enamido-phosphinimine scaffold. Treatment of the iron bromide complex **2.23c** with 1-azidoadamantane in THF overnight afforded the product resulting from intramolecular C–H bond activation of a phenyl isopropyl group, shown in **Scheme 5.7**. Single crystals of **5.12** were grown from a diethyl ether solution cooled to  $-35\text{ }^\circ\text{C}$  and the solid-state molecular structure is shown in **Figure 5.4**.



**Scheme 5.7:** Treatment of **2.23c** with 1-azidoadamantane affords **5.12**.

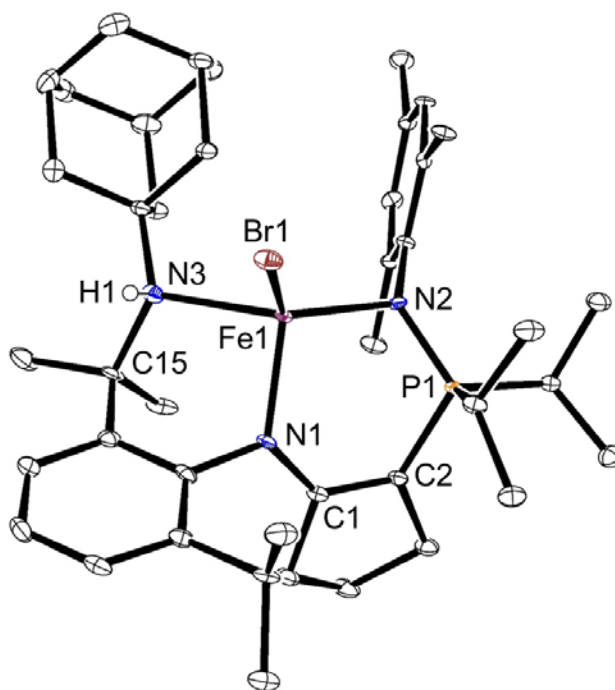


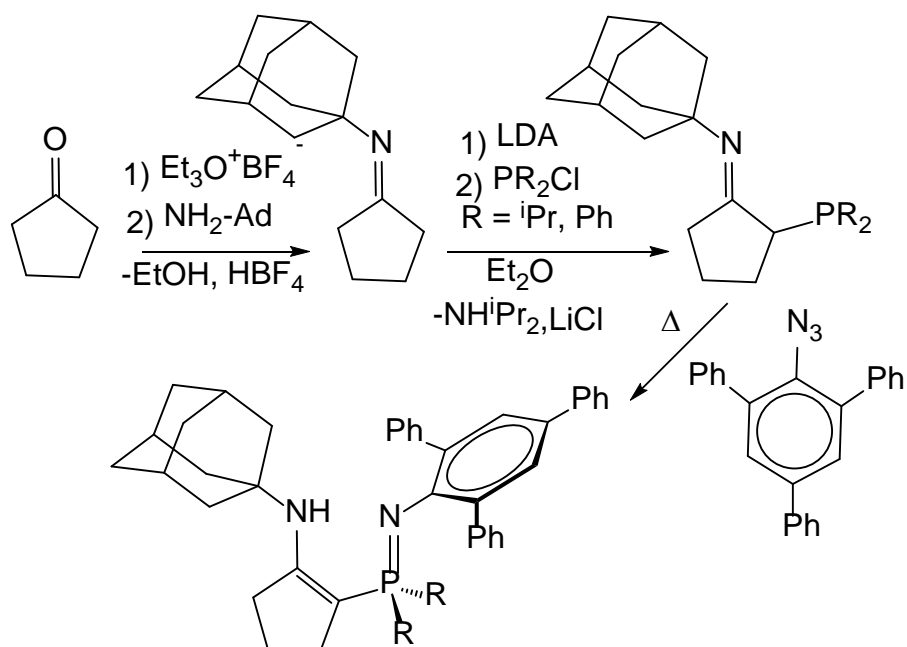
**Figure 5.4:** ORTEP drawing of the solid-state molecular structure of **5.12** (ellipsoids at 50% probability level). All hydrogen atoms except H1 omitted for clarity. Selected bond lengths (Å), and angles (deg): Fe1-Br1: 2.4493(9), Fe1-N1: 1.996(3), Fe1-N2: 2.032(3), Fe1-N3: 2.229(4), P1-N2: 1.630(3), C2-P1: 1.768(4), C1-C2: 1.375(6), C1-N1: 1.362(5), C15-N3: 1.533(6), N1-Fe1-N2: 101.3(1), N1-Fe1-N3: 91.0(1), N2-Fe1-N3: 131.5(1), N1-Fe1-Br1: 110.5(1), N2-Fe1-Br1: 117.7(1), and N3-Fe1-Br1: 100.6(1).

Complex **5.12** has a distorted coordination geometry ( $\tau'_4 = 0.74$ ) that deviates from tetrahedral ( $\tau'_4 = 1$ ).<sup>214</sup> The  $\tau'_4$  calculation is similar to the  $\tau_4$  calculation,<sup>215</sup> but distinguishes between the

two largest angles in the structure, allowing for differentiation of structures with different geometries that would otherwise give similar  $\tau_4$  values. The largest ligand bite angle of  $131.5(1)^\circ$  for N2-Fe1-N3 highlights the strained geometry. The Fe1-N3 distance ( $2.229(4)$  Å) is longer than Fe1-N1 ( $1.996(3)$  Å) and Fe1-N2 ( $2.032(3)$  Å), supporting the neutral amine assignment for the nitrogen donor derived from 1-azidoadamantane.

Having generated a transient imido from the treatment of **2.23c** with an organic azide, the catalytic amination of 1-hexene and styrene was attempted. Unfortunately, there was zero production of aminated product when using 5 mol % loadings of **2.23c** in the presence of equimolar amounts of 1-azidoadamantane and olefin in THF. The rate of intramolecular C–H bond activation of the ligand scaffold dominates the potential intermolecular process, resulting in deactivation of the transient imido species. Thus, future work in C–H bond activation using enamido-phosphinimine iron complexes should focus on improving the stability of the ancillary ligand. A proposed ligand modification is shown in **Scheme 5.8**. An important consideration is the difficulty of the imine-condensation reaction with sterically hindered substrates. The use of alkylating agents, such as triethyloxonium tetrafluoroborate, would likely be necessary in order to force cyclopentanone to react with a sterically hindered amine, such as 1-aminoadamantane.<sup>19</sup> Similarly, the Staudinger reaction could prove challenging with a more hindered azide. Preliminary reactivity studies indicated that the Staudinger reaction does not proceed to completion when reacting 1-azidoadamantane with diisopropylphosphine derivatives. The question remains as to whether 2,4,6-tri(phenyl)phenyl azide would react with an isopropyl substituted phosphorus center. The phenyl decorated phosphine may prove more useful in this regard, as investigations with imine-phosphine precursors indicated that the Staudinger reaction

is facile and proceeds at ambient temperature when 2,6-diisopropylphenyl azide is reacted with phenyl substituted phosphines.



**Scheme 5.8:** Proposed synthesis for an alternate ligand scaffold suitable for intermolecular C–H bond activation.

Unrelated to C–H bond activation, the strained coordination environment of **5.12** may afford interesting reactivity in other applications. For example, bromide abstraction from **5.12** with  $\text{Na}^+[[3,5-(\text{CF}_3)_2\text{C}_6\text{H}_3]_4\text{B}]^-$  ( $\text{NaBAR}^{\text{F}}$ ) could potentially form a cationic complex with an open coordination site. Perhaps the cationic species would activate small molecules, such as  $\text{H}_2$ , and could be used for hydrogenation catalysis.

As a final remark, complexes of first-row transition metals are often stated as being attractive for catalysis due to their low cost and abundance. Besides the financial benefits afforded by base-metal systems, a more enticing reason for studying their chemistry is their unusual reactivity. The once stigmatized nature of paramagnetic complexes is now being harnessed for a range of catalytic processes and unique reactivity. The future is promising for the

increased utilization of first-row transition metals for the resolution of a wide range of chemical challenges.

## Chapter 6: Experimental Details

### 6.1 General Procedures

All manipulations were performed under an atmosphere of dry and oxygen-free dinitrogen ( $N_2$ ) by means of standard Schlenk or glovebox techniques. Anhydrous THF, toluene,  $Et_2O$  and hexanes were purchased from Aldrich, sparged with  $N_2$  and further dried by passage through towers containing activated alumina and molecular sieves. Benzene- $d_6$  was refluxed over sodium, vacuum transferred and freeze-pump-thaw degassed. Tetrahydrofuran- $d_8$  was purchased from Aldrich ( $\geq 99.5$  atom % D) in 1 mL ampoules and was dried over activated 4 Å molecular sieves. Toluene- $d_8$  was purchased from Aldrich (99 atom % D) and was dried over activated 4 Å molecular sieves.  $^1H$ ,  $^{13}C$ ,  $^{31}P$ , and  $^{19}F$  NMR spectra were recorded on a Bruker AV-300 MHz spectrometer or a Bruker AV-400 MHz spectrometer. Unless noted otherwise, all spectra were recorded at room temperature.  $^1H$  NMR spectra were referenced to the residual proton signal in  $d_6$ -benzene ( $\delta$  7.16),  $d_8$ -toluene ( $\delta$  2.08) or  $d_8$ -THF ( $\delta$  1.72);  $^{13}C\{^1H\}$  NMR spectra were referenced to solvent resonances of  $d_6$ -benzene ( $\delta$  128.1) or  $d_8$ -THF ( $\delta$  25.3);  $^{31}P\{^1H\}$  NMR spectra were referenced to an external sample of  $H_3PO_4$  at  $\delta$  0.0;  $^{19}F$  NMR spectra were referenced to fluorobenzene at  $\delta$  -113.15. Evans NMR spectroscopy was performed by measuring the shift in frequency for the  $^1H$  NMR signal of cyclooctane in a sealed capillary containing 1 mol% cyclooctane in  $d_6$ -benzene relative to a 1 mol% cyclooctane in  $d_6$ -benzene solution containing the desired paramagnetic compound. Microanalyses (C, H, N) were performed at the Department of Chemistry at the University of British Columbia. Low and high-resolution mass spectrometry was performed with a Kratos MS 50 at the University of British Columbia. Gas chromatography and mass spectrometry were performed on an Agilent 6890N GC coupled with a 5975B MS detector. Liquid samples were

injected using a split ratio of 50:1 and helium as the carrier gas. Samples were heated to 200 °C from an initial temperature of 40 °C using a ramp rate of 30 °C/min.

Suitable single crystals for X-ray crystallographic analysis were selected in a glovebox, coated in Fomblin oil and mounted on a glass loop. X-ray data were collected on a Bruker X8 Apex II diffractometer with a graphite-monochromated Mo K $\alpha$  radiation ( $\lambda = 0.71073 \text{ \AA}$ ) at a temperature of 90 K. Data were collected and integrated using the Bruker SAINT software package.<sup>216</sup> Absorption corrections were performed using the multiscan technique (SADABS).<sup>217</sup> All structures were solved by direct methods and refined using the Olex2 (version 1.2.5) software package<sup>218</sup> and the ShelXL refinement program.<sup>219</sup> All non-hydrogen atoms were refined anisotropically. ORTEPs were generated using ORTEP-3 (version 2.02).<sup>220</sup>

The  $^{57}\text{Fe}$  Mössbauer spectrum of **2.25c** was recorded using a Topologic Systems Inc. Mössbauer spectrometer at 78 K in constant-acceleration mode.  $^{57}\text{Co}$  (in rhodium matrix) was used as the radiation source. MossWinn 4.0Pre software (<http://www.mosswinn.com/>) was used for quantitative evaluation of spectral parameters (least-squares fitting to Lorentzian peaks). Isomer shifts were determined relative to  $\alpha$ -iron at 298 K. The sample powders were loaded in laminate film sealed into 1 cm x 1 cm squares.  $^{57}\text{Fe}$  Mössbauer spectra for **4.8** and **4.9** were recorded using a W.E.B. Research Mössbauer spectroscopy system at room temperature. A  $^{57}\text{Co}$  (in rhodium matrix) source with a strength of  $\sim 25 \text{ mCi}$  was used. The detector was a Reuters-Stokes Kr/CO $_2$  proportional counter. The sample powders were loaded in a high-density polyethylene flat washer wrapped in parafilm and secured with Kapton tape. The sample chamber was evacuated to  $-28'' \text{ Hg}$  and back filled to  $-25'' \text{ Hg}$  with He. The velocity was scanned between 4 and  $-4 \text{ mms}^{-1}$  using a constant acceleration triangle waveform, and calibrated against

an Fe foil measured at 295 K in zero magnetic field. Fitting of the data was performed using WMOSS software, which is available free of charge at <http://wmoos.org/>.

DFT calculations were performed using the Gaussian 09 package.<sup>221</sup> Calculations were performed using the UB3LYP functional<sup>222</sup> and the valence triple- $\zeta$  (TZV) basis set.

## 6.2 Starting Materials and Reagents

Arylazides were prepared according to a literature procedure.<sup>69</sup> Potassium hydride (30 wt% dispersion in mineral oil) was purchased from Sigma-Aldrich and was washed with hexanes on a glass frit and handled within a glovebox as a dry powder.

Dibromobis(tetrahydrofuran)iron(II)<sup>223</sup> and dichlorotetrakis(pyridine)cobalt(II)<sup>183</sup> were prepared according to literature procedures. The imine-phosphines **2.17a** and **2.17b**<sup>224-225</sup> were synthesized from slight modifications to literature procedures. Potassium triethylborohydride was purchased as a 1.0 M solution in THF from Sigma-Aldrich and was dried under vacuum, affording a crystalline solid that was stored and used in the N<sub>2</sub> glovebox. Hexafluorobenzene, fluorobenzene, 1,3,5-trifluorobenzene, pentafluoropyridine, triethylsilane, butylsilane, and 3-hexyne were degassed and stored over activated molecular sieves before use. 1-azidoadamantane, azobenzene, and triphenylsilane were degassed under vacuum and used within the N<sub>2</sub> glovebox. Trimethyltin fluoride was synthesized according to a literature procedure.<sup>149</sup> Potassium triethylborodeuteride was synthesized from potassium deuteride and triethylborane in toluene and was stored as a solid. Potassium deuteride was synthesized according to a literature procedure, with the modification of D<sub>2</sub> gas being used in place of H<sub>2</sub> gas.<sup>226</sup> Potassium graphite was synthesized according to a literature procedure.<sup>227</sup> Ethylmagnesium chloride was purchased as a 2.0 M solution in THF from Sigma-Aldrich and was used as received. (Trimethylsilyl)methyl lithium was purchased as a 1.0 M solution in pentane, which was cooled to -35 °C causing crystalline

(Trimethylsilyl)methylolithium to precipitate out of solution. The supernatant was decanted, and the crystalline (Trimethylsilyl)methylolithium was dried under vacuum and used as a solid in the N<sub>2</sub> glovebox. All other reagents were purchased from commercial suppliers and were used as received.

### 6.3 Synthesis of Compounds

#### 6.3.1 Compounds Pertaining to Chapter 2

##### [<sup>CY5</sup>NpN<sup>DIPP,DIPP</sup>]H (2.18a)

A toluene solution of 2,6-diisopropylphenylazide (1.150 g, 5.657 mmol) was added to the imine-phosphine **2.17a** (2.035 g, 5.657 mmol). The resulting mixture was transferred to a Kontes-sealed thick glass reaction bomb containing a magnetic stir bar. The solution was heated to 80 °C for 4 days while being stirred. After the reaction was complete, the toluene was removed under vacuum and the resulting brown residue was triturated with 10 mL of hexanes and was again dried under vacuum, yielding the product as a sticky brown solid. Yield: 2.576 g, 4.817 mmol, 85.15%.

<sup>1</sup>H NMR (400 MHz, *d*<sub>6</sub>-benzene, 298 K): δ 9.19 (s, 1H, *NH*), 7.34-7.21 (m, 4H, *ArH*), 7.14-7.09 (m, 2H, *ArH*), 4.09 (sept, 2H, <sup>3</sup>J<sub>HH</sub>= 6.9 Hz, NAr-<sup>i</sup>PrCH), 3.52 (sept, 2H, <sup>3</sup>J<sub>HH</sub>= 6.8 Hz, NAr-<sup>i</sup>PrCH), 2.40 (t, 2H, <sup>3</sup>J<sub>HH</sub>= 6.4 Hz, NArCCH<sub>2</sub>CH<sub>2</sub>CH<sub>2</sub>), 2.35-2.27 (m, 2H, P<sup>i</sup>PrCH), 2.21 (t, 2H, <sup>3</sup>J<sub>HH</sub>= 6.3 Hz, <sup>i</sup>Pr<sub>2</sub>PCCH<sub>2</sub>CH<sub>2</sub>CH<sub>2</sub>), 1.69 (quin, 2H, <sup>3</sup>J<sub>HH</sub>= 7.1 Hz, CH<sub>2</sub>CH<sub>2</sub>CH<sub>2</sub>), 1.41 (d, 12H, <sup>3</sup>J<sub>HH</sub>= 6.9 Hz, <sup>i</sup>PrCH<sub>3</sub>), 1.30 (d, 6H, <sup>3</sup>J<sub>HH</sub>= 7.0 Hz, <sup>i</sup>PrCH<sub>3</sub>), 1.27 (d, 6H, <sup>3</sup>J<sub>HH</sub>= 7.2 Hz, <sup>i</sup>PrCH<sub>3</sub>), and 1.24-1.21 (m, 12H, <sup>i</sup>PrCH<sub>3</sub>).

<sup>31</sup>P{<sup>1</sup>H} NMR (161 MHz, *d*<sub>6</sub>-benzene, 298 K): δ 19.6 (s).

<sup>13</sup>C{<sup>1</sup>H} NMR (101 MHz, *d*<sub>6</sub>-benzene, 298 K): δ 164.2 (d, J<sub>PC</sub>= 4 Hz), 147.1, 146.0 (d, J<sub>PC</sub>=5 Hz), 142.4 (d, J<sub>PC</sub>= 7 Hz), 136.9, 127.3, 123.8, 123.2, 119.6, 85.9, 84.8, 34.5 (d, J<sub>PC</sub>= 13 Hz),

34.4 (d,  $J_{PC}$  = 13 Hz), 29.6, 29.1, 28.4, 28.2, 25.1, 25.0, 23.8, 23.2 (d,  $J_{PC}$  = 10 Hz), 17.8 (d,  $J_{PC}$  = 2 Hz), and 17.0 (d,  $J_{PC}$  = 2 Hz).

EI-MS ( $m/z$ ): 534( $[M]^+$ ), 491( $[M-^iPr]^+$ ), 449.

Anal. Calcd for  $C_{35}H_{55}N_2P$ : C, 78.60; H, 10.37; N, 5.24. Found: C, 78.39; H, 10.57; N, 5.37.

### **[ $CY_5NpN^{DMP,DMP}$ ]H (2.18b)**

A hexane solution of 2,6-dimethylphenylazide (3.551 g, 24.17 mmol) was added to the imine-phosphine **2.17b** (7.321 g, 24.17 mmol). The reaction mixture immediately changed from yellow to very dark brown and was stirred for 30 minutes. After the allotted reaction time had transpired, the solution was cooled to  $-35\text{ }^\circ\text{C}$  overnight, resulting in crystal growth of the enamine-phosphazide intermediate. The crystalline material was collected on a glass frit and was rinsed with *n*-pentane and dried under vacuum. The enamine-phosphazide was dissolved in toluene and was transferred to a Kontes-sealed thick glass reaction bomb containing a magnetic stir bar. The solution was heated to  $80\text{ }^\circ\text{C}$  for one day while being stirred. After the reaction was complete, the toluene was removed under vacuum and the resulting black residue was dissolved in  $Et_2O$  and was again dried under vacuum, yielding the product as a grey powder. Yield: 4.048 g, 9.578 mmol, 39.63 %.

$^1H$  NMR (400 MHz,  $d_6$ -benzene, 298 K):  $\delta$  9.00 (s, 1H, NH), 6.94-6.84 (m, 4H, ArH), 2.54 (s, 6H, Ar( $CH_3$ )<sub>2</sub>), 2.26 (t, 2H,  $^3J_{HH}$ =6.8 Hz, NArCCH<sub>2</sub>CH<sub>2</sub>CH<sub>2</sub>), 2.17 (s, 6H, Ar( $CH_3$ )<sub>2</sub>), 2.10 (dsep, 2H,  $^3J_{HH}$ =9.6 Hz,  $^2J_{PH}$ =2.4 Hz, P- $^iPrCH$ ), 2.00 (t, 2H,  $^3J_{HH}$ =7.1 Hz, P $^iPr_2$ CCH<sub>2</sub>CH<sub>2</sub>CH<sub>2</sub>), 1.55 (quint, 2H,  $^3J_{HH}$ =7.0 Hz, CH<sub>2</sub>CH<sub>2</sub>CH<sub>2</sub>), 1.20 (d, 3H,  $^3J_{HH}$ =7.1 Hz, P- $^iPrCH_3$ ), 1.16 (d, 3H,  $^3J_{HH}$ =7.1 Hz, P- $^iPrCH_3$ ), 1.07 (d, 3H,  $^3J_{HH}$ =7.2 Hz, P- $^iPrCH_3$ ), and 1.03 (d, 3H,  $^3J_{HH}$ =7.2 Hz, P- $^iPrCH_3$ ).

$^{31}P\{^1H\}$  NMR (121 MHz,  $d_6$ -benzene, 298 K):  $\delta$  18.7 (s).

$^{13}\text{C}\{^1\text{H}\}$  NMR (101 MHz,  $d_6$ -benzene, 298 K):  $\delta$  163.5 (d,  $J_{\text{PC}}=4$  Hz), 139.8, 136.9, 132.4, 132.3, 128.5, 128.4, 126.3, 84.6, 83.5, 34.8, 34.2, 29.3, 28.7, 23.2 (d,  $J_{\text{PC}}=10$  Hz), 21.4, 19.3, 17.5 (d,  $J_{\text{PC}}=2$  Hz), and 16.3 (d,  $J_{\text{PC}}=3$  Hz).

EI-MS ( $m/z$ ): 422( $[\text{M}]^+$ ), 407( $[\text{M}-\text{CH}_3]^+$ ), 379( $[\text{M}-i\text{Pr}]^+$ ).

Anal. Calcd for  $\text{C}_{27}\text{H}_{39}\text{N}_2\text{P}$ : C, 76.74; H, 9.30; N, 6.63. Found: C, 76.44; H, 9.33; N, 6.46.

### $[\text{CY}^5\text{NpN}^{\text{DIPP,Mes}}]\text{H}$ (**2.18c**)

A toluene solution of 2,4,6-trimethylphenylazide (1.004 g, 6.230 mmol) was added to the imine-phosphine **2.17a** (2.240 g, 6.230 mmol). The resulting mixture was transferred to a Kontes-sealed thick glass reaction bomb containing a magnetic stir bar and was heated to 80 °C for two days while being stirred. After the reaction was complete, the toluene was removed under vacuum, and the resulting brown sticky oil was dissolved in 5 mL of *n*-pentane and was cooled to -35 °C. The product crystallized out of solution as white crystals, which were collected on a glass frit and were dried under vacuum. Yield: 2.523 g, 5.121 mmol, 82.20%.

$^1\text{H}$  NMR (400 MHz,  $d_6$ -benzene, 298 K):  $\delta$  9.39 (s, 1H, *NH*), 7.27-7.14 (m, overlap with residual solvent peak), 7.06 (s, 2H, *mes ArH*), 3.60 (sept, 2H,  $^3J_{\text{HH}}=6.9$  Hz, *NAr-<sup>i</sup>PrCH*), 2.67 (s, 6H, *mes-(CH<sub>3</sub>)<sub>2</sub>*), 2.40 (s, 3H, *mes-CH<sub>3</sub>*), 2.26-2.16 (m, 4H), 1.69 (quint, 2H,  $^3J_{\text{HH}}=7.0$  Hz, *CH<sub>2</sub>CH<sub>2</sub>CH<sub>2</sub>*), and 1.34-1.16 (m, 24H).

$^{31}\text{P}\{^1\text{H}\}$  NMR (121 MHz,  $d_6$ -benzene, 298 K):  $\delta$  18.6 (s).

$^{13}\text{C}\{^1\text{H}\}$  NMR (101 MHz,  $d_6$ -benzene, 298 K):  $\delta$  164.3 (d,  $J_{\text{PC}}=4$  Hz), 147.4, 146.7 (d,  $J_{\text{PC}}=3$  Hz), 137.0, 131.5 (d,  $J_{\text{PC}}=7$  Hz), 129.3 (d,  $J_{\text{PC}}=2$  Hz), 127.4, 126.6 (d,  $J_{\text{PC}}=3$  Hz), 123.6, 85.0, 83.8, 34.7 (d,  $J_{\text{PC}}=13$  Hz), 34.3 (d,  $J_{\text{PC}}=13$  Hz), 29.6, 29.0, 28.4, 25.1, 23.3, 23.1 (d,  $J_{\text{PC}}=10$  Hz), 21.2, 20.9, 17.6 (d,  $J_{\text{PC}}=2$  Hz), and 16.5 (d,  $J_{\text{PC}}=3$  Hz).

EI-MS ( $m/z$ ): 492( $[\text{M}]^+$ ), 477( $[\text{M}-\text{CH}_3]^+$ ), 449( $[\text{M}-i\text{Pr}]^+$ ).

Anal. Calcd for C<sub>32</sub>H<sub>49</sub>N<sub>2</sub>P: C, 78.00; H, 10.02; N, 5.69. Found: C, 78.23; H, 10.26; N, 5.96.

**INDN<sup>D</sup>IPP (2.19)**

1-Indanone (15.46 g, 117.0 mmol) and 2,6-diisopropylaniline (20.74 g, 117.0 mmol) were added to a 250 mL Schlenk flask equipped with a Dean-Stark trap. The flask was charged with 150 mL of toluene, and under vigorous stirring, N<sub>2</sub> gas was flushed through the system under high pressure for a period of 1.5 hours. After purging, the reaction mixture was heated to 100 °C before a catalytic amount of *p*-toluenesulfonic acid (~0.2 g) was added. The reaction mixture was then heated to 110 °C while being stirred for four days, with the reaction being monitored by the water collected in the Dean-Stark trap. After completion, the reaction mixture was cooled to room temperature, dried over anhydrous MgSO<sub>4</sub>, and filtered. The toluene was removed *in vacuo*, affording a dark orange, viscous oil. This was redissolved in diethyl ether and was poured in a crystallization dish. Slow evaporation resulted in the formation of bright yellow crystals under brown oil. The crystals were transferred to a Büchner funnel and were washed with pentane cooled to -35 °C. The crude product was purified by vacuum sublimation (130 °C, 10<sup>-1</sup> mbar). Yield: 9.85 g, 33.8 mmol, 28.9%. X-ray quality crystals were grown from slow evaporation of a diethyl ether solution of **2.19**.

<sup>1</sup>H NMR (300 MHz, *d*<sub>6</sub>-benzene, 298 K): δ 8.21 (d, 1H, <sup>3</sup>J<sub>HH</sub>=7.2 Hz, ArCH), 7.24-6.99 (m, overlap with residual solvent peak), 3.05 (sept, 2H, <sup>3</sup>J<sub>HH</sub>=6.9 Hz, NAr-<sup>i</sup>PrCH), 2.52 (t, 2H, <sup>3</sup>J<sub>HH</sub>=6.7 Hz, α-CH<sub>2</sub>), 2.19 (t, 2H, <sup>3</sup>J<sub>HH</sub>=6.2 Hz, β-CH<sub>2</sub>), 1.23 (d, 6H, <sup>3</sup>J<sub>HH</sub>=6.8 Hz, NAr-<sup>i</sup>PrCH<sub>3</sub>), and 1.17 (d, 6H, <sup>3</sup>J<sub>HH</sub>=6.9 Hz, NAr-<sup>i</sup>PrCH<sub>3</sub>).

<sup>13</sup>C{<sup>1</sup>H} NMR (101 MHz, *d*<sub>6</sub>-benzene, 298 K): δ 174.2, 150.6, 148.5, 139.7, 136.3, 131.9, 127.5, 126.0, 124.0, 123.6, 123.5, 30.5, 28.7, 28.0, 23.8, and 23.1.

EI-MS (*m/z*): 291([M]<sup>+</sup>), 276 ([M-CH<sub>3</sub>]<sup>+</sup>).

Anal. Calcd for C<sub>21</sub>H<sub>25</sub>N: C, 86.55; H, 8.65; N, 4.81. Found: C, 86.48; H, 8.51; N, 4.76.

**<sup>IND</sup>NpN<sub>3</sub>H<sup>DIPP,DIPP</sup> (2.20)**

A 500 mL Schlenk flask charged with imine **2.19** (6.72 g, 23.1 mmol) and 100 mL diethyl ether was cooled to -78 °C. In a separate 250 mL Schlenk flask, lithium diisopropylamide (LDA) was prepared by the addition of 1.6 M *n*-butyllithium in hexanes (14.4 mL, 23.0 mmol) to diisopropylamine (3.6 mL, 26 mmol) in diethyl ether cooled to -78 °C. The LDA solution was allowed to stir for 30 minutes while warming to room temperature, before being cooled back to -78 °C. The cooled LDA solution was then transferred via cannula to the solution of **2.19**. The resulting mixture was stirred for 1 hour while being allowed to warm to room temperature. Upon warming, the color of the solution changed from yellow to brownish-green. The solution was then cooled back to -78 °C and chlorodiisopropylphosphine (3.7 mL, 23 mmol) in 100 mL of diethyl ether was added dropwise over the course of 1 hour. The resulting orange solution was allowed to slowly warm to room temperature and was stirred overnight. The volatiles were then removed in vacuo and the resulting pale yellow paste was extracted in hexanes and was filtered through celite to remove LiCl. A brownish-yellow filtrate was obtained, which was dried under vacuum yielding a thick brown oil. The product was then dissolved in hexanes (20 mL) and 2,6-diisopropylphenylazide (4.69 g, 23.1 mmol) was added to the solution, which was stirred overnight. The solution was concentrated to 10 mL and was stored at -35 °C for 1 hour. Yellow crystalline material was obtained, which was collected on a glass frit, rinsed with hexanes and dried under vacuum. Yield: 8.3 g, 14 mmol, 61%.

<sup>1</sup>H NMR (300 MHz, *d*<sub>6</sub>-benzene, 298 K): δ 11.62 (s, 1H, NH), 7.27-7.12 (m, overlap with residual solvent peak), 6.99 (t, 1H, <sup>3</sup>J<sub>HH</sub>=7.4 Hz, ArH), 6.75 (t, 1H, <sup>3</sup>J<sub>HH</sub>=7.6 Hz, ArH), 6.58 (d, 1H, <sup>3</sup>J<sub>HH</sub>=7.9 Hz, ArH), 3.61-3.40 (m, 4H, NAr-<sup>i</sup>PrCH), 3.15 (s, 2H, β-CH<sub>2</sub>), 2.42-2.24 (m, 2H,

P-<sup>i</sup>PrCH), 1.32-1.26 (m, 18H, <sup>i</sup>PrCH<sub>3</sub>), 1.22 (d, 3H, <sup>3</sup>J<sub>HH</sub>=7.0 Hz, <sup>i</sup>PrCH<sub>3</sub>), 1.17 (d, 3H, <sup>3</sup>J<sub>HH</sub>=7.0 Hz, <sup>i</sup>PrCH<sub>3</sub>), 1.07 (d, 6H, <sup>3</sup>J<sub>HH</sub>=6.9 Hz, <sup>i</sup>PrCH<sub>3</sub>), 1.03 (d, 3H, <sup>3</sup>J<sub>HH</sub>=7.2 Hz, <sup>i</sup>PrCH<sub>3</sub>), and 0.98 (d, 3H, <sup>3</sup>J<sub>HH</sub>=7.2 Hz, <sup>i</sup>PrCH<sub>3</sub>).

<sup>31</sup>P{<sup>1</sup>H} NMR (121 MHz, *d*<sub>6</sub>-benzene, 298 K): δ 51.9 (s).

<sup>13</sup>C{<sup>1</sup>H} NMR (101 MHz, *d*<sub>6</sub>-benzene, 298 K): δ 162.9 (d, J<sub>PC</sub>=5 Hz), 150.2, 147.9, 146.6 (d, J<sub>PC</sub>=11 Hz), 140.8, 139.6 (d, J<sub>PC</sub>=15 Hz), 137.0, 127.5, 126.6, 125.2, 124.2 (d, J<sub>PC</sub>=2 Hz), 123.8, 123.3, 123.1, 75.3, 74.1, 37.3 (d, J<sub>PC</sub>=14 Hz), 29.4, 28.1, 25.5, 25.0, 22.4, 16.2 (d, J<sub>PC</sub>=3 Hz), and 15.7 (d, J<sub>PC</sub>=2 Hz).

EI-MS (*m/z*): 610 ([M]<sup>+</sup>), 364, 322, 278.

Anal. Calcd for C<sub>39</sub>H<sub>55</sub>N<sub>4</sub>P: C, 76.68; H, 9.08; N, 9.17. Found: C, 76.71; H, 9.09; N, 9.36.

#### [<sup>CY5</sup>NpN<sup>DIPP,DIPP</sup>]K(THF)<sub>2</sub> (**2.21a**)

A THF solution (10 mL) of **2.18a** (1.699 g, 3.177 mmol) was added to potassium hydride (0.140 g, 3.50 mmol) and was stirred for 18 hours before the dark yellow solution was filtered through celite to remove excess KH. The filtrate was dried under vacuum, yielding the product as a pale yellow powder. Yield: 1.610 g, 2.245 mmol, 70.66%.

<sup>1</sup>H NMR (400 MHz, *d*<sub>6</sub>-benzene, 298 K): δ 7.18-7.13 (m, overlap with residual solvent peak), 7.07 (t, 1H, <sup>3</sup>J<sub>HH</sub>=7.4 Hz, ArH), 6.92 (t, 1H, <sup>3</sup>J<sub>HH</sub>=7.3 Hz, ArH), 4.27 (sept, 2H, <sup>3</sup>J<sub>HH</sub>=6.8 Hz, NAr-<sup>i</sup>PrCH), 3.48 (sept, 2H, <sup>3</sup>J<sub>HH</sub>=6.9 Hz, NAr-<sup>i</sup>PrCH), 3.30-3.26 (m, 8H, THF-CH<sub>2</sub>{2,5}), 2.97-2.90 (m, 2H, P<sup>i</sup>PrCH), 2.76 (t, 2H, <sup>3</sup>J<sub>HH</sub>=6.3 Hz, NArCCH<sub>2</sub>CH<sub>2</sub>CH<sub>2</sub>), 2.22 (t, 2H, <sup>3</sup>J<sub>HH</sub>=7.2 Hz, <sup>i</sup>Pr<sub>2</sub>PCCH<sub>2</sub>CH<sub>2</sub>CH<sub>2</sub>), 1.86 (quin, 2H, <sup>3</sup>J<sub>HH</sub>=6.7 Hz, CH<sub>2</sub>CH<sub>2</sub>CH<sub>2</sub>), 1.45 (d, 6H, <sup>3</sup>J<sub>HH</sub>=6.7 Hz, <sup>i</sup>PrCH<sub>3</sub>), 1.33-1.24 (m, 26H, overlap THF-CH<sub>2</sub>{3,4} with <sup>i</sup>PrCH<sub>3</sub>), and 1.10 (d, 12H, <sup>3</sup>J<sub>HH</sub>=6.8 Hz, <sup>i</sup>PrCH<sub>3</sub>).

<sup>31</sup>P{<sup>1</sup>H} NMR (161 MHz, *d*<sub>6</sub>-benzene, 298 K): δ 16.2 (s).

$^{13}\text{C}\{^1\text{H}\}$  NMR (101 MHz,  $d_6$ -benzene, 298 K):  $\delta$  172.2 (d,  $J_{\text{PC}}=9$  Hz), 153.7, 148.9 (d,  $J_{\text{PC}}=7$  Hz), 143.0, 142.9, 141.7, 123.7 (d,  $J_{\text{PC}}=1$  Hz), 123.4, 120.6, 118.6 (d,  $J_{\text{PC}}=2$  Hz), 74.1, 73.1, 67.7, 36.1, 36.0 (d,  $J_{\text{PC}}=3$  Hz), 28.1, 27.6, 27.1, 26.9, 26.7, 25.8, 25.7, 25.1, 24.8, 24.0, 18.7 (d,  $J_{\text{PC}}=3$  Hz), and 18.4.

Anal. Calcd for  $\text{C}_{43}\text{H}_{70}\text{KN}_2\text{O}_2\text{P}$ : C, 72.02; H, 9.84; N, 3.91. Found: C, 71.62; H, 9.60; N, 4.11.

**$[\text{CY}^5\text{NpN}^{\text{DMP,DMP}}]\text{K}(\text{THF})_{0.25}$  (2.21b)**

A THF solution (10 mL) of **2.18b** (1.709 g, 4.044 mmol) was added to potassium hydride (0.178 g, 4.44 mmol) and was stirred for 18 hours before the dark yellow solution was filtered through celite to remove excess KH. The filtrate was removed under vacuum, yielding a dark grey residue. The residue was redissolved in hexanes and was again dried under vacuum, giving the product as a grey foam. Yield: 1.56 g, 3.26 mmol, 80.5%.

$^1\text{H}$  NMR (400 MHz,  $d_6$ -benzene, 298 K):  $\delta$  7.16-7.13 (m, overlap with residual solvent peak), 6.89 (t, 1H,  $^3J_{\text{HH}}=7.4$  Hz, ArH), 6.79 (t, 1H,  $^3J_{\text{HH}}=7.1$  Hz, ArH), 3.27-3.23 (m, 1H, THF- $\text{CH}_2\{2,5\}$ )

), 2.71 (t, 2H,  $^3J_{\text{HH}}=6.4$  Hz, NArCCH<sub>2</sub>CH<sub>2</sub>CH<sub>2</sub>), 2.54 (s, 8H, overlap of Ar-(CH<sub>3</sub>)<sub>2</sub> with P<sup>i</sup>PrCH), 2.20 (s, 6H, Ar-(CH<sub>3</sub>)<sub>2</sub>), 2.15 (t, 2H,  $^3J_{\text{HH}}=7.4$  Hz, <sup>i</sup>Pr<sub>2</sub>PCCH<sub>2</sub>CH<sub>2</sub>CH<sub>2</sub>), 1.88 (quin, 2H,  $^3J_{\text{HH}}=6.7$  Hz, CH<sub>2</sub>CH<sub>2</sub>CH<sub>2</sub>), 1.36-1.32 (m, 1H, THF-CH<sub>2</sub>{3,4}), and 1.26-1.19 (m, 12H, P<sup>i</sup>PrCH<sub>3</sub>).

$^{31}\text{P}\{^1\text{H}\}$  NMR (161 MHz,  $d_6$ -benzene, 298 K):  $\delta$  18.0 (s).

$^{13}\text{C}\{^1\text{H}\}$  NMR (101 MHz,  $d_6$ -benzene, 298 K):  $\delta$  171.1 (d,  $J_{\text{PC}}=9$  Hz), 156.8, 152.1 (d,  $J_{\text{PC}}=6$  Hz), 132.3 (d,  $J_{\text{PC}}=8$  Hz), 131.1, 128.8, 119.3, 117.4, 72.3, 71.3, 67.7, 36.3 (d,  $J_{\text{PC}}=13$  Hz), 35.9 (d,  $J_{\text{PC}}=15$  Hz), 28.6, 27.9, 25.7, 25.3 (d,  $J_{\text{PC}}=11$  Hz), 21.2, 19.9, 18.0, and 17.9 (d,  $J_{\text{PC}}=3$  Hz).

Anal. Calcd for  $\text{C}_{28}\text{H}_{40}\text{KN}_2\text{O}_{0.25}\text{P}$ : C, 70.25; H, 8.42; N, 5.85. Found: C, 70.17; H, 8.32; N, 6.02.

**[<sup>CY5</sup>NpN<sup>DIPP,Mes</sup>]K (2.21c)**

A THF solution (10 mL) of **2.18c** (2.051 g, 4.162 mmol) was added to potassium hydride (0.184 g, 4.58 mmol). The resulting suspension was stirred for 18 hours before the dark yellow solution was filtered through celite to remove excess KH. The filtrate was dried under vacuum, giving a sticky pale yellow, tarry residue. The residue was triturated with hexanes and was again dried under vacuum, yielding a pale yellow powder. Yield: 1.71 g, 3.21 mmol, 77.2 %.

<sup>1</sup>H NMR (400 MHz, *d*<sub>6</sub>-benzene, 298 K): δ 7.18-7.16 (m, overlap with residual solvent peak), 7.05 (t, 1H, <sup>3</sup>J<sub>HH</sub>=7.5 Hz, 2,6-<sup>i</sup>Pr<sub>2</sub>Ar-*para-H*), 6.96 (s, 2H, 2,4,6-Me<sub>3</sub>Ar-*H*), 3.46 (sept, 2H, <sup>3</sup>J<sub>HH</sub>=6.8 Hz, NAr-<sup>i</sup>PrCH), 2.71 (t, 2H, <sup>3</sup>J<sub>HH</sub>=6.2 Hz, ArNCCH<sub>2</sub>CH<sub>2</sub>CH<sub>2</sub>), 2.55-2.47 (m, 8H, mes-(CH<sub>3</sub>)<sub>2</sub> overlap with <sup>i</sup>PrCH), 2.28 (s, 3H, mes-CH<sub>3</sub>), 2.20 (t, 2H, <sup>3</sup>J<sub>HH</sub>=7.1 Hz, <sup>i</sup>Pr<sub>2</sub>PCCH<sub>2</sub>CH<sub>2</sub>CH<sub>2</sub>), 1.86 (quin, 2H, <sup>3</sup>J<sub>HH</sub>=6.6 Hz, CH<sub>2</sub>CH<sub>2</sub>CH<sub>2</sub>), 1.35 (d, 6H, <sup>3</sup>J<sub>HH</sub>=6.8 Hz, <sup>i</sup>PrCH<sub>3</sub>), 1.28-1.20 (m, 12 H, <sup>i</sup>PrCH<sub>3</sub>), and 1.09 (d, 6H, <sup>3</sup>J<sub>HH</sub>=6.9 Hz, <sup>i</sup>PrCH<sub>3</sub>).

<sup>31</sup>P{<sup>1</sup>H} NMR (121 MHz, *d*<sub>6</sub>-benzene, 298 K): δ 17.9 (s).

<sup>13</sup>C{<sup>1</sup>H} NMR (101 MHz, *d*<sub>6</sub>-benzene, 298 K): δ 172.3 (d, J<sub>PC</sub>=9 Hz), 153.5, 149.1 (d, J<sub>PC</sub>= 6 Hz), 141.8, 131.9 (d, J<sub>PC</sub>= 7 Hz), 129.6, 125.8, 123.3, 120.6, 72.4, 71.4, 36.4 (d, J<sub>PC</sub>= 13 Hz), 36.0 (d, J<sub>PC</sub>=15 Hz), 28.5, 27.8, 27.5, 25.5, 25.4, 25.0, 24.6, 20.8, 17.9 (d, J<sub>PC</sub>= 3 Hz), and 17.8. Anal. Calcd for C<sub>32</sub>H<sub>48</sub>KN<sub>2</sub>P: C, 72.41; H, 9.11; N, 5.28. Found: C, 72.48; H, 8.93; N, 5.45.

**(<sup>IND</sup>NpN<sup>DIPP,DIPP</sup>)K (2.22)**

Compound **2.20** (8.28 g, 13.5 mmol) was dissolved in toluene and was transferred into a Kontes-sealed thick glass reaction bomb. The solution was heated to 100 °C for 5 days. After the allotted reaction time, the volatiles were removed under vacuum, yielding a dark orangish-brown tar-like material. The product was dissolved in THF before being transferred to a reaction vessel containing potassium hydride (0.60 g, 15 mmol). The resulting suspension was stirred overnight

before being filtered through a plug of celite. The filtrate was dried under vacuum, giving a black-tar like material. This material was triterated with hexanes and was again dried under vacuum, yielding a pale green solid. Yield: 7.9 g, 13 mmol, 94%. NMR characterization performed with THF adduct of **2.22**. Single crystals of **2.22** suitable for X-ray crystallography were grown from a saturated diethyl ether solution cooled to -35 °C.

$^1\text{H}$  NMR (400 MHz,  $d_6$ -benzene, 298 K):  $\delta$  7.35 (d, 1H,  $^3J_{\text{HH}}=7.3$  Hz, ArH), 7.26 (d, 2H,  $^3J_{\text{HH}}=7.1$  Hz, ArH), 7.20-7.14 (m, overlap with residual solvent peak), 7.08 (t, 1H,  $^3J_{\text{HH}}=7.3$  Hz, ArH), 7.01 (d, 1H,  $^3J_{\text{HH}}=7.8$  Hz, ArH), 6.96 (t, 1H,  $^3J_{\text{HH}}=7.5$  Hz, ArH), 6.87 (t, 1H,  $^3J_{\text{HH}}=7.5$  Hz, ArH), 4.27 (sept, 2H,  $^3J_{\text{HH}}=6.8$  Hz, NAr- $^i\text{PrCH}$ ), 3.81 (s, 2H,  $\beta$ - $\text{CH}_2$ ), 3.61 (sept, 2H,  $^3J_{\text{HH}}=6.9$  Hz, NAr- $^i\text{PrCH}$ ), 3.24-3.21 (m, 4H, THF- $\text{CH}_2\{2,5\}$ ), 3.11-3.04 (m, 2H, P- $^i\text{PrCH}$ ), 1.36-1.26 (m, 24H), 1.18-1.14 (m, 12H,  $^i\text{PrCH}_3$ ), and 1.08 (d, 6H,  $^3J_{\text{HH}}=5.3$  Hz,  $^i\text{PrCH}_3$ ).

$^{31}\text{P}\{^1\text{H}\}$  NMR (121 MHz,  $d_6$ -benzene, 298 K):  $\delta$  15.9 (s).

$^{13}\text{C}\{^1\text{H}\}$  NMR (101 MHz,  $d_6$ -benzene, 298 K):  $\delta$  165.0 (d,  $J_{\text{PC}}=9$  Hz), 153.2, 148.4 (d,  $J_{\text{PC}}=7$  Hz), 147.1 (d,  $J_{\text{PC}}=11$  Hz), 144.1 (d,  $J_{\text{PC}}=14$  Hz), 143.0 (d,  $J_{\text{PC}}=7$  Hz), 141.2, 125.7, 124.8 (d,  $J_{\text{PC}}=26$  Hz), 124.0 (d,  $J_{\text{PC}}=2$  Hz), 123.8, 123.7 (d,  $J_{\text{PC}}=1$  Hz), 120.4, 119.0 (d,  $J_{\text{PC}}=2$  Hz), 80.1, 79.0, 67.7, 39.5 (d,  $J_{\text{PC}}=12$  Hz), 28.1, 27.5, 26.8, 26.5, 25.6, 25.4, 24.6, 23.7, 18.9 (d,  $J_{\text{PC}}=3$  Hz), and 18.3.

Anal. Calcd for  $\text{C}_{39}\text{H}_{54}\text{KN}_2\text{P}$ : C, 75.44; H, 8.77; N, 4.51. Found: C, 75.23; H, 8.89; N, 4.21.

#### $[\text{CY}^5\text{NpN}^{\text{DIPP,DIPP}}]\text{FeBr}$ (**2.23a**)

A toluene solution (10 mL) of **2.21a** (0.500 g, 0.873 mmol) was added to  $\text{FeBr}_2(\text{THF})_2$  (0.312 g, 0.873 mmol). The resulting mixture was stirred for 18 hours before being filtered through celite to remove the KBr by-product. The filtrate was dried under vacuum, yielding an

orange powder. Single crystals of **2.23a** suitable for X-ray diffraction were grown from a concentrated toluene solution cooled to -35 °C. Yield: 0.483g, 0.722 mmol, 82.7%.

<sup>1</sup>H NMR (300 MHz, *d*<sub>6</sub>-benzene, 298 K): δ 109.6 (s, 2H), 40.7 (s, 2H), 37.8 (s, 2H), 26.7 (s, 2H), 19.2 (s, 2H), 6.4 (s, 6H), 4.5 (s, 8H), 3.3 (s, 3H), 1.2 (s, 8H), -0.6 (s, 6H), -16.6 (s, 6H), -19.9 (s, 6H), -23.2 (s, 1H), and -28.6 (s, 1H).

<sup>1</sup>H NMR (400 MHz, *d*<sub>8</sub>-THF, 298 K): δ 101.6 (s, 2H), 31.7 (s, 2H), 27.2 (s, 2H), 15.9 (s, 2H), 5.8 (s, 6H), 5.0 (s, 6H), 1.1 (s, 6H), -1.8 (s, 2H), -4.0 (s, 6H), -12.6 (s, 6H), -26.9 (s, 1H), and -27.8 (s, 1H).

$\mu_{\text{eff}}=5.3 \mu_{\text{B}}$  (Evans).

Anal. Calcd for C<sub>35</sub>H<sub>54</sub>BrFeN<sub>2</sub>P: C, 62.79; H, 8.13; N, 4.18. Found: C, 62.46; H, 8.10; N, 4.42.

#### **([<sup>CY5</sup>NpN<sup>DMP,DMP</sup>]FeBr)<sub>2</sub> (2.23b)**

A toluene solution (10 mL) of **2.21b** (0.606 g, 1.27 mmol) was added to FeBr<sub>2</sub>(THF)<sub>2</sub> (0.453 g, 1.27 mmol). The resulting mixture was stirred for 18 hours before the resulting murky yellow solution was filtered through a glass filter pad to remove the KBr by-product. The filtrate was dried under vacuum, yielding a yellow powder. Single crystals of **2.23b** suitable for X-ray diffraction were grown by slow vapor diffusion of *n*-pentane into a concentrated toluene solution of **2.23b** cooled to -35 °C. Yield: (0.273 g, 0.490 mmol, 38.7%).

<sup>1</sup>H NMR (400 MHz, *d*<sub>8</sub>-THF, 298 K): δ 88.0 (s, 2H), 31.4 (s, 6H), 29.5 (s, 2H), 22.4 (s, 2H), 18.7 (s, 2H), 16.2 (s, 2H), 14.8 (s, 2H), 7.4 (s, 6H), 7.2 (s, 8H), -3.3 (s, 2H), -36.8 (s, 1H), and -39.9 (s, 1H).

$\mu_{\text{eff}}=4.2 \mu_{\text{B}}$  (Evans).

Anal. Calcd for C<sub>27</sub>H<sub>38</sub>BrFeN<sub>2</sub>P: C, 58.19; H, 6.87; N, 5.03. Found: C, 57.86; H, 6.55; N, 5.33.

**$[\text{CY}^5\text{NpN}^{\text{DIPP,Mes}}]\text{FeBr}_2$  (**2.23c**)**

A 10 mL THF solution of **2.21c** (0.953 g, 1.79 mmol) was added to  $\text{FeBr}_2(\text{THF})_2$  (0.642 g, 1.79 mmol). The resulting mixture was stirred for 18 hours and the resulting opaque yellow suspension was filtered through celite to remove the KBr byproduct. The celite was rinsed with 50 mL of THF and the yellow filtrate was dried under vacuum, yielding a yellow powder. Yield: (0.784 g, 1.25 mmol, 69.6 %). Complex **2.23c** is insoluble in nonpolar and aromatic solvents, and is only moderately soluble in THF. Single crystals of **2.23c** suitable for X-ray diffraction were grown from a THF solution cooled to  $-35\text{ }^\circ\text{C}$ .

$^1\text{H}$  NMR (300 MHz,  $d_8$ -THF, 298 K):  $\delta$  84.8 (s, 2H), 37.5 (s, 2H), 28.4 (s, overlap with 28.04, 7H), 23.8 (s, 2H), 18.0 (s, 2H), 14.0 (s, 2H), 8.5 (s, 6H), 6.1 (s, 6H), 4.4 (s, 6H), -1.4 (s, 2H), -10.6 (s, 6H), and -31.7 (s, 1H).

$\mu_{\text{eff}} = 4.0\ \mu_{\text{B}}$  (Evans).

Anal. Calcd for  $\text{C}_{32}\text{H}_{48}\text{BrFeN}_2\text{P}$ : C, 61.25; H, 7.71; N, 4.46. Found: C, 60.99; H, 7.71; N, 4.70.

**$[\text{INDNpN}^{\text{DIPP,DIPP}}]\text{FeBr}_2$  **2.24****

A 50mL round bottom flask was charged with **2.22** (2.958 g, 4.764 mmol) and 20mL of THF. To this solution was added 20 mL of diethyl ether and  $\text{FeBr}_2(\text{THF})_2$  (1.714 g, 4.764 mmol). The reaction mixture gradually became cloudy brown in appearance and was stirred for 18 hours, after which time the suspension was filtered through a glass frit packed with celite to remove KBr. The volatiles were removed in vacuo, yielding an orange powder. Yield: 2.899 g, 4.040 mmol, 84.80%. Single crystals of **2.24** suitable for X-ray diffraction were grown from a concentrated toluene solution cooled to  $-35\text{ }^\circ\text{C}$ .

$^1\text{H}$  NMR (300 MHz,  $d_6$ -benzene, 298 K):  $\delta$  208.4 (s, 2H), 41.8 (s, 4H), 37.2 (s, 2H), 27.9 (s, 2H), 18.6 (s, 2H), 15.0 (s, 2H), 6.3 (s, 12H), 4.0 (s, 2H), 1.6 (s, 2H), -0.9 (s, 6H), -18.4 (s overlap with peak at -22.8, 16H), -28.1 (s, 1H), and -33.0 (s, 1H).

$\mu_{\text{eff}}=5.2 \mu_{\text{B}}$  (evans).

Anal. Calcd for  $\text{C}_{39}\text{H}_{54}\text{BrFeN}_2\text{P}$ : C, 65.28; H, 7.59; N, 3.90. Found: C, 65.29; H, 7.49; N, 3.76.

#### **Impure ( $[\text{CY}^5\text{NpN}^{\text{DIPP,DIPP}}\text{Fe}]_2(\mu\text{-N}_2)$ ) (2.25a)**

To a suspension of  $\text{KC}_8$  (72 mg, 0.53 mmol) in hexanes (30 mL) was added complex **2.23a** (357 mg, 0.533 mmol). The resulting suspension was stirred for one day at room temperature before being filtered through a glass microfiber filter pad to remove the graphite and KBr by-products. The resulting dark red filtrate was dried under vacuum and was redissolved in *n*-pentane. The red solution was again filtered through a glass microfiber filter pad before being cooled to  $-35\text{ }^\circ\text{C}$ . The solid state molecular structure of **2.25a** was obtained through crystal picking of the resulting crystals obtained from the cooled product mixture solution. Crystals of **2.25a** appeared as black needles.

#### **Impure ( $[\text{CY}^5\text{NpN}^{\text{DMP,DMP}}][\text{CY}^5\text{NP}]\text{Fe}$ ) (2.25b)**

A suspension of  $\text{KC}_8$  (131 mg, 0.972 mmol) in THF (5 mL) was prepared in a 20 mL scintillation vial and was cooled in a dinitrogen glovebox coldwell to  $-198\text{ }^\circ\text{C}$ . After the  $\text{KC}_8$  suspension was frozen solid, a magnetic stir bar was placed on top of the frozen THF and a separate THF solution (10 mL) of **2.23b** (542 mg, 0.972 mmol) was layered on top. As the THF thawed, the suspension was stirred and was allowed to gradually warm to room temperature. The mixture was stirred overnight, resulting in a dark red solution. The graphite and by-product salts were removed via filtration through a glass-fiber filter pad. The filtrate was dried under vacuum,

and the resulting solids were triturated with hexanes before again being dried. A crystal of **2.25b** was grown as a red needle from a concentrated *n*-pentane solution cooled to -35 °C.

**$[(^{CY5}NpN^{DIPP,Mes})_2Fe](\mu-N_2)$  (**2.25c**)**

To a suspension of  $KC_8$  (39 mg, 0.29 mmol) in hexanes (5 mL) was added complex **2.23c** (184 mg, 0.294 mmol). The resulting suspension was stirred for one day at room temperature before being filtered through a glass microfiber filter pad to remove the graphite and KBr by-products. The resulting dark red filtrate was dried under vacuum, yielding the product as a red powder. Yield: 89 mg, 0.079 mmol, 54%. Crystalline material suitable for X-ray diffraction was grown from an *n*-pentane solution cooled to -35 °C. Crystalline material containing one molecule of *n*-pentane per molecule of **2.25c** was used for elemental analysis.

$^1H$  NMR (300 MHz,  $d_6$ -benzene, 298 K):  $\delta$  58.4 (s, 2H), 44.0 (s, 4H), 42.1 (s, 2H), 37.2 (s, 2H), 33.8 (s, 2H), 31.9 (s, 2H), 24.6 (s, 2H), 10.9 (s, 6H), 5.8 (s, 1H), 5.0 (s, 3H), -2.6 (s, 4H), -24.0 (s, 6H), -24.6 (broad s), -33.9 (s, 6H), and -41.0 (s, 6H).

$\mu_{eff}=6.2 \mu_B$  (Evans).

Anal. Calcd for  $C_{69}H_{108}Fe_2N_6P_2$ : C, 69.33; H, 9.11; N, 7.03. Found: C, 69.78; H, 9.22; N, 7.03.

**$[^{CY5}NpN^{DIPP,DIPP}]Fe(\mu-N-DIPP)Fe[^{CY5}NP^{DIPP}]$  (**2.26**)**

A Kontes-sealed reaction bomb was charged with complex **2.23a** (132 mg, 0.197 mmol) and  $KC_8$  (27 mg, 0.20 mmol). The mixture was suspended in 40 mL of hexanes. The suspension underwent three freeze-pump-thaw cycles to remove  $N_2$  gas from the reaction mixture. The contents of the bomb were stirred for two days under vacuum. After which time, the suspension was filtered through a glass microfiber filter pad to remove the graphite and KBr by-products. The solvent was removed under vacuum and the resulting residue was extracted with *n*-pentane and transferred to a 20 mL scintillation vial. The solvent was again removed under vacuum,

yielding the product as a red foam. Yield: 62 mg, 0.052 mmol, 53%. Single crystals of **2.26** suitable for X-ray diffraction were grown from a concentrated *n*-pentane solution cooled to -35 °C.

<sup>1</sup>H NMR (300 MHz, *d*<sub>6</sub>-benzene, 298 K): δ 122.9 (s), 118.6 (s), 54.1 (s), 47.9 (s), 47.0 (s), 45.4 (s), 43.6 (s), 42.8 (s), 42.0 (s), 40.6 (s), 39.8 (s), 36.1 (s), 35.5 (s), 34.5 (s), 32.6 (s), 31.1 (s), 25.2 (s), 23.6 (s), 19.2 (s), 17.9 (s), 17.0 (s), 15.6 (s), 14.9 (s), 13.9 (s), 13.1 (s), 11.9 (s), 10.6 (s), 9.1 (s), 8.3 (s), 6.3 (s), 3.4 (s), 2.8 (s), 1.2 (s), 0.9 (s), -0.9 (s), -1.3 (s), -2.7 (s), -3.2 (s), -4.3 (s), -4.9 (s), -5.4 (s), -7.3 (s), -12.0 (s), -13.5 (s), -16.3 (s), -18.7 (s), -21.5 (s), -22.4 (s), -33.0 (s), -42.3 (s), -46.3 (s), -53.9 (s), -54.4 (s), -74.2 (s), -86.6 (s), and -117.1 (s).

$\mu_{\text{eff}}=6.6 \mu_{\text{B}}$  (Evans).

Anal. Calcd for C<sub>70</sub>H<sub>108</sub>Fe<sub>2</sub>N<sub>4</sub>P<sub>2</sub>: C, 71.29; H, 9.23; N, 4.75. Found: C, 71.68; H, 9.45; N, 5.07.

**([<sup>IND</sup>NpN<sup>DIPP,DIPP</sup>]Fe)<sub>2</sub>(μ-N<sub>2</sub>) (2.27)**

Within a N<sub>2</sub> glovebox, the iron bromide complex **2.24** (0.961 g, 1.34 mmol) was added to a 50 mL round-bottomed flask with 30 mL of hexanes. To this suspension was added KC<sub>8</sub> (0.182 g, 1.34 mmol) and the resulting mixture was allowed to stir for 1 day. After the allotted reaction time, the product mixture was blood red in appearance, with graphite in suspension. This mixture was filtered through a glass frit packed with celite to remove graphite and by-product salts and the filtrate was collected in a Schlenk flask and dried under vacuum. The resulting red residue was redissolved in 10 mL of *n*-pentane and was transferred to a vial and cooled to -35 °C. A small amount of black, needle shaped crystals were obtained, which were used for both X-ray crystallography and <sup>1</sup>H NMR analysis. Yield of crystalline product: 0.138 g, 0.106 mmol, 15.8%). Complex **2.27** was only characterized by <sup>1</sup>H NMR spectroscopy and X-ray crystallography.

$^1\text{H}$  NMR (300 MHz,  $d_6$ -benzene, 298 K):  $\delta$  41.8 (s), 31.1 (s), 23.9 (s), 18.4 (s), 16.0 (s), 15.2 (s), 15.0 (s), 13.9 (s), 13.5 (s), 6.3 (s), -0.9 (s), -5.3 (s), -14.8 (s), -18.3 (s), -28.1 (s), -33.0 (s), -37.9 (s), and -41.9 (s).

**Predicted complex ( $[\text{INDNpN}^{\text{DIPP,DIPP}}\text{Fe}]_2(\mu\text{-N}_2)^2\text{Li}_2$  [2.28]**

A Schlenk flask was charged with a hexanes solution (20 mL) of **2.27** (75 mg, 0.057 mmol). The Schlenk flask was cooled to  $-78\text{ }^\circ\text{C}$  and 1.6 M *n*-butyllithium in hexanes (0.07 mL, 0.1 mmol) was added via syringe. The resulting mixture was then allowed to warm to ambient temperature and was stirred for 4 hours. A noticeable color change did not occur. The volatiles were removed under vacuum, yielding the product as a brown residue. [2.28] was only characterized by  $^1\text{H}$  NMR spectroscopy.

$^1\text{H}$  NMR (300 MHz,  $d_6$ -benzene, 298 K):  $\delta$  27.7 (s), 20.4 (s), 18.9 (s), 18.6 (s), 15.8 (s), 15.4 (s), 13.1 (s), 12.6 (s), 12.0 (s), 3.6 (s), 3.1 (s), 1.2 (s), 0.9 (s), -3.0 (s), -6.3 (s), -8.8 (s), and -11.8 (s).

**( $\text{INDNpN}^{\text{DIPP,DIPP}}\text{KLi}(\text{THF})$  (2.29)**

A Schlenk flask charged with a yellow diethyl ether (20 mL) solution of **2.22** (0.957 g, 1.38 mmol) was cooled to  $-78\text{ }^\circ\text{C}$ . A 1.6 M *n*-butyllithium solution in hexanes (0.86 mL, 1.4 mmol) was added via syringe to the cooled solution of **2.22**. The resulting mixture was then allowed to warm to ambient temperature, becoming viscous and acquiring a purple color. After stirring at ambient temperature for 1 hour, the volatiles were removed under vacuum and the resulting silvery-purple solid was dissolved in THF (10 mL) and stored at  $-35\text{ }^\circ\text{C}$  overnight to grow crystalline product. The purple crystalline solids were collected on a glass frit and were washed with hexanes before being dried under vacuum for 3 hours. After the drying procedure, the crystals changed color from purple to turquoise. Yield: 0.607 g, 0.868 mmol, 62.9%. Single crystals of **2.29** suitable for X-ray diffraction were grown from a THF solution cooled to  $-35\text{ }^\circ\text{C}$ .

Drying samples of **2.29** under vacuum for extended periods of time causes the loss of three of the THF molecules found in the solid state structure, as determined by  $^1\text{H}$  NMR spectroscopy.

$^1\text{H}$  NMR (400 MHz,  $d_8$ -THF, 298 K):  $\delta$  6.94 (d, 2H,  $^3J_{\text{HH}}=7.9$  Hz, ArH), 6.81 (d, 2H,  $^3J_{\text{HH}}=7.4$  Hz, ArH), 6.77-6.72 (m, 2H, ArH), 6.53 (t, 1H,  $^3J_{\text{HH}}=7.4$  Hz, ArH), 6.30 (d, 1H,  $^3J_{\text{HH}}=8.3$  Hz, ArH), 5.91 (t, 1H,  $^3J_{\text{HH}}=7.2$  Hz, ArH), 5.45 (s, 1H,  $\beta$ -CH), 5.36 (t, 1H,  $^3J_{\text{HH}}=7.1$  Hz, ArH), 3.92-3.83 (m, 4H, NAr- $^i\text{PrCH}$ ), 3.62-3.57 (m, 8H, THF- $\text{CH}_2\{2,5\}$ , overlap of residual THF with coordinated THF), 2.76-2.67 (m, 2H, P- $^i\text{PrCH}$ ), 1.78-1.75 (m, 8H, THF- $\text{CH}_2\{3,4\}$ , overlap of residual THF with coordinated THF), 1.26-1.17 (m, 18H,  $^i\text{PrCH}_3$ ), 1.09 (d, 6H,  $^3J_{\text{HH}}=6.7$  Hz,  $^i\text{PrCH}_3$ ), 0.99 (d, 6H,  $^3J_{\text{HH}}=6.8$  Hz,  $^i\text{PrCH}_3$ ), and 0.92 (d, 6H,  $^3J_{\text{HH}}=6.7$  Hz,  $^i\text{PrCH}_3$ ).

$^{13}\text{C}\{^1\text{H}\}$  NMR (101 MHz,  $d_8$ -THF, 298 K): 157.9 (s), 148.7 (d,  $J_{\text{PC}}=8$  Hz), 148.5 (d,  $J_{\text{PC}}=8$  Hz), 144.7 (d,  $J_{\text{PC}}=5$  Hz), 144.0 (s), 126.4 (d,  $J_{\text{PC}}=18$  Hz), 125.2 (s), 123.3 (d,  $J_{\text{PC}}=3$  Hz), 122.3 (s), 120.5 (d,  $J_{\text{PC}}=3$  Hz), 119.2 (s), 116.9 (s), 115.8 (d,  $J_{\text{PC}}=16$  Hz), 114.5 (s), 105.8 (s), 89.6 (d,  $J_{\text{PC}}=68$  Hz), 88.9 (d,  $J_{\text{PC}}=30$  Hz), 68.0 (s), 28.9 (d,  $J_{\text{PC}}=58$  Hz), 28.4 (s), 27.9 (s), 26.6 (s), 26.2 (s), 24.6 (s), 23.3 (s), 19.2 (s), and 17.5 (s).

$^{31}\text{P}\{^1\text{H}\}$  NMR (121 MHz,  $d_8$ -THF, 298 K):  $\delta$  33.1 (s).

$^7\text{Li}$  NMR (155 MHz,  $d_8$ -THF, 298 K):  $\delta$  1.69 (s).

Anal. Calcd for  $\text{C}_{45}\text{H}_{61}\text{KLiN}_2\text{OP}$ : C, 73.89; H, 8.80; N, 4.01. Found: C, 73.54; H, 8.64; N, 3.97.

### Complex [2.30]

A purple THF (5 mL) solution of **2.29** (0.230 g, 0.329 mmol) was added to a small piece of magnesium ribbon (8 mg, 0.3 mmol). The solution of **2.29** was stirred vigorously over the Mg ribbon and an orange THF (5 mL) solution of trichloro(pentamethylcyclopentadienyl)titanium (IV) (0.095 g, 0.33 mmol) as slowly added via pipette into the solution of **2.29** over Mg. The mixture was left to stir overnight. Following the allotted reaction time, the intense blue reaction

mixture was filtered through celite to remove insoluble material and the filtrate was dried under vacuum. The resulting residue was triturated with hexanes and was again dried under vacuum, yielding a blue powder.

$^1\text{H}$  NMR (400 MHz,  $d_6$ -benzene, 298 K):  $\delta$  7.49 (dd, 1H,  $^3J_{\text{HH}}=7.2$  Hz,  $^3J_{\text{PH}}=1.9$  Hz,  $\beta\text{-CH}$ ), 7.13-6.96 (m, 6H, ArH), 5.07 (d, 1H,  $^3J_{\text{HH}}=3.4$  Hz, ArH), 4.78 (d, 1H,  $^3J_{\text{HH}}=7.6$  Hz, ArH), 4.21 (d, 1H,  $^3J_{\text{HH}}=6.7$  Hz, ArH), 4.15 (sept, 1H,  $^3J_{\text{HH}}=6.5$  Hz, NAr- $^i\text{PrCH}$ ), 3.77-3.71 (m, 2H), 3.59 (sept, 2H,  $^3J_{\text{HH}}=6.8$  Hz, NAr- $^i\text{PrCH}$ ), 3.38 (triplet overlap with broad resonance, 11H), 2.99 (sept, 1H,  $^3J_{\text{HH}}=6.7$  Hz, NAr- $^i\text{PrCH}$ ), 2.33-2.23 (m, 2H, P- $^i\text{PrCH}$ ), 2.07 (d, 3H,  $^3J_{\text{HH}}=6.7$  Hz,  $^i\text{PrCH}_3$ ), 1.79 (s, 11H), 1.46 (d, 3H,  $^3J_{\text{HH}}=6.8$  Hz,  $^i\text{PrCH}_3$ ), 1.41 (d, 3H,  $^3J_{\text{HH}}=7.1$  Hz,  $^i\text{PrCH}_3$ ), 1.37 (d, 3H,  $^3J_{\text{HH}}=7.2$  Hz,  $^i\text{PrCH}_3$ ), 1.32 (dd, 6H,  $^3J_{\text{HH}}=6.8$  Hz,  $^3J_{\text{PH}}=1.9$  Hz, P- $^i\text{PrCH}_3$ ), 1.13 (d, 3H,  $^3J_{\text{HH}}=6.7$  Hz,  $^i\text{PrCH}_3$ ), 1.08-0.95 (m, 15 H), and 0.95-0.84 (m, 4H).

$^{31}\text{P}\{^1\text{H}\}$  NMR (121 MHz,  $d_6$ -benzene, 298 K):  $\delta$  26.61 (s).

$^7\text{Li}$  NMR (155 MHz,  $d_6$ -benzene, 298 K):  $\delta$  1.12 (s) and -6.04 (s).

### $\text{INDNpN}^{\text{DIPP,DIPP}}$ (**2.31**)

A THF (5 mL) solution of **2.29** (90 mg, 0.13 mmol) was added to  $\text{FeBr}_2(\text{THF})_2$  (46 mg, 0.13 mmol) and the resulting suspension was stirred for 18 hours. The resulting mixture was murky brown in appearance and was filtered through a filter pipet packed with celite to remove the solid by-products. The filtrate was dried under vacuum, leaving a sticky orange residue. Trituration with hexanes yielded the product as an orange powder. Single crystals of **2.31** were grown from an *n*-pentane solution cooled to  $-35$  °C.

$^1\text{H}$  NMR (400 MHz,  $d_6$ -benzene, 298 K):  $\delta$  8.13 (d, 1H,  $^3J_{\text{HH}}=8.4$  Hz,  $\beta\text{-CH}$ ), 7.29 (d, 2H,  $^3J_{\text{HH}}=7.6$  Hz, ArH), 7.18-7.16 (overlap with residual solvent peak, ArH), 7.11 (t, 2H,  $^3J_{\text{HH}}=8.0$  Hz, ArH), 6.72 (t, 1H,  $^3J_{\text{HH}}=7.0$  Hz, ArH), 6.62 (d, 1H,  $^3J_{\text{HH}}=7.2$  Hz, ArH), 6.47 (t, 1H,  $^3J_{\text{HH}}=7.5$

Hz, ArH), 6.41 (d, 1H,  $^3J_{\text{HH}}=7.4$  Hz, ArH), 3.81 (sept, 2H,  $^3J_{\text{HH}}=6.8$  Hz, NAr- $^i\text{PrCH}$ ), 2.96 (sept, 2H,  $^3J_{\text{HH}}=6.9$  Hz, NAr- $^i\text{PrCH}$ ), 2.90-2.81 (m, 2H, P- $^i\text{PrCH}$ ), 1.38-1.26 (m, 24H,  $^i\text{PrCH}_3$ ), 1.14 (d, 6H,  $^3J_{\text{HH}}=6.9$  Hz,  $^i\text{PrCH}_3$ ), and 0.94 (d, 6H,  $^3J_{\text{HH}}=6.9$  Hz,  $^i\text{PrCH}_3$ ).

$^{31}\text{P}\{^1\text{H}\}$  NMR (121 MHz,  $d_6$ -benzene, 298 K):  $\delta$  2.8 (s).

### Attempted Functionalization of $\text{N}_2$ to $\text{NH}_3$ with **2.25c**

A diethyl ether solution (10 mL) of **2.25c** (0.006 g, 0.005 mmol, 2 mol%) in a 20 mL scintillation vial was cooled to  $-78$  °C in the glovebox coldwell.  $\text{KC}_8$  (0.036 g, 0.26 mmol) was added while the solution was vigorously stirred, followed by the addition of a cold ( $-78$  °C) diethyl ether solution (5 mL) of  $[\text{H}(\text{Et}_2\text{O})_2]^+[[3,5-(\text{CF}_3)_2\text{C}_6\text{H}_3]_4\text{B}]^-$  (0.272 g, 0.264 mmol). A large amount of gas was evolved, and the mixture was stirred for 1 hour as it was allowed to warm to ambient temperature. All of the material in the vial was transferred to a Schlenk flask, which was transported outside of the glovebox. A separate Schlenk flask was charged with HCl in  $\text{Et}_2\text{O}$  (4 mL, 1M) before being frozen at  $-196$  °C and degassed. The volatiles in the Schlenk flask containing the reaction mixture were transferred to the flask containing HCl in  $\text{Et}_2\text{O}$  via a distillation bridge. The flask containing the acid mixture was warmed to room temperature and stirred for 10 minutes. The volatiles were removed under vacuum and 1 mL of distilled  $\text{H}_2\text{O}$  was added to flask. The aqueous solution was tested for  $\text{NH}_4\text{Cl}$  using the indophenol method.<sup>121</sup>

### 6.3.2 Compounds Pertaining to Chapter 3

#### $[(^{\text{CY5}}\text{NpN}^{\text{DIPP,DIPP}})\text{FeH}]_2$ (**3.6a**)

Complex **2.23a** (0.242 g, 0.361 mmol) and potassium triethylborohydride (0.050 g, 0.36 mmol) were each dissolved separately in toluene (5 mL) and the two solutions were cooled to  $-35$  °C in the glovebox freezer. The cooled solution of  $\text{KBET}_3\text{H}$  was quickly added to the cooled solution of **2.23a** while the mixture was stirred with a magnetic stir bar. The reaction mixture

rapidly changed color from yellow-orange to dark brown and was allowed to stir for 3 minutes before being filtered through a filter pipet packed with celite. The filtrate was dried under vacuum and the resulting residue was redissolved in Et<sub>2</sub>O and again dried to give the product as an orange-brown powder. Yield: 0.161 g, 0.136 mmol, 75.6%. Single crystals of **3.6a** suitable for X-ray diffraction were grown from a toluene solution cooled to -35 °C.

<sup>1</sup>H NMR (400 MHz, *d*<sub>6</sub>-benzene, 25 °C): δ 31.8 (s), 29.5 (s), 23.4 (s), 20.3 (s), 17.9 (s), 13.6 (s), 11.3 (s), 9.6 (s), 9.0 (s), 8.5 (s), 6.7 (s), 6.6 (s), 5.7 (s), 5.2 (s), 4.0 (s), 3.8 (s), 3.0 (s), 2.6 (s), 1.3 (s), 1.1 (s), -0.0 (s), -0.3 (s), -0.7 (s), -1.2 (s), -5.5 (s), -8.6 (s), -9.7 (s), -11.9 (s), -23.5 (s), and -31.6 (s).

$\mu_{\text{eff}} = 4.2 \mu_{\text{B}}$  (evans)

Anal. Calcd. for C<sub>70</sub>H<sub>110</sub>Fe<sub>2</sub>N<sub>4</sub>P<sub>2</sub>: C, 71.17; H, 9.39; N, 4.74. Found: C, 71.33; H, 9.52; N, 4.61.

#### Isolation of Single Crystals of [(<sup>CY5</sup>NpN<sup>DIPP,Mes</sup>)FeH]<sub>2</sub> (**3.6b**)

Complex **2.23c** (0.360 g, 0.287 mmol) and potassium triethylborohydride (0.079 g, 0.57 mmol) were dissolved in 10 mL of 1:1 THF:Et<sub>2</sub>O and were stirred together for 3 hours at ambient temperature. The dark brown reaction mixture was then filtered through a glass-fiber filter pad to remove the KBr by-product. The filtrate was dried under vacuum, yielding the product as an orange-brown powder. Single crystals of **3.36b** suitable for X-ray diffraction were grown from a toluene solution cooled to -35 °C.

#### Isolation of Single Crystals of (<sup>CY5</sup>NpN<sup>DIPP,DIPP</sup>)FeH<sub>2</sub>BEt<sub>2</sub> (**3.7**)

A toluene solution (5 mL) of **2.23a** (0.158 g, 0.236 mmol) was added to KBEt<sub>3</sub>H (0.032 g, 0.24 mmol). The solution immediately changed color from yellow to dark brown and was stirred for 15 minutes at 25 °C. The resulting suspension was filtered through a glass-fiber filter pad to remove KBr and the filtrate was dried under vacuum, yielding the product mixture as a

brown powder. Single crystals of **3.7** suitable for X-ray diffraction were grown from a concentrated diethyl ether solution cooled to -35 °C.

**(CY<sup>5</sup>NpN<sup>DIPP,DIPP</sup>)FeEt (3.8a)**

Complex **2.23a** (0.190 g, 0.284 mmol) was dissolved in THF (10 mL) and was transferred to a Schlenk vessel. A solution of ethylmagnesium chloride (2.0 M in THF, 0.14 mL, 0.28 mmol) was added via syringe to the solution of **2.23a**. The color of the reaction mixture immediately changed from yellow to brown/green. The reaction mixture was allowed to stir for 1 hour before the volatiles were removed under vacuum and the Schlenk vessel was transferred into a dinitrogen glovebox. The residue in the Schlenk flask was dissolved in minimal diethyl ether and was filtered through a glass fiber filter pad to remove the MgBrCl by-product. The filtrate was again dried under vacuum, yielding the product as a yellow powder. Yield: 0.077 g, 0.12 mmol, 44 %. Single crystals suitable for X-ray diffraction were grown from slow evaporation of a diethyl ether solution of **3.8a**.

<sup>1</sup>H NMR (300 MHz, *d*<sub>6</sub>-benzene, 25 °C): δ 96.8 (s), 26.9 (s), 25.7 (s), 24.7 (s), 12.7 (s), 12.1 (s), 3.8 (s), 1.8 (s), 1.3 (s), 0.3 (s), -3.5 (s), -20.9 (s), -26.6 (s), -30.3 (s), -33.3 (s), and -35.8 (s).

$\mu_{\text{eff}} = 4.0 \mu_{\text{B}}$  (evans)

HRMS (EI-Double Focusing Sector) *m/z*: [M]<sup>+</sup> Calcd for C<sub>37</sub>H<sub>59</sub>N<sub>2</sub>PFe: 618.37653; Found: 618.37668, [M-CH<sub>2</sub>CH<sub>3</sub>]<sup>+</sup> Calcd for C<sub>35</sub>H<sub>54</sub>N<sub>2</sub>PFe: 589.33740; Found: 589.33715.

**Reaction of 3.6a with Triethylborane**

Hydride complex **3.6a** (0.008 g, 0.01 mmol) was dissolved in *d*<sub>8</sub>-toluene (0.6 mL) and was transferred to a J. Young NMR tube. The tube was charged with 1 M triethylborane in hexanes (13.6 μL, 0.013 mmol) before being sealed and heated to 60 °C for 2 hours. <sup>1</sup>H NMR spectroscopy performed at 25 °C.

$^1\text{H}$  NMR (300 MHz,  $d_8$ -toluene, 25 °C):  $\delta$  113.4, 109.0, 96.3, 40.2, 37.4, 31.5, 26.6, 25.5, 24.7, 22.8, 20.2, 19.9, 19.2, 16.3, 14.8, 12.8, 12.1, 9.4, 4.3, 2.9, 1.2, 0.9, -0.3, -3.5, -6.2, -8.5, -16.9, -20.8, -26.6, -30.3, -33.1, -35.8, and -36.4.

Comparison to **3.8a**:  $^1\text{H}$  NMR (300 MHz,  $d_6$ -benzene, 25 °C):  $\delta$  96.8, 26.9, 25.7, 24.7, 12.7, 12.1, 3.8, 1.8, 1.3, 0.3, -3.5, -20.9, -26.6, -30.3, -33.3, and -35.8.

**(CY<sup>5</sup>NpN<sup>DIPP,Mes</sup>)FeEt (3.8b)**

Complex **2.23c** (0.212 g, 0.338 mmol) was dissolved in THF (10 mL) and was transferred to a Schlenk vessel. A solution of ethylmagnesium chloride (2.0 M in THF, 0.17 mL, 0.34 mmol) was added via syringe to the THF solution of **2.23c**. The color of the solution immediately changed from yellow to brown. The mixture was stirred for 10 minutes before the volatiles were removed under vacuum. The residue was extracted with diethyl ether and was filtered through a glass fiber filter pad to remove the MgBrCl by-product salt. The filtrate was left to evaporate, yielding the product as yellow crystalline material. Yield: 0.151 g, 0.261 mmol, 77.4%. Single crystals suitable for X-ray diffraction were grown from slow evaporation of a diethyl ether solution of **3.8b**.

$^1\text{H}$  NMR (300 MHz,  $d_6$ -benzene, 25 °C):  $\delta$  100.1 (s), 51.2 (s), 41.8 (s), 26.7 (s), 24.8 (s), 23.2 (s), 17.2 (s), 10.3 (s), 3.8 (s), 1.4 (s), -24.5 (s), -34.2 (s), and -35.5 (s).

$\mu_{\text{eff}} = 4.4 \mu_{\text{B}}$  (evans)

HRMS (EI-Double Focusing Sector)  $m/z$ :  $[\text{M}]^+$  Calcd for  $\text{C}_{34}\text{H}_{53}\text{N}_2\text{PFe}$  576.32958; Found: 576.32922,  $[\text{M}-\text{CH}_2\text{CH}_3]^+$  Calcd for  $\text{C}_{32}\text{H}_{48}\text{N}_2\text{PFe}$ : 547.29045; Found: 547.29001.

**(CY<sup>5</sup>NpN<sup>DIPP,DIPP</sup>)FeN(Ph)NHPPh (3.9)**

A THF solution (5 mL) of complex **3.6a** (0.075 mg, 0.13 mmol) was added to a THF solution (5 mL) of azobenzene (0.023 g, 0.13 mmol). The resulting dark red reaction mixture

was stirred for 5 minutes before exposing the sample to vacuum in order to remove the volatiles. Yield: 0.094 g, 0.12 mmol, 96%. Single crystals suitable for X-ray diffraction were grown from the slow evaporation of a diethyl ether solution of **3.9**.

$^1\text{H}$  NMR (300 MHz,  $d_6$ -benzene, 25 °C):  $\delta$  112.0 (s), 108.6 (s), 107.3 (s), 61.9 (s), 40.4 (s), 37.5 (s), 26.3 (s), 25.1 (s), 23.4 (s), 20.0 (s), 19.0 (s), 17.6 (s), 14.3 (s), 13.2 (s), 8.0 (s), 3.6 (s), 1.4 (s), 0.3 (s), -0.6 (s), -1.8 (s), -3.2 (s), -5.3 (s), -9.0 (s), -10.9 (s), -13.0 (s), -16.4 (s), -18.8 (s), -23.1 (s), -27.3 (s), -28.3 (s), -31.4 (s), -39.7 (s), and -59.3 (s).

$\mu_{\text{eff}}=4.1 \mu_{\text{B}}$  (Evans).

Anal. Calcd. for  $\text{C}_{47}\text{H}_{65}\text{FeN}_4\text{P}$ : C, 73.04; H, 8.48; N, 7.25. Found: C, 70.84; H, 8.47; N, 7.10.

Repeated attempts at elemental analysis failed to provide successful results. The analogous iron hydrazido  $\beta$ -diketiminato complex has been reported to be too thermally sensitive to provide satisfactory elemental analysis results.<sup>132</sup>

#### **(CY<sub>5</sub>NpN<sup>DIPP,DIPP</sup>)Fe(3-hexene) (3.10)**

Complex **3.6a** (0.070 g, 0.12 mmol) was dissolved in THF (5 mL) and the solution was added to excess 3-hexyne (0.015 g, 0.18 mmol). The reaction mixture was stirred overnight at room temperature, with the color of the solution gradually changing from orange to yellow over the course of the reaction. The volatiles were then removed under vacuum, leaving the product as a yellow powder. Yield: 0.066 g, 0.098 mmol, 82 %. Single crystals suitable for X-ray diffraction were grown from the slow evaporation of a diethyl ether solution of **3.10**.

$^1\text{H}$  NMR (300 MHz,  $d_6$ -benzene, 25 °C):  $\delta$  98.7 (s), 32.7 (s), 27.2 (s), 26.0 (s), 25.1 (s), 16.7 (s), 15.3 (s), 10.4 (s), 2.9 (s), 1.2 (s), -3.4 (s), -22.0 (s), -23.1 (s), -25.4 (s), -29.0 (s), and -36.0 (s).

$\mu_{\text{eff}}=4.8 \mu_{\text{B}}$  (evans)

HRMS (EI-Double Focusing Sector)  $m/z$ :  $[M]^+$  Calcd for  $C_{41}H_{65}N_2PFe$ : 672.42348; Found: 672.42306.

**$(CY^5NpN^{DIPP,DIPP})Fe(\eta^2-HNNAAd)$  (3.11)**

Complex **3.6a** (0.063 g, 0.11 mmol) was dissolved in diethyl ether (5 mL) and was added to 1-azidoadamantane (0.019 g, 0.11 mmol). The resulting mixture was stirred overnight at ambient temperature. The volatiles were then removed under vacuum, yielding the product as a brown powder. Yield: 0.070 g, 0.091 mmol, 85%. Single crystals suitable for X-ray diffraction were grown from a toluene solution of **3.11** cooled to  $-35\text{ }^\circ\text{C}$ .

$^1\text{H}$  NMR (400 MHz,  $d_6$ -benzene,  $25\text{ }^\circ\text{C}$ ):  $\delta$  96.0 (s), 30.6 (s), 26.4 (s), 23.5 (s), 12.0 (s), 11.3 (s), 8.8 (s), 8.2 (s), 6.1 (s), 5.2 (s), 4.6 (s), 3.3 (s), 2.3 (s), 1.9 (s), 1.3 (s), 1.1 (s), -2.0 (s), -3.2 (s), -4.7 (s), -6.1 (s), -8.6 (s), -11.2 (s), -17.2 (s), and -18.8 (s).

$\mu_{\text{eff}}=4.3\ \mu_{\text{B}}$  (evans)

Anal. Calcd. for  $C_{45}H_{70}FeN_5P$ : C, 70.39; H, 9.19; N, 9.12. Found: C, 70.52; H, 9.46; N, 6.72.

Repeated attempts at elemental analysis consistently yielded results low in nitrogen. The  $\beta$ -diketiminato iron triazenido analogue to **3.11** is reported to be too thermally unstable to obtain accurate elemental analysis results.<sup>130</sup>

**$(CY^5NpN^{DIPP,DIPP})Fe(NHPh)$  (3.12)**

Complex **3.6a** (0.037 g, 0.063 mmol) and azobenzene (0.011 g, 0.063 mmol) were dissolved in  $d_6$ -benzene and the resulting solution was transferred to a J. Young NMR tube. The J. Young tube was sealed and heated to  $50\text{ }^\circ\text{C}$  for 1 day. The conversion of the hydrazido species **3.9** to the anilido complex **3.12** was monitored by  $^1\text{H}$  NMR spectroscopy, accompanied by a color change from orange to green. After the reaction reached completion, the solution was transferred from the J. Young tube to a scintillation vial and the volatiles were removed under

vacuum. The resulting green residue was dissolved in a minimal amount of hexanes and single crystals of **3.12** suitable for X-ray crystallography were grown at -35 °C. The half an equivalent of azobenzene formed from the thermolysis of the hydrazido N–N bond of **3.9** was not removed from the crude material and additional purification and characterization were not performed.

<sup>1</sup>H NMR (300 MHz, *d*<sub>6</sub>-benzene, 25 °C): δ 116.0 (s), 52.3 (s), 29.4 (s), 22.0 (s), 20.9 (s), 15.2 (s), 8.0 (s), 3.6 (s), 1.4 (s), 1.2 (s), -0.1 (s), -0.3 (s), -5.9 (s), -7.6 (s), -13.2 (s), -20.5 (s), -30.0 (s), -37.8 (s), -44.7 (s), and -66.0 (s).

### Spectroscopic observation of [3.13]

Complex **3.11** was dissolved in *d*<sub>6</sub>-benzene and was transferred to a J. Young NMR tube. The tube was sealed and heated to 80 °C for 3 days, with the formation of a new paramagnetic species observed by <sup>1</sup>H NMR spectroscopy.

<sup>1</sup>H NMR (300 MHz, *d*<sub>6</sub>-benzene, 25 °C): δ 113.4 (s), 34.7 (s), 32.8 (s), 28.2 (s), 23.5 (s), 21.4 (s), 15.7 (s), 15.0 (s), 13.8 (s), 12.4 (s), 8.8 (s), 3.5 (s), 1.9 (s), 1.3 (s), 1.1 (s), -8.7 (s), -9.5 (s), -31.7 (s), -37.0 (s), and -40.0 (s).

### [(<sup>15</sup>NpN<sup>DIPP,DIPP</sup>)FeF]<sub>2</sub> (3.14)

Hexafluorobenzene (1.960g, 10.53 mmol) was added to a THF solution (10 mL) of **3.6a** (0.140 g, 0.237 mmol). The mixture was allowed to stir for 18 hours at ambient temperature with the color of the solution gradually changing from orange to yellowish-green. The volatiles were removed under vacuum, yielding the product as a flaky yellow-green solid. Yield: 0.137 g, 0.225 mmol, 95.1 %. Single crystals suitable for X-ray diffraction were grown from a toluene solution of **3.14** cooled to -35 °C.

<sup>1</sup>H NMR (300 MHz, *d*<sub>6</sub>-benzene, 25 °C): δ 109.1 (s), 89.2 (s), 81.7 (s), 51.0 (s), 48.6 (s), 40.6 (s), 37.7 (s), 26.4 (s), 23.1 (s), 19.2 (s), 16.3 (s), 14.6 (s), 10.7 (s), 8.8 (s), 6.4 (s), 4.5 (s), 2.3 (s), 1.2

(s), -0.7 (s), -7.7 (s), -9.3 (s), -13.2 (s), -16.7 (s), -20.4 (s), -23.1 (s), -24.1 (s), -28.5 (s), -30.2 (s), -52.8 (s), and -66.7 (s).

$\mu_{\text{eff}}=6.2 \mu_{\text{B}}$  (evans)

Anal. Calcd. for  $\text{C}_{70}\text{H}_{108}\text{F}_2\text{Fe}_2\text{N}_4\text{P}_2$ : C, 69.07; H, 8.94; N, 4.60. Found: C, 65.84; H, 8.01; N,

3.97. Repeated attempts at elemental analysis consistently yielded unsatisfactory results. Parent mass peak not detected in low-res EI mass spectrum.

### **HDF catalysis**

For each independent trial, 10-15 mg of **3.6a** was weighed and dissolved in approximately 0.6 mL of deuterated solvent. The substrates under investigation were measured to be in excess so that **3.6a** would be at a catalyst loading of 5 mol %. Substrates were added via Hamilton syringe to the solution of **3.6a** and the resulting solution was transferred into a J. Young NMR tube. The tube was heated to 50 °C and was monitored periodically by  $^1\text{H}$  and  $^{19}\text{F}$  NMR spectroscopy.

### **Kinetics of pentafluoropyridine HDF**

A standard solution containing **3.6a** and fluorobenzene in  $d_8$ -THF ( $[\text{Fe}]=5.5 \times 10^{-3}$  M,  $[\text{C}_6\text{H}_5\text{F}]=0.11\text{M}$ ) was used for each catalytic run. In each trial, a J. Young NMR tube was charged with 600  $\mu\text{L}$  of the  $d_8$ -THF solution containing **3.6a** and the  $\text{C}_6\text{H}_5\text{F}$  internal standard using a Hamilton syringe. The amount of pentafluoropyridine and triethylsilane for each trial was calculated and was measured with a Hamilton syringe and added to the J. Young tube. For the trial where  $[\text{Fe}] \times 2$  was measured, a new solution with  $[\text{Fe}]=0.011$  M was prepared. Each tube was heated to 50 °C, but was cooled to 25 °C when monitored using  $^{19}\text{F}$  NMR spectroscopy. A relaxation delay of 70 seconds was used to insure integration values were quantitative. Lines of

best fit for [*p*-C<sub>5</sub>HF<sub>4</sub>N] versus time were plotted using linear regression and the error was calculated using Microsoft Excel's LINEST function.

### Stepwise HDF reactivity

A solution of **3.6a** (0.010 g, 0.017 mmol) and hexafluorobenzene (2  $\mu$ L, 0.02 mmol) in *d*<sub>8</sub>-THF (0.6 mL) was transferred to a J. Young NMR tube. The tube was sealed and heated to 50 °C for 1 day before being monitored by <sup>1</sup>H NMR spectroscopy. Triethylsilane (3  $\mu$ L, 0.02 mmol) was added to the solution and the tube was heated for an additional 1 day at 50 °C before being monitored by <sup>1</sup>H NMR spectroscopy.

### Attempted Reaction of **3.8a** with Me<sub>3</sub>SnF

A J. Young NMR tube was charged with a *d*<sub>8</sub>-toluene solution of **3.8a** (0.014g, 0.023 mmol). To this solution was added solid trimethyltin fluoride (0.008 g, 0.04 mmol) before the J. Young tube was sealed and heated to 80 °C for 1 day. No change in the resulting <sup>1</sup>H NMR spectrum was observed in comparison to the <sup>1</sup>H NMR spectrum for **3.8a**.

## 6.3.3 Compounds Pertaining to Chapter 4

### CYPNpN<sub>3</sub>H<sup>DIPP,DMP</sup> (**4.6**)

2,6-Dimethylphenylazide (532 mg, 3.61 mmol) was added to a 10 mL THF solution of imine-phosphine **2.17a** (1.181 g, 3.285 mmol). The resulting mixture was stirred at room temperature overnight. After removal of the volatiles under vacuum, the resulting viscous oil was redissolved in hexanes (2 mL) and was stored at -35 °C. The desired compound was yielded as colorless crystals (1.648 g, 3.252 mmol, 98.99%).

<sup>1</sup>H{<sup>31</sup>P} NMR (300 MHz, benzene-*d*<sub>6</sub>, 298 K):  $\delta$  10.88 (s, 1H, *NH*), 6.97-7.22 (m, overlap with residual solvent peak, *ArH*), 3.43 (sept, 2H, <sup>3</sup>J<sub>HH</sub>=6.9 Hz, *NAr-<sup>i</sup>PrCH*), 2.38 (s, 6H, *NAr-CH<sub>3</sub>*), 2.16-2.28 (m, 4H), 2.07 (t, 2H, <sup>3</sup>J<sub>HH</sub>=7.5 Hz, *<sup>i</sup>Pr<sub>2</sub>PCCH<sub>2</sub>*), 1.55 (quin, 2H, <sup>3</sup>J<sub>HH</sub>=6.8 Hz

CH<sub>2</sub>CH<sub>2</sub>CH<sub>2</sub>), 1.24-1.28 (m, 12H, P-<sup>i</sup>PrCH<sub>3</sub>), 1.14 (d, 6H, <sup>3</sup>J<sub>HH</sub>=7.0 Hz, NAr-<sup>i</sup>PrCH<sub>3</sub>), and 1.02 (d, 6H, <sup>3</sup>J<sub>HH</sub>=7.2 Hz, NAr-<sup>i</sup>PrCH<sub>3</sub>).

<sup>31</sup>P{<sup>1</sup>H} NMR (121 MHz, benzene-*d*<sub>6</sub>, 298 K): δ 50.9 (s).

<sup>13</sup>C{<sup>1</sup>H} NMR (75 MHz, benzene-*d*<sub>6</sub>, 298 K): δ 168.9 (d, 6 Hz), 152.7, 147.6, 137.6, 130.6, 128.9, 128.0, 124.6, 123.9, 72.3, 70.8, 34.8 (d, 14 Hz), 33.5 (d, 14 Hz), 29.4, 25.3, 25.1, 24.4, 23.9 (d, 9 Hz), 23.0, 19.5, 16.6 (d, 2 Hz), and 15.9 (d, 2 Hz).

Anal. Calcd for C<sub>31</sub>H<sub>47</sub>N<sub>4</sub>P: C, 73.48; H, 9.35; N, 11.06. Found: C, 73.62; H, 9.30; N, 11.29.

#### [<sup>CYP</sup>NpN<sub>3</sub><sup>DIPP,DMP</sup>]K(THF) (4.7)

A 10mL THF solution of **4.6** (1.648 g, 3.252 mmol) was added to potassium hydride (143 mg, 3.58 mmol). The resulting suspension was stirred at room temperature overnight. When the reaction was complete, the dark yellow solution was filtered through celite to remove excess potassium hydride. The volatiles were removed in vacuo, yielding bright yellow solid. (1.780 g, 2.885 mmol, 88.71%.) Yellow single crystals of ([<sup>CYP</sup>NpN<sub>3</sub><sup>DIPP,DMP</sup>]K•2THF)<sub>n</sub> suitable for X-ray diffraction were grown from a THF solution cooled to -35°C.

<sup>1</sup>H{<sup>31</sup>P} NMR (300 MHz, benzene-*d*<sub>6</sub>, 298 K): δ 7.14-7.20 (m, overlap with residual solvent peak), 7.02-7.09 (m, 2H, Ar-*H*), 3.51-3.56 (m, 4H, THF-CH<sub>2</sub>{2,5}), 3.38 (sept, 2H, <sup>3</sup>J<sub>HH</sub>=6.9 Hz, NAr-<sup>i</sup>PrCH), 2.66 (t, 2H, <sup>3</sup>J<sub>HH</sub>=6.5 Hz, ArNCCH<sub>2</sub>), 2.49 (sept, 2H, <sup>3</sup>J<sub>HH</sub>=7.1 Hz, P-<sup>i</sup>PrCH), 2.35 (s, 6H, NAr-CH<sub>3</sub>), 2.30 (t, 2H, <sup>3</sup>J<sub>HH</sub>=7.3 Hz, <sup>i</sup>Pr<sub>2</sub>PCCH<sub>2</sub>), 1.91 (quin, 2H, <sup>3</sup>J<sub>HH</sub>=7.1 Hz, CH<sub>2</sub>CH<sub>2</sub>CH<sub>2</sub>), 1.41-1.45 (m, 4H, THF-CH<sub>2</sub>{3,4}), 1.34 (d, 6H, <sup>3</sup>J<sub>HH</sub>=6.9 Hz, NAr-<sup>i</sup>PrCH<sub>3</sub>), 1.20-1.25 (m, 12H, P-<sup>i</sup>PrCH<sub>3</sub>), and 1.03 (d, 6H, <sup>3</sup>J<sub>HH</sub>=6.9 Hz, NAr-<sup>i</sup>PrCH<sub>3</sub>).

<sup>31</sup>P{<sup>1</sup>H} NMR (121 MHz, benzene-*d*<sub>6</sub>, 298 K): δ 44.2 (s).

$^{13}\text{C}\{^1\text{H}\}$  NMR (75 MHz, benzene- $d_6$ , 298 K):  $\delta$  175.5 (d,  $J_{\text{PC}}=9$  Hz), 152.7, 151.8, 141.2, 130.4, 128.9, 124.1, 123.3, 120.8, 67.7 (THF-  $\text{CH}_2\{2,5\}$ ), 50.9 (d,  $J_{\text{PC}}=125$  Hz), 36.6 (d,  $J_{\text{PC}}=15$  Hz), 34.3 (d,  $J_{\text{PC}}=16$  Hz), 27.5, 25.9, 25.7 (THF- $\text{CH}_2\{3,4\}$ ), 25.0, 24.5 (d,  $J_{\text{PC}}=21$  Hz), 19.9, 17.2, and 16.6. Anal. Calcd for  $\text{C}_{35}\text{H}_{54}\text{KN}_4\text{OP}$ : C, 68.14; H, 8.82; N, 9.08. Found: C, 68.10; H, 8.99; N, 9.25.

**$[\text{CYPNpN}_3^{\text{DIPP,DMP}}]\text{FeBr}(\text{THF})$  (**4.8**)**

A 10mL diethyl ether solution of ligand potassium salt **4.7** (1.728 g, 2.801 mmol) was added to  $\text{FeBr}_2(\text{THF})_2$  (1.008, 2.801 mmol) and the reaction mixture was stirred at room temperature overnight. The resulting suspension consisted of gray precipitate and blood red supernatant. The suspension was filtered through celite to remove KBr and the filtrate was concentrated to a volume of approximately 1mL before being cooled to  $-35$  °C for 3 hours. **4.8** was yielded as orange crystals, which were collected on a glass frit and were dried in vacuo (567 mg, 0.795 mmol, 28.4 %).

$^1\text{H}$  NMR (300 MHz,  $d_6$ -benzene, 298 K):  $\delta$  101.7 (s), 26.1 (s), 17.6 (s), 17.4 (s), 12.3 (s), 11.4 (s), 5.2 (s), 4.0 (s), -4.3 (s), -7.1 (s), -14.9 (s), and -34.9 (s).

$\mu_{\text{eff}} = 4.8 \mu_{\text{B}}$  (Evans).

Anal. Calcd for  $\text{C}_{35}\text{H}_{54}\text{BrFeN}_4\text{OP}$ : C, 58.91; H, 7.63; N, 7.85. Found: C, 58.65; H, 7.62; N, 7.72.

**$([\text{CYPNpN}^{\text{DIPP}}]\text{Fe})_2$  (**4.9**)**

Potassium triethylborohydride (15 mg, 0.11 mmol) was dissolved in 5 mL of THF and was added dropwise to a stirred 5 mL THF solution of **4.8** (80 mg, 0.11 mmol). The color of the solution immediately changed from bright orange to dark brown. The reaction mixture was allowed to stir for 30 minutes before the volatiles were removed under vacuum. The resulting brown residue was then extracted in toluene and was filtered through celite. The toluene was removed in vacuo and

the dark brown solids were rinsed with *n*-pentane. The supernatant was decanted away, yielding a yellowish-tan powder which was dried under vacuum (11 mg, 0.013 mmol, 23% yield).

$^1\text{H}$  NMR (300 MHz, benzene- $d_6$ , 298 K):  $\delta$  12.3 (s, 2H), 9.7 (s, 2H), 8.4 (s, 2H), 5.4 (s, 2H), 4.5 (s, 1H), 3.9 (s, 2H), 3.0 (s, 6H), 2.0 (s, 6H), 1.3 (s, 6H), 0.9 (s, 2H) and -3.0 (s, 6H).

$\mu_{\text{eff}} = 3.1 \mu_{\text{B}}$  (Evans).

Anal. Calcd for  $\text{C}_{46}\text{H}_{74}\text{Fe}_2\text{N}_4\text{P}_2$ : C, 64.49; H, 8.71; N, 6.54. Found: C, 64.56; H, 8.71; N, 6.84.

### Alternate Synthesis ( $[\text{CYPNpN}^{\text{DIPP}}\text{Fe}]_2$ (**4.9**) in Toluene

Potassium triethylborohydride (111 mg, 0.807 mmol) was added to a 10 mL toluene solution of **4.8** (524 mg, 0.734 mmol) while the solution was vigorously stirred at room temperature. The solution immediately changed from bright orange to dark brown and was stirred for 1 hour. The supernatant was then filtered through celite and the volatiles were removed in vacuo. The resulting dark brown powder was rinsed with *n*-pentane until a fine yellow powder was obtained, which was dried in vacuo (51 mg, 0.059 mmol, 16 %). Single crystals of **4.9** suitable for X-ray diffraction were grown from a toluene/*n*-pentane solution cooled to  $-35\text{ }^\circ\text{C}$ .

$^1\text{H}\{^{31}\text{P}\}$  NMR (300 MHz, benzene- $d_6$ , 298 K):  $\delta$  12.3 (s, 2H), 9.7 (s, 2H), 8.4 (s, 2H), 5.4 (s, 2H), 4.5 (s, 1H), 3.9 (s, 2H), 3.0 (s, 6H), 2.0 (s, 6H), 1.3 (s, 6H), 0.9 (s, 2H) and -3.0 (s, 6H).

### General radical trapping procedure (Reaction of **4.8** with $\text{KBET}_3\text{H}$ )

An apparatus consisting of two Kontes-sealed glass bulbs (10 mL and 25 mL in volume) joined together by a Kontes-sealed glass bridge was used in all radical trapping experiments. Addition of reagents to the apparatus occurred within a  $\text{N}_2$ -filled glovebox. To the 10 mL bulb of the apparatus was added a micro stir bar (10 x 3 mm) and a 1 mL solution of **4.8** in the solvent under investigation. The Kontes seals for both the empty 25 mL bulb and the bridge connecting the two bulbs were closed. A stoichiometric amount of potassium triethylborohydride was

dissolved in 1 mL of the same solvent under investigation and was added dropwise to the solution of **4.8** while stirring. The opening to the 10 mL bulb was sealed after the addition was complete. The solution color immediately changed from bright orange to dark brown, regardless of the solvent employed. After stirring for 30 minutes, the apparatus was removed from the glovebox and the 25 mL bulb was exposed to vacuum. The evacuated bulb was cooled using liquid N<sub>2</sub> before closing the seal to the 25 mL bulb. The Kontes seal on the bridge connecting the two glass bulbs was then opened, and the solvent in the 10 mL reaction bulb was condensed into the cooled, evacuated bulb. After the transfer was complete, the seal on the bridge was closed and the 25 mL bulb containing the reaction solvent was allowed to warm to room temperature. The solvent was removed from the bulb in air and was analyzed by GC-MS and NMR (if a deuterated solvent was investigated).

**[<sup>CYP</sup>NpN<sub>3</sub><sup>DIPP,DMP</sup>]CoCl(Py) (4.11)**

A THF solution (10 mL) of **4.7** (0.580 g, 0.940 mmol) was added to pink CoCl<sub>2</sub>(Py)<sub>4</sub> (0.419 g, 0.940 mmol) and the resulting suspension was stirred at ambient temperature for 1 day. The resulting dark green product mixture was filtered through celite to remove salt by-products. The filtrate was then dried under vacuum to remove volatiles, and the resulting blue-green residue was dissolved in minimal diethyl ether and was cooled overnight at -35 °C. A light blue solid precipitated from solution, which was collected on a glass frit and was rinsed with *n*-pentane before being dried under vacuum. Yield: 0.434 g, 0.637 mmol, 67.8%. Single crystals of **4.11** were grown from a THF solution of **4.11** cooled to -35 °C.

<sup>1</sup>H NMR (300 MHz, benzene-*d*<sub>6</sub>, 298 K): δ 87.2 (s), 69.2 (s), 43.0 (s), 38.9 (s), 29.4 (s), 24.0 (s), 19.8 (s), 19.1 (s), 16.8 (s), 15.2 (s), 15.0 (s), 12.2 (s), 10.9 (s), 9.0 (s), 4.2 (s), 1.0 (s), 0.3 (s), -0.3 (s), -2.5 (s), -6.4 (s), -8.3 (s), -13.0 (s), -27.4 (s), and -42.0 (s).

$\mu_{\text{eff}} = 4.0 \mu_{\text{B}}$  (Evans).

Anal. Calcd for  $\text{C}_{36}\text{H}_{51}\text{ClCoN}_5\text{P}$ : C, 63.66; H, 7.57; N, 10.31. Found: C, 63.76; H, 7.41; N, 9.99.

### Complex [4.12]

A THF solution (10 mL) of **4.7** (0.256 g, 0.470 mmol) was added to blue  $\text{CoCl}_2$  (61 mg, 0.47 mmol) and the resulting mixture was stirred at ambient temperature for one day. A dark green solution was obtained, which was filtered through a glass-fiber filter pad and the solvent was removed under vacuum yielding the product as a green powder. Attempted to grow single crystals from a concentrated THF solution cooled to  $-35^\circ\text{C}$ .

$^1\text{H}$  NMR (300 MHz, benzene- $d_6$ , 298 K):  $\delta$  25.1 (s), 22.4 (s), 18.1 (s), 16.0 (s), 12.9 (s), 9.4 (s), 8.7 (s), 3.1 (s), 1.2 (s), 0.5 (s), -8.6 (s), -27.8 (s), -32.4 (s), -34.3 (s), -41.5 (s), and -46.2 (s).

### $[\text{CYPNpN}_3^{\text{DIPP,DMP}}]\text{Co}(\text{CH}_2\text{Si}(\text{Me})_3)(\text{Py})$ (**4.13**)

Crystalline  $\text{LiCH}_2\text{Si}(\text{CH}_3)_3$  (0.042 g, 0.44 mmol) was added to a THF solution (10 mL) of **4.11** (0.301 g, 0.443 mmol) and the resulting mixture was stirred at ambient temperature for 2 hours. The color of the solution changed from dark green to orange-brown. The product mixture was filtered through a glass-fiber filter pad to remove the by-product  $\text{LiCl}$  and the filtrate was dried under vacuum. The brown residue was dissolved in *n*-pentane and the solution was cooled to  $-35^\circ\text{C}$  for 2 hours. Crystalline product was obtained, which was collected on a glass frit and was dried under vacuum. Yield: 0.147 g, 0.201 mmol, 45%. Single crystals of **4.13** suitable for X-ray diffraction were grown from an *n*-pentane solution of **4.13** cooled to  $-35^\circ\text{C}$ .

$^1\text{H}$  NMR (300 MHz, benzene- $d_6$ , 298 K):  $\delta$  108.4 (s), 59.1 (s), 47.7 (s), 43.5 (s), 35.5 (s), 18.4 (s), 14.0 (s), 12.2 (s), 8.4 (s), 1.2 (s), 0.9 (s), -0.6 (s), -2.0 (s), -2.8 (s), -3.5 (s), -4.7 (s), -22.5 (s), and -37.9 (s).

$\mu_{\text{eff}} = 4.5 \mu_{\text{B}}$  (Evans)

Anal. Calcd for C<sub>40</sub>H<sub>62</sub>CoN<sub>5</sub>PSi: C, 65.73; H, 8.55; N, 9.58. Found: C, 65.59; H, 8.51; N, 9.30.

### Attempted Hydrogenation of Benzophenone Using Sub-stoichiometric **4.13**

A 200 mL Kontes-sealed glass reaction bomb was charged with **4.13** (22 mg, 0.030 mmol), [H(Et<sub>2</sub>O)<sub>2</sub>]<sup>+</sup>[[3,5-(CF<sub>3</sub>)<sub>2</sub>C<sub>6</sub>H<sub>3</sub>]<sub>4</sub>B]<sup>-</sup> (31 mg, 0.030 mmol), and benzophenone (0.109 g, 0.598 mmol) and the solids were dissolved in *d*<sub>6</sub>-benzene (5 mL). The contents of the vessel underwent three freeze-pump-thaw cycles and the bomb was backfilled with 1 atm of H<sub>2</sub>. The mixture was allowed to stir at 25 °C for one day. The contents of the bomb were then exposed to air and the solution was filtered through a short plug of basic alumina and the filtrate was analyzed by <sup>1</sup>H NMR. Only resonances belonging to benzophenone and diethyl ether were observed.

### Reaction of **4.13** with HBAr<sup>F</sup>

To a diethyl ether (10 mL) solution of **4.13** (0.075 g, 0.10 mmol) was added [H(Et<sub>2</sub>O)<sub>2</sub>]<sup>+</sup>[[3,5-(CF<sub>3</sub>)<sub>2</sub>C<sub>6</sub>H<sub>3</sub>]<sub>4</sub>B]<sup>-</sup> (0.105 g, 0.103 mmol). The resulting mixture was stirred for 1 day at ambient temperature before the solvent was removed under vacuum and the residue was analyzed by <sup>1</sup>H NMR.

<sup>1</sup>H NMR (300 MHz, benzene-*d*<sub>6</sub>, 298 K): δ 95.9 (s), 47.4 (s), 41.0 (s), 24.5 (s), 20.5 (s), 16.6 (s), 14.6 (s), 11.1 (s), 10.2 (s), 7.7 (s), 5.5 (s), 5.1 (s), 4.1 (s), 3.3 (s), 2.1 (s), 1.7 (s), 1.4 (s), 1.1 (s), 1.0 (s), 0.9 (s), 0.4 (s), -0.1 (s), -10.2 (s), -20.0 (s), and -35.4 (s).

## 6.3.4 Compounds Pertaining to Chapter 5

### (<sup>CY5</sup>NpN<sup>DIPP,Mes</sup>)CoCl [**5.3**]

The potassium salt **2.21c** (1.425 g, 2.684 mmol) was dissolved in THF (10 mL) and was added to CoCl<sub>2</sub>(THF)<sub>1.5</sub> (0.639 g, 2.68 mmol). The resulting mixture was stirred overnight, resulting in a green suspension. The suspension was filtered through celite, giving a green

filtrate. The trapped solids on the celite were rinsed with THF until the collected filtrate was no longer green in color. The filtrate was passed through a glass-fiber filter before being dried under vacuum, giving a brown solid (0.650 g, 1.11 mmol, 41.3%). Attempted to grow single crystals from a toluene solution cooled to -35 °C, but was not successful.

<sup>1</sup>H NMR (400 MHz, *d*<sub>8</sub>-THF, 298 K): δ 105.2 (broad s), 37.1 (s), 28.6 (s), 16.1 (s), 15.0 (s), 0.1 (s), -12.3 (s), and -35.4 (s).

### (CY<sup>5</sup>NpNNH<sup>DIPP,Mes,Ad</sup>)FeBr (**5.12**)

The dimeric iron bromide complex **2.23c** (0.300 g, 0.239 mmol) was suspended in THF before 1-azidoadamantane (0.085 g, 0.48 mmol) was added to the mixture. The reaction was allowed to proceed overnight, with the color of the solution having changed from yellow to green. The solvent was removed under vacuum, yielding the product as a green powder (0.352 g, 0.453 mmol, 95%). Single crystals of **5.12** suitable for X-ray diffraction were grown from a diethyl ether solution of **5.12** cooled to -35 °C. Signals observed for the major species in the <sup>1</sup>H NMR spectrum listed below.

<sup>1</sup>H NMR (400 MHz, benzene-*d*<sub>6</sub>, 298 K): δ 87.1 (s), 73.1 (s), 61.2 (s), 38.7 (s), 35.1 (s), 32.4 (s), 30.5 (s), 25.9 (s), 23.8 (s), 23.3 (s), 22.1 (s), 18.2 (s), 17.3 (s), 15.3 (s), 14.6 (s), 11.8 (s), 10.0 (s), 2.8 (s), 1.8 (s), 1.6 (s), 1.3 (s), 0.7 (s), -0.9 (s), -2.5 (s), -2.7 (s), -3.7 (s), -5.2 (s), -5.6 (s), -6.3 (s), -6.6 (s), -9.7 (s), -10.9 (s), -11.4 (s), -20.7 (s), and -27.7 (s).

$\mu_{\text{eff}} = 4.9 \mu_{\text{B}}$  (Evans)

### Attempted Aziridination Catalysis of 1-hexene with **2.23c**

1-azidoadamantane (0.057 g, 0.32 mmol) and 1-hexene (0.027 g, 0.32 mmol) were dissolved in THF (10 mL). The solution was added to **2.23c** (0.010 g, 0.016 mmol) and the resulting mixture was allowed to stir overnight. Subsequently, the mixture was filtered through a

small plug of basic alumina and an aliquot of the filtrate was dried under vacuum and analyzed by  $^1\text{H}$  NMR spectroscopy. Only resonances corresponding to 1-azidoadamantane and 1-hexene were observed. An analogous procedure was used for the attempted aziridination of styrene.

## Bibliography

1. Alyea, E. C.; Basi, J. S.; Bradley, D. C.; Chisholm, M. H. *Chem. Commun. (London)* **1968**, 495-495.
2. Bürger, H.; Wannagat, U. *Monatsh. Chem.* **1963**, *94*, 1007-1012.
3. Andersen, R. A.; Faegri, K.; Green, J. C.; Haaland, A.; Lappert, M. F.; Leung, W. P.; Rypdal, K. *Inorg. Chem.* **1988**, *27*, 1782-1786.
4. Bartlett, R. A.; Chen, H.; Power, P. P. *Angew. Chem. Int. Ed.* **1989**, *28*, 316-317.
5. Arduengo, A. J.; Gamper, S. F.; Calabrese, J. C.; Davidson, F. *J. Am. Chem. Soc.* **1994**, *116*, 4391-4394.
6. Zhang, H.; Ouyang, Z.; Liu, Y.; Zhang, Q.; Wang, L.; Deng, L. *Angew. Chem. Int. Ed.* **2014**, *53*, 8432-8436.
7. Ung, G.; Rittle, J.; Soleilhavoup, M.; Bertrand, G.; Peters, J. C. *Angew. Chem. Int. Ed.* **2014**, *53*, 8427-8431.
8. Laskowski, C. A.; Hillhouse, G. L. *J. Am. Chem. Soc.* **2008**, *130*, 13846-13847.
9. Kelly, C. M.; Kwon, D.-H.; Ferguson, M. J.; Bischof, S. M.; Sydora, O. L.; Ess, D. H.; Stradiotto, M.; Turculet, L. *Angew. Chem. Int. Ed.* **2015**, *54*, 14498-14502.
10. Stauber, J. M.; Wadler, A. L.; Moore, C. E.; Rheingold, A. L.; Figueroa, J. S. *Inorg. Chem.* **2011**, *50*, 7309-7316.
11. Lavallo, V.; Canac, Y.; DeHope, A.; Donnadiou, B.; Bertrand, G. *Angew. Chem.* **2005**, *117*, 7402-7405.
12. Fohlmeister, L., et al. *Angew. Chem. Int. Ed.* **2012**, *51*, 8294-8298.
13. Sydora, O. L.; Wolczanski, P. T.; Lobkovsky, E. B.; Buda, C.; Cundari, T. R. *Inorg. Chem.* **2005**, *44*, 2606-2618.
14. Hicks, J.; Jones, C. *Inorg. Chem.* **2013**, *52*, 3900-3907.
15. Laskowski, C. A.; Miller, A. J. M.; Hillhouse, G. L.; Cundari, T. R. *J. Am. Chem. Soc.* **2011**, *133*, 771-773.
16. Holland, P. L. *Acc. Chem. Res.* **2008**, *41*, 905-914.
17. LaPointe, R. E.; Wolczanski, P. T.; Mitchell, J. F. *J. Am. Chem. Soc.* **1986**, *108*, 6382-6384.
18. Laplaza, C. E.; Cummins, C. C. *Science* **1995**, *268*, 861-863.
19. Complexes of Bulky  $\beta$ -Diketiminato Ligands. In *Inorg. Synth.*, John Wiley & Sons, Inc.: 2010; pp 1-55.
20. Budzelaar, P. H. M., Bart van Oort, A., Guy Orphen, A. *Eur. J. Inorg. Chem.* **1998**, 1485-1494.
21. Stender, M.; Wright, R. J.; Eichler, B. E.; Prust, J.; Olmstead, M. M.; Roesky, H. W.; Power, P. P. *J. Chem. Soc., Dalton Trans.* **2001**, 3465-3469.
22. Bonnett, R.; Bradley, D. C.; Fisher, K. J. *Chem. Commun. (London)* **1968**, 886-887.
23. McGeachin, S. G. *Can. J. Chem.* **1968**, *46*, 1903-1912.
24. Cheng, M.; Lobkovsky, E. B.; Coates, G. W. *J. Am. Chem. Soc.* **1998**, *120*, 11018-11019.
25. Feldman, J.; McLain, S. J.; Parthasarathy, A.; Marshall, W. J.; Calabrese, J. C.; Arthur, S. D. *Organometallics* **1997**, *16*, 1514-1516.
26. Smith, J. M.; Lachicotte, R. J.; Holland, P. L. *Chem. Commun.* **2001**, 1542-1543.
27. Holland, P. L.; Tolman, W. B. *J. Am. Chem. Soc.* **1999**, *121*, 7270-7271.

28. Monillas, W. H.; Yap, G. P. A.; MacAdams, L. A.; Theopold, K. H. *J. Am. Chem. Soc.* **2007**, *129*, 8090-8091.
29. Pfirrmann, S.; Limberg, C.; Herwig, C.; Stöber, R.; Ziemer, B. *Angew. Chem. Int. Ed.* **2009**, *48*, 3357-3361.
30. Tran, B. L., et al. *Angew. Chem. Int. Ed.* **2010**, *49*, 9871-9875.
31. Tran, B. L., et al. *J. Am. Chem. Soc.* **2012**, *134*, 13035-13045.
32. Gupta, A. K.; Tolman, W. B. *Inorg. Chem.* **2012**, *51*, 1881-1888.
33. Bai, G.; Wei, P.; Stephan, D. W. *Organometallics* **2006**, *25*, 2649-2655.
34. Smith, J. M.; Lachicotte, R. J.; Pittard, K. A.; Cundari, T. R.; Lukat-Rodgers, G.; Rodgers, K. R.; Holland, P. L. *J. Am. Chem. Soc.* **2001**, *123*, 9222-9223.
35. Yao, S.; Bill, E.; Milsmann, C.; Wieghardt, K.; Driess, M. *Angew. Chem. Int. Ed.* **2008**, *47*, 7110-7113.
36. Ding, K.; Pierpont, A. W.; Brennessel, W. W.; Lukat-Rodgers, G.; Rodgers, K. R.; Cundari, T. R.; Bill, E.; Holland, P. L. *J. Am. Chem. Soc.* **2009**, *131*, 9471-9472.
37. Shimokawa, C.; Teraoka, J.; Tachi, Y.; Itoh, S. *J. Inorg. Biochem.* **2006**, *100*, 1118-1127.
38. Li, Y.; Gao, M.; Wu, Q. *Appl. Organomet. Chem.* **2007**, *21*, 965-969.
39. Cowley, R. E.; Golder, M. R.; Eckert, N. A.; Al-Afyouni, M. H.; Holland, P. L. *Organometallics* **2013**, *32*, 5289-5298.
40. Zhou, W.; MacLeod, K. C.; Patrick, B. O.; Smith, K. M. *Organometallics* **2012**, *31*, 7324-7327.
41. Chang, K.-C.; Lu, C.-F.; Wang, P.-Y.; Lu, D.-Y.; Chen, H.-Z.; Kuo, T.-S.; Tsai, Y.-C. *Dalton Trans.* **2011**, *40*, 2324-2331.
42. Chen, C.; Hecht, M. B.; Kavara, A.; Brennessel, W. W.; Mercado, B. Q.; Weix, D. J.; Holland, P. L. *J. Am. Chem. Soc.* **2015**, *137*, 13244-13247.
43. Spencer, D. J. E.; Aboeella, N. W.; Reynolds, A. M.; Holland, P. L.; Tolman, W. B. *J. Am. Chem. Soc.* **2002**, *124*, 2108-2109.
44. Aboeella, N. W.; Gherman, B. F.; Hill, L. M. R.; York, J. T.; Holm, N.; Young, V. G.; Cramer, C. J.; Tolman, W. B. *J. Am. Chem. Soc.* **2006**, *128*, 3445-3458.
45. Vela, J.; Stoian, S.; Flaschenriem, C. J.; Münck, E.; Holland, P. L. *J. Am. Chem. Soc.* **2004**, *126*, 4522-4523.
46. Tonzetich, Z. J.; Do, L. H.; Lippard, S. J. *J. Am. Chem. Soc.* **2009**, *131*, 7964-7965.
47. Randall, D. W.; George, S. D.; Holland, P. L.; Hedman, B.; Hodgson, K. O.; Tolman, W. B.; Solomon, E. I. *J. Am. Chem. Soc.* **2000**, *122*, 11632-11648.
48. Camp, C.; Arnold, J. *Dalton Trans.* **2016**, *45*, 14462-14498.
49. Chen, C.; Bellows, S. M.; Holland, P. L. *Dalton Trans.* **2015**, *44*, 16654-16670.
50. Guzei, I. A.; Wendt, M. *Dalton Trans.* **2006**, 3991-3999.
51. Gololobov, Y. G.; Kasukhin, L. F. *Tetrahedron* **1992**, *48*, 1353-1406.
52. Tian, W. Q.; Wang, Y. A. *J. Org. Chem.* **2004**, *69*, 4299-4308.
53. Al-Benna, S.; Sarsfield, M. J.; Thornton-Pett, M.; Ormsby, D. L.; Maddox, P. J.; Bres, P.; Bochmann, M. *J. Chem. Soc., Dalton Trans.* **2000**, 4247-4257.
54. Zhu, T.; Wambach, T. C.; Fryzuk, M. D. *Inorg. Chem.* **2011**, *50*, 11212-11221.
55. Wambach, T. C.; Ahn, J. M.; Patrick, B. O.; Fryzuk, M. D. *Organometallics* **2013**, *32*, 4431-4439.
56. Wambach, T. C.; Fryzuk, M. D. *Inorg. Chem.* **2015**, *54*, 5888-5896.
57. Bebbington, M. W. P.; Bourissou, D. *Coord. Chem. Rev.* **2009**, *253*, 1248-1261.

58. Tang, J.; Dopke, J.; Verkade, J. G. *J. Am. Chem. Soc.* **1993**, *115*, 5015-5020.
59. Shalev, D. E.; Chiacchiera, S. M.; Radkowsky, A. E.; Kosower, E. M. *J. Org. Chem.* **1996**, *61*, 1689-1701.
60. Molina, P.; Arques, A.; Vinader, M. V. *J. Org. Chem.* **1990**, *55*, 4724-4731.
61. Saxon, E.; Bertozzi, C. R. *Science* **2000**, *287*, 2007-2010.
62. Stephan, D. W. *Organometallics* **2005**, *24*, 2548-2560.
63. García-Álvarez, J.; García-Garrido, S. E.; Cadierno, V. *J. Organomet. Chem.* **2014**, *751*, 792-808.
64. Mitsuyo, F.; Kenji, I.; Yoshio, I. *Bull. Chem. Soc. Jpn.* **1975**, *48*, 2044-2046.
65. Wang, Z.-X.; Wang, L. *Chem. Commun.* **2007**, 2423-2425.
66. Buchard, A.; Heuclin, H.; Auffrant, A.; Le Goff, X. F.; Le Floch, P. *Dalton Trans.* **2009**, 1659-1667.
67. Wheaton, C. A.; Hayes, P. G. *Dalton Trans.* **2010**, *39*, 3861-3869.
68. Buchard, A.; Auffrant, A.; Klempe, C.; Vu-Do, L.; Boubekeur, L.; Goff, X. F. L.; Floch, P. L. *Chem. Commun.* **2007**, 1502-1504.
69. Spencer, L. P.; Altwer, R.; Wei, P.; Gelmini, L.; Gauld, J.; Stephan, D. W. *Organometallics* **2003**, *22*, 3841-3854.
70. LePichon, L.; Stephan, D. W.; Gao, X.; Wang, Q. *Organometallics* **2002**, *21*, 1362-1366.
71. Masuda, J. D.; Wei, P.; Stephan, D. W. *Dalton Trans.* **2003**, 3500-3505.
72. Conroy, K. D.; Piers, W. E.; Parvez, M. *J. Organomet. Chem.* **2008**, *693*, 834-846.
73. Suzuki, T.; Wasada-Tsutsui, Y.; Ogawa, T.; Inomata, T.; Ozawa, T.; Sakai, Y.; Fryzuk, M. D.; Masuda, H. *Inorg. Chem.* **2015**, *54*, 9271-9281.
74. Brooks-Bartlett, J. C.; Garman, E. F. *Interdiscip. Sci. Rev.* **2015**, *40*, 244-264.
75. Keeler, J., *Understanding NMR Spectroscopy*. University of Cambridge, 2002.
76. *Coord. Chem. Rev.* **1996**, *150*, 1-28.
77. *Coord. Chem. Rev.* **1996**, *150*, 77-110.
78. *Coord. Chem. Rev.* **1996**, *150*, 243-264.
79. Housecroft, C. E.; Sharpe, A. G., *Inorganic Chemistry*. Third ed.; Pearson Education Limited: Essex, England, 2008.
80. Deutsch, J. L.; Poling, S. M. *J. Chem. Educ.* **1969**, *46*, 167.
81. Evans, D. F. *J. Chem. Soc. (Resumed)* **1959**, 2003-2005.
82. Piguet, C. *J. Chem. Educ.* **1997**, *74*, 815.
83. Fultz, B., *Mössbauer Spectrometry*. In *Characterization of Materials*, Kaufmann, E., Ed. John Wiley New York, 2011.
84. Kandemir, T.; Schuster, M. E.; Senyshyn, A.; Behrens, M.; Schlögl, R. *Angew. Chem. Int. Ed.* **2013**, *52*, 12723-12726.
85. Smil, V. *Nature* **1999**, *400*, 415-415.
86. Fryzuk, M. D. *Nature* **2004**, *427*, 498-499.
87. Rayment, T.; Schlögl, R.; Thomas, J. M.; Ertl, G. *Nature* **1985**, *315*, 311-313.
88. Ertl, G. *J. Vac. Sci. Technol., A* **1983**, *1*, 1247-1253.
89. Hellman, A., et al. *J. Phys. Chem. B* **2006**, *110*, 17719-17735.
90. Einsle, O.; Tezcan, F. A.; Andrade, S. L. A.; Schmid, B.; Yoshida, M.; Howard, J. B.; Rees, D. C. *Science* **2002**, *297*, 1696-1700.
91. Barney, B. M.; Lee, H.-I.; Dos Santos, P. C.; Hoffman, B. M.; Dean, D. R.; Seefeldt, L. C. *Dalton Trans.* **2006**, 2277-2284.

92. Hu, Y.; Ribbe, M. W. *Acc. Chem. Res.* **2010**, *43*, 475-484.
93. Spatzal, T.; Aksoyoglu, M.; Zhang, L.; Andrade, S. L. A.; Schleicher, E.; Weber, S.; Rees, D. C.; Einsle, O. *Science* **2011**, *334*, 940-940.
94. Lancaster, K. M.; Roemelt, M.; Ettenhuber, P.; Hu, Y.; Ribbe, M. W.; Neese, F.; Bergmann, U.; DeBeer, S. *Science* **2011**, *334*, 974-977.
95. Wiig, J. A.; Hu, Y.; Lee, C. C.; Ribbe, M. W. *Science* **2012**, *337*, 1672-1675.
96. Barney, B. M., et al. *Biochemistry* **2005**, *44*, 8030-8037.
97. Eady, R. R. *Coord. Chem. Rev.* **2003**, *237*, 23-30.
98. Hinnemann, B.; Norskov, J. K. *PCCP* **2004**, *6*, 843-853.
99. Allen, A. D.; Senoff, C. V. *Chem. Commun. (London)* **1965**, 621-622.
100. Yandulov, D. V.; Schrock, R. R. *Science* **2003**, *301*, 76-78.
101. Del Castillo, T. J.; Thompson, N. B.; Peters, J. C. *J. Am. Chem. Soc.* **2016**, *138*, 5341-5350.
102. Ung, G.; Peters, J. C. *Angew. Chem. Int. Ed.* **2015**, *54*, 532-535.
103. Kuriyama, S.; Arashiba, K.; Nakajima, K.; Tanaka, H.; Kamaru, N.; Yoshizawa, K.; Nishibayashi, Y. *J. Am. Chem. Soc.* **2014**, *136*, 9719-9731.
104. Arashiba, K.; Kinoshita, E.; Kuriyama, S.; Eizawa, A.; Nakajima, K.; Tanaka, H.; Yoshizawa, K.; Nishibayashi, Y. *J. Am. Chem. Soc.* **2015**, *137*, 5666-5669.
105. Kuriyama, S.; Arashiba, K.; Nakajima, K.; Matsuo, Y.; Tanaka, H.; Ishii, K.; Yoshizawa, K.; Nishibayashi, Y. *Nat. Commun.* **2016**, *7*, 12181.
106. Yuki, M.; Tanaka, H.; Sasaki, K.; Miyake, Y.; Yoshizawa, K.; Nishibayashi, Y. *Nat. Commun.* **2012**, *3*, 1254.
107. Smith, J. M., et al. *J. Am. Chem. Soc.* **2006**, *128*, 756-769.
108. Sadique, A. R.; Brennessel, W. W.; Holland, P. L. *Inorg. Chem.* **2008**, *47*, 784-786.
109. Yu, Y.; Smith, J. M.; Flaschenriem, C. J.; Holland, P. L. *Inorg. Chem.* **2006**, *45*, 5742-5751.
110. Rodriguez, M. M.; Bill, E.; Brennessel, W. W.; Holland, P. L. *Science* **2011**, *334*, 780-783.
111. MacLeod, K. C.; Vinyard, D. J.; Holland, P. L. *J. Am. Chem. Soc.* **2014**, *136*, 10226-10229.
112. Grubel, K.; Brennessel, W. W.; Mercado, B. Q.; Holland, P. L. *J. Am. Chem. Soc.* **2014**, *136*, 16807-16816.
113. Bertrand, J. A.; Smith, J. H.; Eller, P. G. *Inorg. Chem.* **1974**, *13*, 1649-1653.
114. Hay, P. J.; Thibeault, J. C.; Hoffmann, R. *J. Am. Chem. Soc.* **1975**, *97*, 4884-4899.
115. Carlin, R. L., Introduction to Magnetic Exchange: Dimers and Clusters. In *Magnetochemistry*, Springer-Verlag: Heidelberg, 1986; pp 70-111.
116. Stoian, S. A.; Vela, J.; Smith, J. M.; Sadique, A. R.; Holland, P. L.; Münck, E.; Bominaar, E. L. *J. Am. Chem. Soc.* **2006**, *128*, 10181-10192.
117. Vrajmasu, V.; Münck, E.; Bominaar, E. L. *Inorg. Chem.* **2003**, *42*, 5974-5988.
118. Hendrich, M. P.; Gunderson, W.; Behan, R. K.; Green, M. T.; Mehn, M. P.; Betley, T. A.; Lu, C. C.; Peters, J. C. *Proc. Natl. Acad. Sci.* **2006**, *103*, 17107-17112.
119. Rudd, P. A.; Planas, N.; Bill, E.; Gagliardi, L.; Lu, C. C. *Eur. J. Inorg. Chem.* **2013**, *2013*, 3898-3906.
120. Reger, D. L.; Gardinier, J. R.; Elgin, J. D.; Smith, M. D.; Hautot, D.; Long, G. J.; Grandjean, F. *Inorg. Chem.* **2006**, *45*, 8862-8875.
121. Weatherburn, M. W. *Anal. Chem.* **1967**, *39*, 971-974.
122. Sunner, J.; Nishizawa, K.; Kebarle, P. *J. Phys. Chem.* **1981**, *85*, 1814-1820.
123. De Wall, S. L.; Barbour, L. J.; Gokel, G. W. *J. Am. Chem. Soc.* **1999**, *121*, 8405-8406.

124. McWilliams, S. F.; Holland, P. L. *Acc. Chem. Res.* **2015**, *48*, 2059-2065.
125. Holland, P. L. *Acc. Chem. Res.* **2015**, *48*, 1696-1702.
126. Vedernikov, A. N. *ChemCatChem* **2014**, *6*, 2490-2492.
127. King, E. R.; Hennessy, E. T.; Betley, T. A. *J. Am. Chem. Soc.* **2011**, *133*, 4917-4923.
128. Lee, Y.; Anderton, K. J.; Sloane, F. T.; Ermert, D. M.; Abboud, K. A.; García-Serres, R.; Murray, L. J. *J. Am. Chem. Soc.* **2015**, *137*, 10610-10617.
129. Gehring, H.; Metzinger, R.; Braun, B.; Herwig, C.; Harder, S.; Ray, K.; Limberg, C. *Dalton Trans.* **2016**, *45*, 2989-2996.
130. Yu, Y., et al. *J. Am. Chem. Soc.* **2008**, *130*, 6624-6638.
131. Bellows, S. M.; Arnet, N. A.; Gurubasavaraj, P. M.; Brennessel, W. W.; Bill, E.; Cundari, T. R.; Holland, P. L. *J. Am. Chem. Soc.* **2016**, *138*, 12112-12123.
132. Smith, J. M.; Lachicotte, R. J.; Holland, P. L. *J. Am. Chem. Soc.* **2003**, *125*, 15752-15753.
133. Eckert, N. A.; Smith, J. M.; Lachicotte, R. J.; Holland, P. L. *Inorg. Chem.* **2004**, *43*, 3306-3321.
134. Lemal, D. M. *J. Org. Chem.* **2004**, *69*, 1-11.
135. Müller, K.; Faeh, C.; Diederich, F. *Science* **2007**, *317*, 1881-1886.
136. Key, B. D.; Howell, R. D.; Criddle, C. S. *Environ. Sci. Technol.* **1997**, *31*, 2445-2454.
137. Whittlesey, M. K.; Peris, E. *ACS Catalysis* **2014**, *4*, 3152-3159.
138. Jones, W. D. *Dalton Trans.* **2003**, 3991-3995.
139. Piglosiewicz, I. M.; Kraft, S.; Beckhaus, R.; Haase, D.; Saak, W. *Eur. J. Inorg. Chem.* **2005**, *2005*, 938-945.
140. Rieth, R. D.; Brennessel, W. W.; Jones, W. D. *Eur. J. Inorg. Chem.* **2007**, *2007*, 2839-2847.
141. Aizenberg, M.; Milstein, D. *Science* **1994**, *265*, 359-361.
142. Peterson, A. A.; McNeill, K. *Organometallics* **2006**, *25*, 4938-4940.
143. Schwartsburd, L.; Mahon, M. F.; Poulten, R. C.; Warren, M. R.; Whittlesey, M. K. *Organometallics* **2014**, *33*, 6165-6170.
144. Kuhl, S.; Schneider, R.; Fort, Y. *Adv. Synth. Catal.* **2003**, *345*, 341-344.
145. Zhao, W.; Wu, J.; Cao, S. *Adv. Synth. Catal.* **2012**, *354*, 574-578.
146. Xiao, J.; Wu, J.; Zhao, W.; Cao, S. *J. Fluorine Chem.* **2013**, *146*, 76-79.
147. Sun, A. D.; Leung, K.; Restivo, A. D.; LaBerge, N. A.; Takasaki, H.; Love, J. A. *Chem. Eur. J.* **2014**, *20*, 3162-3168.
148. Fischer, P.; Götz, K.; Eichhorn, A.; Radius, U. *Organometallics* **2012**, *31*, 1374-1383.
149. Vela, J.; Smith, J. M.; Yu, Y.; Ketterer, N. A.; Flaschenriem, C. J.; Lachicotte, R. J.; Holland, P. L. *J. Am. Chem. Soc.* **2005**, *127*, 7857-7870.
150. Dugan, T. R.; Holland, P. L. *J. Organomet. Chem.* **2009**, *694*, 2825-2830.
151. Yu, Y.; Brennessel, W. W.; Holland, P. L. *Organometallics* **2007**, *26*, 3217-3226.
152. Miura, M. *Angew. Chem. Int. Ed.* **2004**, *43*, 2201-2203.
153. Harper, K. C.; Sigman, M. S. *Science* **2011**, *333*, 1875-1878.
154. Hoyt, J. M.; Schmidt, V. A.; Tondreau, A. M.; Chirik, P. J. *Science* **2015**, *349*, 960-963.
155. Zhang, G.; Vasudevan, K. V.; Scott, B. L.; Hanson, S. K. *J. Am. Chem. Soc.* **2013**, *135*, 8668-8681.
156. Horwitz, C. P.; Fooksman, D. R.; Vuocolo, L. D.; Gordon-Wylie, S. W.; Cox, N. J.; Collins, T. J. *J. Am. Chem. Soc.* **1998**, *120*, 4867-4868.
157. Lundgren, R. J.; Stradiotto, M. *Chem. Eur. J.* **2012**, *18*, 9758-9769.

158. Reger, D. L.; Pascui, A. E.; Smith, M. D.; Jezierska, J.; Ozarowski, A. *Inorg. Chem.* **2012**, *51*, 7966-7968.
159. Reger, D. L.; Pascui, A. E.; Foley, E. A.; Smith, M. D.; Jezierska, J.; Wojciechowska, A.; Stoian, S. A.; Ozarowski, A. *Inorg. Chem.* **2017**, *56*, 2884-2901.
160. Chaudhary, P.; Bieringer, M.; Hazendonk, P.; Gerken, M. *Dalton Trans.* **2015**, *44*, 19651-19658.
161. Reuter, H.; Puff, H. *J. Organomet. Chem.* **1989**, *379*, 223-234.
162. Leclerc, M. C., et al. *J. Am. Chem. Soc.* **2015**, *137*, 16064-16073.
163. Chung, R.; Yu, D.; Thai, V. T.; Jones, A. F.; Veits, G. K.; Read de Alaniz, J.; Hein, J. E. *ACS Catalysis* **2015**, *5*, 4579-4585.
164. Fortman, G. C.; Captain, B.; Hoff, C. D. *Inorg. Chem.* **2009**, *48*, 1808-1810.
165. Kennedy, R. D. *Chem. Commun.* **2010**, *46*, 4782-4784.
166. Naka, H.; Kanase, N.; Ueno, M.; Kondo, Y. *Chem. Eur. J.* **2008**, *14*, 5267-5274.
167. Broderick, E. M.; Thuy-Boun, P. S.; Guo, N.; Vogel, C. S.; Sutter, J.; Miller, J. T.; Meyer, K.; Diaconescu, P. L. *Inorg. Chem.* **2011**, *50*, 2870-2877.
168. Hillhouse, G. L.; Goeden, G. V.; Haymore, B. L. *Inorg. Chem.* **1982**, *21*, 2064-2071.
169. LePichon, L.; Stephan, D. W. *Inorg. Chem.* **2001**, *40*, 3827-3829.
170. Cadierno, V.; Zablocka, M.; Donnadiu, B.; Igau, A.; Majoral, J.-P. and Skowronska, A. *Chem. Eur. J.* **2000**, *6*, 345-352.
171. Bebbington, M. W. P.; Bontemps, S.; Bouhadir, G.; Bourissou, D. *Angew. Chem. Int. Ed.* **2007**, *46*, 3333-3336.
172. Stute, A.; Heletta, L.; Frohlich, R.; Daniliuc, C. G.; Kehr, G.; Erker, G. *Chem. Commun.* **2012**, *48*, 11739-11741.
173. Chidester, C. G.; Szmuszkowicz, J.; Duchamp, D. J.; Laurian, L. G.; Freeman, J. P. *Acta Crystallogr. Sect. C* **1988**, *44*, 1080-1083.
174. Liu, B.; Cui, D. *Dalton Trans.* **2009**, 550-556.
175. Pauling, L. *Proc. Natl. Acad. Sci.* **1976**, *73*, 4290-4293.
176. Laplaza, C. E.; Odom, A. L.; Davis, W. M.; Cummins, C. C.; Protasiewicz, J. D. *J. Am. Chem. Soc.* **1995**, *117*, 4999-5000.
177. Edwards, P. R.; Johnson, C. E.; Williams, R. J. P. *J. Chem. Phys.* **1967**, *47*, 2074-2082.
178. Scharf, A. B.; Betley, T. A. *Inorg. Chem.* **2011**, *50*, 6837-6845.
179. Hernández Sánchez, R.; Bartholomew, A. K.; Powers, T. M.; Ménard, G.; Betley, T. A. *J. Am. Chem. Soc.* **2016**, *138*, 2235-2243.
180. Hess, C. R.; Weyhermüller, T.; Bill, E.; Wieghardt, K. *Angew. Chem. Int. Ed.* **2009**, *48*, 3703-3706.
181. Zall, C. M.; Zherebetsky, D.; Dzubak, A. L.; Bill, E.; Gagliardi, L.; Lu, C. C. *Inorg. Chem.* **2012**, *51*, 728-736.
182. Halpern, J. *Acc. Chem. Res.* **1982**, *15*, 238-244.
183. Zhu, D.; Janssen, F. F. B. J.; Budzelaar, P. H. M. *Organometallics* **2010**, *29*, 1897-1908.
184. Fryzuk, M. D.; Leznoff, D. B.; Thompson, R. C.; Rettig, S. J. *J. Am. Chem. Soc.* **1998**, *120*, 10126-10135.
185. Baudry, D.; Ephritikhine, M.; Felkin, H. *J. Chem. Soc., Chem. Commun.* **1978**, 694-695.
186. Biswas, S.; Huang, Z.; Choliy, Y.; Wang, D. Y.; Brookhart, M.; Krogh-Jespersen, K.; Goldman, A. S. *J. Am. Chem. Soc.* **2012**, *134*, 13276-13295.

187. Scarso, A.; Colladon, M.; Sgarbossa, P.; Santo, C.; Michelin, R. A.; Strukul, G. *Organometallics* **2010**, *29*, 1487-1497.
188. Donohoe, T. J.; O'Riordan, T. J. C.; Rosa, C. P. *Angew. Chem. Int. Ed.* **2009**, *48*, 1014-1017.
189. Price, C. C.; Snyder, W. H. *J. Am. Chem. Soc.* **1961**, *83*, 1773-1773.
190. Sivaramakrishna, A.; Mushonga, P.; Rogers, I. L.; Zheng, F.; Haines, R. J.; Nordlander, E.; Moss, J. R. *Polyhedron* **2008**, *27*, 1911-1916.
191. Grotjahn, D. B.; Larsen, C. R.; Gustafson, J. L.; Nair, R.; Sharma, A. *J. Am. Chem. Soc.* **2007**, *129*, 9592-9593.
192. Larsen, C. R.; Grotjahn, D. B. *J. Am. Chem. Soc.* **2012**, *134*, 10357-10360.
193. Grotjahn, D. B. *Pure. Appl. Chem.* **2010**, *82*, 635-647.
194. Tokmic, K.; Fout, A. R. *J. Am. Chem. Soc.* **2016**, *138*, 13700-13705.
195. Erdogan, G.; Grotjahn, D. B. *Org. Lett.* **2014**, *16*, 2818-2821.
196. Timsina, Y. N.; Biswas, S.; RajanBabu, T. V. *J. Am. Chem. Soc.* **2014**, *136*, 6215-6218.
197. Chen, C.; Dugan, T. R.; Brennessel, W. W.; Weix, D. J.; Holland, P. L. *J. Am. Chem. Soc.* **2014**, *136*, 945-955.
198. Tuner, M.; Jouanne, J. v.; Brauer, H. D.; Kelm, H. *J. Mol. Catal.* **1979**, *5*, 433-445.
199. Bellows, S. M.; Cundari, T. R.; Holland, P. L. *Organometallics* **2013**, *32*, 4741-4751.
200. Bergman, R. G. *Nature* **2007**, *446*, 391-393.
201. Krebs, C.; Galonić Fujimori, D.; Walsh, C. T.; Bollinger, J. M. *Acc. Chem. Res.* **2007**, *40*, 484-492.
202. Lansky, D. E.; Goldberg, D. P. *Inorg. Chem.* **2006**, *45*, 5119-5125.
203. Waidmann, C. R.; Zhou, X.; Tsai, E. A.; Kaminsky, W.; Hrovat, D. A.; Borden, W. T.; Mayer, J. M. *J. Am. Chem. Soc.* **2009**, *131*, 4729-4743.
204. Parsell, T. H.; Yang, M.-Y.; Borovik, A. S. *J. Am. Chem. Soc.* **2009**, *131*, 2762-2763.
205. Collet, F.; Dodd, R. H.; Dauban, P. *Chem. Commun.* **2009**, 5061-5074.
206. Hennessy, E. T.; Betley, T. A. *Science* **2013**, *340*, 591-595.
207. Cowley, R. E.; Eckert, N. A.; Vaddadi, S.; Figg, T. M.; Cundari, T. R.; Holland, P. L. *J. Am. Chem. Soc.* **2011**, *133*, 9796-9811.
208. Hennessy, E. T.; Liu, R. Y.; Iovan, D. A.; Duncan, R. A.; Betley, T. A. *Chem. Sci.* **2014**, *5*, 1526-1532.
209. King, E. R.; Betley, T. A. *Inorg. Chem.* **2009**, *48*, 2361-2363.
210. Xiao, J.; Deng, L. *Dalton Trans.* **2013**, *42*, 5607-5610.
211. Cowley, R. E., et al. *Inorg. Chem.* **2010**, *49*, 6172-6187.
212. Eckert, N. A.; Vaddadi, S.; Stoian, S.; Lachicotte, R. J.; Cundari, T. R.; Holland, P. L. *Angew. Chem. Int. Ed.* **2006**, *45*, 6868-6871.
213. Cowley, R. E.; Holland, P. L. *Inorg. Chem.* **2012**, *51*, 8352-8361.
214. Okuniewski, A.; Rosiak, D.; Chojnacki, J.; Becker, B. *Polyhedron* **2015**, *90*, 47-57.
215. Yang, L.; Powell, D. R.; Houser, R. P. *Dalton Trans.* **2007**, 955-964.
216. SAINT, Version 7.03A; Bruker AXS Inc: Madison, Wisconsin, USA, 1997-2003.
217. SADABS, V2.10; Bruker AXS Inc.: Madison, Wisconsin, USA, 2003.
218. Dolomanov, O. V.; Bourhis, L. J.; Gildea, R. J.; Howard, J. A. K.; Puschmann, H. *J. Appl. Crystallogr.* **2009**, *42*, 339-341.
219. Sheldrick, G. *Acta Crystallogr. Sect. A* **2008**, *64*, 112-122.
220. Farrugia, L. J. *J. Appl. Crystallogr.* **1997**, *30*, 565-565.

221. Frisch, M. J., et al. *Gaussian 09*, Gaussian Inc: Wallingford, CT, 2009.
222. Stephens, P. J.; Devlin, F. J.; Chabalowski, C. F.; Frisch, M. J. *J. Phys. Chem.* **1994**, *98*, 11623-11627.
223. Ittel, S. D.; English, A. D.; Tolman, C. A.; Jesson, J. P. *Inorg. Chim. Acta* **1979**, *33*, 101-106.
224. Keim, W.; Killat, S.; Nobile, C. F.; Suranna, G. P.; Englert, U.; Wang, R.; Mecking, S.; Schröder, D. L. *J. Organomet. Chem.* **2002**, *662*, 150-171.
225. Guan, Z.; Marshall, W. J. *Organometallics* **2002**, *21*, 3580-3586.
226. Pi, R.; Friedl, T.; Schleyer, P. v. R.; Klusener, P.; Brandsma, L. *J. Org. Chem.* **1987**, *52*, 4299-4303.
227. Lalancette, J.-M.; Rollins, G.; Dumas, P. *Can. J. Chem.* **1972**, *50*, 3058-3062.

## Appendices

### Appendix A - Crystallographic Information

	2.19	2.20
Empirical formula	C <sub>21</sub> H <sub>25</sub> N	C <sub>39</sub> H <sub>55</sub> N <sub>4</sub> P
Formula weight	291.42	610.84
Temperature (K)	90	90.15
Crystal system	triclinic	monoclinic
Space group	P-1	P2 <sub>1</sub> /c
a (Å)	8.5400(7)	13.301(5)
b (Å)	10.3907(8)	14.313(6)
c (Å)	10.9422(9)	19.285(7)
α (°)	113.943(2)	90
β (°)	101.308(2)	120.346(8)
γ (°)	99.969(2)	90
Volume (Å <sup>3</sup> )	834.89(12)	3586(2)
Z	2	4
ρ (g/cm <sup>3</sup> )	1.159	1.131
μ (mm <sup>-1</sup> )	0.066	0.108
F(000)	316.0	1328.0
2θ range (°)	4.264 to 60.156	3.134 to 55.096
hkl range	-11,12/-14,14/-15,15	-17,17/-18,18/-25,22
Reflections collected	17775	32054
Unique reflections [R <sub>int</sub> , R <sub>sigma</sub> ]	4869 [0.0267, 0.0248]	8228 [0.0465, 0.0471]
Data/restraints/parameters	4869/0/219	8228/0/409
Completeness to θ (%)	99.6	99.4
Goodness-of-fit on F <sup>2</sup>	1.045	1.035
Final R indexes [I ≥ 2σ(I)]	R <sub>1</sub> = 0.0399, wR <sub>2</sub> = 0.1289	R <sub>1</sub> = 0.0626, wR <sub>2</sub> = 0.1517
Final R indexes [all data]	R <sub>1</sub> = 0.0489, wR <sub>2</sub> = 0.1379	R <sub>1</sub> = 0.0867, wR <sub>2</sub> = 0.1647
Largest diff. peak/hole (eÅ <sup>-3</sup> )	0.42/-0.20	0.76/-0.44

	<b>2.22</b>	<b>2.23a</b>
Empirical formula	C <sub>47</sub> H <sub>74</sub> KN <sub>2</sub> O <sub>2</sub> P	C <sub>35</sub> H <sub>54</sub> N <sub>2</sub> PF <sub>e</sub> Br
Formula weight	769.15	669.53
Temperature (K)	90	90
Crystal system	monoclinic	orthorhombic
Space group	P2 <sub>1</sub>	Pbca
a (Å)	10.993(5)	17.3586(5)
b (Å)	18.545(5)	16.9214(5)
c (Å)	11.703(5)	23.4188(7)
α (°)	90	90
β (°)	107.095(5)	90
γ (°)	90	90
Volume (Å <sup>3</sup> )	2280.4(16)	6878.8(4)
Z	2	8
ρ (g/cm <sup>3</sup> )	1.120	1.293
μ (mm <sup>-1</sup> )	0.189	1.672
F(000)	840.0	2832.0
2θ range (°)	3.64 to 53.012	3.478 to 55.02
hkl range	-13,13/-23,23/-14,14	-22,15/-21,18/-24,30
Reflections collected	35630	34340
Unique reflections [R <sub>int</sub> , R <sub>sigma</sub> ]	9364 [0.0525, 0.0487]	7900 [0.0476, 0.0481]
Data/restraints/parameters	9364/1/502	7900/0/373
Completeness to θ (%)	99.1	99.8
Goodness-of-fit on F <sup>2</sup>	1.017	1.037
Final R indexes [I ≥ 2σ(I)]	R <sub>1</sub> = 0.0333, wR <sub>2</sub> = 0.0686	R <sub>1</sub> = 0.0528, wR <sub>2</sub> = 0.1149
Final R indexes [all data]	R <sub>1</sub> = 0.0417, wR <sub>2</sub> = 0.0715	R <sub>1</sub> = 0.0814, wR <sub>2</sub> = 0.1265
Largest diff. peak/hole (eÅ <sup>-3</sup> )	0.21/-0.24	2.57/-2.34

	<b>2.24 + Tol</b>	<b>2.23c</b>
Empirical formula	C <sub>46</sub> H <sub>62</sub> N <sub>2</sub> PFeBr	C <sub>64</sub> H <sub>96</sub> N <sub>4</sub> P <sub>2</sub> Fe <sub>2</sub> Br <sub>2</sub>
Formula weight	809.70	1254.90
Temperature (K)	90	90
Crystal system	monoclinic	triclinic
Space group	P2 <sub>1</sub> /c	P-1
a (Å)	10.890(5)	9.999(3)
b (Å)	33.651(5)	13.544(5)
c (Å)	12.666(5)	13.905(5)
α (°)	90	62.101(6)
β (°)	114.393(5)	72.296(7)
γ (°)	90	85.151(7)
Volume (Å <sup>3</sup> )	4227(3)	1581.7(9)
Z	4	1
ρ (g/cm <sup>3</sup> )	1.272	1.317
μ (mm <sup>-1</sup> )	1.373	1.813
F(000)	1712.0	660.0
2θ range (°)	2.42 to 52.504	3.41 to 54.974
hkl range	-9,12/-35,41/-15,10	-12,12/-17,17/-18,18
Reflections collected	14167	24642
Unique reflections [R <sub>int</sub> , R <sub>sigma</sub> ]	6021 [0.0541, 0.0986]	7107 [0.0767, 0.0839]
Data/restraints/parameters	6021/0/226	7107/0/345
Completeness to θ (%)	74.6	99.2
Goodness-of-fit on F <sup>2</sup>	1.097	1.055
Final R indexes [I ≥ 2σ(I)]	R <sub>1</sub> = 0.1202, wR <sub>2</sub> = 0.2751	R <sub>1</sub> = 0.0665, wR <sub>2</sub> = 0.1553
Final R indexes [all data]	R <sub>1</sub> = 0.1608, wR <sub>2</sub> = 0.2915	R <sub>1</sub> = 0.1019, wR <sub>2</sub> = 0.1683
Largest diff. peak/hole (eÅ <sup>-3</sup> )	1.88/-1.78	1.58/-0.68

	<b>2.23b</b>	<b>2.25a</b>
Empirical formula	C <sub>27</sub> H <sub>38</sub> N <sub>2</sub> PF <sub>e</sub> Br	C <sub>70</sub> H <sub>108</sub> N <sub>6</sub> P <sub>2</sub> Fe <sub>2</sub>
Formula weight	557.32	1207.26
Temperature (K)	90	90
Crystal system	triclinic	monoclinic
Space group	P-1	P2 <sub>1</sub> /c
a (Å)	13.121(3)	10.3990(6)
b (Å)	15.896(4)	28.6698(15)
c (Å)	16.706(4)	22.9617(13)
α (°)	90.837(4)	90
β (°)	109.446(4)	100.9200(10)
γ (°)	101.917(4)	90
Volume (Å <sup>3</sup> )	3201.6(14)	6721.8(6)
Z	4	4
ρ (g/cm <sup>3</sup> )	1.156	1.193
μ (mm <sup>-1</sup> )	1.783	0.523
F(000)	1160.0	2608.0
2θ range (°)	2.596 to 53.036	2.298 to 55.11
hkl range	-16,16/-19,19/-20,20	-13,13/-37,20/-24,29
Reflections collected	44303	62062
Unique reflections [R <sub>int</sub> , R <sub>sigma</sub> ]	13084 [0.1318, 0.1376]	15498 [0.0760, 0.0902]
Data/restraints/parameters	13084/0/545	15498/0/745
Completeness to θ (%)	98.5	99.7
Goodness-of-fit on F <sup>2</sup>	0.909	1.001
Final R indexes [I ≥ 2σ(I)]	R <sub>1</sub> = 0.0827, wR <sub>2</sub> = 0.2030	R <sub>1</sub> = 0.0479, wR <sub>2</sub> = 0.0834
Final R indexes [all data]	R <sub>1</sub> = 0.1452, wR <sub>2</sub> = 0.2298	R <sub>1</sub> = 0.0986, wR <sub>2</sub> = 0.0966
Largest diff. peak/hole (eÅ <sup>-3</sup> )	2.17/-1.04	0.48/-0.39

	<b>2.26</b>	<b>2.25c</b>
Empirical formula	C <sub>35.5</sub> H <sub>55.5</sub> N <sub>2</sub> PFe	C <sub>64</sub> H <sub>93.11</sub> N <sub>6</sub> P <sub>2</sub> Fe <sub>2</sub>
Formula weight	597.14	1120.19
Temperature (K)	90.15	90
Crystal system	monoclinic	monoclinic
Space group	C2/c	C2/c
a (Å)	26.340(3)	21.642(5)
b (Å)	11.8226(16)	20.337(5)
c (Å)	24.864(3)	16.105(5)
α (°)	90	90
β (°)	106.786(3)	98.831(5)
γ (°)	90	90
Volume (Å <sup>3</sup> )	7413.1(17)	7004(3)
Z	8	4
ρ (g/cm <sup>3</sup> )	1.070	1.062
μ (mm <sup>-1</sup> )	0.473	0.498
F(000)	2588.0	2404.0
2θ range (°)	3.23 to 50.36	2.764 to 50.8
hkl range	-31,21/-14,14/-22,29	-24,26/-24,24/-19,19
Reflections collected	51121	25483
Unique reflections [R <sub>int</sub> , R <sub>sigma</sub> ]	6599 [0.0389, 0.0248]	6423 [0.0696, 0.0688]
Data/restraints/parameters	6599/651/682	6423/0/362
Completeness to θ (%)	99.0	99.6
Goodness-of-fit on F <sup>2</sup>	1.066	1.071
Final R indexes [I ≥ 2σ(I)]	R <sub>1</sub> = 0.1319, wR <sub>2</sub> = 0.3467	R <sub>1</sub> = 0.0622, wR <sub>2</sub> = 0.1602
Final R indexes [all data]	R <sub>1</sub> = 0.1488, wR <sub>2</sub> = 0.3535	R <sub>1</sub> = 0.0865, wR <sub>2</sub> = 0.1682
Largest diff. peak/hole (eÅ <sup>-3</sup> )	0.67/-1.77	1.25/-0.34

	<b>2.25b</b>	<b>2.27 + pentane</b>
Empirical formula	C <sub>46</sub> H <sub>67</sub> N <sub>3</sub> P <sub>2</sub> Fe	C <sub>44</sub> H <sub>66</sub> N <sub>3</sub> PFe
Formula weight	779.81	723.81
Temperature (K)	90	90
Crystal system	monoclinic	monoclinic
Space group	P2 <sub>1</sub> /n	P2 <sub>1</sub> /c
a (Å)	19.562(3)	14.0913(8)
b (Å)	11.2091(14)	23.5984(12)
c (Å)	20.674(3)	13.2922(7)
α (°)	90	90
β (°)	112.138(3)	107.1377(19)
γ (°)	90	90
Volume (Å <sup>3</sup> )	4199.1(9)	4223.8(4)
Z	4	4
ρ (g/cm <sup>3</sup> )	1.234	1.138
μ (mm <sup>-1</sup> )	0.471	0.427
F(000)	1680.0	1568.0
2θ range (°)	2.444 to 55.158	3.024 to 52.102
hkl range	-25,24/-10,14/-26,26	-17,16/-29,28/-16,13
Reflections collected	37081	31009
Unique reflections [R <sub>int</sub> , R <sub>sigma</sub> ]	9688 [0.1579, 0.1611]	8329 [0.0350, 0.0456]
Data/restraints/parameters	9688/0/483	8329/0/482
Completeness to θ (%)	99.4	99.6
Goodness-of-fit on F <sup>2</sup>	0.974	0.981
Final R indexes [I ≥ 2σ(I)]	R <sub>1</sub> = 0.0807, wR <sub>2</sub> = 0.1703	R <sub>1</sub> = 0.0488, wR <sub>2</sub> = 0.1262
Final R indexes [all data]	R <sub>1</sub> = 0.1598, wR <sub>2</sub> = 0.2062	R <sub>1</sub> = 0.0747, wR <sub>2</sub> = 0.1489
Largest diff. peak/hole (eÅ <sup>-3</sup> )	1.23/-0.89	0.70/-0.38

	<b>2.29 + THF</b>	<b>2.31</b>
Empirical formula	C <sub>59</sub> H <sub>92</sub> KLiN <sub>2</sub> O <sub>5</sub> P	C <sub>39</sub> H <sub>53</sub> N <sub>2</sub> P
Formula weight	986.35	580.80
Temperature (K)	90	90
Crystal system	monoclinic	monoclinic
Space group	P2 <sub>1</sub>	P2 <sub>1</sub> /c
a (Å)	11.2314(10)	21.381(2)
b (Å)	19.9822(18)	19.8758(19)
c (Å)	13.5410(12)	16.7819(16)
α (°)	90	90
β (°)	110.104(2)	98.731(2)
γ (°)	90	90
Volume (Å <sup>3</sup> )	2853.8(4)	7049.1(12)
Z	2	8
ρ (g/cm <sup>3</sup> )	1.148	1.095
μ (mm <sup>-1</sup> )	0.168	0.106
F(000)	1074.0	2528.0
2θ range (°)	3.796 to 52.208	2.812 to 55.164
hkl range	-13,11/-23,24/-9,16	-27,26/-25,25/-21,20
Reflections collected	22333	64062
Unique reflections [R <sub>int</sub> , R <sub>sigma</sub> ]	10697 [0.0252, 0.0427]	16206 [0.0495, 0.0532]
Data/restraints/parameters	10697/676/642	16206/0/757
Completeness to θ (%)	94.2	99.4
Goodness-of-fit on F <sup>2</sup>	1.035	1.016
Final R indexes [I ≥ 2σ(I)]	R <sub>1</sub> = 0.0428, wR <sub>2</sub> = 0.0964	R <sub>1</sub> = 0.0479, wR <sub>2</sub> = 0.1071
Final R indexes [all data]	R <sub>1</sub> = 0.0523, wR <sub>2</sub> = 0.1011	R <sub>1</sub> = 0.0789, wR <sub>2</sub> = 0.1205
Largest diff. peak/hole (eÅ <sup>-3</sup> )	0.50/-0.38	0.35/-0.47

	<b>3.6a + Tol</b>	<b>3.7</b>
Empirical formula	C <sub>77</sub> H <sub>118</sub> N <sub>4</sub> P <sub>2</sub> Fe <sub>2</sub>	C <sub>39</sub> H <sub>66</sub> BN <sub>2</sub> PFe
Formula weight	1273.39	660.56
Temperature (K)	90	90
Crystal system	monoclinic	monoclinic
Space group	C2/c	P2 <sub>1</sub> /c
a (Å)	27.742(2)	16.9333(7)
b (Å)	14.1520(11)	11.7516(5)
c (Å)	19.4285(16)	20.0066(7)
α (°)	90	90
β (°)	109.947(2)	100.5590(10)
γ (°)	90	90
Volume (Å <sup>3</sup> )	7170.2(10)	3913.8(3)
Z	4	4
ρ (g/cm <sup>3</sup> )	1.180	1.121
μ (mm <sup>-1</sup> )	0.493	0.453
F(000)	2760.0	1440.0
2θ range (°)	3.124 to 61.13	4.036 to 50.136
hkl range	-39,39/-20,20/-27,27	-20,17/-12,14/-23,22
Reflections collected	83546	29547
Unique reflections [R <sub>int</sub> , R <sub>sigma</sub> ]	10979 [0.0645, 0.0380]	6921 [0.0605, 0.0656]
Data/restraints/parameters	10979/6/396	6921/0/419
Completeness to θ (%)	99.6	99.7
Goodness-of-fit on F <sup>2</sup>	1.047	1.005
Final R indexes [I ≥ 2σ(I)]	R <sub>1</sub> = 0.0488, wR <sub>2</sub> = 0.1171	R <sub>1</sub> = 0.0500, wR <sub>2</sub> = 0.1031
Final R indexes [all data]	R <sub>1</sub> = 0.0708, wR <sub>2</sub> = 0.1290	R <sub>1</sub> = 0.0809, wR <sub>2</sub> = 0.1143
Largest diff. peak/hole (eÅ <sup>-3</sup> )	2.20/-0.68	0.45/-0.49

	<b>3.8a</b>	<b>3.8b</b>
Empirical formula	C <sub>37</sub> H <sub>56.67</sub> N <sub>2</sub> PFe	C <sub>37</sub> H <sub>53</sub> N <sub>2</sub> PFe
Formula weight	616.33	576.60
Temperature (K)	90	90
Crystal system	orthorhombic	triclinic
Space group	Pbca	P-1
a (Å)	19.4365(19)	9.0734(18)
b (Å)	17.908(2)	12.849(3)
c (Å)	19.954(2)	14.551(3)
α (°)	90	99.626(4)
β (°)	90	105.346(4)
γ (°)	90	95.949(4)
Volume (Å <sup>3</sup> )	6945.5(13)	1593.3(5)
Z	8	2
ρ (g/cm <sup>3</sup> )	1.179	1.202
μ (mm <sup>-1</sup> )	0.507	0.548
F(000)	2669.0	624.0
2θ range (°)	3.706 to 59.222	3.254 to 61.168
hkl range	-27,26/-24,23/-27,27	-12,12/-18,18/-20,20
Reflections collected	76719	37596
Unique reflections [R <sub>int</sub> , R <sub>sigma</sub> ]	9766 [0.0354, 0.0205]	9738 [0.0321, 0.0297]
Data/restraints/parameters	9766/0/436	9738/0/355
Completeness to θ (%)	99.9	99.5
Goodness-of-fit on F <sup>2</sup>	1.027	1.020
Final R indexes [I ≥ 2σ(I)]	R <sub>1</sub> = 0.0309, wR <sub>2</sub> = 0.0840	R <sub>1</sub> = 0.0306, wR <sub>2</sub> = 0.0767
Final R indexes [all data]	R <sub>1</sub> = 0.0379, wR <sub>2</sub> = 0.0889	R <sub>1</sub> = 0.0380, wR <sub>2</sub> = 0.0804
Largest diff. peak/hole (eÅ <sup>-3</sup> )	0.42/-0.30	0.49/-0.25

	<b>3.6b + Tol</b>	<b>3.9</b>
Empirical formula	C <sub>71</sub> H <sub>106</sub> N <sub>4</sub> P <sub>2</sub> Fe <sub>2</sub>	C <sub>47</sub> H <sub>65</sub> N <sub>4</sub> PFe
Formula weight	1189.23	772.85
Temperature (K)	90	90
Crystal system	monoclinic	orthorhombic
Space group	P2 <sub>1</sub> /c	P2 <sub>1</sub> 2 <sub>1</sub> 2 <sub>1</sub>
a (Å)	11.309(2)	11.4731(10)
b (Å)	28.217(5)	19.0046(18)
c (Å)	23.023(4)	20.1296(17)
α (°)	90	90
β (°)	103.683(4)	90
γ (°)	90	90
Volume (Å <sup>3</sup> )	7138(2)	4389.1(7)
Z	4	4
ρ (g/cm <sup>3</sup> )	1.107	1.170
μ (mm <sup>-1</sup> )	0.491	0.416
F(000)	2568.0	1664.0
2θ range (°)	2.324 to 55.208	4.086 to 55.73
hkl range	-14,14/-32,36/-30,26	-14,14/-24,24/-26,26
Reflections collected	64714	64774
Unique reflections [R <sub>int</sub> , R <sub>sigma</sub> ]	16471 [0.0978, 0.1099]	10218 [0.0931, 0.0757]
Data/restraints/parameters	16471/4/701	10218/0/490
Completeness to θ (%)	99.2	98.1
Goodness-of-fit on F <sup>2</sup>	1.054	1.015
Final R indexes [I ≥ 2σ(I)]	R <sub>1</sub> = 0.0904, wR <sub>2</sub> = 0.2392	R <sub>1</sub> = 0.0535, wR <sub>2</sub> = 0.1355
Final R indexes [all data]	R <sub>1</sub> = 0.1404, wR <sub>2</sub> = 0.2615	R <sub>1</sub> = 0.0643, wR <sub>2</sub> = 0.1405
Largest diff. peak/hole (eÅ <sup>-3</sup> )	3.62/-1.18	0.68/-0.32

	<b>3.12</b>	<b>3.10</b>
Empirical formula	C <sub>41</sub> H <sub>60</sub> N <sub>3</sub> PFe	C <sub>41</sub> H <sub>65</sub> N <sub>2</sub> PFe
Formula weight	681.74	672.77
Temperature (K)	90	90
Crystal system	monoclinic	triclinic
Space group	P2 <sub>1</sub> /n	P-1
a (Å)	12.4468(9)	10.5433(8)
b (Å)	21.4043(16)	11.8988(9)
c (Å)	28.757(2)	16.9020(12)
α (°)	90	95.482(4)
β (°)	93.036(2)	100.646(4)
γ (°)	90	108.968(4)
Volume (Å <sup>3</sup> )	7650.5(10)	1942.9(3)
Z	8	2
ρ (g/cm <sup>3</sup> )	1.184	1.150
μ (mm <sup>-1</sup> )	0.467	0.458
F(000)	2944.0	732.0
2θ range (°)	2.374 to 43.522	3.672 to 55.088
hkl range	-12,12/-21,21/-28,28	-13,13/-15,15/-21,21
Reflections collected	57697	34076
Unique reflections [R <sub>int</sub> , R <sub>sigma</sub> ]	7887 [0.1170, 0.0593]	8917 [0.0423, 0.0403]
Data/restraints/parameters	7887/5/849	8917/0/420
Completeness to θ (%)	86.8	99.5
Goodness-of-fit on F <sup>2</sup>	1.818	1.051
Final R indexes [I ≥ 2σ(I)]	R <sub>1</sub> = 0.0975, wR <sub>2</sub> = 0.2482	R <sub>1</sub> = 0.0443, wR <sub>2</sub> = 0.1188
Final R indexes [all data]	R <sub>1</sub> = 0.1257, wR <sub>2</sub> = 0.2629	R <sub>1</sub> = 0.0575, wR <sub>2</sub> = 0.1277
Largest diff. peak/hole (eÅ <sup>-3</sup> )	2.87/-0.76	0.88/-0.54

	<b>3.11 + Tol</b>	<b>3.14 + Tol</b>
Empirical formula	C <sub>32.33</sub> H <sub>49.33</sub> N <sub>3.33</sub> P <sub>0.67</sub> Fe <sub>0.67</sub>	C <sub>73.5</sub> H <sub>112</sub> N <sub>4</sub> F <sub>2</sub> P <sub>2</sub> Fe <sub>2</sub>
Formula weight	542.63	1263.30
Temperature (K)	100	90
Crystal system	monoclinic	monoclinic
Space group	P2 <sub>1</sub> /n	P2 <sub>1</sub> /c
a (Å)	10.4848(10)	20.445(6)
b (Å)	24.631(3)	13.612(4)
c (Å)	17.7095(19)	26.186(9)
α (°)	90	90
β (°)	98.444(4)	92.564(9)
γ (°)	90	90
Volume (Å <sup>3</sup> )	4523.9(8)	7280(4)
Z	6	4
ρ (g/cm <sup>3</sup> )	1.195	1.153
μ (mm <sup>-1</sup> )	0.407	0.489
F(000)	1764.0	2716.0
2θ range (°)	4.26 to 53.61	1.994 to 44.786
hkl range	-13,9/-31,30/-22,18	-21,21/0,14/0,28
Reflections collected	28699	9266
Unique reflections [R <sub>int</sub> , R <sub>sigma</sub> ]	9560 [0.0604, 0.0799]	9266 [R <sub>sigma</sub> = 0.1002]
Data/restraints/parameters	9560/0/531	9266/735/802
Completeness to θ (%)	98.7	97.9
Goodness-of-fit on F <sup>2</sup>	1.052	1.031
Final R indexes [I ≥ 2σ(I)]	R <sub>1</sub> = 0.0452, wR <sub>2</sub> = 0.1076	R <sub>1</sub> = 0.0613, wR <sub>2</sub> = 0.1311
Final R indexes [all data]	R <sub>1</sub> = 0.0716, wR <sub>2</sub> = 0.1177	R <sub>1</sub> = 0.0948, wR <sub>2</sub> = 0.1454
Largest diff. peak/hole (eÅ <sup>-3</sup> )	0.48/-0.34	0.53/-0.48

	<b>4.6</b>	<b>4.7</b>
Empirical formula	C <sub>31</sub> H <sub>47</sub> N <sub>4</sub> P	C <sub>19.5</sub> H <sub>31</sub> N <sub>2</sub> OP <sub>0.5</sub> K <sub>0.5</sub>
Formula weight	506.70	344.50
Temperature (K)	90	90
Crystal system	triclinic	triclinic
Space group	P-1	P-1
a (Å)	8.4137(10)	9.742(2)
b (Å)	12.3149(14)	10.616(2)
c (Å)	16.0458(19)	19.454(5)
α (°)	68.433(2)	74.814(5)
β (°)	80.379(2)	79.099(5)
γ (°)	83.219(3)	84.049(5)
Volume (Å <sup>3</sup> )	1521.5(3)	1903.6(8)
Z	2	4
ρ (g/cm <sup>3</sup> )	1.106	1.202
μ (mm <sup>-1</sup> )	0.115	0.220
F(000)	552.0	748.0
2θ range (°)	2.76 to 59.42	3.982 to 61.088
hkl range	-7,11/-16,17/-22,22	-13,13/-15,15/-27,25
Reflections collected	32276	39455
Unique reflections [R <sub>int</sub> , R <sub>sigma</sub> ]	8629 [0.0207, 0.0199]	11257 [0.0302, 0.0353]
Data/restraints/parameters	8629/0/339	11257/0/434
Completeness to θ (%)	99.7	96.6
Goodness-of-fit on F <sup>2</sup>	1.032	1.207
Final R indexes [I ≥ 2σ(I)]	R <sub>1</sub> = 0.0372, wR <sub>2</sub> = 0.0976	R <sub>1</sub> = 0.0625, wR <sub>2</sub> = 0.1580
Final R indexes [all data]	R <sub>1</sub> = 0.0438, wR <sub>2</sub> = 0.1026	R <sub>1</sub> = 0.0765, wR <sub>2</sub> = 0.1637
Largest diff. peak/hole (eÅ <sup>-3</sup> )	0.61/-0.27	0.92/-0.39

	<b>4.8</b>	<b>4.9</b>
Empirical formula	C <sub>35</sub> H <sub>54</sub> N <sub>4</sub> OPFeBr	C <sub>23</sub> H <sub>37</sub> N <sub>2</sub> PFe
Formula weight	713.55	428.36
Temperature (K)	90	90
Crystal system	orthorhombic	triclinic
Space group	Pca2 <sub>1</sub>	P-1
a (Å)	17.547(5)	8.526(3)
b (Å)	10.262(5)	11.951(3)
c (Å)	20.588(5)	12.272(4)
α (°)	90	69.55(2)
β (°)	90	87.64(3)
γ (°)	90	80.07(3)
Volume (Å <sup>3</sup> )	3707(2)	1153.8(6)
Z	4	2
ρ (g/cm <sup>3</sup> )	1.278	1.233
μ (mm <sup>-1</sup> )	1.559	0.733
F(000)	1504.0	460.0
2θ range (°)	3.956 to 46.666	3.542 to 60.168
hkl range	-19,16/-11,10/-19,22	-12,11/-16,16/-17,17
Reflections collected	11758	26609
Unique reflections [R <sub>int</sub> , R <sub>sigma</sub> ]	5063 [0.0558, 0.0794]	6724 [0.0208, 0.0194]
Data/restraints/parameters	5063/109/349	6724/0/244
Completeness to θ (%)	99.2	99.4
Goodness-of-fit on F <sup>2</sup>	1.022	1.050
Final R indexes [I ≥ 2σ(I)]	R <sub>1</sub> = 0.0472, wR <sub>2</sub> = 0.1014	R <sub>1</sub> = 0.0313, wR <sub>2</sub> = 0.0794
Final R indexes [all data]	R <sub>1</sub> = 0.0712, wR <sub>2</sub> = 0.1105	R <sub>1</sub> = 0.0393, wR <sub>2</sub> = 0.0852
Largest diff. peak/hole (eÅ <sup>-3</sup> )	0.63/-0.55	0.58/-0.23

	<b>4.11 + 2 THF</b>	<b>4.13</b>
Empirical formula	C <sub>44</sub> H <sub>67</sub> N <sub>5</sub> O <sub>2</sub> PClCo	C <sub>40</sub> H <sub>62</sub> N <sub>5</sub> SiPCo
Formula weight	823.37	730.93
Temperature (K)	90	90
Crystal system	monoclinic	triclinic
Space group	P2 <sub>1</sub> /n	P-1
a (Å)	8.8388(13)	8.930(3)
b (Å)	25.147(4)	12.010(4)
c (Å)	20.100(3)	20.038(7)
α (°)	90	95.382(6)
β (°)	99.259(3)	90.604(6)
γ (°)	90	106.093(6)
Volume (Å <sup>3</sup> )	4409.2(11)	2054.2(12)
Z	4	2
ρ (g/cm <sup>3</sup> )	1.240	1.182
μ (mm <sup>-1</sup> )	0.527	0.519
F(000)	1764.0	786.0
2θ range (°)	2.614 to 55.084	3.548 to 55.042
hkl range	-11,11/-32,29/-26,25	-11,10/-24,24/0,28
Reflections collected	37633	8480
Unique reflections [R <sub>int</sub> , R <sub>sigma</sub> ]	10160 [0.0427, 0.0484]	8480 [R <sub>sigma</sub> = 0.3702]
Data/restraints/parameters	10160/0/505	8480/0/446
Completeness to θ (%)	99.7	89.6
Goodness-of-fit on F <sup>2</sup>	1.039	1.065
Final R indexes [I ≥ 2σ(I)]	R <sub>1</sub> = 0.0455, wR <sub>2</sub> = 0.0974	R <sub>1</sub> = 0.1222, wR <sub>2</sub> = 0.2791
Final R indexes [all data]	R <sub>1</sub> = 0.0714, wR <sub>2</sub> = 0.1076	R <sub>1</sub> = 0.2338, wR <sub>2</sub> = 0.3208
Largest diff. peak/hole (eÅ <sup>-3</sup> )	0.84/-0.92	1.48/-1.02

---

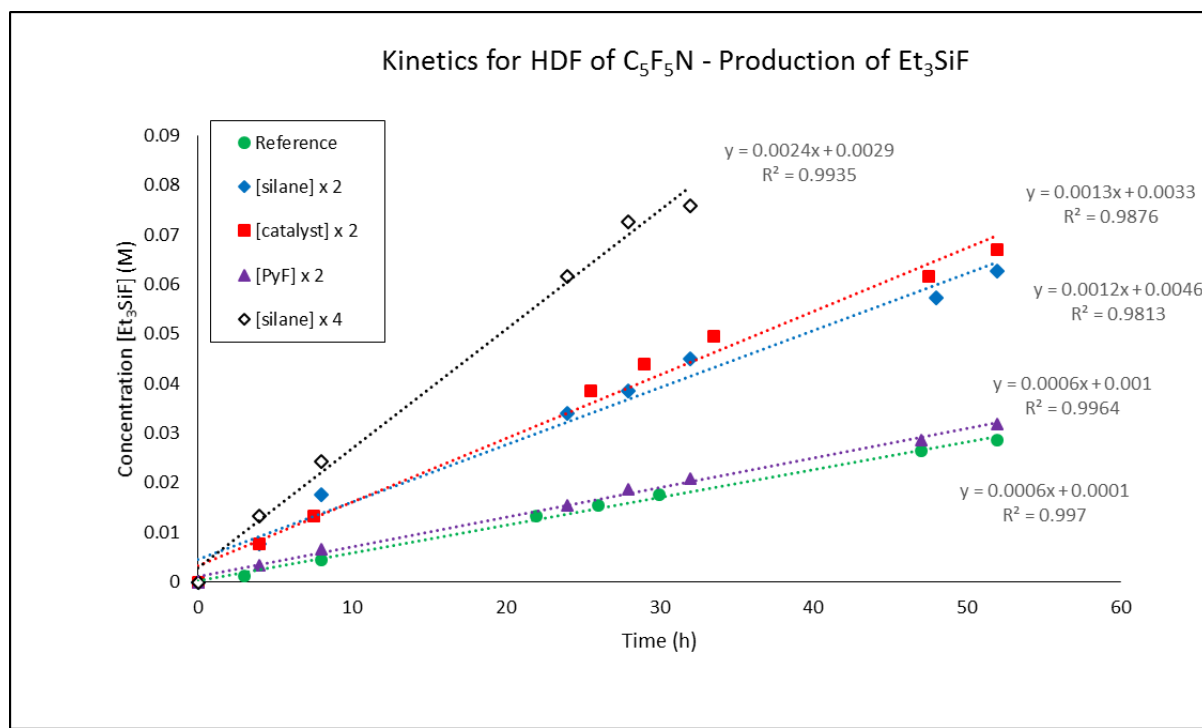
**5.12**

---

Empirical formula	C <sub>42</sub> H <sub>63</sub> N <sub>3</sub> PFeBr
Formula weight	776.68
Temperature (K)	90
Crystal system	monoclinic
Space group	P2 <sub>1</sub> /c
a (Å)	15.474(5)
b (Å)	9.807(3)
c (Å)	25.757(8)
α (°)	90
β (°)	92.632(6)
γ (°)	90
Volume (Å <sup>3</sup> )	3905(2)
Z	4
ρ (g/cm <sup>3</sup> )	1.321
μ (mm <sup>-1</sup> )	1.483
F(000)	1648.0
2θ range (°)	2.634 to 55.222
hkl range	-20,20/-12,12/0,33
Reflections collected	16753
Unique reflections [R <sub>int</sub> , R <sub>sigma</sub> ]	8973 [0.1003, 0.2002]
Data/restraints/parameters	8973/0/448
Completeness to θ (%)	99.0
Goodness-of-fit on F <sup>2</sup>	1.004
Final R indexes [I ≥ 2σ(I)]	R <sub>1</sub> = 0.0672, wR <sub>2</sub> = 0.1406
Final R indexes [all data]	R <sub>1</sub> = 0.1278, wR <sub>2</sub> = 0.1591
Largest diff. peak/hole (eÅ <sup>-3</sup> )	1.75/-0.83

---

## Appendix B - Kinetics for HDF of C<sub>5</sub>F<sub>5</sub>N – Production of Et<sub>3</sub>SiF



Kinetic evaluation for the production of Et<sub>3</sub>SiF during the hydrodefluorination of pentafluoropyridine. The trials shown in the above figure are from the same conditions outlined in the main text (reference: [silane]=[PyF]=0.11 M, [Fe]=5.5 × 10<sup>-3</sup> M using d<sub>8</sub>-THF at 50 °C).